UNIVERSITÀ DEGLI STUDI DI PADOVA

Centro interdipartimentale "Centro Ricerche Fusione"

UNIVERSITÀ DEGLI STUDI DI NAPOLI FEDERICO II

Dipartimento di Ingegneria Elettrica e delle Tecnologie dell'Informazione

Joint research doctorate in Fusion Science and Engineering

CYCLE XXXVI

FINAL DISSERTATION

Influence of plasma formation and expansion on beam extraction in large negative ion sources

Chair of Academic Board: Prof. Eng. Gianmaria De Tommasi

Supervisors: Prof. Eng. Emanuele Sartori

Dr. Gianluigi Serianni

Candidate: Valeria Candeloro

November 23, 2023

To my family
and Mattia

木の根(ね)が 僕(ぼく)たちを守(まも)つてくたれんだ

“sono state le radici ad averci protetto”

Abstract

Several countries worldwide are collaborating for building ITER, an international experiment with the goal of showcasing the feasibility of generating energy through controlled thermonuclear fusion. To achieve the necessary conditions for producing energy by fusion reactions, it is essential to confine an extremely hot plasma for a sufficiently long period. To this purpose additional heating systems are envisaged in ITER, including Neutral Beam Injection (NBI): this technique allows to deliver additional heating power via a high-energy neutral beam, created by neutralizing a precursor negative ion beam. In the ITER case, the NBI requirements in terms of beam current, energy, focusing, and uniformity are very demanding, and they have never been achieved so far. In addition, the ITER NBI will employ radio-frequency (RF) driven ion sources to produce and extract negative ions, differently from the negative NBI systems of other fusion experiments which instead are based on the more established arc-filament discharge method. The R&D activities on the ITER NBI are mainly being carried out in the Neutral Beam Test Facility (NBTF), hosted by Consorzio RFX in Padua (Italy). The goal of the NBTF is to build and successfully operate the full scale prototype of the ITER NBI, named MITICA, which is currently under construction. The NBTF also includes the SPIDER experiment, namely the full size prototype of the ITER NBI ion source equipped with a 100 kV *accelerator. Recent operation of the SPIDER experiment highlighted the need for a more thorough characterisation of the plasma properties in the ion source, as the latter were found to directly influence the extracted negative ion beam features. In this framework, the aim of this thesis work is to investigate the plasma behaviour in large negative ion sources, possibly defining their correlation with the extracted beam current density uniformity and the beam divergence. To this purpose, both experimental tools such as Langmuir probes and numerical tools have been exploited. In particular, a Particle-In-Cell simulation code was improved and used to study the main plasma mechanisms in different regions of the ion source.*

Sommario

Una collaborazione mondiale tra molte nazioni è in corso per costruire ITER, un esperimento internazionale devoto a dimostrare la fattibilità di generare energia elettrica tramite fusione termonucleare controllata. Per raggiungere le condizioni necessarie a produrre energia tramite reazioni di fusione nucleare, è necessario confinare un plasma estremamente caldo per tempi sufficientemente estesi. A questo scopo, diversi meccanismi di riscaldamento addizionale verranno integrati su ITER, inclusa l'iniezione di fasci di neutri: questa tecnica permette di trasferire potenza di riscaldamento addizionale al plasma tramite fasci di neutri ad alta energia, creati tramite la neutralizzazione di un fascio prescursore di ioni negativi. Nel caso di ITER, i requisiti per l'iniettore di neutri in termini di corrente, energia, focalizzazione e uniformità del fascio sono molto esigenti, e non sono mai stati soddisfatti finora. Inoltre, l'iniettore di ITER è basato sull'utilizzo di sorgenti a radiofrequenza (RF) per produrre ed estrarre gli ioni negativi, a differenza di altri iniettori basati su fascio di ioni negativi utilizzati in ambito fusionistico, che invece prevedono l'utilizzo di una tecnica più consolidata come le sorgenti ad arco. Le attività di ricerca e sviluppo sull'iniettore di ITER sono per la maggior parte svolte nella Neutral Beam Test Facility (NBTF), presso il Consorzio RFX a Padova. Lo scopo di NBTF è quello di costruire e operare il prototipo in scala 1:1 dell'iniettore, chiamato MITICA, che è al momento in fase di costruzione. NBTF include anche SPIDER, il prototipo della sorgente di ioni negativi con un acceleratore da 100 kV. *La recente sperimentazione in SPIDER ha messo in risalto il bisogno di caratterizzare in modo più accurato le proprietà del plasma nella sorgente, poiché esse influenzano direttamente le caratteristiche del fascio estratto di ioni negativi. In questo contesto, lo scopo di questa tesi è quello di studiare il comportamento del plasma in sorgenti di ioni negativi per la fusione nucleare, possibilmente delineando la correlazione tra le proprietà del plasma in sorgente e quelle del fascio estratto, nello specifico l'uniformità della densità di corrente del fascio e la sua divergenza. Metodi sia sperimentali che numerici sono stati utilizzati a questo scopo. In particolare, un codice Particle-In-Cell è stato migliorato e utilizzato per studiare i principali meccanismi alla base del funzionamento della sorgente nelle sue diverse regioni.*

Contents

List of Figures

List of Tables

List of Acronyms

AES Allison Emittance Scanner.

BCM Beamlet Current Monitor.

BES Beamlet Emission Spectroscopy.

BiCGSTAB BiConjugate Gradient STABilized method.

BP Bias Plate.

BSI Back-Streaming Ions.

BUG BATMAN (BAvarian Test MAchine for Negative ions) UpGrade.

CE Co-extracted Electrons.

CESM Co-extracted Electrons Suppression Magnets.

CPU Central Processing Unit.

CR Collisional Radiative.

CRDS Cavity-Ring Down Spectroscopy.

EG Extraction Grid.

ELISE Extraction from a Large Ion Source Experiment.

EP Electrostatic Probes.

FDM Finite Differences Method.

FF Filter Field.

FSFS2D Fluid Solver For Spider 2D.

GG Grounded Grid.

GMRES Generalized Minimal RESidual method.

GPGPU General Purpose Graphics Processing Units.

GPPIC General Purpose Particle In Cell.

GPU Graphics Processing Unit.

HNB Heating Neutral Beam.

ICF Inertial Confinement Fusion.

IEDF Ion Energy Distribution Function.

IPP Max-Planck Institut für Plasma Physik.

JAERI Japan Atomic Energy Research Institute.

LAS Laser Absorption Spectroscopy.

MANITU Multi-Ampere Negative Ion Test Unit.

MANTIS MANTIS.

MCF Magnetic Confinement Fusion.

MITICA Megavolt ITER Injector and Concept Advancement.

MPW MacroParticle Weight.

MTF Megavolt Test Facility.

NBI Neutral Beam Injection/Injector.

NBTF Neutral Beam Test Facility.

NIFS National Institute for Fusion Science.

NNBI Negative ion-based Neutral Beam Injector.

OES Optical Emission Spectroscopy.

PEZ Plasma Exclusion Zone.

PG Plasma Grid.

PGM Plasma Grid Mask.

PI Proportional-Integral.

PIC Particle In Cell.

PL Plasma Light.

PNBI Positive ion-based Neutral Beam Injector.

PWI Plasma-Wall Interaction.

QST National Institutes for Quantum Science and Technology.

RF Radio-Frequency.

RFEA Retarding Field Energy Analyser.

RFF Reversed Filter Field Configuration.

RID Residual Ion Dump.

RNIS Research and development Negative Ion Source.

SFF Standard Filter Field Configuration.

SPIDER Source for the Production of Ions of Deuterium Extracted from a RF plasma.

STRIKE Short-Time Retractable Instrumented Kalorimeter Experiment.

TLP Triple Langmuir Probe.

Framework

Sustainable energy production is undeniably one of the most urgent challenges for humankind. The Earth's climate can only be preserved by employing new, clean, and safe energy sources, as predicted bt the energy scenarios for the next 30 years. Controlled thermonuclear fusion can provide a powerful and sustainable way to produce electrical energy. To this purpose, several nations around the world are cooperating for the construction of the ITER experiment, aiming at demonstrating the feasibility of large scale fusion energy production.

World energy scenarios

Global energy scenarios significantly impact our daily lives, shaping and supporting our societies in numerous ways. Since the 19th century, there has been a rapid growth in energy demand, leading to the development of innovative techniques for energy production. These advancements forged remarkable scientific and technological progress, fueling economic development and contributing to the widespread adoption of digital technologies, improving our living standards. This resulted in an exponential surge in the demand for electricity, heating, cooling, and transportation, which is currently straining the world's energy system[1],[2].

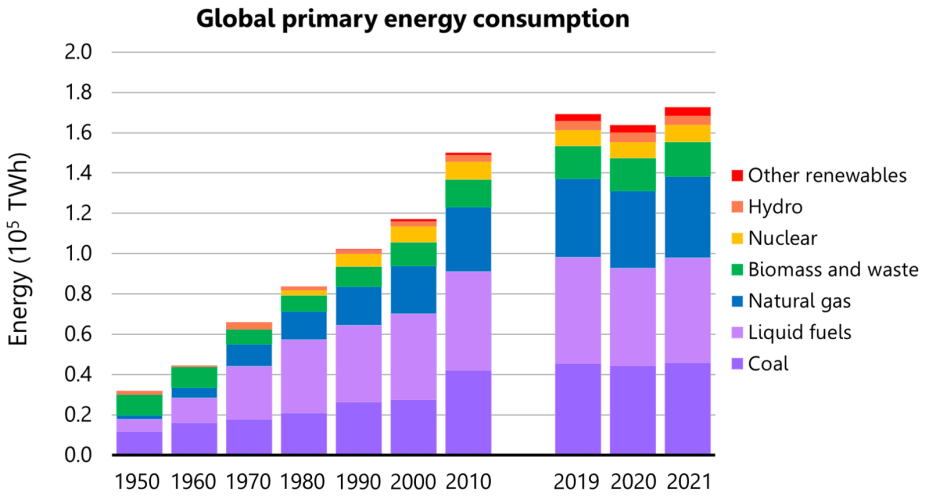

Figure 1: World primary energy demand divided by source type. Liquid fuels still provide roughly 30% of the total consumed energy.

According to projections[3], a 30% increase in the global final energy consumption can be expected by 2050. This upward trend is influenced by several factors, including population

growth, urbanization, and an increase in primary energy end-use per capita. To comply with this escalating energy demand while mitigating excessive costs, fossil fuels have remained the primary source of energy (as depicted in Figure 1). Their relatively low production costs and ease of transportation have contributed to the continued reliance on them. However, the consequences of our fossil fuel-based energy production on the Earth's climate have become strikingly evident over the past few decades, with greenhouse gas emissions posing a significant threat to the planet's well-being[4].

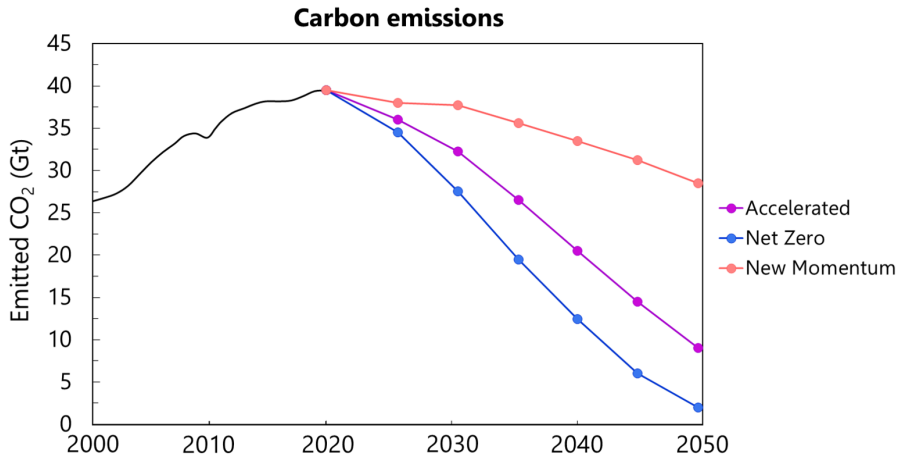

Figure 2: Global carbon emissions, including CO_2 emitted from energy use, industrial processes, natural gas flaring and methan emission for energy production. Future projections from three different energy scenarios are shown.

Today, addressing the challenge of increasing the primary energy supply while harnessing renewable energy sources has become an urgent priority. Following the adoption of the Glasgow Climate Pact in November 2021, the international community aims to achieve net zero global CO_2 emissions by 2050, as demonstrated by the *Net Zero* scenario (blue line) depicted in Figure 2. Two other energy scenarios, called *Accelerated* and *New Momentum*, are also presented. Similarly to *Net Zero*, *Accelerated* assumes the adoption of low-carbon energy systems in most of the global climate policies, as well as an important change in our lifestyle. The *New Momentum* scenario instead is based on the decarbonization trend of the most recent years.

Achieving sustainable energy production necessitates a reduction in fossil fuel exploitation by a factor between 25% or 75% depending on the specific energy scenarios, in favor of renewable energy sources, including the most diffused solar energy, wind power, hydropower, and biofuels. Nonetheless, the production efficiency of these latter energy sources is influenced by various factors such as geographic location, availability, continuity of supply and climate conditions, making them insufficient to meet the future primary energy demand.

Nuclear fission reactors have significantly contributed to energy production, in the context of a pool of various, mostly renewable, energy sources since the second half of the 20th century. These reactors sustain controlled fission chain reactions, generating energy by splitting heavy nuclei, primarily Uranium-236, into lighter nuclei. The resulting heat energy is subsequently converted into kinetic energy through turbines, ultimately producing electricity. While safety measures for fission reactors have significantly improved, inherent risks associated with chain reactions and the production of highly radioactive waste remain a challenge. Moreover, most currently operating fission reactors are approaching the end of their operational lifespan, with scheduled decommissioning within the next 5 to 10 years, although efforts are being made to implement new policies supporting the renewal of existing reactors.

Within this context, the pursuit of controlled thermonuclear fusion emerges as a compelling solution to address the challenges of sustainable energy production. The basic operational scheme of a fusion reactor is similar to the one already described for nuclear fission, although the primary energy production mechanism is substantially different: in fact, through nuclear fusion light nuclei are combined into heavier nuclei, producing energy. Nuclear fusion holds the promise of providing a long lasting and clean energy source, releasing an immense amount of energy. In fact, 1 g of fusion fuel has the potential to yield approximately the same amount of energy produced through combustion of 1 ton of fossil fuel. Moreover, unlike nuclear fission, fusion reactions generate minimal radioactive waste and operate with a nearly infinite fuel supply. Harnessing the power of nuclear fusion has the potential to revolutionize the global energy landscape, offering a long-term sustainable solution to meet the growing energy demand.

Nuclear fusion as the future energy source

The most promising nuclear fusion reactions for obtaining controlled thermonuclear fusion in laboratories involve hydrogen isotopes and helium, namely:

$$
\begin{array}{lcl}
{}^{2}_{1}\mathrm{D}+{}^{3}_{2}\mathrm{He} & \rightarrow & {}^{4}_{2}\mathrm{He}(3.6\,\mathrm{MeV})+p(14.7\,\mathrm{MeV}) \\
{}^{2}_{1}\mathrm{D}+{}^{3}_{1}\mathrm{T} & \rightarrow & {}^{4}_{2}\mathrm{He}(3.5\,\mathrm{MeV})+n(14.1\,\mathrm{MeV}) \\
{}^{2}_{1}\mathrm{D}+{}^{2}_{1}\mathrm{D} & \rightarrow & {}^{3}_{1}\mathrm{T}(1.0\,\mathrm{MeV})+p(3.0\,\mathrm{MeV}) \\
{}^{2}_{1}\mathrm{D}+{}^{2}_{1}\mathrm{D} & \rightarrow & {}^{3}_{2}\mathrm{He}(0.8\,\mathrm{MeV})+n(2.5\,\mathrm{MeV})
\end{array}
$$

Table 1: Suitable reactions for controlled thermonuclear fusion, in descending order of produced energy.

The D-T reaction features the highest cross section for lower values of ion temperatures, as depicted by the blue curve in Figure 3, with the peak probability centered around 100 keV. The D-D reactions have significantly lower cross sections, therefore the D-T process is the most relevant one for controlled thermonuclear fusion despite the rather low tritium availability.

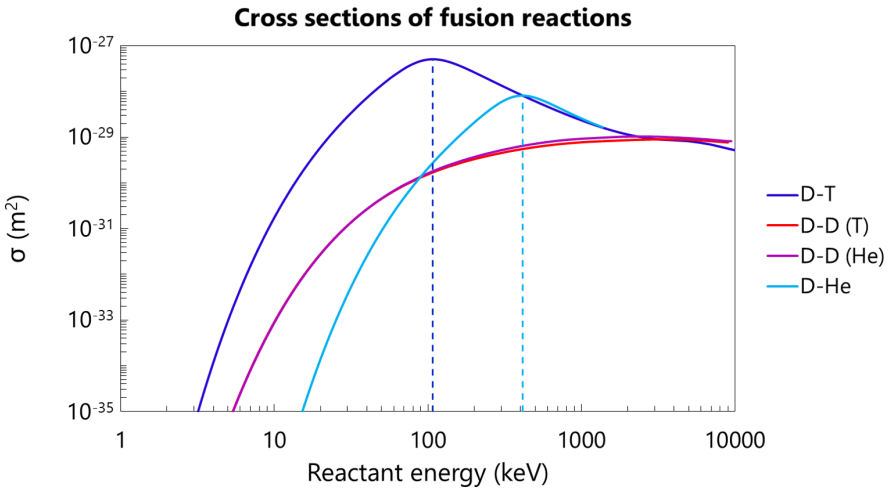

Figure 3: Cross sections of D-T, D-D(He), D-D(T), D-He fusion reactions. Yielding the highest probability for lower ion temperatures, the D-T process will be exploited in future reactors.

In order to fuse together, the reactants will need to overcome the repulsive Coulomb barrier due to the positive charge of their nuclei. To this purpose, either inertial or magnetic confinement can be exploited: Inertial Confinement Fusion (ICF) takes place by heating deuterium or tritium targets with high power laser beams; this energy causes the outer layer of the targets to explode, producing shock waves that compress and heat the targets, eventually generating fusion energy. Magnetic Confinement Fusion (MCF) instead requires strong magnetic fields to confine the reactants in *plasma* state: fusion reactions will hence take place between *ionized* nuclei. Research activities on possible magnetic topologies for plasma confinement began in the last century. At the end of 1958, the first *tokamak* machine T-1 began operation in Russia: this peculiar magnetic field configuration allows to confine the plasma in a toroidal shape. The tokamak configuration was later exploited in approximately 60 new experiments, most of them still operating today.

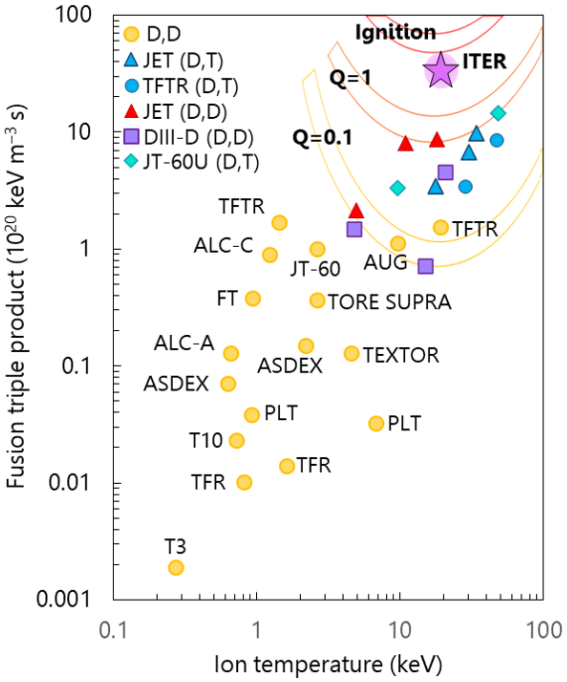

Figure 4: Triple product as a function of the ion temperature for different MCF experiments.

Nonetheless, magnetic confinement alone is not sufficient to achieve controlled thermonuclear fusion: in order to actually produce energy, a plasma of density n and temperature T must be confined for a sufficiently long time, usually called **energy confinement time** τ_E. The product of these three quantities, named *triple product*[5], allows to estimate the efficiency of the plasma confinement in fusion experiments, as shown in Figure 4. The power balance equation for a fusion plant can be written as $P_{net} = P_{fus} - P_{loss} - P_{heat}$, where P_{net} is the net power gain, P_{fus} is the fusion-produced energy, P_{loss} accounts for all loss terms, and P_{heat} is the external heating power supplied to sustain the plasma. Different techniques, including Heating Neutral Beam (HNB) and Radio-Frequency heating, are usually exploited to supply power to the plasma in addition to ohmic heating. The ratio between fusion power and heating power is commonly defined **energy gain factor Q**. If the triple product is high enough, the fusion power can balance the heating power $P_{fus} = P_{heat}$, achieving the so-called *breakeven* condition (Q=1). In this latter case, if the fusion energy production rate exceeds the energy loss rate, the fusion reactions can be self-sustained without any external heating: this condition is called *ignition*, and will be required for the design and operation of future fusion reactors.

ITER: The Way to fusion energy

ITER[6], which is latin for *The Way*, is the world's largest fusion experiment currently under construction. The European Union, Japan, Russia, India, China, South Korea and the United States joined forces to build and operate the first tokamak for demonstrating the feasibility of large-scale energy production, reaching an energy gain factor of $Q = 10$ by exploiting the ${}^{2}_{1}\mathrm{D}+{}^{3}_{1}\mathrm{T}$ fusion reaction.

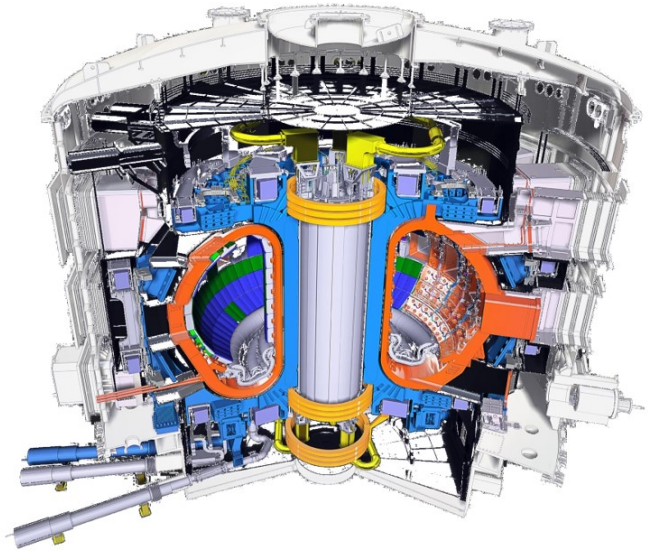

Figure 5: Rendering of the full ITER tokamak assembly.

The ITER experiment aims at:

- Exploring operation regimes for achieving the *burning plasma* condition, in which fusion reactions are mostly sustained by self-heating;
- Producing 500 MW of fusion power from 50 MW of heating power, reaching Q=10;
- Integrating different advanced technologies including superconductive magnets, control, vacuum systems, plasma diagnostics, and remote maintenance, paving the way for future fusion power plants;
- Demonstrating tritium breeding, i.e. on-site tritium production from lithium, to address the tritium scarcity issue;
- Demonstrating the safety of a nuclear fusion-based power plant.

Among the numerous challenges associated with ITER, there is the necessity to provide an effective external heating system. In the ITER case, two Radio-Frequency heating systems will provide 44 MW of power, together with two Neutral Beam Injectors delivering 16.5 MW of heating power each. As further described in the following chapter, the realization of a one-of-a-kind system such as the ITER NBI represents an extraordinary undertaking, involving significant scientific and engineering complexities.

Part I

Introduction

Chapter 1

Negative ion based Neutral Beam Injectors

This chapter provides a comprehensive overview of the operating principles and key components of Negative ion-based Neutral Beam Injector (NNBI). Emphasis is placed on discussing the technical and physical challenges associated with meeting the rigorous requirements of ITER NBIs. These challenges are examined in light of the latest findings from the ITER Neutral Beam Test Facility (NBTF). Within this framework, the primary objective of this thesis is outlined.

1.1 The ITER NBI: why negative ions?

The ITER HNB system is required to provide 33 MW of heating power by means of two high-energy NNBIs. In order to comply with such challenging requirement, a beam energy of 1 MeV needs to be reached.

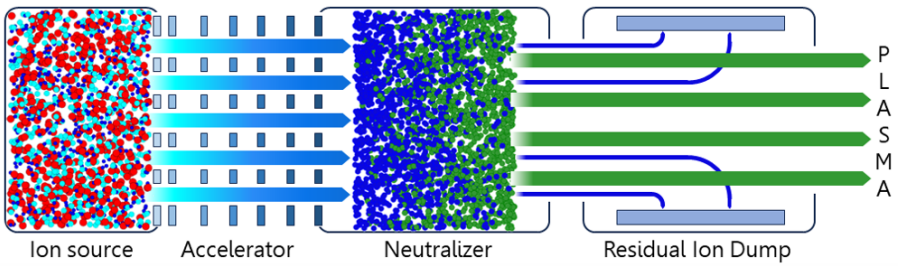

Figure 1.1: Simplified scheme of the main components of a negative ion based neutral beam injector.In the ion source, positive charges, negative ions and electrons are shown in red, cyan and blue respectively. In the neutralizer, energetic negative ions (in blue) lose their charge, becoming fast atoms (in green).

The main components of a NBI system are depicted in Figure 1.1. A high energy neutral beam is obtained from a precursor ion beam: more precisely, the precursor ions are extracted from a plasma source, electrostatically accelerated up to the target energy, and subsequently neutralized. The most diffused neutralization technique requires the beam to enter into a chamber filled with neutral gas, where fast beam ions lose their charge by interacting with the background gas molecules. Before entering the tokamak chamber, the beam travels through a Residual Ion Dump (RID) to get rid of the remaining ions.

Concerning the Hydrogen (H) and Deuterium (D) beams required for ITER, the neutralization efficiency strongly depends on the precursor ion beam charge, as shown in Figure 1.2. For beam energies $\geq 100\,\text{keV}$, the efficiency of positive ion neutralization decays rapidly; on the other hand, negative ions maintain a rather high neutralization efficiency, mainly because the bonding energy of their additional electron is as low as 0.75 eV, thus it can be easily stripped off by interaction with the background gas.

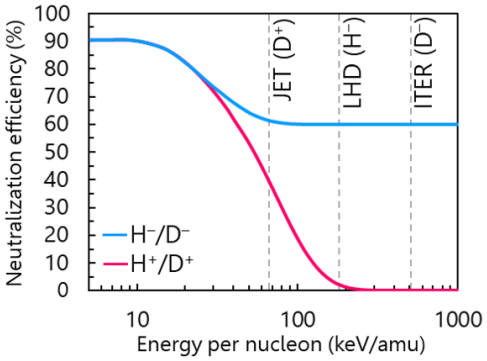

Figure 1.2: Neutralization efficiency of H,D ions as a function of the neutralized atom energy per nucleon[7].

Due to the higher neutralization efficiency, the ITER HNB system will be based on NNBIs, despite Positive ion-based Neutral Beam Injector (PNBI) being more widespread and easier to operate: indeed, positive ions are much more abundant in plasma sources and, furthermore, extracting a clean positive ion beam is easier with respect to a negative ion beam due to the co-extraction of electrons, which results in lower heating efficiency and higher damage risk, as further discussed in the following sections.

1.1.1 Producing negative ions

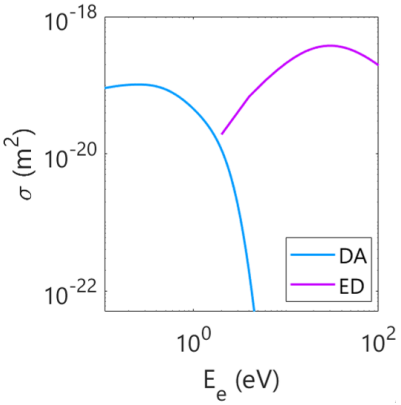

Figure 1.3: Cross sections of (e,H_2) dissociative attachment (DA, in light blue) and (e,H^-) electron detachment (ED, in purple) processes.

In H/D plasmas, negative ions are produced by dissociative attachment (DA) of vibrationally excited background gas molecules via electron impact, whereas the are mainly destroyed via electron detachment (ED):

$$e^- + H_2(v > 3) \rightarrow H_2^- \rightarrow H + H^-$$
$$e^- + H^- \rightarrow e^- + H + e^-$$

The cross section of the generation process reaches its maximum value for very low electron temperature T_e, whereas the cross section of the destruction process increases for larger T_e, as depicted in Figure 1.3. This already provides a constraint for the electron temperature, which needs to be low enough for enabling H^- production, and avoiding their destruction.

On the other hand, plasma generation requires background gas ionization, which can occur either via thermionic emission from a hot filament or via inductive coupling, starting an avalanche reaction to reach plasma ignition. This process requires T_e values larger than 10 eV, not compatible with the previously mentioned need for low T_e values. To meet both requirements, negative ion sources are based on the *tandem* concept: a magnetic field, usually called Filter Field (FF), is applied to the region of the source in proximity of the extraction area. This allows to restrain fast electrons from diffusing in this region, locally reducing the electron temperature. However, as further discussed in this work, the presence of an oriented, static magnetic field inevitably affects plasma uniformity within the source.

Knowing the main H^- production and destruction processes, the time variation of the negative ion density n_{H^-} in a hydrogen plasma slab of volume V can be written as:

$$\frac{dn_{H^-}}{dt} = (\alpha n_e n_{H_2} \langle \sigma v \rangle_{DA} - n_e n_{H^-} \langle \sigma v \rangle_{ED}) - \frac{j_{beam} A_{beam}}{q\,V} \tag{1.1}$$

where n_{H_2} and n_e are the background gas molecular density and plasma electron density respectively, $\langle \sigma v \rangle_k$ is the reactivity of the k^{th} process, α is a factor taking into account that only a certain fraction of molecules ($\alpha = 3\%$[8]) has sufficient vibrational energy for dissociative attachment, j_{beam} is the extracted negative ion beam current density, A_{beam} is the beam area, and q is the elementary charge. For a stationary state we can assume dn_{H^-}/dt=0, therefore:

$$\bar{n}_{H^-} = \frac{1}{n_e \langle \sigma v \rangle_{ED}} \left(\alpha n_e n_{H_2} \langle \sigma v \rangle_{DA} - \frac{j_{beam} A_{beam}}{qV} \right) \tag{1.2}$$

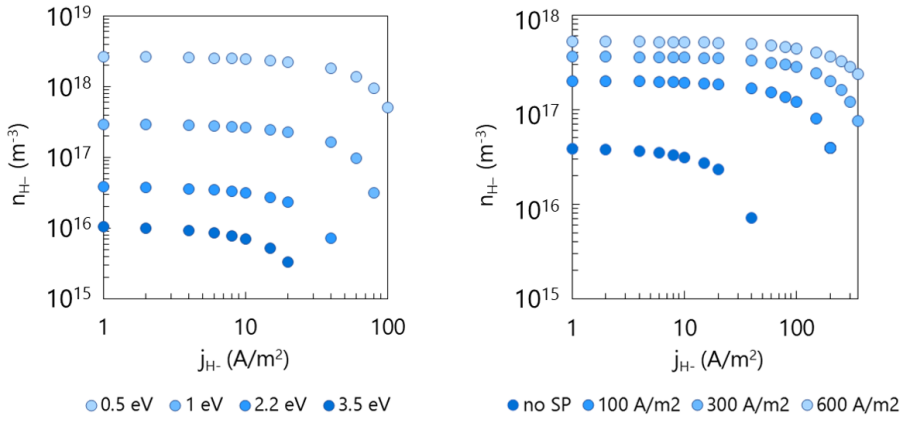

Figure 1.4: Equilibrium negative ion density n_{H^-} as a function of the extracted beam current density j_{H^-} for (a) pure volume production with different values of electron temperature T_e and (b) including surface production for different values of emitted negative ion current at the converter surface, with T_e=2.2 eV.

Figure 1.4 shows the equilibrium negative ion density $\bar{n}_{H^-}$ obtained from Eq. 1.2 as a function of the extracted current density for different T_e values, with A_{beam} =0.2 m^2, and $V = A_{beam} L$ =0.4 m^3, which are dimensions similar to the ones of the ITER HNB ion source. For achieving j_{beam} =100 A/m^2, an electron temperature as low as T_e =0.5 eV is required in the extraction region. In the case of the ITER HNB, the extracted current density needs to be j_{beam} =355 A/m^2, for which no equilibrium density can be provided by Eq. 1.2.

Surface production mechanism

The negative ion production has to be significantly increased: for this reason, the ITER HNB ion source will exploit an additional process, that is the surface production mechanism[9]. This technique relies on the evaporation of caesium (Cs) atoms inside the source, which are ionized and transported by the plasma itself towards the chamber surfaces, where they are deposited. Being an alkali metal, caesium can easily donate electrons to fast hydrogen atoms or positive ions impinging on the surface: more precisely, the caesium layer lowers the surface work function ϕ, allowing the formation of negative ions close to the caesiated surfaces. At optimal Cs coverage, the maximum variation of the surface work function is[10]:

$$\Delta\phi \simeq -1.24\,[\phi_0 - 0.5\,(I_A + E_A)]\ \text{V} \tag{1.3}$$

where ϕ_0 is the surface work function in non-caesiated conditions, I_A and E_A are the first ionization potential and electron affinity respectively of the adsorbed material (caesium in this case). For molybdenum surfaces, like the inner walls of the ITER ion source, the work function is roughly 5 eV, which can be lowered down to 1.5 eV thanks to Cs covering. As a result, a net H^- current density j_{surf} will flow from the caesiated surfaces towards the plasma. Besides caesium coverage, the efficacy of surface conversion also depends on the impinging fluxes of the precursor species, namely positive ions and neutral atoms:

$$j_{surf} = q\left[\Gamma_H\left(\frac{1}{4}n_H\sqrt{\frac{8qT_H}{\pi m_H}}\right) + \Gamma_i n_i\sqrt{\frac{qT_i}{m_i}}\right] \tag{1.4}$$

where Γ_H and Γ_i are the negative ion yields for impacting atoms and positive ions respectively, multiplied by the impinging fluxes. The atom yield Γ_H is maximized for $T_H \approx 0.8$ eV, reaching Γ_H=0.12, whereas the positive ion yield Γ_i is roughly equal to 0.11 for ion energies ≥10 eV[11]. However, the emitted negative ion current is limited by the plasma potential profile in the proximity of the converter surface, as discussed in the following section.

Virtual cathode formation

Surface-produced negative ions are produced on the caesiated surfaces, and need to be transported away. In negative ion sources, this process takes place in the Debye sheath in front of the surface, where a strong electric field builds up. At first, the emitted negative ions will face a steep potential increase, so they are easily attracted towards the plasma; as more negative ions are generated, negative charge locally builds up reducing the emitted negative ion current. The presence of negative ions in the very proximity of the surface locally modifies the plasma potential profile, until it becomes lower than the wall potential: this phenomenon is known as virtual cathode formation or double sheath layer[12],[13].

Once the virtual cathode is formed, the transported negative ion current is limited whatever the emitted negative ion current at the converter surface, as depicted in Figure 1.5.

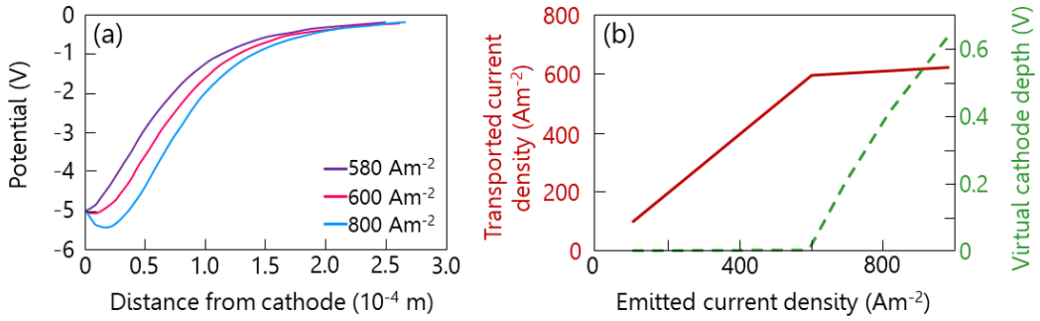

Figure 1.5: (a) sheath potential as a function of the distance from the cathode surface for negative ion current densities of 580 Am^{-2}, 600 Am^{-2}, and 800 Am^{-2} at the surface; (b) transported negative ion current density (red line) and virtual cathode depth (green line) as functions of the emitted current density. Adapted from[12].

To conclude, given the surface emitted negative ion current density effectively transported within the plasma j_{surf}, one can modify Eq. 1.2 to include the surface production mechanism, namely:

$$\frac{dn_{H^-}}{dt} = (\alpha n_e n_{H_2}\langle\sigma v\rangle_{DA} - n_e n_{H^-}\langle\sigma v\rangle_{ED})V + \frac{(j_{surf} - j_{beam})A_{beam}}{q} \tag{1.5}$$

and in stationary conditions:

$$\bar{n}_{H^-} = \frac{1}{n_e \langle \sigma v \rangle_{ED}} \left(\alpha n_e n_{H_2} \langle \sigma v \rangle_{DA} + \frac{(j_{surf} - j_{beam}) A_{beam}}{qV} \right) \tag{1.6}$$

For typical plasma properties in large negative ion sources one obtains $j_{surf} \propto 100\,A/m^2$: the presence of this additional source term allows to extract higher negative ion currents, as shown in Figure 1.4, making surface production fundamental for achieving the ITER NBI requirements.

1.1.2 Extracting a negative ion beam

Beam extraction takes place in the region of the source where the electron temperature is lowered by the filter field. The ion source is connected to a multi-grid, multi-aperture accelerator (Figure 1.6) which allows to electrostatically extract surface produced negative ions, generating numerous negative ion beamlets in such a way to minimize the ratio between the aperture radius r and the electrode gap d for optimal beam optics[14].

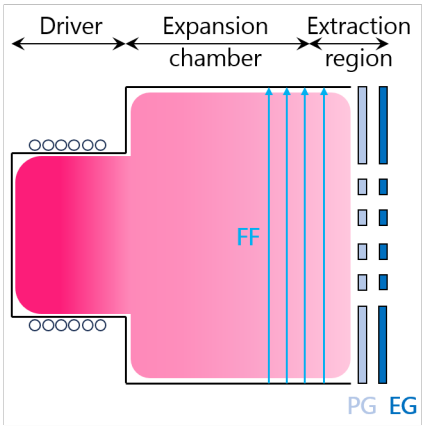

Figure 1.6: Basic scheme of a negative ion source with the extractor.

Despite being created in a low T_e region, the negative ion mean free path is of the order of tens of mm due to other destruction processes, including the ones listed in Table 1.1. This implies that only the negative ions created in the proximity of the accelerator can be extracted. More precisely, the first grid is commonly named Plasma facing Grid (PG), and acts as a negative ion converter thanks to caesium deposition. Despite being emitted along the opposite direction with respect to beam extraction, surface-produced negative ions manage to invert their motion thanks to Coulomb collisions with positive ions[15], and to the penetration of the extraction potential: indeed, a strong electric field ($\propto 100\,kV/m$) is present between the PG and the second accelerator grid, named Extraction Grid (EG), which is positively polarized with respect to PG. The extraction field enters the source volume through the PG apertures, where it is shielded by the plasma itself. This leads to the formation of a transition layer between the source plasma and the accelerator vacuum, called *plasma meniscus*[16], which defines an equipotential surface where the electric field is equal to zero (see Figure 1.7). Only negative charges, namely negative ions and electrons, can cross the meniscus and enter the accelerator.

$$\begin{aligned} H^- + H &\rightarrow e^- + H_2 \\ H^- + H^+ &\rightarrow H + H \\ H^- + H_2^+ &\rightarrow H + H_2 \\ H^- + H_3^+ &\rightarrow H_2 + H_2 \end{aligned}$$

Table 1.1: Negative ion destruction processes via positive ion and atom impact.

Beam perveance

The value of the extracted beam current mainly depends on the system geometry, on the extraction potential, and on the negative ion availability. The plasma meniscus and the EG electrode can be thought of as the emitter and collector of a diode. In the case of a cylindrical geometry with spherical emitter as the one shown in Figure 1.7, the extracted negative ion current is given by the Langmuir-Blodgett law[17]:

$$I_{H^-} = \pi r^2 j_{H^-} = \frac{4\pi\varepsilon_0}{9}\sqrt{\frac{2q}{m_{H^-}}}\left(1-1.6\frac{d}{R}\right)\frac{r^2}{d^2}U_{ext}^{3/2} = \mathbb{P}U_{ext}^{3/2} \tag{1.7}$$

where ε_0 is the dielectric constant in vacuum, d is the distance between the diode electrodes, R is the curvature radius of the emitter, and U_{ext} is the extraction potential. The parameter $\mathbb{P}$ is called *beam perveance* and takes into account all the geometrical features of the extracting system.

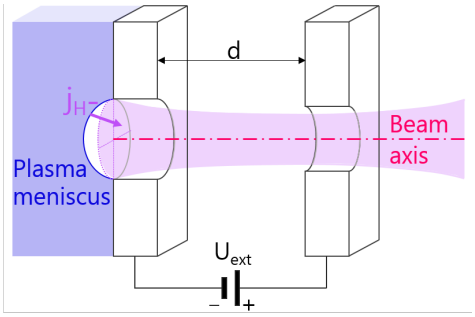

Figure 1.7: Schematics of the plasma meniscus and beam optics with cylindrical symmetry.

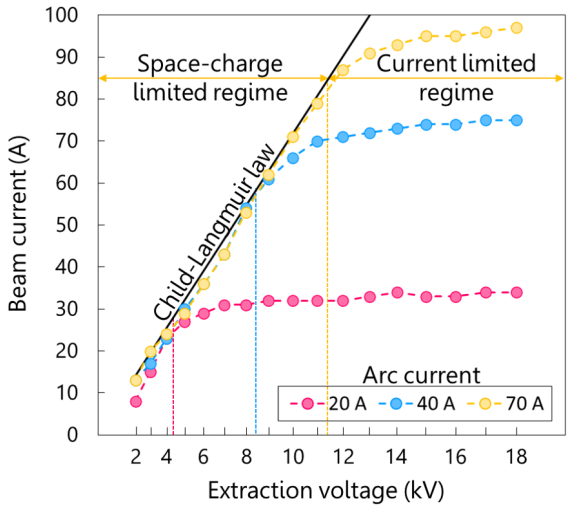

Figure 1.8: Measured beam current as a function of the extraction voltage in a filament negative ion source, for different values of arc current (arc polarisation fixed at ≈20 V. The space-charge and current limited regimes are highlighted for the 70 A arc current case. Adapted from[18].

According to Eq. 1.7, at fixed perveance the extracted beam current increases for larger extraction potentials: however, I_{H^-} is limited by the negative ion availability at the emitter. When this threshold is reached, there is a transition from a space-charge limited regime to a current-limited regime, in which Eq.1.7 is no longer valid. The extracted beam current becomes independent of the applied extraction potential[18], as shown in Figure 1.8.

Beam divergence

The plasma meniscus acts as an electrostatic lense for the negative ion beamlet: for this reason, the shape of the meniscus strongly affects the extracted beam properties. In order to quantify the goodness of the beam optics, the *beam divergence* θ is defined for each beamlet as the average angle between the ion trajectories at the accelerator exit and the beamlet axis. The beam divergence shows a minimum as a function of the beam perveance: this condition is usually called *perveance match*, and represents the optimal conditions for beam extraction. Figure 1.9 shows experimental measurement of the beam divergence performed in SPIDER[19].

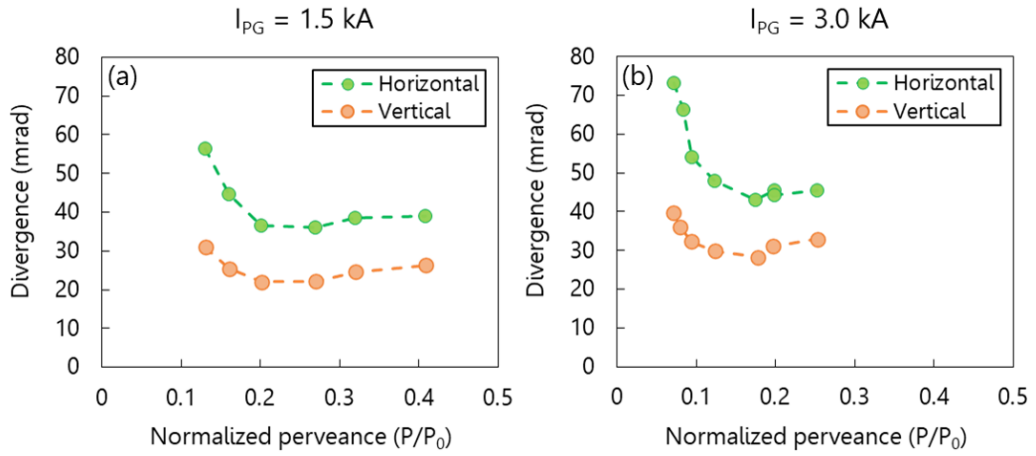

Figure 1.9: Horizontal (green) and vertical (orange) beam divergence as functions of normalized perveance measured in SPIDER during an extraction voltage scan for I_{PG}=1.5 kA (a) and I_{PG}=3.0 kA (b), with 20 keV beam energy. Data courtesy of M. Barbisan.

According to experimental findings[20], there can be a fraction of negative ions with exit angle significantly larger than the average beam divergence, even in perveance match conditions. These particles are usually referred to as *beam halo*, to distinguish them from *beam core* particles. The beam halo can be caused by aberrations of the electrostatic lenses, and are more likely to intercept the accelerator components, leading to overheating and unwanted beam power dissipation.

Co-extracted electrons deflection

As already mentioned, the presence of Co-extracted Electrons (CE) in negative ion sources is unavoidable. The ratio between CE and H^- extracted currents needs to be minimized in order to limit beam power losses. To do so, the EG is equipped with properly arranged permanent magnets[21] creating a magnetic field that deflects the electron trajectories on the EG itself, where they are lost. Despite the presence of these deflecting magnets, the CE fraction needs to be reduced already in the source plasma to avoid excessive heat loads on the EG itself. Having larger mass, the negative ions are only slightly affected by this deflecting magnetic field; nonetheless, they need to be aimed back along their original direction by means of either electrostatic or magnetic compensation[21] at the accelerator grids.

1.1.3 Beam acceleration and neutralization

Once extracted from the ion source, the negative ion beam is electrostatically accelerated up to the desired energy. The beam ions can then interact with neutral molecules incoming from the source (the accelerator is directly connected to the ion source), or impact on the accelerator

grids, losing their charge due to either single or double electron stripping (Table 1.2). For this reason, in order to limit stripping losses in the accelerator the background gas pressure in the ion source needs to be kept as low as possible. The formation of positively charged Back-Streaming Ions (BSI)[22] can also occur: these ions are accelerated back into the ion source. When dealing with high beam energies, the ion source surfaces are usually coated with Molybdenum in order to avoid possible damage induced by these latter BSI.

$$
\begin{array}{rcl}
\underline{H}^- + H_2 & \rightarrow & \underline{H}_0 + e^- + H_2 \\
\underline{H}^+ + H_2 & \rightarrow & \underline{H}^+ 2e^- + H_2 \\
\underline{H}_0 + H_2 & \rightarrow & \underline{H}^+ + e^- + H_2 \\
\underline{H}_0 + H_2 & \rightarrow & \underline{H}^- + H_2^+ \\
\underline{H}^+ + H_2 & \rightarrow & \underline{H}^- + 2H^+ \\
\underline{e}^- + H_2 & \rightarrow & \underline{e}^- + H_2^+ + e^-
\end{array}
$$

Table 1.2: Main processes involving fast beam ions and electrons interacting with background gas. Fast beam particles are underlined.

After being accelerated, the beam enters the neutralization chamber where it interacts with the background gas again through the processes listed in Table 1.2, changing its charge composition along the neutralizer. The different beam species fractions change according to the so-called *gas thickness*, that is the spatial integral of the background gas density along the neutralizer.

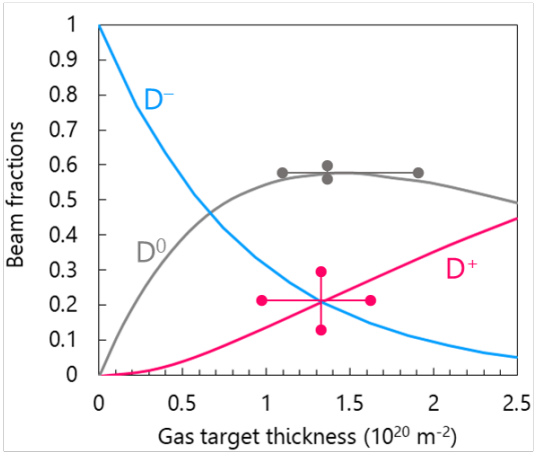

Figure 1.10: Beam species fractions variation as a function of the gas target thickness for the ITER NBI case. The fraction of neutralized beam particles displays a broad maximum above a certain threshold of gas thickness.

The neutral H fraction features a maximum for certain gas thickness values, as shown in Figure 1.10. The neutral fraction maximum is very broad, whereas the positive ion fraction increases more rapidly: for this reason, the neutralizer is usually operated with lower gas thickness values, in such a way to limit the residual ion fraction to be removed by the Residual Ion Dump.

Chapter 2

Neutral Beam Test Facility

Having briefly discussed the main aspects of negative ion beam extraction, acceleration and neutralisation, the specific requirements[23] of the ITER NBI system will be presented in the following. The Neutral Beam Test Facility (NBTF) is introduced, as well as the most relevant R&D topics presently being investigated.

2.1 Requirements of the ITER NBI

As already mentioned, ITER will be equipped with two high-energy NNBI to provide a total of 33 MW of additional heating power to the tokamak plasma. To this purpose, high negative ion beam current and energy are required, with the beam divergence being limited up to 7 mrad in order to avoid beam losses along the beam-line while maximizing the beam power fraction actually transmitted to the plasma. In addition, with the beam area being of roughly 0.2 A/m^2, beam uniformity is also fundamental for extracting and accelerating a well-focused beam.

	H	D
Beam energy	870 keV	1000 keV
Accelerated beam current	46 A	40 A
Extracted current density	330 A/m^2	280 A/m^2
Co-extracted electron fraction j_e/j_-	< 0.5	< 1
Beam-on time	1000 s	3600 s
Extraction area	0.2 m^2	
Core divergence	$\leq$7 mrad	
Max. beam deflection	2 mrad	
Beam uniformity	within $\pm$10%	
Max. source filling pressure	0.3 Pa	
Source plasma discharge	Inductively Coupled Plasma (ICP)	

Table 2.1: ITER NBI requirements for hydrogen and deuterium operation.

R&D activities on the NNBI components have been carried out mainly in european facilities such as the Max-Planck Institut für Plasma Physik in Garching (Germany), where extensive research on RF-based negative ion sources is ongoing in the BUG and ELISE experiments[24], and in Japanese laboratories such as the National Institute for Fusion Science (NIFS) and the National Institutes for Quantum Science and Technology (QST), where high-energy NNBI based on filament sources have been routinely operated over the past decades[25],[26].

Nonetheless, the ITER NBI requirements listed in Table 2.1 have never been simultaneously attained. For this reason, the full-scale prototype of the ITER NBI, called MITICA (Megavolt ITER Injector and Concept Advancement) is currently under construction at the ITER Neutral Beam Test Facility[27] (NBTF), hosted by Consorzio RFX in Padova (Italy). The NBTF also hosts SPIDER (Source for the Production of Ions of Deuterium Extracted from a RF plasma), the 1:1 prototype of the ITER NBI ion source equipped with a 100 keV accelerator. Since the investigation of the plasma properties in the ion source is the main topic of this thesis work, the design of the SPIDER experiment will be described in the following section.

2.2 The SPIDER ion source

As already mentioned, SPIDER[28] is the full-scale prototype of the ITER NBI ion source. Differently from other RF negative ion sources, the SPIDER beam source, extractor and accelerator are enclosed in the same vacuum of the beam drift region, as can be seen in Figure 2.1.

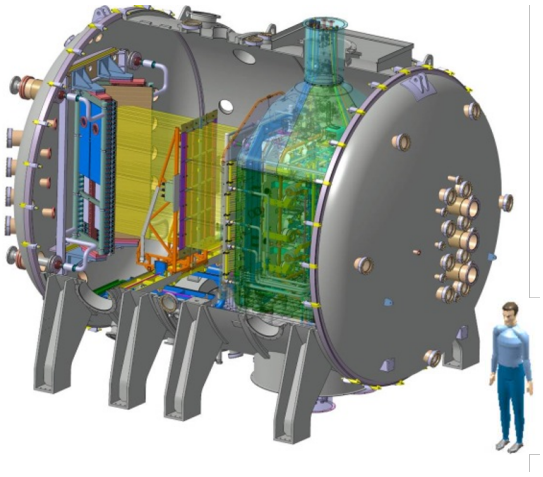

Figure 2.1: Schematic view of the SPIDER negative ion source, accelerator, calorimeter and beam dump.

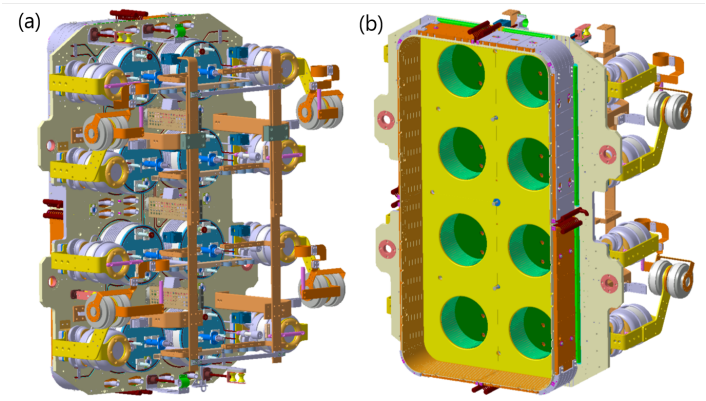

Figure 2.2: Schematic view of the SPIDER plasma box, rear (a) and front (b) view.

The beam source is composed of eight cylindrical chambers of ≈140 mm radius and 150 mm length, called *drivers*, arranged in a 4×2 matrix (see Figure 2.2). A cylindrical RF antenna is wrapped around each driver.

Four generators independently supply each row of drivers with up to 200 kW power at a driving RF frequency of 1 MHz, for a total RF power of 800 kW. Each row of drivers is usually referred to as RF *segment*. The drivers are connected to a single *expansion chamber* 1760 mm high, 866 mm wide, and 240 mm deep. Three caesium ovens[29] are installed in between the four driver segments for Cs evaporation inside the source. A set of permanent magnets is placed on the lateral walls of the expansion chamber for multi-cusp confinement.

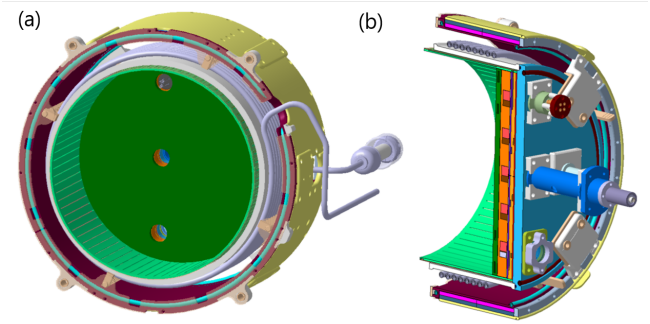

Figure 2.3: Front view (a) and section (b) of one SPIDER driver.

The expansion chamber is connected to a triode accelerating system composed of a Plasma Grid (PG), an Extraction Grid (EG) and a Grounded Grid (GG). All grids share the same design, featuring 1280 apertures through which the negative ion beam is extracted and accelerated in a multi-beamlet form. The apertures are arranged in 4×4 beamlet groups with 5×16 beamlets each. Each row of beamlet groups is usually referred to as beam segment. A fourth electrode, the Bias Plate (BP), is placed upstream of the PG and features 16 wide apertures in correspondence of the beamlet groups.

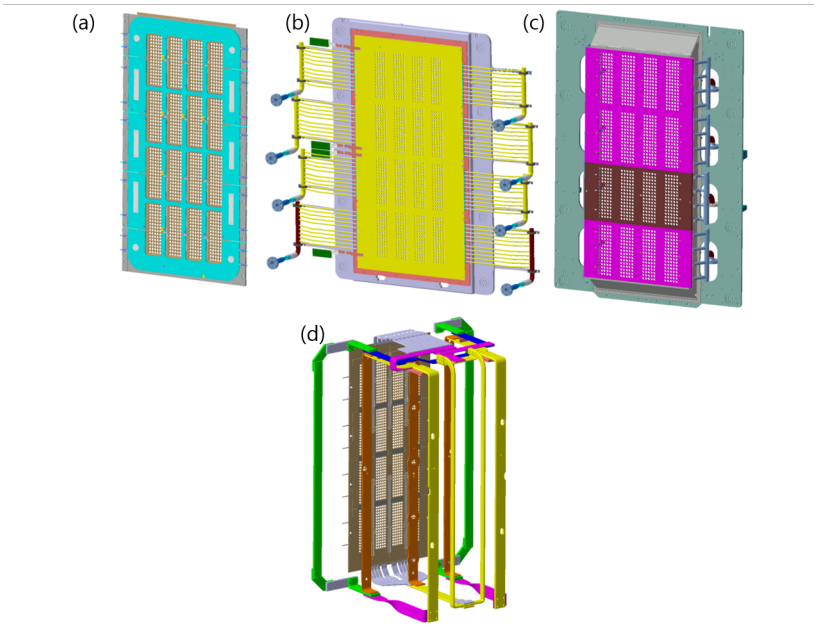

Figure 2.4: Schematic view of the SPIDER grids: Plasma Grid and Bias Plate in light blue (a), Extraction Grid (b), and Grounded Grid (c); PG and busbars system used to generate the magnetic filter field (d).

The EG hosts the Co-extracted Electrons Suppression Magnets (CESM)[21], for the deflection of the co-extracted electrons onto the EG itself. The GG instead hosts permanent magnets in the first, third and fourth segments for balancing the magnetic deflection of the negative ions caused by the CESM; the second GG segment instead features a slightly different design for electrostatic compensation of negative ion beamlet deflection.

In SPIDER, the magnetic Filter Field is generated by a current I_{PG} of the order of 1 kA (max 5 kA) flowing along the PG electrode and a system of return busbars, as depicted in Figure 2.4. Two FF configurations are possible: the Standard Filter Field Configuration (SFF), with the I_{PG} current flowing downwards along the PG electrode, and the Reversed Filter Field Configuration (RFF), with the I_{PG} current flowing upwards the PG electrode. In the proximity of the PG, the FF intensity can be obtained as a function of the PG current as $B_{FF} = 1.6\, I_{\mathrm{PG}}$ mT/kA.

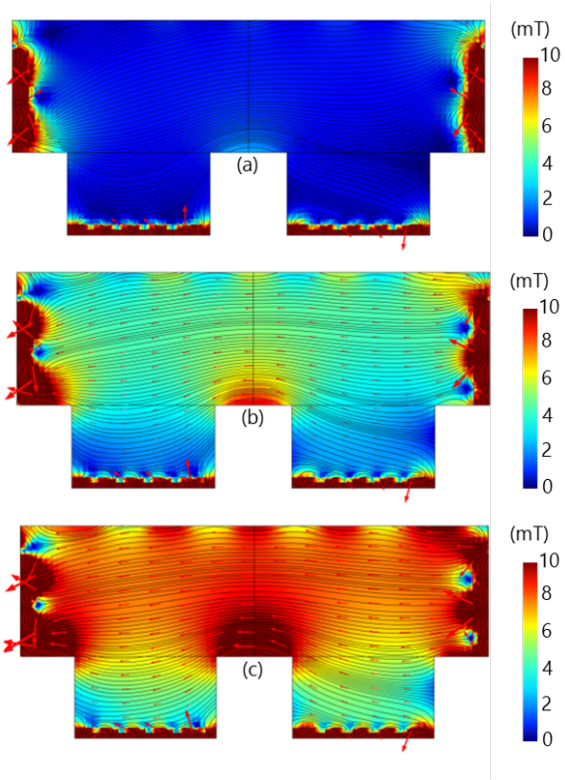

Figure 2.5: Magnetic Filter Field on a horizontal cross section along the midplane of one RF segment with I_{PG} equal to 1 kA (a), 3 kA (b) and 5 kA (c). Adapted from[30].

2.2.1 Electrical connections

The extraction and acceleration potentials are defined as:

$$\begin{aligned} V_{\mathrm{ext}} &= (V_{\mathrm{EG}} - V_{\mathrm{PG}}) \\ V_{\mathrm{acc}} &= (V_{\mathrm{GG}} - V_{\mathrm{EG}}) \end{aligned} \tag{2.1}$$

with $V_{\mathrm{PG}} < V_{\mathrm{EG}} < V_{\mathrm{GG}} = 0$ V. The maximum potential difference between the PG and the EG is 12 kV, whereas between EG and GG is up to 96 kV. When operating at full beam power, the ion source is biased at $V_{\mathrm{source}} = -(V_{\mathrm{ext}} + V_{\mathrm{acc}}) = -108$ kV with respect to ground.

Thanks to dedicated power supplies, the BP and PG electrodes can be independently polarised up to roughly 50 V with respect to the ion source. This polarisation can be either voltage

or current controlled. Since there is a R=0.6 Ω resistor in parallel with each grid, the effective bias potentials can be obtained as:

$$\tilde{V}_{\mathrm{BI,BP}} = V_{\mathrm{BI,BP}} - RI_{\mathrm{BI,BP}} \tag{2.2}$$

where U and I are the voltage and current respectively measured at the power supplies. The PG and BP bias are labelled as "BI" and "BP" respectively.

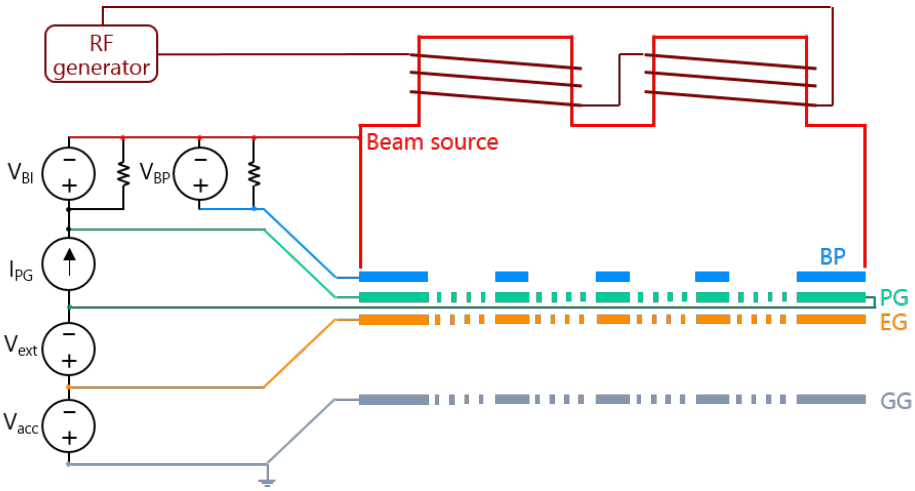

Figure 2.6: Simplified scheme of the electrical connections in the SPIDER source. Additional details on the power supplies and on their connection to the source components can be found in[31].

2.2.2 The SPIDER diagnostic system

SPIDER is equipped with a diversified set of source and beam diagnostics, as listed in the following[32]. Besides the ones described below, some new diagnostics are currently being installed in the ion source[33]. Among source diagnostics one can find:

- Plasma Light (PL) telescopes, which can measure the H_α radiation emitted from the plasma thanks to interference filters. Lines of sight parallel to the axis of each driver are available;
- Optical Emission Spectroscopy (OES), which can infer measurements of electron temperature and density, as well as of H^-, H, and Cs densities, by interpreting the raw data through a Collision-Radiative model (CR). The OES can measure along horizontal and vertical lines of sight parallel to the grids; in addition, each driver is equipped with a dedicated OES line of sight parallel to the beam axis;
- Cavity-Ring Down Spectroscopy (CRDS), which can measure the H^- density along one line of sight parallel to the grids, in correspondence of the bottom beam segment;
- Laser Absorption Spectroscopy (LAS), which can measure the atomic Cs density along a set of lines of sight parallel to the grids;
- A matrix of Electrostatic Probes (EP) embedded in the BP and PG electrodes, which can measure the positive ion saturation current and, in some cases, plasma density, electron temperature and plasma potential.

As for beam diagnostics, SPIDER is equipped with:

- STRIKE calorimeter, which can measure the infrared beam footprint on 16 CFC tiles, one for each beamlet group. The STRIKE resolution allows to measure beam uniformity and, in specific conditions, to resolve single beamlet footprints, estimating the beam divergence;

- Beamlet Emission Spectroscopy (BES), which can measure beam uniformity, divergence, and stripping losses;
- Beam tomography, which can measure beam divergence, and beam uniformity with an expected resolution of 2.5 cm^2;
- Allison Emittance Scanner (AES), which allows to measure the single beamlet divergence and emittance;
- Beamlet Current Monitor (BCM), which allow to characterise both the DC and AC components of the single beamlet current.

A movable set of electrostatic sensors entering from the accelerating column was temporarily operated in SPIDER[34]. This set included single and double Langmuir probes, Mach probes and compact Retarding Field Energy Analyser (RFEA) for positive and negative ions.

SPIDER has been operating since 2018, with the first beam extraction in May 2019. Most of the initial experiments were devoted to the resolution of several issues such as RF-induced discharges occurring in the rear side of the source, caused by too high a pressure in the vacuum vessel[35]. To reduce the vessel pressure and mitigate the risk of discharges in the rear of the soruce, the gas conductance of the accelerator was lowered by installing a thin molybdenum sheet downstream of the PG[36], called Plasma Grid Mask (PGM), properly machined to leave 80 out of 1280 apertures open. In this way, it was possible to operate the ion source with limited RF power (50 kW/driver), also studying single beamlet optics. During caesium operation in 2021, the number of open beamlets was reduced down to 28.

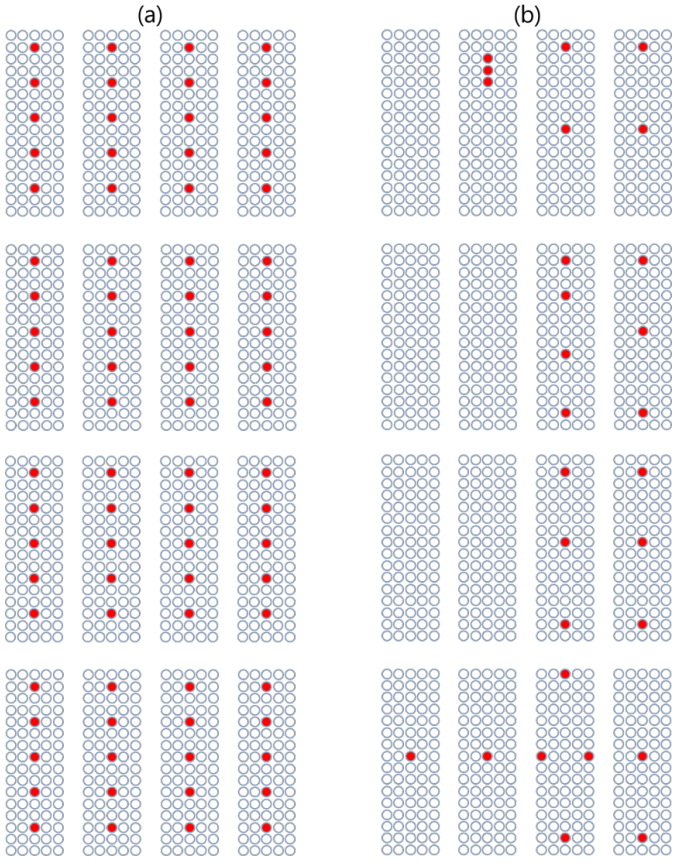

Figure 2.7: Plasma Grid Mask layout for SPIDER operations without (a) and with (b) caesium evaporation, view from the drivers. Red-filled circles represent the left open apertures.

2.3 Thesis motivation and background

This work aims at contributing to the optimization of the ITER NBI system. In this framework, my work was focused on the investigation of the source plasma inside negative ion sources for fusion, particularly for the full-size ion source prototype SPIDER. The latter is a fundamental step for understanding the beam features measured in fusion relevant RF negative ion sources so far. Key R&D topics stem from the recent SPIDER experimentation, to which I actively contributed. The main experimental findings can be summarised as follows:

- Asymmetric plasma expansion from the RF drivers;
- Global and local non-uniformity of the vertical beam profile;
- Large single beamlet divergence.

These topics, which are the main subject of my thesis work, will be discussed in the following.

2.3.1 Asymmetric plasma expansion from the RF drivers

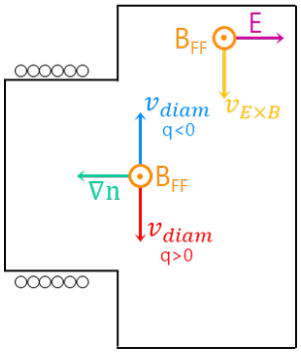

Figure 2.8: Schematic representation of the main drift motions occurring in a RF-based negative ion source.

As mentioned in Section 1.1.1, the magnetic FF affects plasma diffusion in the ion source, restraining fast electrons from reaching the extraction region. This static, horizontally oriented magnetic field enhances the already present density gradient along the source axis, due to the plasma generation being localised inside the eight drivers. As a consequence, several types of drifts build up, namely the $\vec{E} \times \vec{B}$ drift, the diamagnetic drift, and the $\vec{B} \times \nabla B$ drift.

$$\begin{aligned} v_{E\times B} &= \frac{\vec{E} \times \vec{B}}{B^2} \\ v_{\text{diam}} &= -\frac{\nabla p_\perp \times \vec{B}}{nqB^2} \\ v_{\nabla B} &= \left(\frac{mv_\perp^2}{2qB}\right)\vec{B} \times \nabla B \end{aligned} \tag{2.3}$$

At the driver's exit, as shown in Figure 2.8, the $\vec{E} \times \vec{B}$ drift is directed downards along the vertical direction, independently of the charge; the diamagnetic drift, instead, is directed either downwards or upwards for positive and negative charges respectively. This causes asymmetries in the plasma flowing out from the drivers and, consequently, vertical non-uniformity of the plasma properties in the expansion chamber[37],[38].

As a result of this asymmetry, energetic electrons coming from the driver region flow perpendicularly to the source axis, causing a Hall current along the vertical direction. This was predicted by numerical models[37],[39],[40], as well as confirmed experimentally. In fact, source diagnostics in SPIDER, mainly OES and EP[41], highlighted a non-uniformity of the plasma properties in the expansion chamber and also in the extraction region, along both the vertical and horizontal direction. Plasma light measurements along the axes of the eight drivers were found to be different from each other, showing a dependence on the I_{PG} current, hence on the FF intensity and orientation[42].

2.3.2 Global and local non-uniformity of the vertical beam profile

The aforementioned source plasma inhomogeneity in the expansion chamber might be the underlying cause for a non-uniformity in the extracted beam current density, specifically along

the direction perpendicular to the FF, i.e. the vertical direction. This beam non-uniformity was confirmed experimentally in SPIDER by both the STRIKE calorimeter and beam tomography, which measured different values of extracted beam current density among the four beam segments[43],[44].

In addition, the vertical beam profile featured local inhomogeneities also on the beamlet group scale, displaying a higher beamlet current in the center of the group, as shown in Figure 2.9. This phenomenon was indirectly detected in ELISE thanks to the BES measurements of beam divergence variation along the vertical direction, which implies a non-uniform extracted beamlet current densities[45]. In SPIDER, the presence of the PG mask allowed a first spatially resolved characterisation of this non-uniformity along the vertical profile of the extracted beam current[46].

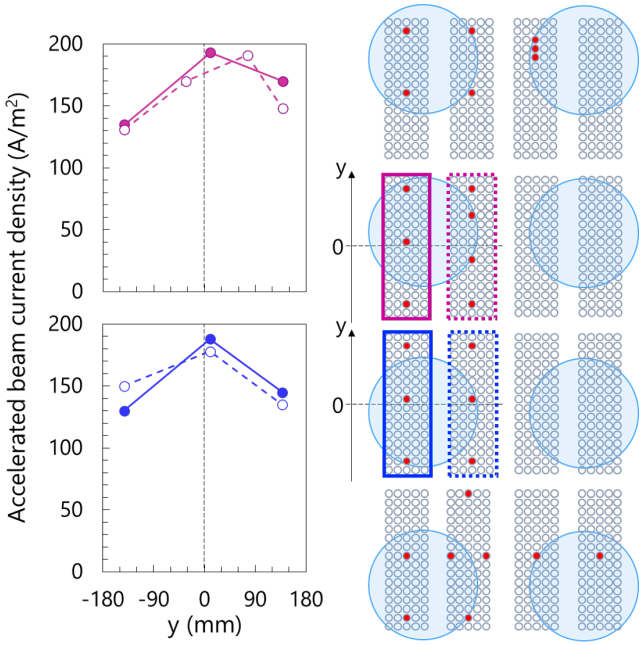

Figure 2.9: Experimental evidence of local non-uniformity within beam segments in SPIDER, measured by STRIKE. Presented by E. Sartori at the ICIS 2023 conference.

2.3.3 High single beamlet divergence

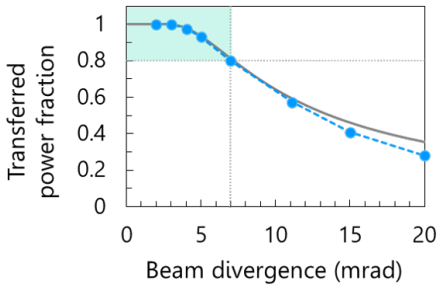

Figure 2.10: Numerical (blue points) and analytical (grey line) estimations of the heating power fraction delivered to the ITER plasma as a function of the single beamlet 1/e divergence.

The beamline components of the ITER NBI were designed considering a single beamlet divergence between 3 mrad and 7 mrad. The heating power delivered to ITER will effectively reach the 16.5 MW requirement if, assuming ideal aiming for the single beamlets, the beam divergence is below 7 mrad as shown in Figure 2.10. This upper limit is mainly due to the intersection of the beam along the horizontal direction by the rear edge of the Residual Ion Dump channels at 7.2 m from the GG. The delivered power fraction can be estimated as:

$$F = \mathrm{erf}\left(\frac{\omega_{\mathrm{lim}}}{\omega}\right) \tag{2.4}$$

where $\omega_{\mathrm{lim}} \approx 6.6$ mrad. Being a simple two-dimensional estimation, the analytical calculation overestimates the transmitted power fraction for high divergence values, compared to three-dimensional simulations. It is understood that the acceleration at high energies can provide lower experimental divergence values by reducing the divergence contribution due to the negative ion temperature, which scales as $(E_{\perp}/E_{\mathrm{beam}})^{1/2}$.

This being said, extrapolating SPIDER results towards MITICA is not straightforward. In SPIDER, independent measurements of the single beamlet optics by means of BES, AES, STRIKE and beam tomography were in agreement concerning the rather high beam divergence. In particular, a minimum value of about 12 mrad was measured for hydrogen operation at 38 keV beam energy[47], with a beam halo component around 10%[48]. On the other hand, in filament-based negative ion sources (RNIS), a divergence value of 5.6 mrad was measured with 40 keV beam energy[49].

The high beam divergence in RF sources is most probably caused by too energetic negative ions at the plasma meniscus, although the underlying reason for such high H^-/D^- energy still needs to be investigated. A possible explanation could be related to the precursor properties, both positive ions and fast atoms, or to Coulomb collisions between negative and positive ions exhibiting a too high temperature T_+. To clarify this point, a comparison of the plasma properties between RF- and filament-based negative ion sources is being carried out, also with the help of dedicated test facilities[50].

2.3.4 Aim of this thesis and outline

The aim of my thesis is to build a comprehensive view of how the ITER NBI source works. I approached the interpretation of the beam source behaviour exploiting the available experimental measurements and developing new numerical tools. My research work was balanced between the need of understanding basic plasma phenomena and processes, and the necessity of addressing the key issues highlighted by the SPIDER experimentation and the correlation with the extracted beam features. To this purpose, I developed a numerical tool for plasma modelling, tackling challenging aspects of algorithm implementation and numerical plasma physics. In parallel, I also designed and operated specific diagnostics, addressing all aspects of their realisation.

In the first part of this thesis, the adopted numerical algorithm is briefly described in the Chapter 3, whereas the new code implementations are discussed in Chapter 4. The second part instead is dedicated to the experimental and numerical results of the ion source investigation. First, plasma expansion mechanism will be discussed, with a particular focus on positive ion properties and vertical drifts, which might be a cause for the high single beamlet divergence and the global non-uniformity of the vertical beam profile respectively (Chapters 5, 6, and 7). Moving towards the extraction region, the influence of the bias electrodes on both source and beam properties is discussed in Chapters 8 and 9 respectively. Particularly, the effect of using a reduced number of beamlet apertures on the experimental findings is discussed. Having assessed the plasma behaviour along the vertical direction, the results of the investigation of the influence of permanent magnets on the horizontal uniformity of plasma properties will be presented in Chapter 11, after discussing the influence of multi-cusp magnetic confinement on plasma properties on a more general level in Chapter 10. Finally, with the aim of supporting future experimental comparison between RF and filament sources, a first numerical characterization of the latter is presented in Chapter 12.

Part II

The GPPIC model

Chapter 3

General Purpose Particle-In-Cell: GPPIC code

This chapter provides a brief introduction on the Particle In Cell (PIC) method for plasma simulation. The main algorithm blocks of GPPIC, the code used in this work, are described. In some cases, the CUDA[51] implementation of basic features are shown.

3.1 Particle-In-Cell basics

The Particle In Cell (PIC) method[52] is a widespread Lagrangian scheme for plasma simulation. In order to reproduce plasma behavior, a finite number of charged plasma particles is considered. The particles can freely move inside a defined simulation domain, whereas the plasma properties are obtained on a mesh, as better explained in the following.

3.1.1 Time-space discretization and constraints

Plasma properties are obtained on a discretized domain, called *mesh*, which is structured: the shape and size of its unitary element, called *cell*, is kept constant for the entire duration of the simulation run. For example, a very simple two-dimensional structured mesh can be composed of squared cells, with size $dx = dy$ (see Figure 3.1).

The PIC method is iterative, thus a defined sequence of operations is cyclically repeated. Each iteration corresponds to a certain amount of time dt, called $timestep$. In this way, PIC algorithms can describe the system evolution, while following the particle kinetics.

The parameters for space and time discretization should be chosen in such a way to provide accurate results in a manageable amount of time. Generally speaking, for small dt, dx, and dy values, the accuracy of the obtained results is improved, although more iterations are needed to simulate a given amount of time. Nonetheless, in order to correctly reproduce the plasma behaviour, both the timestep and the mesh cell size should satisfy the following constraints:

$$dt < \frac{0.2}{\omega_{pe}} \qquad dx, dy < \lambda_{De} \tag{3.1}$$

where ω_{pe} and λ_{De} are the plasma electron frequency and the Debye length for the simulated system. If the first constraint is not satisfied, the simulation would not be able to follow the particle kinetics for an entire plasma oscillation. The violation of the second constraint would

also cause a bad description of plasma kinetics since the particles inside each cell would be screened from the electrostatic field, resulting in an altered motion. When dealing with large systems, these constraints can be modified as follows:

$$dt < \frac{1}{\omega_{pe}} \qquad dx, dy < 3\lambda_{De} \tag{3.2}$$

In the case of non-uniform plasma properties, the most stringent conditions shall be chosen for determining the timestep and cell size.

3.1.2 Macroparticle weight

Real plasmas can have very high densities, thus the simulation algorithms should follow the kinetics of numerous particles. Even if the available computational power and memory are sufficient to consider all the degrees of freedom of the system, the simulation wall-time would be too high. For this reason, real particles are "grouped" into numerical particles, called *macroparticles*: in this way, the algorithm will describe the system evolution by following the kinetics of these numerical particles, reducing the computational cost.

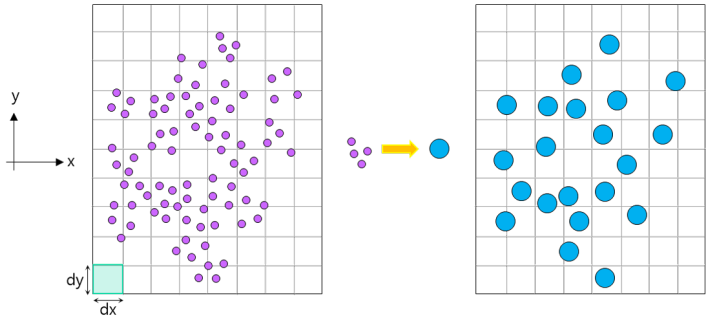

Figure 3.1: Simple example of particle grouping in a rectangular domain discretized with squared cells.

The ratio between the number of real particles N and the number of simulated macroparticles N_{MP} is defined MacroParticle Weight (MPW):

$$\mathrm{MPW} = \frac{N}{N_{\mathrm{MP}}} = \frac{nV}{N_{\mathrm{MP}}}$$

where n and V are the plasma density and volume of the real system. From now on, the macroparticles will be referred to as particles for the sake of simplicity.

By increasing the MPW, the average number of particles per cell decreases. As a consequence, the numerical noise of the calculated macroscopic properties of the system increases because of the low statistics. In order to avoid excessive worsening of the numerical results, the number of particles per cell shall be not smaller than 30, as derived from some sensitivity analyses performed on the GPPIC code (Figure 3.2).

3.1.3 Density scaling factor

The introduction of the MPW is still not sufficient when describing high density plasmas. For this reason, the simulated plasma density n_{PIC} is reduced by a *density scaling factor* β, in such a way that:

$$n_{\mathrm{PIC}} = \beta n \tag{3.3}$$

where n is the real plasma density and $\beta \leq 1$. This density scaling does not influence the description of the system kinetics[39]. However, the Debye sheath thickness will be affected by this scaling, hence β should be kept as close to 1 as possible. From now on, a simpler notation will be adopted and the simulated density n_{PIC} will be referred to as density n.

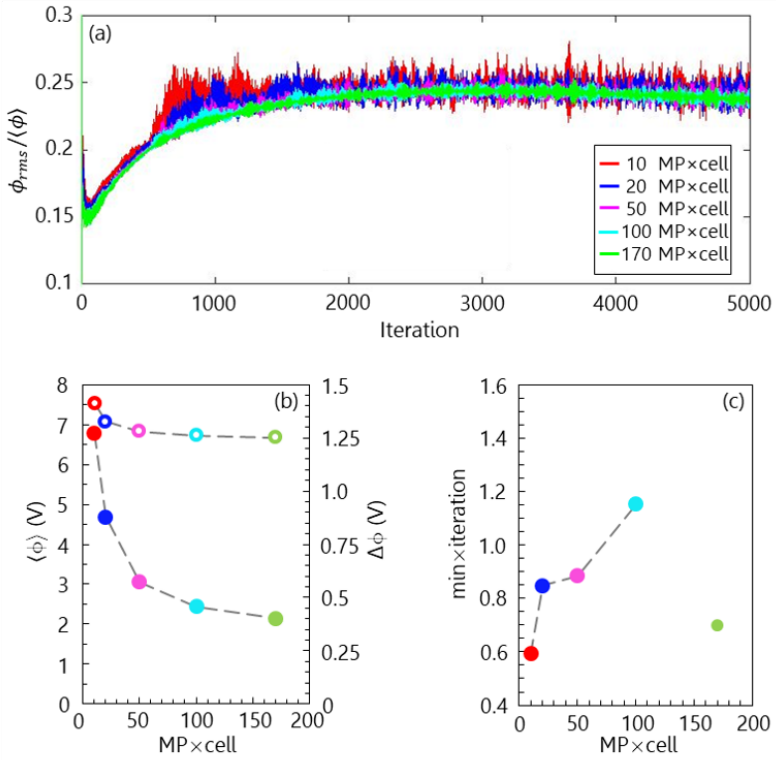

Figure 3.2: (a) Normalized potential rms evolution for different values of macroparticles per cell; (b) average potential (filled points) and potential fluctuation $\Delta\phi = \phi_{\max} - \phi_{\min}$ (empty points) and (c) minutes per iteration as a function of the number of macroparticles per cell; the 170 MP×cell simulation was performed with a different hardware configuration.

3.2 Main features of the GPPIC algorithm

The most relevant algorithm blocks of the GPPIC code will be described in the following. The code is implemented in C++/CUDA, and exploits General Purpose Graphics Processing Units (GPGPU) for parallel computation.

3.2.1 Initialization

Before starting the iterative part of the algorithm, all the aforementioned basic properties such as domain size, mesh, timestep, together with several boundary conditions such as magnetic field topology, wall potentials, included species etc. need to be either defined or loaded as input. Most of these parameters depend on the simulation type, thus they can differ from one run to another. Concerning the simulations discussed in this thesis, the considered plasma species are the ones generated in hydrogen plasma discharges, namely electrons e^-, positive ions H^+, $H_2{}^+$, $H_3{}^+$, negative ions H^-, and neutrals H, H_2. Other parameters such as the timestep dt, the mesh cell size dx, dy, the macroparticle weight MPW and the density scaling factor β will be specified later in this work, when discussing the results obtained from the simulations.

3.2.2 Fundamental steps of the iteration cycle

The simulation can start either from a previously obtained configuration by loading a list containing the space and velocity coordinates of all the particles, or from scratch. In both cases, while the iteration number is smaller than the defined maximum number of iterations, the algorithm will repeat a series of tasks, as described in the following. If $it \geq it_{\text{MAX}}$, the simulation will end.

In the GPPIC case, the first operation is the calculation of the system properties such as plasma density, average velocity and temperature on the structured mesh. These macroscopic properties are calculated through a first order bi-linear interpolation[53]. Implementing this method requires the repetition of the same operation for each particle of each species, resulting in roughly 6×10^6 computations. For this reason, parallel computing is of primary importance as it allows to significantly reduce the simulation wall-time. The host (CPU) and device (GPU) codes performing the bi-linear interpolation for obtaining the two-dimensional density maps of each species are described in Example 3.1. The instructions in the `for` cycle are repeated `specie_count` times, with the latter being the number of included species. Two CUDA functions, usually called *kernels*, are launched in lines 2 and 6. The kernel calls are structured as follows:

```
deviceFunctionName
<<<numberOfBlocks,numberOfThreads>>>
(list of arguments);
```

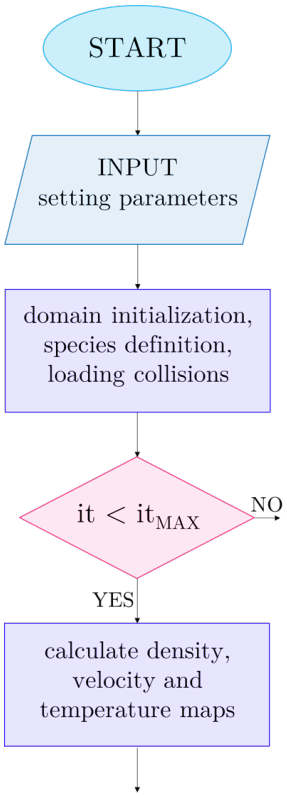

Figure 3.3: Main GPPIC algorithm blocks (part 1/4).

The list of instructions contained in the CUDA kernel `deviceFunctionName` are performed in parallel by `numberOfBlocks` blocks, each one containing `numberOfThreads` threads. All the threads contained in one block must perform the same operation.

```
1  //host code for density calculation
2
3  for(int i=0;i<specie_count;i++){
4    mapReset<<<blocksMAP,prop.maxThreadsPerBlock>>>(specie[i].d_n);
5    checkcudaerror(__LINE__,verbosecudaerror);
6
7    partDepositDensity<<<blocksMAP,prop.maxThreadsPerBlock>>>
8      (specie[i].d_X,specie[i].number,specie[i].d_index,specie[i].d_n,
9       specie[i].weight*MPW);
10   checkcudaerror(__LINE__,verbosecudaerror);
11
12   //additional code for density map smoothing
13 }
```

Listing 3.1: Host code for plasma density bi-linear interpolation.

Concerning the code snippet shown in Example 3.1, the kernel `mapReset` sets all the entries of the density map for the i-th species `specie[i].d_n` to zero.

The `partDepositDensity` kernel receives as input the particle coordinates as a linearized vector, structured as $(x_1,\ldots,x_N,y_1,\ldots,y_N,z_1,\ldots,z_N)$ as well as other properties, and executes the bi-linear interpolation as shown in Example 3.2. The kernel is declared as a void function, thus it will not return a value. In addition, the `__global__` directive specifies that this definition is shared on the *global* memory of the GPU.

```
1  __global__ void partDepositDensity
2    (float*X,int number,float*index,float*n,float weight)
3  {
4  int idx=blockDim.x*blockIdx.x+threadIdx.x;
5  if(idx<number)
6   if(index[idx]==0){
7    int iW=X[number*0+idx]/dx;
8    int jS=X[number*1+idx]/dx;
9    if(iW>=0 && jS>=0){
10    int iE=iW+1;
11    int jN=jS+1;
12    float resx=X[number*0+idx]-dx*(float)iW;
13    float resy=X[number*1+idx]-dx*(float)jS;
14    float dx_resx=dx-resx;
15    float dy_resy=dy-resy;
16    float dxdy=dx*dy;
17    if(YMAPSIZE*iW+jS<XMAPSIZE*YMAPSIZE &&
18       YMAPSIZE*iE+jS<XMAPSIZE*YMAPSIZE &&
19       YMAPSIZE*iW+jN<XMAPSIZE*YMAPSIZE &&
20       YMAPSIZE*iE+jN<XMAPSIZE*YMAPSIZE)
21     if(iE<=XMAPSIZE-1 && jN<=YMAPSIZE-1){
22      atomicAdd(&n[YMAPSIZE*iW+jS],weight*dx_resx*dy_resy/dxdy/dxdy);
23      atomicAdd(&n[YMAPSIZE*iE+jS],weight*resx*dy_resy/dxdy/dxdy);
24      atomicAdd(&n[YMAPSIZE*iW+jN],weight*dx_resx*resy/dxdy/dxdy);
25      atomicAdd(&n[YMAPSIZE*iE+jS],weight*resx*resy/dxdy/dxdy);
26     }
27   }
28  }
29 }
```

Listing 3.2: Definition of the `partDepositDensity` kernel.

The `idx` (line 2) variable represents the GPU thread index along the matrix of `numberOfBlocks` blocks, with `blockDim.x` being the block dimension, `blockIdx.x` being the block index and `threadIdx.x` being the thread index within the block to which it belongs. The `if` statement in line 3 is needed to prevent the GPU from accessing not allocated memory; the `if` statement in line 4 instead verifies whether the particle is "active", meaning that it is contained in the domain: the active particles are flagged by `index[idx]=0`. The integer values defined between lines 5 and 9 represent the cell nodes, with `i,j` being the row and column indexes respectively, and with `W,S,E,N` being the cardinal points: the bottom-left node will thus have coordinates `(iW,jS)`, the bottom-right `(iE,jS)` and so on. The `if` statements at lines 7, 15 and 19 are needed to check whether the kernel is accessing nodes contained in the mesh, which has size `XMAPSIZE`×`YMAPSIZE`. Finally, the bi-linear interpolation is performed in lines 20-23 by means of a CUDA atomic function, `atomicAdd`. This function allows the kernel to access the memory address of a specific node of the `n` density map, which is stored in the GPU memory as a column-ordered linearized array, and add the value passed as second argument. These atomic functions ensure that the threads perform the summation one by one: this is fundamental to avoid data race conditions, since the `n` density map is passed to the threads as a shared argument.

Average velocity maps are obtained in a similar way, with the quantity to be deposited on the nodes defined as:

```
atomicAdd(&Vmap[k*XMAPSIZE*YMAPSIZE+YMAPSIZE*iW+jS],V[number*k+idx]*
        weight*dx_resx*dy_resy/dxdy/dxdy/n[YMAPSIZE*iW+jS]);
```

with `k` being the k-th velocity component and `Vmap` being a linearized vector map, with size `3*XMAPSIZE*YMAPSIZE`. The squared velocity is also calculated as:

```
atomicAdd(&Vsq[YMAPSIZE*iW+jS],vsquared*
weight*dx_resx*dy_resy/dxdy/dxdy/n[YMAPSIZE*iW+jS]);
```

with:

```
float vsquared=powf(V[0*number+idx],2.0)+ powf(V[1*number+idx],2.0)+
                powf(V[2*number+idx],2.0);
```

Given the average velocity and squared velocity maps, the temperature value for each node is obtained as:

```
Tmap[idx]=mass/3.0/kB*(Vsq[idx]-(powf(Vijk[idx],2.0)+
        powf(Vijk[1*XMAPSIZE*YMAPSIZE+idx],2.0)+
       powf(Vijk[2*XMAPSIZE*YMAPSIZE+idx],2.0)));
```

with `mass` being the mass of the considered specie, `kB` the Boltzmann constant, and `idx` the cell index.

3.2.3 Solving the Poisson equation

Given the density of the plasma species, the charge density map can be obtained and used to solve the Poisson equation:

$$\nabla^2 \phi = -\frac{\rho}{\varepsilon_0} \tag{3.4}$$

with $\rho = q(n_{H^+} + n_{H_2^+} + n_{H_3^+} - n_e - n_{H^-})$. Since both space and time are discretized, the Poisson equation is solved with the Finite Differences Method[54]. From the computational point of view, a linearized matrix system $\mathbf{A}\cdot\mathbf{x} = \mathbf{b}$ needs to be solved, with $\mathbf{A}$ being a large, sparse matrix. To this purpose, iterative methods such as GMRES[55] or BiCGSTAB[56] are applied to obtain the discretized electrostatic potential ϕ on the structured mesh, in such a way that the electric field can be derived as $\vec{E} = -\vec{\nabla}\phi$.

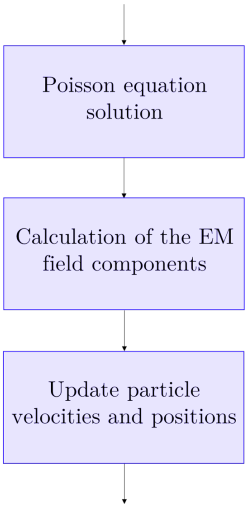

Figure 3.4: Main GPPIC algorithm blocks (part 2/4).

3.2.4 Particle kinetics

The motion of the i-th particle is described by Newton's equations, with the total force acting on the particle defined as:

$$\vec{F}_i = \pm\frac{q_i}{m_i}\left(\vec{E}(\vec{x}_i) + \vec{v}_i \times \vec{B}(\vec{x}_i)\right) \tag{3.5}$$

where $\vec{x}_i$ and $\vec{v}$ are the i-th particle coordinates and velocity components, m_i is the particle mass, q_i is the particle charge, $\vec{B}$ is the externally imposed magnetic field. The $\vec{E}$ field value at the particle position is obtained by reversing the bi-linear interpolation method. The same holds for the externally imposed $\vec{B}$ field if not calculated analytically. For all the simulations shown in this work, the included magnetic field has both intensity and direction constant over time,

hence the solution of Eq.3.4 is sufficient to describe the system. Knowing the force $\vec{F}_i$, the new particle velocities are obtained by implementing the Boris[57] algorithm.

Given the new velocities, the particle spatial coordinates can be updated. Once this operation is done for all the included species, the new particle positions are checked with respect to the domain boundaries, and a certain flag is assigned to each particle according to its position. This allows to pre-select which particles will undergo specific operations such as collisions, interaction with walls, exit from the domain and so on.

3.2.5 Implementing the physics of an ion source

Once the particle positions and velocities have been updated and checked, several operations can be performed depending on the simulation type. The most important ones are briefly described in the following.

Plasma-wall interaction

When interacting with the chamber surfaces, plasma particles can either be reflected, change their charge status, recombine, etc. The Plasma-Wall Interaction (PWI) is a new feature of the GPPIC code, and its implementation will be described in the next chapter.

Regarding neutral particles, H_2 molecules impacting on the walls are either lost with a certain pumping probability s specific to the considered boundary, or reflected with an energy accomodation coefficient α_E. The same processes can occur also for neutral atoms H impacting on the surfaces, although in this case recombination in H_2 molecules shall also be included, with probability $Y_{\text{rec}} = 0.12$. The energy of the recombined H_2 molecules is different depending on their birth mechanism[58]: indeed, they can either be generated by fast ion or atom impact through the Eley-Rideal (ER) mechanism, or due to slow atom impact through the Langmuir-Hinshelwood (LW) mechanism. The difference between these processes is that, in the first case, the molecule is directly emitted from the wall, whereas in the second one the neutralised atom is absorbed at the surface and later re-emitted as a slow molecule (see Figure 3.6).

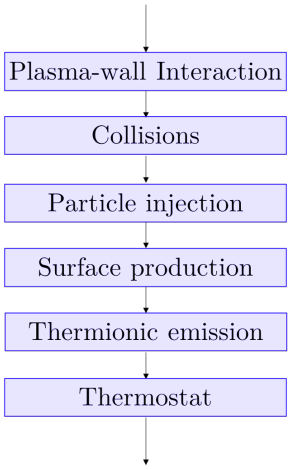

Figure 3.5: Main GPPIC algorithm blocks (part 3/4).

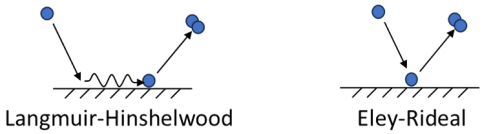

Figure 3.6: Simplified scheme of the Langmuir-Hinselwood and Eley-Rideal processes. In the first case, the impinging atom remains on the surface and recombines later, when a second atom impacts on the surface. In the second case, the molecule is emitted immediately.

Collisions

The most relevant collisions occurring in hydrogen plasma discharges are included in the GPPIC code. The cross sections are loaded from the `Sammy` library, which was developed at Consorzio

RFX. The collision cycle is implemented with three nested `for` cycles: the first one over the projectile species, the second one over the target species, and the last one over the possible collision processes, as described in the following. The collision probabilities are obtained by means of the *P-null* collision method[59].

```
int i,ij,ii;
for(i=0;i<specie_count;i++){
 for(ij=0;ij<target_count;ij++){
  //save indexes of colliding particles
  partMarkForPnull
    <<<specie[i].blocks,prop.maxThreadsPerBlock>>>(...);
  checkcudaerror(__LINE__,verbosecudaerror);

  //get energy of colliding particles and save shortlist
  shortlistedPartGetEnergy
    <<<specie[i].blocks,prop.maxThreadsPerBlock>>>(...);
  checkcudaerror(__LINE__,verbosecudaerror);

  //for each shortlisted particle, assign a flag
  //to distinguish which process it will undergo
  //and count how many times each process will occur
  shortlistedPartCheckPnull
    <<<specie[i].blocks,prop.maxThreadsPerBlock>>>(...);
  checkcudaerror(__LINE__,verbosecudaerror);

  for(ii=0;ii<numCollisions;i++){
   //create particle shortlist for ii-th process
   shortlistedPartShortListCollisions
     <<<specie[i].blocks,prop.maxThreadsPerBlock>>>(...);
   checkcudaerror(__LINE__,verbosecudaerror);

   //there is an if statement for each possible process
   if(ii=ProcessId){
     //launch collision kernel
   }
  }//end cycle over processes
 }//end cycle over targets
}//end cycle over projectiles
```

Listing 3.3: Host code for the collision cycle.

In the former version of GPPIC, this collision cycle was applied only to plasma particles interacting with neutral atoms and molecules. Furthermore, the target species could only be treated as fixed backgrounds with uniform density and temperature. During this work, the collision cycle has been extended to all types of collisions, including the ones among plasma species; this required the implementation of a new version of the `target` class for treating all collisions in a pseudo-binary way. Coulomb collisions[60] are excluded from this main cycle, and performed with dedicated CUDA kernels.

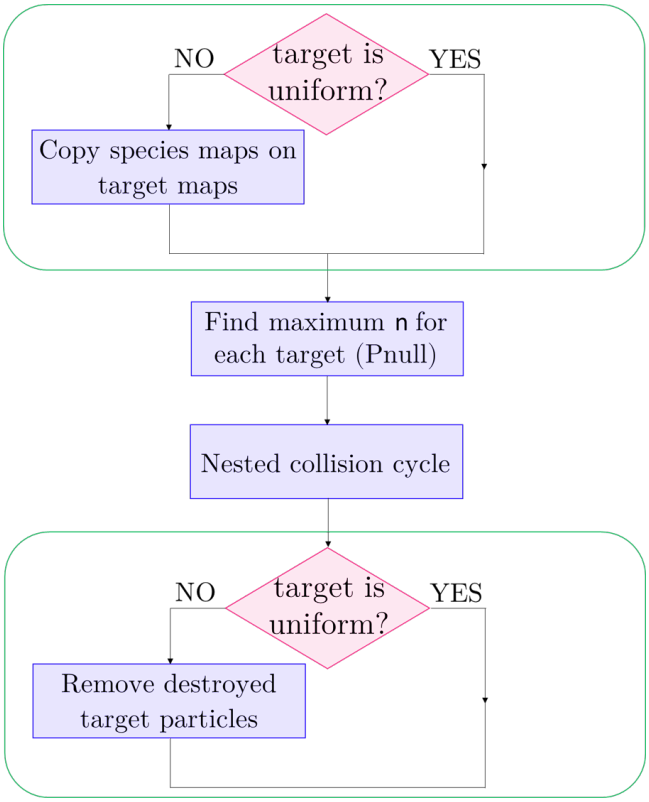

Figure 3.7: Main algorithm steps for collisions in GPPIC. Blocks inside the green rectangle have been added during this work.

With reference to Figure 3.7, if the considered target species is not treated as fixed background (e.g. for plasma species), the density map for this target species is copied in the correspondent `target` object. The two central blocks are left unchanged: the maximum density value is identified, and the collision processes are performed. If the considered target is not uniform, the needed target properties at the projectile location are calculated from the correspondent maps, otherwise constant values are considered. The space and velocity coordinates of new particles eventually created during the collisions are defined within the respective collision kernels. If target particles are destroyed during the process and the target is not uniform, a dedicated map (`target[ij].d_removetarget`) is used to save this information: for instance, if a target particle needs to be removed from the k-th cell, a unit will be added to the k-th element of the `d_removetarget` map. At the end of the main collision cycle, a CUDA kernel will remove the required N_k particles from each k-th cell.

The collision processes included in GPPIC are summarized in Tables 3.1, 3.2, and 3.3. All cross sections are taken from[61], unless specified otherwise.

Reactants	Processes
H, H_2	Ionization, electron detachment, charge exchange, dissociative ionization, elastic scattering
H, H	Elastic scattering
H_2, H_2	Elastic scattering

Table 3.1: Collision processes between neutrals included in the GPPIC code.

Reactants	Processes
e, H_2	Ionization[60], dissociation, dissociative ionization, dissociative attachment, vibrational excitation, rotational excitation, elastic scattering
e, H	Ionization, atomic excitation, elastic scattering
H^+, H_2	Charge exchange, dissociation, dissociative ionization, elastic scattering
H^+, H	Charge exchange
H_2^+, H_2	Dissociation, particle exchange, charge exchange, elastic scattering
H_2^+, H	Dissociation
H_3^+, H_2	Dissociation, elastic scattering
H^-, H_2	Electron detachment, double electron detachment, ioniztion, ionization, dissociative ionization, elastic scattering
H^-, H	Charge exchange, electron detachment, associative detachment

Table 3.2: Collision processes between charged particles and neutrals included in the GPPIC code.

Reactants	Processes
e,e	Coulomb scattering
e, H^+	Coulomb scattering
e, H_2^+	Coulomb scattering, dissociative ionization, dissociative recombination, dissociative excitation
e, H_3^+	Coulomb scattering, dissociative ionization, dissociative recombination
e, H^-	Electron detachment
H^+, H^-	Coulomb scattering, recombination, associative detachment
H^+, H_2^+	Dissociation
H_2^+, H^-	Coulomb scattering
H_3^+, H^-	Coulomb scattering
H_2^+, H^-	Coulomb scattering
H_3^+, H^-	Coulomb scattering

Table 3.3: Collision processes between charged particles included in the GPPIC code.

Particle injection

If required by the boundary conditions, plasma or neutral particles can enter the domain from a specific boundary. The number of particles injected in the domain can be obtained from input parameters such as plasma fluxes or gas throughput.

Surface production

The surface production mechanism is implemented by emitting negative hydrogen atoms H^- from a defined boundary with a given energy. The number of H^- particles to be injected in the domain is obtained from the net surface emitted current density j_{surf} (e.g. the current actually transported through the plasma sheath, see Section 1.1.1), which is given as input parameter, as:

$$N_{H^-} = \frac{j_{\text{surf}}}{q} A_{\text{emitter}} dt \tag{3.6}$$

where q is the elementary charge, dt is the simulation timestep, and A_{emitter} is the emitter surface. When defining the new H^- velocity components, the plasma potential in the proximity of

the new particle must be taken into account as it might either slow down or accelerate the ion, thus the velocity module is corrected accordingly.

Thermionic emission

Electron thermionic emission from a hot filament is needed for simulating arc discharges. In this case, the filament current I_{arc} and polarization voltage V_{pol} are given as input parameters, and the number of emitted electrons is obtained as:

$$N_e = I_{\text{arc}} A_{\text{fil}} dt \tag{3.7}$$

where q is the elementary charge, dt is the simulation timestep, and A_{fil} is the emitting surface of the filament. Also in this case, it is necessary to take into account the plasma potential in the proximity of the filament in such a way to provide the new electrons with the correct energy.

Thermostat

When needed, the electron temperature over a specific region of the domain can be kept at a constant value by re-sampling the electron velocity components with a Maxwellian distribution centered at a temperature value T_{heat}, which is given as input parameter. The original particle direction is preserved. The heating probability is generally obtained as $P = \nu_{\text{heat}} f(x,y) dt$, where dt is the simulation timestep, ν_{heat} is an imposed frequency defining the re-sampling velocity, and $f(x,y)$ is a normalised probability density function which depends on the spatial coordinates and can be specified for each simulation.

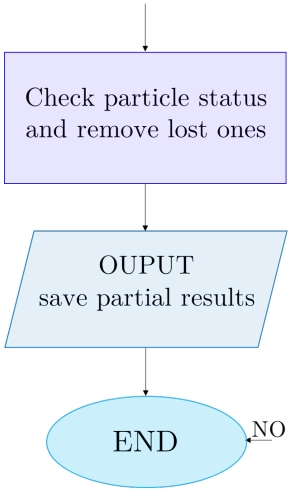

Figure 3.8: Main GPPIC algorithm blocks (part 4/4).

3.2.6 Algorithm end

At the end of the iteration cycle, all the particles that are still out of the domain also after the previously mentioned operations are flagged as “inactive”. Some results are saved as output files before repeating all the operations. The simulation run stops when the maximum number of iterations is reached.

Chapter summary

The basic aspects of the Particle In Cell method applied to plasma simulations have been presented in this chapter. In particular, the space and time discretization, as well as the constraints on the choice of both timestep value and cell dimensions have been explained. The density scaling factor β and the MacroParticle Weight have been introduced, also showing how the number of macroparticles per cell can affect the quality of the simulation results. The GPPIC algorithm has been explained also by giving some examples of CUDA based parallel computing. Finally, the implementation of the most relevant physical processes in negative ion sources has been discussed.

Chapter 4

Newly implemented GPPIC features

This chapter describes new features of the GPPIC code implemented throughout this work, including: improved description of the magnetic field, neutral kinetics description, PWI, thermionic emission and surface production mechanism.

4.1 Magnetic field topology

Externally imposed magnetic fields can be included in GPPIC simulations. This was originally done by calculating the x, y, and z components of the magnetic field from analytical formulae, such as the ones describing multi-cusp confinement[62]. Nonetheless, a more accurate description of the magnetic field topology can be obtained by approximating the real filter field topology with a set of properly positioned infinitely long current wires. As an example, the calculation of the SPIDER Filter Field is described in the following.

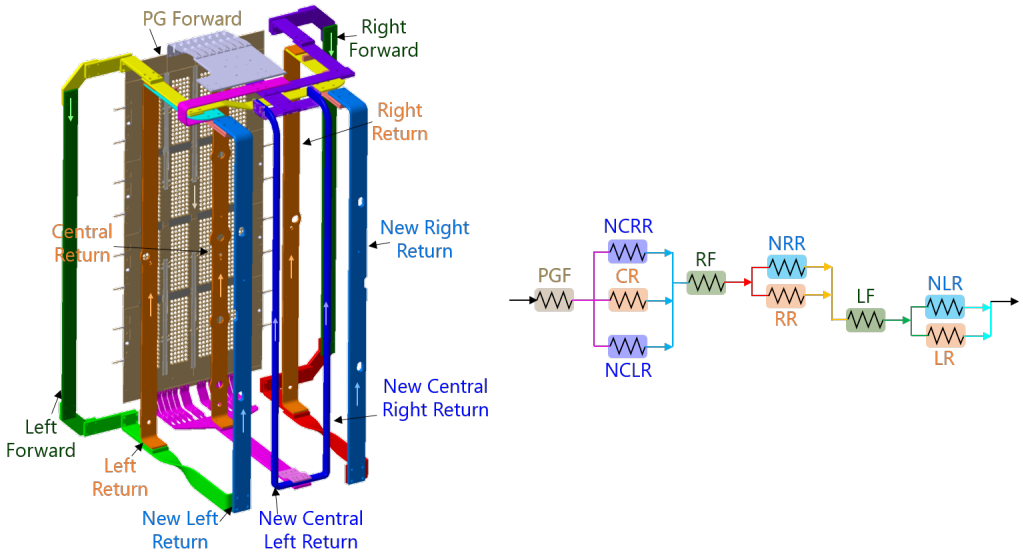

Figure 4.1: Scheme of the PG electrode and busbars system for generating the SPIDER Filter Field. The current flow direction is indicated by the coloured arrows on the busbars.

4.1.1 Calculation of the SPIDER filter field

The SPIDER Filter Field along a two-dimensional plane horizontally cutting the source volume in correspondence of the mid-plane of a pair of drivers will be considered. As previously mentioned, the FF is obtained by letting a current flow along the busbar system shown in Figure 4.1[63]. In the Standard Filter Field Configuration configuration, the current flows downwards along the PG and the forward return bars, depicted in green, whereas it flows in the opposite direction along all the other return bars (yellow and orange). In order to calculate the field components in a two-dimensional domain, the PG and the busbars can be approximated as a set of infinitely long current wires located at $\vec{x} = (x_1, \ldots, x_N, y_1, \ldots, y_N)$ with current $\vec{I} = (I_1, \ldots, I_N)$ flowing along the z direction. These values are passed as input to the GPPIC code and processed by a CUDA kernel which generates the magnetic field map by applying the Biot-Savart law, as shown below.

```
1  __global__ void createMagneticFieldMap
2    (float*wires,int size,float*Bmap)
3  {
4   int idx=blockDim.x*blockIdx.x+threadIdx.x;
5   if(idx<XMAPSIZE*YMAPSIZE){
6    int ix=(int)(idx/YMAPSIZE);
7    int iy=(idx%YMAPSIZE);
8    for(int i=0;i<size;i++){
9     float rx=ix*dx-wires[6*i+0];
10    float ry=iy*dx-wires[6*i+1];
11    float rz=0.0*dx-wires[6*i+2];
12
13    float Ix=wires[6*i+3];
14    float Iy=wires[6*i+4];
15    float Iz=wires[6*i+5];
16
17    float rmod=powf((powf(rx,2.0)+powf(ry,2.0)+powf(rz,2.0)),0.5);
18    float Imod=powf((powf(Ix,2.0)+powf(Iy,2.0)+powf(Iz,2.0)),0.5);
19
20    float Btan=mu0*Imod/2.0/PI/rmod;
21
22    //save field components intensity on Bmap
23    Bmap[YMAPSIZE*XMAPSIZE*0+id]+=(Iy*rz-Iz*ry)/Imod/rmod*Btan;
24    Bmap[YMAPSIZE*XMAPSIZE*1+id]+=(Iz*rx-Ix*rz)/Imod/rmod*Btan;
25    Bmap[YMAPSIZE*XMAPSIZE*2+id]+=(Ix*ry-Iy*rx)/Imod/rmod*Btan;
26   }
27  }
28 }
```

Listing 4.1: Definition of the `createMagneticFieldMap` kernel.

The `float` variable `wires` is a linearized array storing a matrix of `size` rows and 6 columns. Each k-th row stores the position coordinates and current components of the k-th current wire. The Biot-Savart law is exploited in lines 20-25, where the contribution of each current wire is summed to the magnetic field map `Bmap`. In the case of the SPIDER filter field, 1410 current wires were considered to obtain the two-dimensional map shown in Figure 4.2.

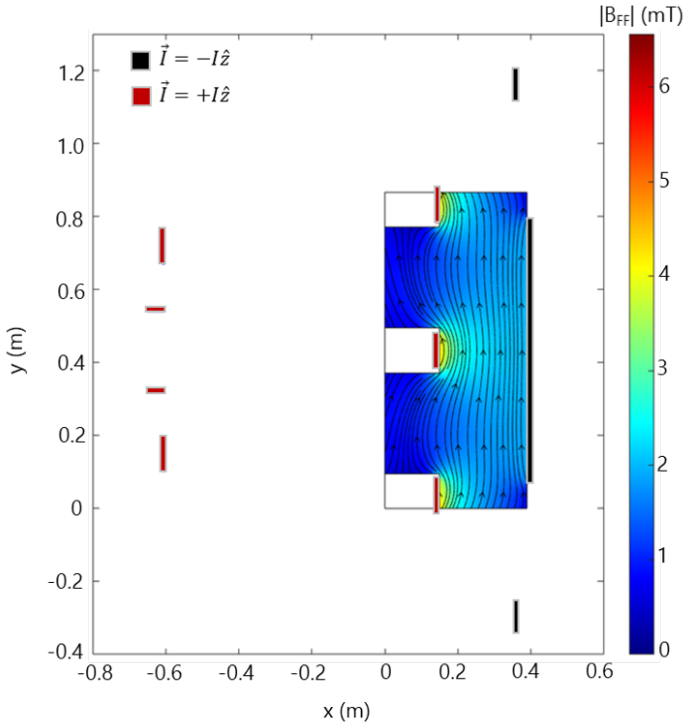

Figure 4.2: Filter Field topology (intensity and direction) obtained on a horizontal plane cutting the source volume in correspondence of the midplane of one RF segment.

4.1.2 Permanent magnets field

In a similar way, the magnetic field generated by permanent magnets along a two-dimensional plane can be approximated by a set of infinitely long current wires as schematically shown in Figure 4.3. The same reasoning presented in Section 4.1.1 holds also for calculating the magnetic field generated by the permanent magnets at a certain location $\vec{x}$ in the domain.

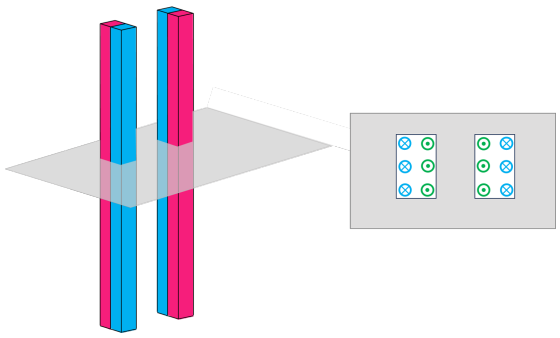

Figure 4.3: Infinitely long current wires positioning for approximating a permanent magnet. This approximation is valid if the permanent magnets orientation is unchanged along the vertical direction.

In the SPIDER case, the permanent magnets located at the lateral walls can be implemented, as shown in Figure 4.4. As further discussed in Chapter 10, the presence of these permanent magnets causes a left-right asymmetry in the filter field topology, possibly affecting the source plasma properties. Figure 4.4 also includes the magnetic field generated by the permanent magnets located downstream of the drivers' backplates, even though in this case the current wire approximation is not completely valid since these magnets are arranged in a chequered configuration.

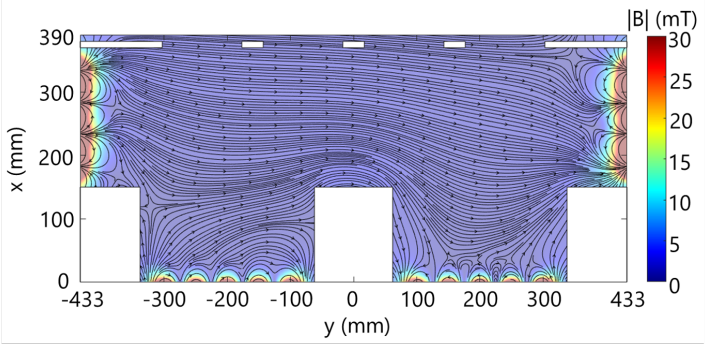

Figure 4.4: Total magnetic field (FF and cusp field) topology obtained on a horizontal plane cutting the source volume in correspondence of the midplane of one RF segment. Both field intensity and direction are shown.

4.2 Neutral kinetics

When simulating the negative ion source, the neutral gas background was formerly considered to be uniform in the entire domain, without taking into account the neutral depletion caused by the interaction between the plasma and the gas itself[64]. Within this approach, both electron temperature and density do not scale correctly with the background gas density: more precisely, the ionization rate in the driver becomes too high, causing simulation divergence. The neutral depletion was eventually implemented through an analytical formula, namely:

$$n(x,y) = n_{\mathrm{bg}}\left[\frac{1}{3} + \frac{1}{6}\left(1 + \tanh\left(\frac{x - 0.15\,\mathrm{m}}{0.05\,\mathrm{m}}\right)\right)\right] \tag{4.1}$$

with n_{bg} being the background gas density obtained from the input gas filling pressure as $n_{\mathrm{bg}} = p_{\mathrm{fill}}/(k_B T_{\mathrm{room}})$. Despite not describing the cold neutral dynamics, this approach was still viable by tuning the electron density and temperature with a PI controller, allowing to obtain significant results regarding plasma properties. However, it was not possible to infer information about other key features of H^-/D^- ion sources such as the dissociation degree of the neutral background. To this purpose, the GPPIC algorithm was modified to treat background neutrals in a similar way as plasma species, i.e. following their kinetics.

However, if both neutrals and plasma macroparticles are given the same MPW, the number of numerical particles describing neutrals would be significantly larger since the neutral background density n_{bg} is at least of one order of magnitude larger than the plasma density. As a consequence, the density scaling factor β should be strongly decreased to comply with the computational limits, yielding less accurate simulation results. For this reason, the neutral MPW has been multiplied by a new parameter $\Sigma > 1$, allowing to describe the gas background with a reduced number of macroparticles.

Another aspect that needs to be considered is that H_2 molecules have larger mass with respect to electrons and also than the positive ion effective mass, and are not subject to the electromagnetic field. As a consequence, their time evolution is much slower and they would employ many iterations to reach a stationary state. For this reason, when dealing with background gas kinetics, the simulation timestep dt is multiplied by Σ: on one hand, this allows a faster convergence of the simulation run; on the other hand, the time evolution of the system loses its physical meaning, hence only stationary states shall be considered as final results.

4.2.1 Influence of neutral scaling on simulation results

Similarly to the MacroParticle Weight, the higher Σ, the lower the number of neutral macroparticles per cell. The value of Σ should be defined in such a way to have a sufficiently large number of neutral macroparticles per cell, avoiding excessive numerical noise, while complying with the computational limits. Other aspects of the modified simulation algorithm are discussed in the following.

Gas injection

When dealing with neutral dynamics, in order to avoid any dependence of the number of injected neutral macroparticles on the neutral scaling Σ, the timestep dt is multiplied by Σ as well. Indeed, considering a gas throughput Q at room temperature, one obtains:

$$\begin{aligned} N_{\mathrm{MP},n} &= \frac{Q}{k_B T} \frac{\beta dt_\Sigma}{\mathrm{MPW} \cdot \Sigma} \\ &= \frac{Q}{k_B T} \frac{\beta dt}{\mathrm{MPW}} \end{aligned} \tag{4.2}$$

with $dt_\Sigma = \Sigma dt$. This allows to safely modify the neutral scaling Σ when needed.

Collision rates

A similar reasoning holds also for the collision rates. For example, one can consider a system in a volume V where only electron impact ionisation can take place, with no gas injection. The evolution of neutrals and plasma ions can be described by the following system:

$$\begin{cases} \dfrac{dn_{\mathrm{H}_2}}{dt_\Sigma} = -n_e n_{\mathrm{H}_2} \langle \sigma v \rangle \\ \dfrac{dn_{\mathrm{H}_2^+}}{dt} = n_e n_{\mathrm{H}_2} \langle \sigma v \rangle \end{cases} \tag{4.3}$$

where dt_Σ labels the neutral timescale. If time discretization is introduced, system 4.3 can be rewritten as:

$$\begin{cases} \dfrac{\Delta n_{\mathrm{H}_2}}{\Sigma \Delta t} = -n_e n_{\mathrm{H}_2} \langle \sigma v \rangle \\ \dfrac{\Delta n_{\mathrm{H}_2^+}}{\Delta t} = n_e n_{\mathrm{H}_2} \langle \sigma v \rangle \end{cases} \tag{4.4}$$

The particle density can be expressed in terms of number of macroparticles, namely $n_{\mathrm{H}_2} = (\beta \cdot V)^{-1} N_{\mathrm{H}_2} \mathrm{MPW} \cdot \Sigma$ and $n_{\mathrm{H}_2^+} = (\beta \cdot V)^{-1} N_{\mathrm{H}_2^+} \mathrm{MPW}$. By substitution:

$$\begin{cases} \dfrac{(\beta \cdot V)^{-1} \mathrm{MPW} \cdot \Sigma \Delta N_{\mathrm{H}_2}}{\Sigma \Delta t} &= -n_e (\beta \cdot V)^{-1} N_{\mathrm{H}_2} \mathrm{MPW} \cdot \Sigma \langle \sigma v \rangle \\ \dfrac{(\beta \cdot V)^{-1} \mathrm{MPW} \Delta N_{\mathrm{H}_2^+}}{\Delta t} &= n_e (\beta \cdot V)^{-1} N_{\mathrm{H}_2} \mathrm{MPW} \cdot \Sigma \langle \sigma v \rangle \end{cases} \tag{4.5}$$

By simplifying both equations:

$$\begin{cases} \dfrac{\Delta N_{\mathrm{H}_2}}{\Delta t} &= -n_e N_{\mathrm{H}_2} \langle \sigma v \rangle \Sigma \\ \dfrac{\Delta N_{\mathrm{H}_2^+}}{\Delta t} &= n_e N_{\mathrm{H}_2} \langle \sigma v \rangle \Sigma \end{cases} \Rightarrow \frac{\Delta N_{\mathrm{H}_2}}{\Delta t} = -\frac{\Delta N_{\mathrm{H}_2^+}}{\Delta t} \tag{4.6}$$

Hence the variation of the number of macroparticles per timestep is the same, as if the neutral scaling Σ was equal to 1. Although only the $e, H_2 \rightarrow e, H_2^+, e$ reaction was taken as example, this result is valid for all types of processes including neutrals. For this reason, after the collision cycle (described in Section 3.2.5), neutral macroparticles can be safely removed without modifying the destruction rates.

4.2.2 Validation of neutral model: transmission through a slit

In order to benchmark the implementation of neutral kinetics description in GPPIC, gas transmission through a two dimensional slit of height b and length L as shown in Figure 4.5 was considered as a test-case. Hydrogen molecules are injected from the left side of the domain with a defined gas throughput Q. When impacting on the bottom and top surfaces, the molecules undergo diffused reflection. Both the left and right boundaries have unitary sticking coefficient, hence particles can freely exit from the domain.

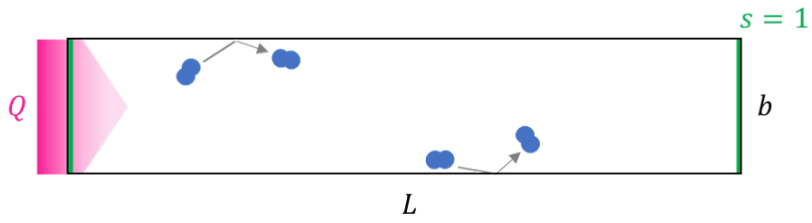

Figure 4.5: Simulation domain for neutral model benchmarking.

Free molecular regime

The transmission probability along the slit P can be defined as the ratio between the outgoing particle flux leaving the domain from the right boundary, and the injected particle flux at the left boundary:

$$P = \frac{\Phi_{\text{out,DX}}}{\Phi_{\text{in,SX}}} = \frac{N_{\text{H}_2,\text{DX,out}}(\beta^{-1}\Sigma \cdot \text{MPW})}{A_{\text{slit}} dt_\Sigma} \cdot \frac{A_{\text{slit}} dt_\Sigma}{N_{\text{H}_2,\text{SX,in}}(\beta^{-1}\Sigma \cdot \text{MPW})} = \frac{N_{\text{H}_2,\text{DX,out}}}{N_{\text{H}_2,\text{SX,in}}} \tag{4.7}$$

In free molecular regime, when the H_2 mean free path is much larger than the domain length L, the transmission probability across a narrow slit ($b \ll L$) can be approximated as[65]:

$$P = \frac{1 + ln(0.433(L/b) + 1)}{(L/b) + 1} \tag{4.8}$$

In order to verify whether the simulation results correctly reproduced Eq.4.8, the three cases listed in Table 4.1 with different b/L ratio were considered.

Case #	L (m)	b (m)	L/b	P_{th}	P_{PIC}
1	0.5	0.1	5	0.359	0.355
2	1	0.1	10	0.243	0.239
3	2	0.1	20	0.156	0.151

Table 4.1: Simulated cases for code benchmark in free molecular regime. The transmission probability obtained with the PIC code is compatible with the theoretical estimations provided by Eq.4.8).

As depicted in Figure 4.6, the obtained values for the transmission probability P are in very good agreement with the theoretical predictions.

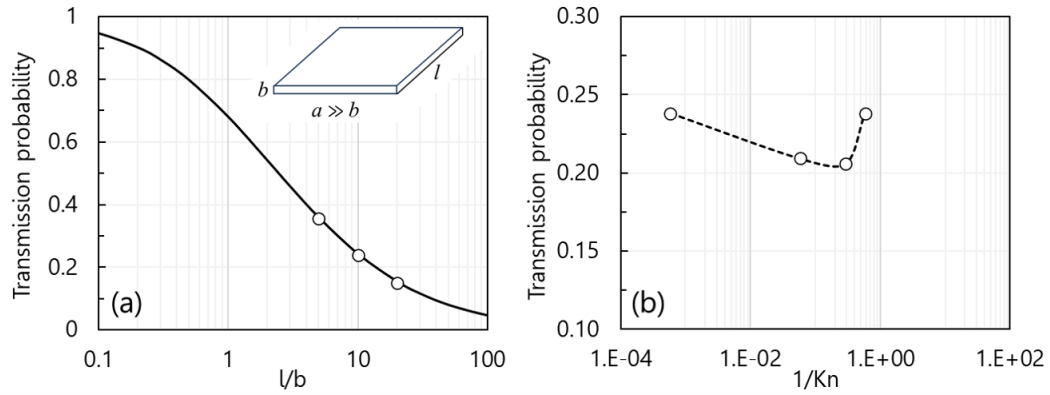

Figure 4.6: (a) theoretical prediction (solid black line) and PIC estimations (white circles) for the gas transmission probability P along a narrow slit; (b) PIC estimations (white circles) for the gas transmission probability P along a narrow slit in collisional regime, with L/b=10.

Collisional regime

If collisions among the H_2 molecules are included, the transmission probability will depend on the Knudsen number $K_n = 1/\lambda_n$, with λ_n being the molecular mean free path. In order to benchmark the code also in these conditions, a CUDA kernel performing elastic scattering among the hydrogen molecules was implemented, while keeping the same simulation domain as shown in Figure 4.5. The transmission probability along the slit was calculated for different Knudsen numbers, as shown in Figure 4.6. As expected[65], the transmission probability features a minimum for Knudsen numbers close to 1.

The diffusion of a gas across a slit can be described by the Fick's law $\Gamma = D\nabla n$, where Γ is the gas flux, n the gas density, and D is the diffusion coefficient. The spatial evolution of the gas density can be obtained by applying the gradient operation to Fick's law, yielding $\nabla \cdot \Gamma = D\nabla^2 n$. In free molecular regime, the diffusion coefficient can be defined as the ratio between the characteristic length and evolution timescale of the domain. If no collisions are included, the diffusion coefficient D only depends on geometrical properties of the system and is uniform in space, hence for a one-dimensional domain without gas source terms (i.e. $\nabla\cdot\Gamma = 0$) one obtains a simple differential equation:

$$D\frac{\partial^2 n(x)}{\partial x^2} = 0 \rightarrow n(x) = c_1 x + c_2 \tag{4.9}$$

The solution is a linear function, with the coefficients c_1 and c_2 determined by imposing boundary conditions. Therefore, in free molecular regime one should obtain a linear solution for the density profile across the slit.

On the other hand, in the collisional regime, the diffusion coefficient D will also depend on the spatial coordinates: the characteristic length of the system can be estimated as the neutral mean free path, which is inversely proportional to the density n thus one can assume $D \propto 1/n(x)$. In this case, by applying the gradient operation to the Fick's law one obtains $\nabla D\nabla n + D\nabla^2 n = 0$, which in one dimension yields:

$$\frac{\partial}{\partial x}\left(\frac{1}{n(x)}\right)\frac{\partial n(x)}{\partial x} + \frac{1}{n(x)}\frac{\partial^2 n(x)}{\partial x^2} = 0 \rightarrow n(x) = c_2 e^{c_1 x} \tag{4.10}$$

In this case the solution is an exponential function, with the coefficients c_1 and c_2 given by boundary conditions. Figure 4.7 shows the simulated density profiles across a narrow slit for both free molecular and collisional regimes. As previously mentioned, the solution in the free

molecular regime is a linear density profile, whereas in the collisional regime it becomes an exponential profile.

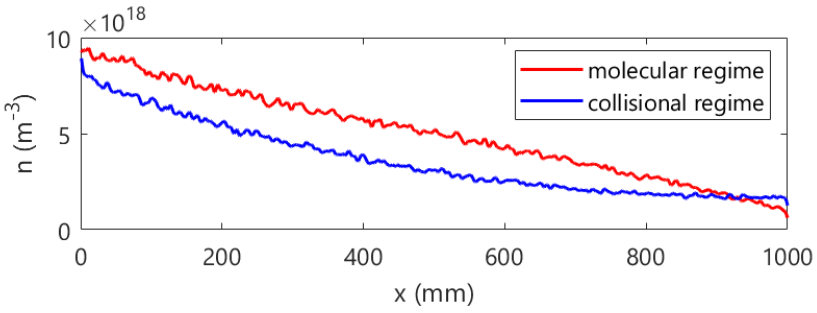

Figure 4.7: Simulated density profiles in free molecular (red) and collisional (blue) regimes. As expected, collisions modify the linear profile, yielding an exponential solution.

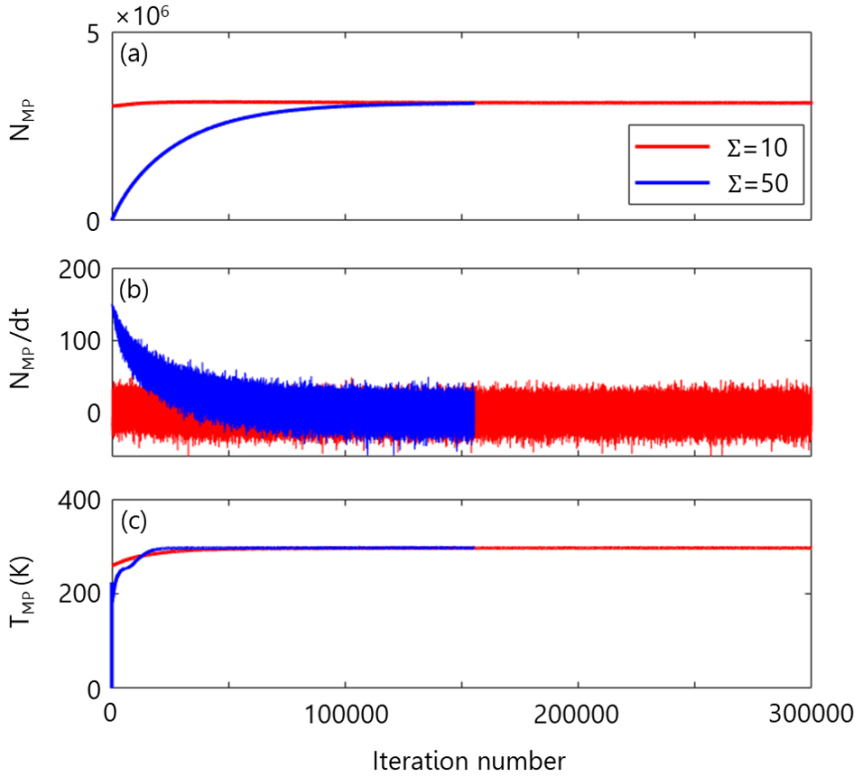

Figure 4.8: (a) Number of neutral macroparticles, (b) macroparticle rates, and (c) average macroparticle temperature as a function of the iteration number for low (red) and high (blue) Σ scaling.

4.2.3 Validation of the neutral scaling

Since both the timestep dt and the neutral particle weight are multiplied by the same Σ factor, the evolution of the neutral background is not influenced by variations of dt: this allows to use a larger timestep $dt_{\text{neu}} > dt_{\text{plasma}}$ for obtaining the vacuum solution of the system, and then load the latter as the starting configuration for the plasma discharge simulation. In fact, neutral

particles are not affected by the electrostatic field, hence neither of the timestep constraints defined in 3.1 need to be satisfied.

Figure 4.8 shows the evolution of the number of neutral particles N_{MP}, their rate dN_{MP}/dt, and the average temperature T_{MP} for two simulation runs with identical boundary conditions, but different timestep. The simulation with Σ=50 reaches the same stationary conditions of the one obtained with Σ=10.

4.3 Plasma-wall interaction

As introduced in Section 3.2.5, the interaction between all the considered plasma species and the domain walls has been implemented in the GPPIC code. The included processes, as well as their probability and the energy accommodation coefficient α_E are listed in Table 4.2.

Process			Probability	α_E
H^+	$\rightarrow$	H_2	0.2	-
H^+	$\rightarrow$	H	0.8	0.15
H_2^+	$\rightarrow$	H_2	0.5	0.15
H_2^+	$\rightarrow$	H	0.5	0.1
H_3^+	$\rightarrow$	H_2	1/3	0.15
H_3^+	$\rightarrow$	H	2/3	0.1
H^-	$\rightarrow$	H	1	0.15
H_2	$\rightarrow$	H_2	1	0.15
H	$\rightarrow$	H_2	0.12	0.15

Table 4.2: Included PWI processes in the GPPIC code.

Regarding the code implementation, as a first step some C++ structures dedicated to the description of the domain boundaries were defined. More precisely, horizontal, vertical and round boundary types are considered. For linear boundaries:

```
1 horizBoundary[0].setBoundary(
2  float m, float q, float n,
3  float x1, float x2, float y1, float y2,
4  float s, float gamma, float alphaE, float Twall,
5  float gasFluxH2, float gasFluxH)
6 //the same definition holds for vertical boundaries
```

Listing 4.2: Linear boundary definition example.

The `m` and `q` parameters are the slope and intercept of a line defining the boundary interface. The variable `n` is the normal versor to the surface, and is always directed towards the inner chamber volume. The parameters `x1`,`x2`,`y1`,`y2` determine a control area, in such a way to shortlist the particles that could potentially interact with the boundary. The value s is the sticking coefficient of the boundary, that is the probability of losing particles across the surface. The parameters `gamma`, `alphaE`, and `Twall` are the interaction probability, the energy accommodation coefficient and the wall temperature respectively. Finally, `gasFluxH2` and `gasFluxH` are the fluxes that can eventually be injected from the boundary, with their values being initialised to zero by default.

A similar definition holds for the round boundaries:

```
roundBoundary[0].setBoundary(
 float r, float n, float xc, float yc,
 float r1, float r2, float th1, float th2,
 float s, float gamma, float alphaE, float Twall,
 float gasFluxH2, float gasFluxH)
```

Listing 4.3: Round boundary definition example.

In this case, a circumference of radius `r`, centered in (`xc`,`yc`), is defined from the angle `th1` up to the angle `th2`. The normal to the versor surface, `n`, can be either parallel or anti-parallel with respect to the radial direction. The parameters `r1` and `r2` allow to define a control area, whereas all the other parameters are defined in the same way as for linear boundaries.

Given the aforementioned boundary definitions, it is possible to determine whether a particle of coordinates (x,y) is out of the wall by checking if the `n`(m`x`+`q`-y) ≥ 0 condition for horizontal boundaries or the `n`(m`y`+`q`-x) ≥ 0 one for vertical boundaries is verified. For round surfaces, the particle radius r_p with respect to the boundary center is calculated and then compared to the boundary radius `r`, hence the condition to be checked is `n`(`r`-r_p) ≥ 0. Figure 4.9 shows some examples of different boundary definitions.

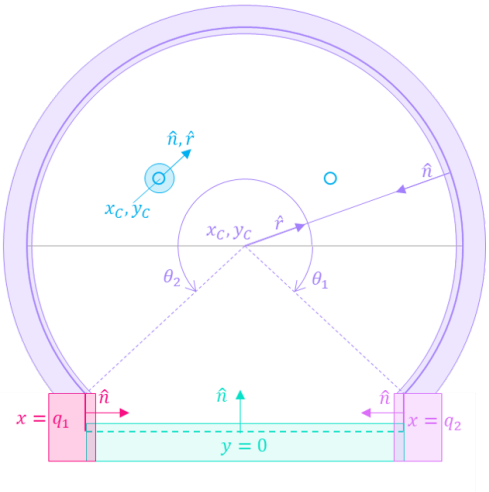

Figure 4.9: Simulation domain including two round boundaries, two vertical boundaries and one horizontal boundary. In each case, the definition of boundary parameters such as control area and normal to the surface are depicted.

In order to assess whether the particle has actually crossed the boundary, it is necessary to check whether it was inside the domain in the previous timestep. If both these conditions are verified, the impact position can be derived. The implementation of this latter part is common for all kernels implementing PWI processes, as shown in code snippet 4.4.

```
__global__ void partBoundaryDiffuseRefRec_Horiz
 (int number,float*X,float*V,int*flag,float x1,float x2,float y1,
  float y2,float n,float m,float q,float s,float gammarec,float Tw,
  float alpha_E,float mass,int*sl_np,int*nvi_np,int*flag_np,float*X_np,
  float*V_np,float mass_np,float mydt,curandState* globalState)
{
 int idx=blockDim.x*blockIdx.x+threadIdx.x;
 float R,xold,yold,zold,qpart,mpart;
```

```
9   float xint,yint,zint,normp,normw;
10  float timpact;
11  if(idx<number){
12   curandState localState=globalState[idx];
13   //recall that X, V are linarised matrices structured as:
14   //X=(x1,...,xN,y1,...,yN,z1,...,zN)
15   //V=(vx1,...,vxN,vy1,...,vyN,vz1,...,vzN)
16   if(flag[idx]!=0 && flag[idx]!=4)
17    if(X[number*0+idx]>x1 && X[number*0+idx]<x2 &&
18       X[number*1+idx]>y1 && X[number*1+idx]<y2) //control volume
19     //check if particle is out of boundary
20     if(n*(X[number*1+idx]-m*X[number*0+idx]-q)<=0.0){
21      //check if particle was in at previous timestep
22      xold=X[number*0+idx]-V[number*0+idx]*mydt;
23      yold=X[number*1+idx]-V[number*1+idx]*mydt;
24      zold=X[number*2+idx]-V[number*2+idx]*mydt;
25      if(n*(yold-m*xold-q)>0.0){
26       float mRatio=mass/mass_np;
27       R=curand_uniform(&localState);
28       if(R>=s+mRatio*gammarec){
29        //find impact position coordinates
30        qpart=X[number*1+idx]-X[number*0+idx]*
31             (X[number*1+idx]-yold)/(X[number*0+idx]-xold);
32        mpart=(X[number*1+idx]-yold)/(X[number*0+idx]-xold);
33        xint=(qpart-q)/(m-mpart);
34        yint=m*xint+q;
35        if(X[number*0+idx]==xold){
36         xint=X[number*0+idx];
37         yint=q;
38        }
39        normp=sqrtf(powf(xold-X[number*0+idx],2.0)+
40                    powf(yold-X[number*1+idx],2.0));
41        normw=sqrtf(powf(xold-xint,2.0)+powf(yold-yint,2.0));
42        timpact=normw/normp*mydt;
43        zint=zold+V[number*2+idx]*timpact;
44        //PWI interaction code
45       } else { //particle is pumped out or recombined
46        flag[idx]=4;
47       }
48      }
49     }
50  }
51 }
```

Listing 4.4: Checking of particle position with respect to a horizontal boundary.

This `partBoundaryDiffuseRefRec_Horiz` kernel describes the plasma-wall interaction for neutral atoms, and is called for all horizontal boundaries. The `if` statement at line 16 is needed to perform the position check only on those particles who are not either active or inactive. The `if` statement at line 17 determines whether the particle belongs to the control volume of the considered boundary. If this is verified, the `if` statement at line 20 actually checks whether the particle has crossed that specific boundary. At this point, the particle coordinates at the previous timestep are obtained in lines 22-24. The `if` statement at line 25 determines whether the particle was inside the domain in the previous timestep. This being said, the kernel calculates the

impact position coordinates only if the interaction is going to happen, as checked by the `if` statement at line 28: a random number `R` is compared to a probability P=`s+mRatio*gammarec`, where `s` is the boundary sticking coefficient, and `gammarec` is the recombination coefficient, which is multiplied by the mass ratio of the impacting particle `mass` and the recombined particle `mass_np`. This multiplication is needed for mass conservation: indeed, the recombined particle cannot be generated each time a neutral atom impacts on the surface, but rather every `mass/mass_np` time, since `mass_np/mass` neutral atoms are needed to obtain a recombined new particle. If `R`<P, then the neutral atom is lost either because it is pumped away (`R`<`s`), or because it recombined without generating a new particle. If `R`>P instead, the impact position coordinates are calculated by finding the intercept between the line describing the boundary, and the one connecting the actual and old particle position, as shown in Figure 4.10. The impact time at line 42 is obtained by multiplying the simulation timestep dt for the ratio of the distance between the old particle position and the boundary, over the distance between the new and old particle positions.

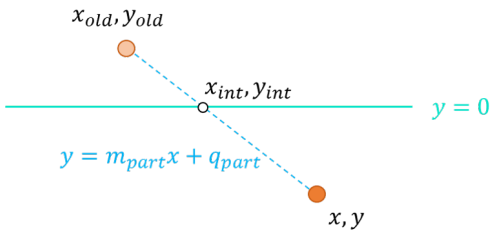

Figure 4.10: Schematic representation of a particle crossing an horizontal boundary. The interception between the boundary and the line connecting the particle old and new position is depicted.

The PW interaction code is shown in the following snippet:

```
1  //PW interaction code
2   //obtain diffusion versor
3   float wx,wy,wz;
4   float nx=0.0;
5   float ny=n;
6   float nz=0.0;
7   float a=0.0;
8   do{
9    randompointonunitsphere(wx,wy,wz,localState);
10   wx=wx+nx;
11   wy=wy+ny;
12   wz=wz+nz;
13   a=powf(wx*wx+wy*wy+wz*wz,0.5);
14  } while (a==0.0);
15  wx=wx/a;
16  wy=wy/a;
17  wz=wz/a;
18
19  if(R<s+gammarec){// recombination and H2 generation
20   //projectile is lost
21   flag[idx]=4;
22
23   //recombined particle is created
24   int sl_np_idx=atomicAdd(nvi_np,1);
25   int idx_np=sl_np[sl_np_idx];
```

```
26    if(idx_np<number){
27     //new particle velocity
28     float stddev_w=sqrtf(kB*Tw/mass_np);
29     V_np[number*0+idx_np]=wx*stddev_w;
30     V_np[number*1+idx_np]=wy*stddev_w;
31     V_np[number*2+idx_np]=wz*stddev_w;
32
33     //new particle position
34     X_np[number*0+idx_np]=xint+V_np[number*0+idx_np]*(mydt-timpact);
35     X_np[number*1+idx_np]=yint+V_np[number*1+idx_np]*(mydt-timpact);
36     X_np[number*2+idx_np]=zint+V_np[number*2+idx_np]*(mydt-timpact);
37
38     flag_np[idx_np]=0;
39    }
40   } else {//diffusion
41    //new coordinates of impacting particle
42    float normV=sqrt(powf(V[number*0+idx],2.0)+
43                     powf(V[number*1+idx],2.0)+
44                     powf(V[number*2+idx],2.0));
45    float E0=0.5*mass*normV*normV;
46    float E1=E0-alpha_E*(E0-1.5*Tw*kB);
47    normV=powf(E1*2./mass,0.5);
48
49    V[number*0+idx]=wx*normV;
50    V[number*1+idx]=wy*normV;
51    V[number*2+idx]=wz*normV;
52
53    X[number*0+idx]=xint+V[number*0+idx]*(mydt-timpact);
54    X[number*1+idx]=yint+V[number*1+idx]*(mydt-timpact);
55    X[number*2+idx]=zint+V[number*2+idx]*(mydt-timpact);
56
57    flag[idx]=0;
58   }
```

Listing 4.5: PW interaction code.

From line 3 to line 17, a versor (`wx,wy,wx`) is randomly extracted from a spherical distribution located at the impact position on the boundary. If the random number `R` is smaller than the P=`s+gammarec`, the projectile becomes inactive (line 21), and a new recombined particle is created (lines 23-39) at wall temperature `Tw`. Finally, if `R`>P, the impacting atom is diffused with energy `E1`<`E0` due to the energy accomodation coefficient. Other kernels implementing processes from Table 4.2 are all very similar, thus they will not be described.

This implementation was verified by simulating a neutral flux entering through a bidimensional rectangular channel, as the one shown in Figure 4.5. Wall recombination was enabled on all the domain walls only after having reached a stationary solution. The time evolution of the two species H and H_2 is shown in Figure 4.11. Specifically, mass conservation is verified, as can be seen from the graph on the right: in fact, the number of atoms decreases from $4.1 \times 10^6$to 1.5×10^6 atoms, meaning that 1.3×10^6 H_2 recombined molecules were generated. By considering that the molecules are free to leave the domain from the left wall, and that the sticking coefficient at the right wall is s=0.15, roughly 85% of these molecules are staying in the domain, which is compatible with the resulting increment of the H_2 molecules number.

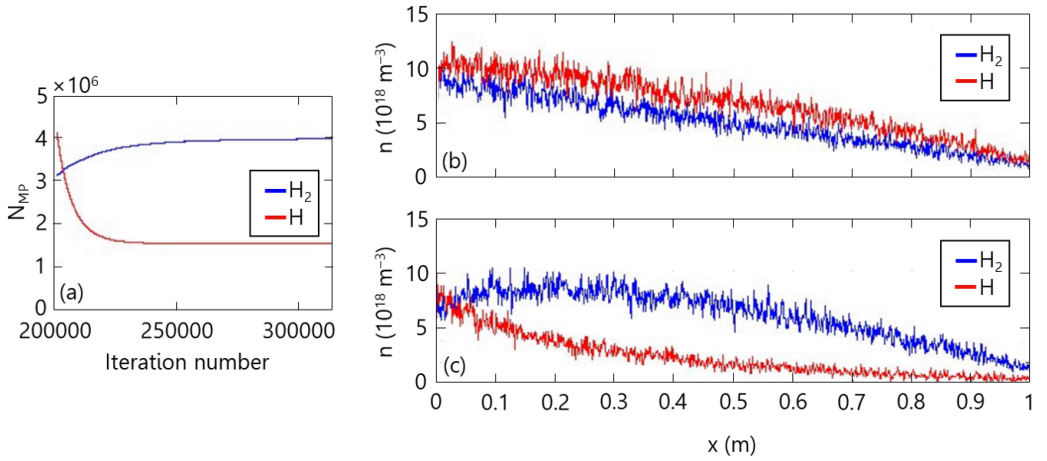

Figure 4.11: (a) Number of H and H_2 macroparticles in the domain as a function of the iteration number, activating H recombination at walls with coefficient Y=0.12 from an equilibrium flow with Y=0; (b) initial and (c) final n_H and n_{H_2} profiles along the slit, L/d=10, molecular regime, recombination coefficient Y=0.12.

4.4 Particle emission in electric fields

4.4.1 Thermionic emission

In order to simulate plasma discharges in filament-based negative ion sources, thermionic electron emission from filaments was implemented. The number of electrons to be generated is obtained as described in Eq. 3.7. The GPPIC kernel performing thermionic emission from a round filament perpendicular to the simulation domain is described in Example 4.6.

```
__global__ void partThermionicEmission_roundwire
 (float*X,float*V,int*flag,int*Indx,int*nvi,int number,
  float qsign,float radius,float xcenter,float ycenter,
  float mydt,int nOfElectrons,float Vemitter,float mass,
  float thermalEnergy_eV,float*phi,int seed)
{
 int idx=blockDim.x*blockIdx.x+threadIdx.x;
 if(idx<nOfElectrons){
  int id=atomicAdd(nvi,1);
  int i=Indx[id];
  if(i<number){
    curandState state;
    curand_init(seed,i,0,&state);

    float R=curand_uniform(&state);
    float theta=PI*(-1.0+2.0*R);

    X[number*0+i]=xcenter+radius*cosf(theta);
    X[number*1+i]=ycenter+radius*sinf(theta);
    X[number*2+i]=0.0;

    X[number*0+i]=((float)(__float2int_rn(X[number*0+i]/dx)))*dx;

```

```
24      //Local potential correction
25      int iW=(int)(X[number*0+i]/dx), iE=iW+1,
26          jS=(int)(X[number*1+i]/dy), jN=jS+1;
27      float resx=X[number*0+i]-(float)(iW*dx),
28            resy=X[number*1+i]-(float)(jS*dy),
29            dx_resx=dx-resx,
30            dy_resy=dy-resy;
31
32      float pot=0.0;
33
34      if(0<=iW  iE<XMAPSIZE  0<=jS  jN<YMAPSIZE)
35       pot=((phi[YMAPSIZE*iW+jS]*dx_resx+
36             phi[YMAPSIZE*iE+jS]*resx)*dy_resy+
37            (phi[YMAPSIZE*iW+jN]*dx_resx+
38             phi[YMAPSIZE*iE+jN]*resx)*resy)/(dx*dy);
39
40       float stddev=sqrtf(ELEMENTARY_CHARGE*thermalEnergy_eV/mass);
41       float v_ri=stddev*curand_normal(&state);
42       float v_rj=stddev*curand_normal(&state);
43       float v_rk=stddev*curand_normal(&state);
44
45       //Renormalise velocity taking into account
46       //local potential and total energy
47       float K0=0.5*mass*powf(v_ri,2.0)/ELEMENTARY_CHARGE;
48       //K0+qsign*Vemitter=qsign*pot+K1
49       float K1=K0+(Vemitter-pot)*qsign; // eV
50       if(K1>=0.0){
51         v_ri=sqrtf(2.0*K1*ELEMENTARY_CHARGE/mass);
52         flag[i]=0;
53
54         V[number*0+i]=cosf(theta)*v_ri-sinf(theta)*v_rj;
55         V[number*1+i]=sinf(theta)*v_ri+cosf(theta)*v_rj;
56         V[number*2+i]=v_rk;
57       }
58     }
59   }
60 }
```

Listing 4.6: Thermionic emission kernel.

In lines 15 and 16, a random emission angle `theta` is generated between $-\pi$ and π. The temporary position coordinates are defined in lines 18-20 as a random position along the round filament boundary; indeed, `xcenter`, `ycenter`, and `radius` are the filament center coordinates and radius respectively. The x position of the particle is modified in line 22, in such a way to discretize the x coordinate, obtaining $x = Ndx$ with N being an integer number. This is needed because the simulated mesh is composed of squared cells, hence the boundary of the filament is actually serrated rather than round as shown in Figure 4.12. By discretizing the x coordinate, the electrons are emitted along a path with length more similar to the filament circumference, as a result of a reasonable geometrical simplification.

After having defined the new electron position, the local value of the electrostatic potential `pot` is obtained from the two-dimensional map `phi` by reversing the bilinear interpolation method. The three velocity components are randomly generated assuming that the new electron is emitted with an energy correspondent to the filament temperature (lines 41-43). One of the

velocity components is renormalised in order to take into account the fact that the new electron is emitted in a region featuring a non-negligible electric field. Finally, a rotation is applied to the x and y velocity components.

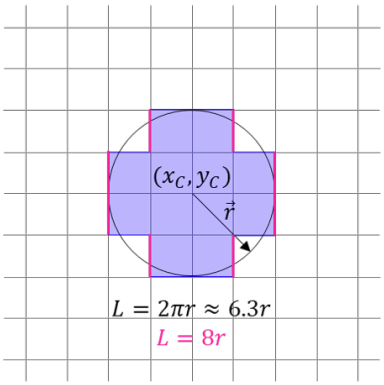

Figure 4.12: Discretization of a filament of radius r, centered in (x_C, y_C). The mesh nodes belonging to the filament are the ones covered by the blue area (edges included). Thermionic electrons are emitted on the sides highlighted in magnenta only.

4.4.2 Surface production mechanism

The implementation of the surface production mechanism is quite similar to the thermionic emission one. In this case, however, negative ions are emitted perpendicularly to mostly plain horizontal or vertical boundaries. Assuming H^- emission along the x direction, the x position of the new particles is obtained as $x = x_0 + \mathrm{R} \cdot (v_x dt)$, where x_0 is the emitter position, v_x is the x component of the particle velocity, and R is a random number uniformly distributed in $[0, 1)$; this ensures that the emitted particles are evenly distributed in space. The new particle velocity is obtained from the energy conservation equation.

Chapter summary

The implementation of some new features of the GPPIC code has been described in this chapter. More precisely, the new way of describing the magnetic field topology, the introduction of the neutral kinetics description, Plasma-Wall Interaction, and thermionic emission have been introduced. The implementation of neutral kinetics, although not complete, has been an important improvement of the GPPIC code. Besides describing the upgraded algorithm, the validation of this kinetic model in both free molecular regime and collisional regime has been described, taking the gas transmission through a slit as a case-study. Better results were obtained in the free molecular regime, suggesting that some further improvements are needed for including collisions among neutral particles in a more efficient way. The neutral scaling factor, Σ, has been shown to be a key element for reducing the computational cost of the simulation. Furthermore, it was demonstrated that the presence of this factor does not affect the simulation outcomes. It is important to point out that, in this way, these simulations can well describe only stationary states, since the time evolution of the system has no longer physical meaning. The method adopted for including the PWI, based on the definition of specific boundaries, has been described, as well as its parallel implementation. Finally, the implementation of electron thermionic emission has been described, also explaining the issues related to space discretization in the case of round elements.

Part III

Plasma properties in giant negative ion sources

Chapter 5

Plasma expansion in RF sources

Plasma expansion from a single RF driver is discussed in this chapter, starting from experimental findings from the SPIDER ion source. The influence of some source operating parameters on the axial plasma profiles is analysed, with a particular focus on how the latter affect the positive ion energy distribution in the extraction region. To this purpose, selected results from an experimental campaign carried out at BUG (IPP) with a RFEA sensor are shown.

5.1 Axial profiles in the SPIDER source

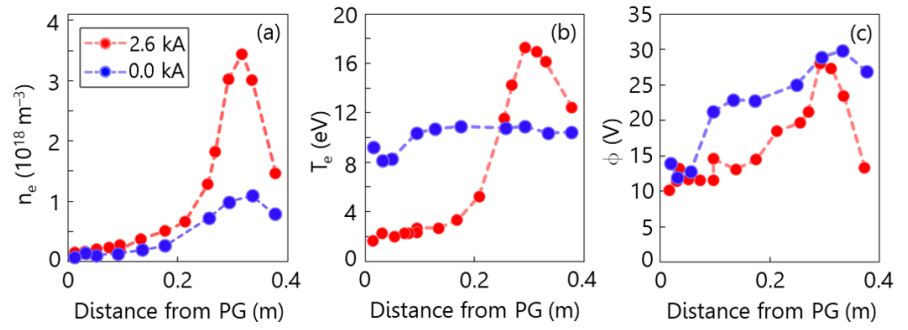

Figure 5.1: (a) Electron density n_e, (b) electron temperature T_e, and (c) plasma potential ϕ as a function of the distance from the PG electrode, with I_{PG}=0 kA (blue) and 2.6 kA (4.2 mT at PG electrode, red). The RF power per driver was 50 kW, the source operating pressure 0.3 Pa, the biases were current-controlled resulting in V_{BI}=29 V, V_{BP}=22 V. All profiles were obtained by repeating the same pulse while moving the Langmuir probe at a different location along the axis. Data courtesy of E. Sartori.

In RF based sources, the plasma discharge occurs in the driver region, where the inductive coupling between the RF antennas and the plasma takes place. In the absence of the magnetic filter field, plasma expansion is a diffusive and collisional process, thus one can expect the plasma density to decay roughly exponentially. Figure 5.1 shows experimental measurements of the electron density n_e and temperature T_e profiles obtained in one of the eight drivers in the SPIDER ion source with a movable Langmuir probe[34]. The presence of the magnetic Filter Field restrains fast electrons from diffusing along the expansion chamber, confining them in the driver region: as a consequence, the peak plasma density inside the drivers will increase, as shown in Figure 5.1, whereas the plasma density in the expansion chamber will be only slightly

larger. At the same time, the electron temperature profile will no longer be uniform in the source, as well as the plasma potential profile. The presence of a stronger density gradient at the driver's exit, in combination with the filter field, causes significant diamagnetic drifts along the vertical direction, yielding asymmetries in the plasma properties within the expansion chamber, as discussed in the following.

5.2 Asymmetries in the expansion chamber

By interpolating the results obtained in SPIDER with a set of movable Langmuir probes[34] measuring at different locations along the axis and along the vertical direction, a two-dimensional distribution of plasma properties in the expansion chamber could be obtained, as shown in Figure 5.2. These maps show clearly visible asymmetries.

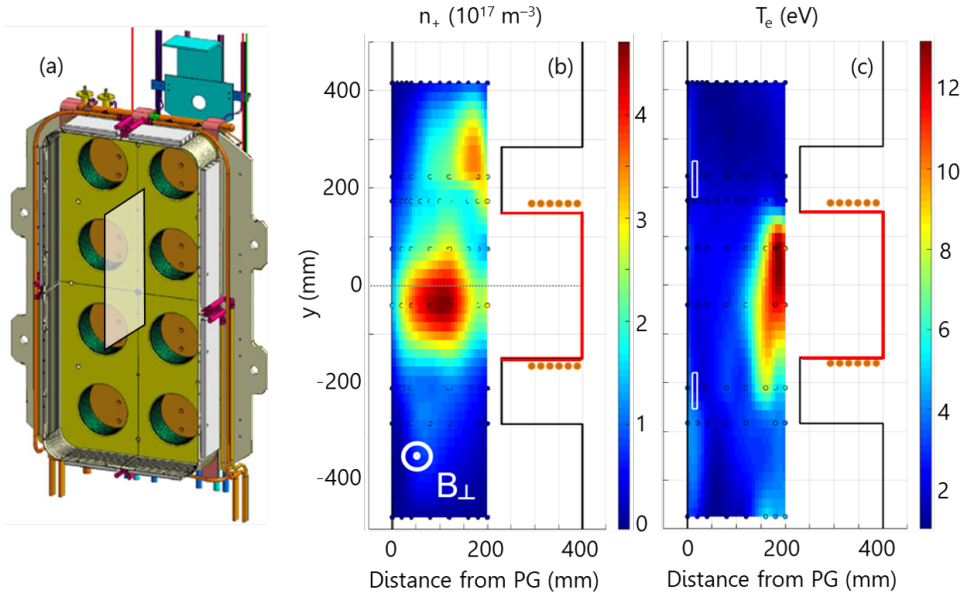

Figure 5.2: On the left: schematic representation of the position of the measurement plane inside the ion source; on the right: positive ion density n_+ and electron temperature T_e two-dimensional maps obtained by interpolating data collected with movable Langmuir probes. The measurements points are highlighted with empty black circles. All measurements were taken by repeating a pulse with the following operating conditions: one RF segment powered at 50 kW per driver, source pressure 0.3 Pa, filter field at the PG≈5 mT, different conditions of V_{BI}, V_{BP}. The obtained two-dimensional maps of positive ion density n_+ and electron temperature T_e at the drivers' exit are not exactly on the source midplane. Data courtesy of E. Sartori.

In particular, the electron temperature is larger right below the driver exit, as if energetic electrons were flowing towards the bottom of the surface when entering the expansion volume. As mentioned in Chapter 2, this might be related to the presence of a Hall electron current. The positive ion density is also asymmetric with respect to the driver axis.

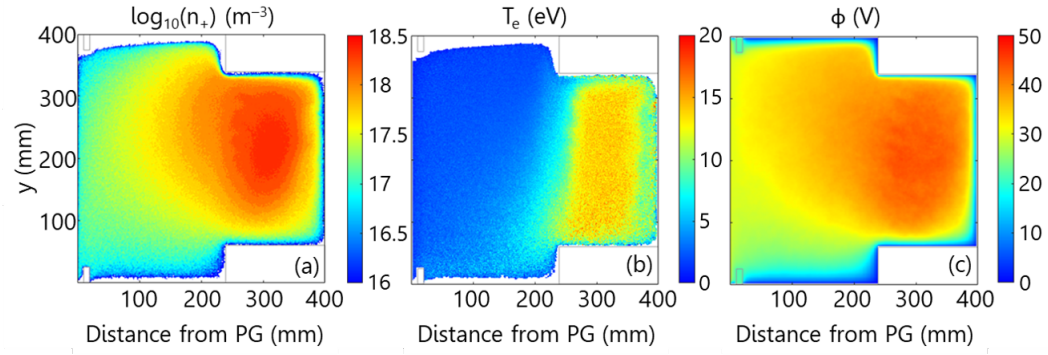

Figure 5.3: (a) Positive ion density n_+, (b) electron temperature T_e, and (c) plasma potential ϕ obtained with the GPPIC code. The simulation parameters were: 0.34 Pa background gas pressure, 4 mT filter field intensity at the PG. The peak density and temperature inside the driver were tuned with a PI controller for matching the experimental values.

Plasma expansion from a single driver was analysed also numerically by means of the GPPIC code, as shown in Figure 5.3, which depicts the two-dimensional maps of positive ion density, electron temperature, and plasma potential obtained in similar source operating conditions. A fair qualitative agreement can be found between experimental and numerical results, even though a reasonable comparison should be limited to the expansion region only since no RF coupling is included in the GPPIC model. The numerical investigation was particularly useful to study the positive ion energy distribution at the extraction region, as better described in the following section.

5.3 Plasma potential and positive ion energy distribution

As shown in Figure 5.1, increasing the filter field current strongly affects also the plasma potential profile, making the potential difference between the driver and the extraction region larger. In the SPIDER case it was shown that, at equal Filter Field intensity and RF power, other parameters such as background gas pressure or polarization of the PG and BP electrodes can also change the plasma potential profile, which will anyway feature the high peak within the driver as shown in Figure 5.4. This specific feature of the plasma profiles was already measured in other RF negative ion sources, such as BUG[66].

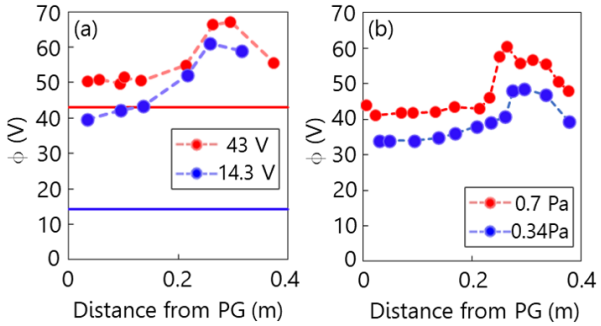

Figure 5.4: Plasma potential profiles measured for (a) V_{BI}=V_{BP}=14.3 V (blue) and V_{BI}=V_{BP}=43 V (red) and (b) p=0.34 Pa (blue) and p=0.7 Pa (red). Unless otherwise specified, the other source parameters are pressure 0.3 Pa, V_{BI}=29 V, V_{BP}=22 V, RF power per driver 50 kW, I_{PG}=2.6 kA. All profiles were obtained by repeating the same pulse while moving the Langmuir probe at a different location along the axis. Data courtesy of E. Sartori.

The presence of a large potential difference between the driver and the extraction region directly affects the positive ion behaviour in the ion source: in fact, plasma ions will reach the extraction region with a certain energy that will depend on their birth position along the source axis itself, as schematically shown in Figure 5.5.

Figure 5.6 shows two simulated plasma potential profiles for different background gas densities, compared with the calculated positive ion energy distribution at the PG electrode. The width of the distribution is equal to the potential difference between the driver and the extraction region, as also indicated by the arrows in Figure 5.6.

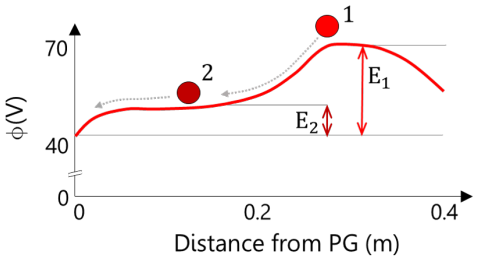

Figure 5.5: Simple representation of how the peaked plasma potential profile can effect the positive ion energy: particle n.1 arrived at the PG starting from the driver, gaining more energy than particle n.2, which instead was born within the expansion chamber.

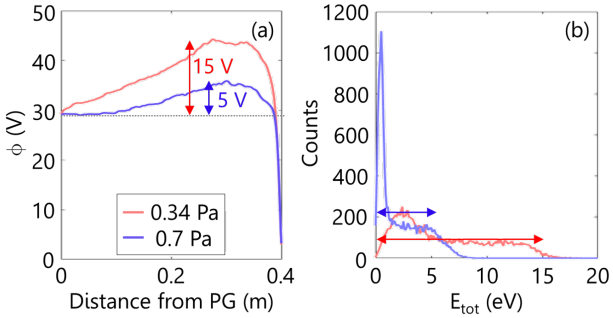

Figure 5.6: (a) Plasma potential profiles and (b) positive ion energy distribution simulated with GPPIC for low (red) and high (blue) source operating pressure. Other parameters: V_{BI}=29 V, electron density and temperature PI-tuned to match experimental values.

The same correlation was also highlighted experimentally in the SPIDER beam source while varying the PG, BP biases, as shown in Figure 5.7. The experimental estimations of the positive Ion Energy Distribution Function (IEDF) were obtained with a Retarding Field Energy Analyser (RFEA) sensor. Also in this case, the width of the distribution is very similar to the potential difference between driver and extraction region.

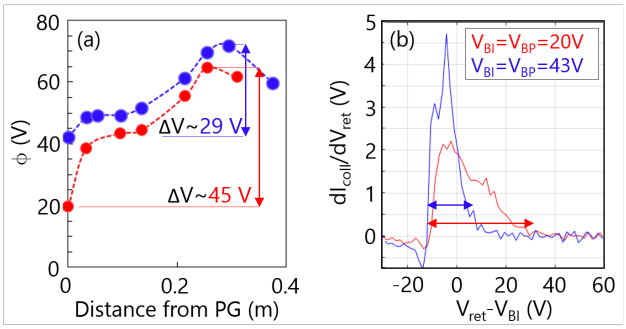

Figure 5.7: (a) Plasma potential profiles and (b) positive IEDF (right) measured in SPIDER for low (red) and high (blue) PG and BP electrodes polarisation. Other parameters: 50 kW RF power per driver, p=0.34 Pa, filter field at PG≈3 mT, deuterium operation. Presented on March 11th 2022 during the ITER NBTF Experimental Advisory Committee by E. Sartori.

5.3.1 Influence of source parameters on positive ion energy distribution

The influence of source operating conditions on both width and shape of the positive IEDF was investigated in the BUG negative ion source with a RFEA sensor. The sensor was installed on the upstream side of the PG, in such a way to be positioned in correspondence of the RF driver center. Four source parameters were varied, namely source operating pressure, RF power, PG polarization (the BP electrode is always at source potential in BUG), and FF intensity. The results are shown in Figure 5.8.

By increasing the source operating pressure, the positive IEDF width is reduced, and the mean value is shifted towards lower potential values, i.e. lower energy values for the positive ions. This can be related with the higher collisionality caused by the larger background gas density.

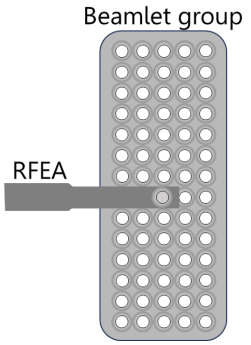

Figure 5.8: Simplified scheme of the RFEA sensor location in the BUG ion source, view from the driver.

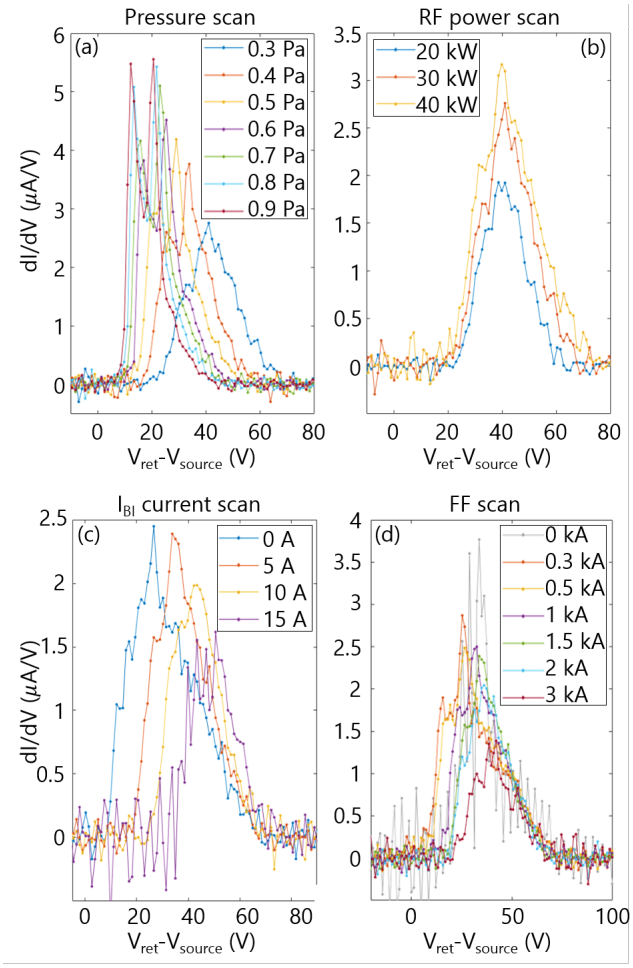

Figure 5.9: Positive ion energy distribution variation as a function of different (a) pressure values, (b) RF power values, (c) PG polarisation, and (d) FF intensity. V_{source} is the source potential. When not changed, the source operating conditions were: 0.3 Pa, 30 kW, 5 A, and 1.5 kA. Data collected during joint experimental campaign at BUG.

When the RF power is increased, the mean value of the distribution increases as well as the width of the distribution. In this case, the integral of the IEDF is increasing linearly with the RF power, meaning that more positive ions are reaching the sensor.

The effect of the PG bias and of the FF intensity is of less straightforward interpretation. Increasing the PG polarization causes the distribution to shrink and shift towards higher values: in fact, having higher PG polarization is helpful to reduce the potential difference between the driver and the extraction region, leading to a narrower IEDF. Concerning the magnetic filter field, increasing the FF current from 0 kA up to 0.5 kA causes a slight increase of the distribution width, although for values $\geq$1 kA the width starts to decrease and, similarly to the other cases, the mean value is shifted towards higher energies. Overall, increasing either the PG polarization or the FF intensity has a very similar effect on the positive IEDF.

5.3.2 Distribution width and single beamlet divergence

As mentioned in Section 2.3.3, positive ions are one of the precursor species for surface produced negative ions. The latter are emitted from the converter surface in the opposite direction with respect to beam extraction: for this reason, the PG electrode usually features conically-shaped apertures. Besides this, positive ions are fundamental for aiding the negative ion extraction: in fact, Coulomb collisions with positive ions which are going towards the beam apertures allow the reversal of the negative ion birth motion direction. According to numerical studies[15], the lower the positive ion energy in the proximity of the PG electrode, the better the negative ion optics. In this view, the single beamlet divergence measured in BUG and RFEA parameters are shown in 5.10 for both pressure and PG bias current scan.

As expected, for increasing pressure the beam divergence is reduced, as well as both the distribution width and mean value. In the PG bias scan case, the beam divergence is higher for larger biases, as well as the mean value of the IEDF with respect to source potential (e.g. considering the bias contribution), whereas the distribution width is decreasing. Also in this case, the bias effect on source performances is not straightforward and deserves further investigations.

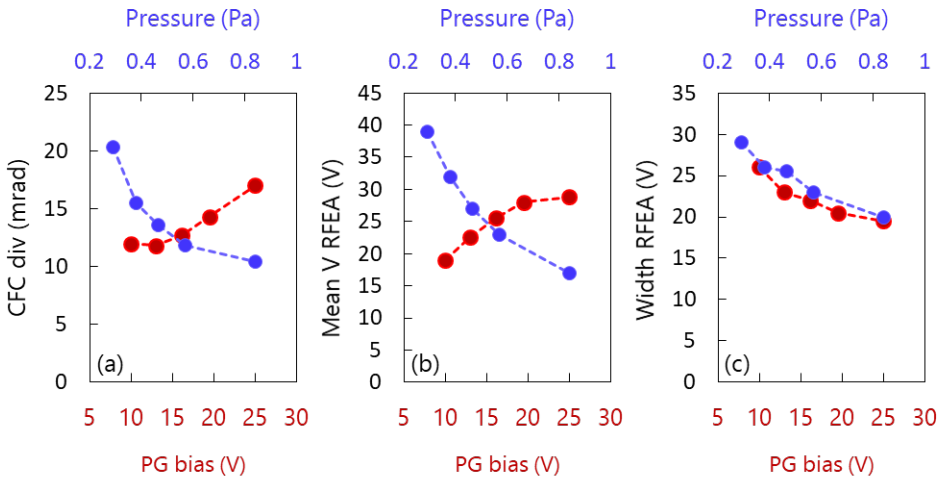

Figure 5.10: (a) single beamlet divergence measured by the CFC tile, (b) mean value and (c) width of the IEDF for different values of pressure (blue) and PG bias current (red). Other parameters were: 30 kW RF power, and 1.5 kA FF current. Data collected during joint experimental campaign at BUG. CFC data courtesy of M. Barnes.

Chapter summary

The influence of source operating conditions on the plasma expansion mechanism was discussed. The experimental measurements performed with movable Langmuir probes highlighted the presence of peaked axial profiles in the ion source. Based on the acquired data, an interpolation of the plasma properties on a two-dimensional vertical plane was obtained, and compared with results from numerical simulations. Finally, the influence of a peaked plasma density profile on the energy of positive ions reaching the PG electrode is discussed. In particular, the width of the ion energy distribution was found to be very similar to the potential difference between driver and extraction region. Finally, the influence of source operating conditions on RFEA measurements performed in the BUG ion source is discussed, also providing some insights on how the distribution width and the single beamlet divergence might be related.

Chapter 6

Influence of filter field in RF drivers

The effect of having a non-negligible filter field intensity also within the drivers on plasma expansion is discussed in this chapter. The GPPIC simulation results on two planes, one parallel and the other perpendicular to the magnetic filter field are presented, also in comparison with the same cases simulated with the Fluid Solver For Spider 2D (FSFS2D) code.

6.1 Filter field influence on plasma properties

In SPIDER, the FF intensity is significantly high within the drivers. This might cause differences in the plasma properties with respect to other sources in which the FF intensity in the drivers is much lower, as shown in 6.1. For instance, in BUG[67] the FF is roughly equal to 0 in the driver region, then it grows almost linearly within the expansion chamber until it reaches its highest value in the very proximity of the extraction region. In the SPIDER case, the FF is already as high as 2 mT in the driver region, then it increases more slowly and reaches a quasi-stationary value in the second half of the source.

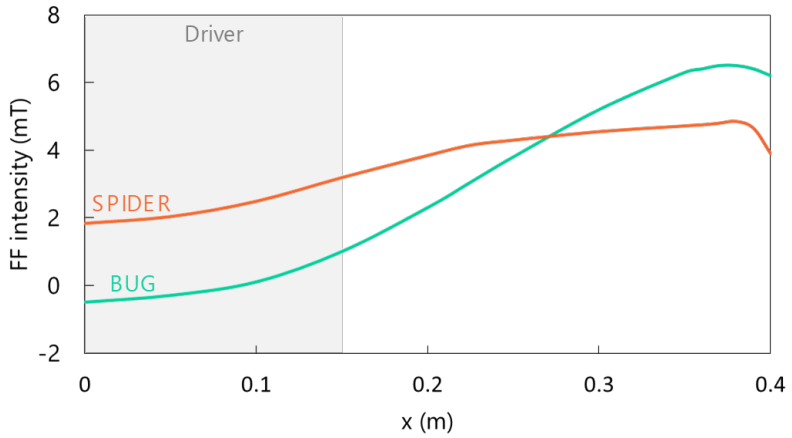

Figure 6.1: Numerical estimation of the FF intensity along the driver axis in SPIDER (orange) and BUG (light green) negative ion sources. In the SPIDER case, different I_{PG} current values are considered. The driver region is shaded in grey.

The presence of a non-negligible horizontal component of the magnetic FF inside the drivers causes the electrons to drift along the field lines, resulting in asymmetric plasma properties with

respect to the driver axis. In addition, the plasma properties inside the drivers will strongly depend on the FF intensity, as experimentally measured in SPIDER, as shown in Figure 6.2[68],[69]. On the other hand, in the BUG ion source, the plasma density and electron temperature in the driver do not show any dependence on the FF intensity[70].

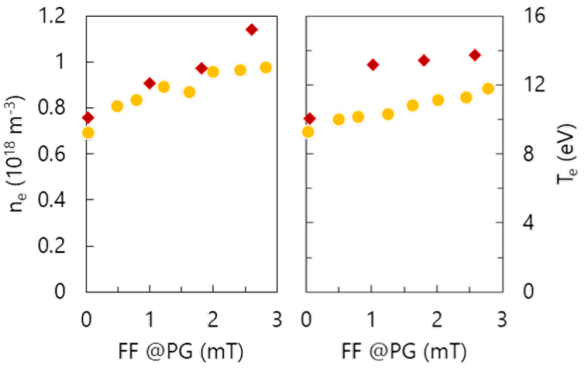

Figure 6.2: Electron density (left) and temperature (right) measured inside the driver by OES (yellow points) and Langmuir probes (red points), as functions of the FF intensity. LP data courtesy of E. Sartori, OES data courtesy of B. Zaniol.

6.2 Perpendicular and parallel plasma expansion

In order to investigate this phenomenon, some dedicated numerical simulations were carried out on two different planes, one parallel and the other perpendicular to the filter field direction, as schematically shown in Figure 6.3.

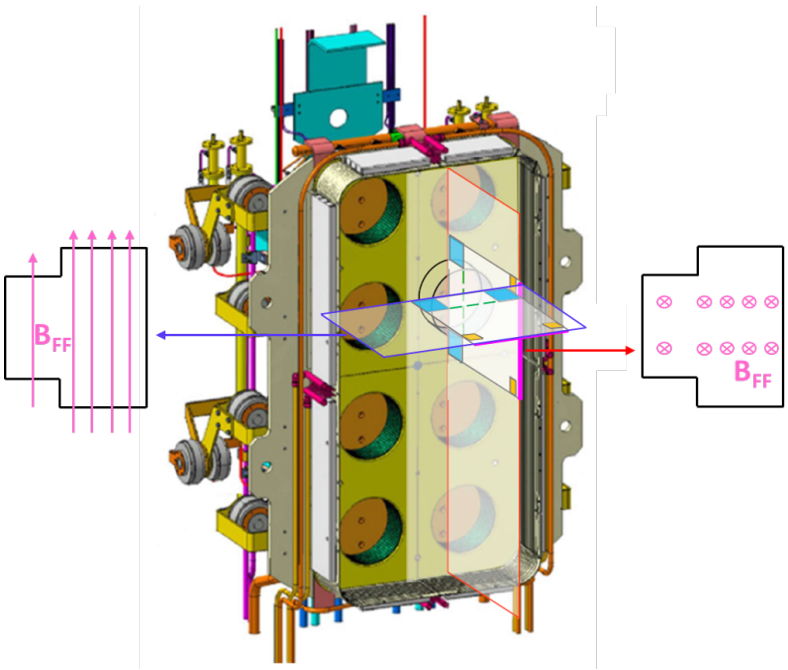

Figure 6.3: Schematic view of the two simulation domains, one parallel to the filter field (on the left) and one perpendicular to the filter field (on the right), and how they are positioned in the SPIDER source.

As already discussed in Chapter 5, plasma expansion along the perpendicular direction is asymmetric, as shown in Figure 6.4. It is worth pointing out that both simulation codes yield similar results in terms of density and electron temperature. The plasma potential shows the same qualitative behaviour, since in both cases it is slightly asymmetric at the driver's exit, and is lower in front of the bottom surface of the expansion chamber if compared to the upper surface. However, there is roughly a 10 V difference between the two cases.

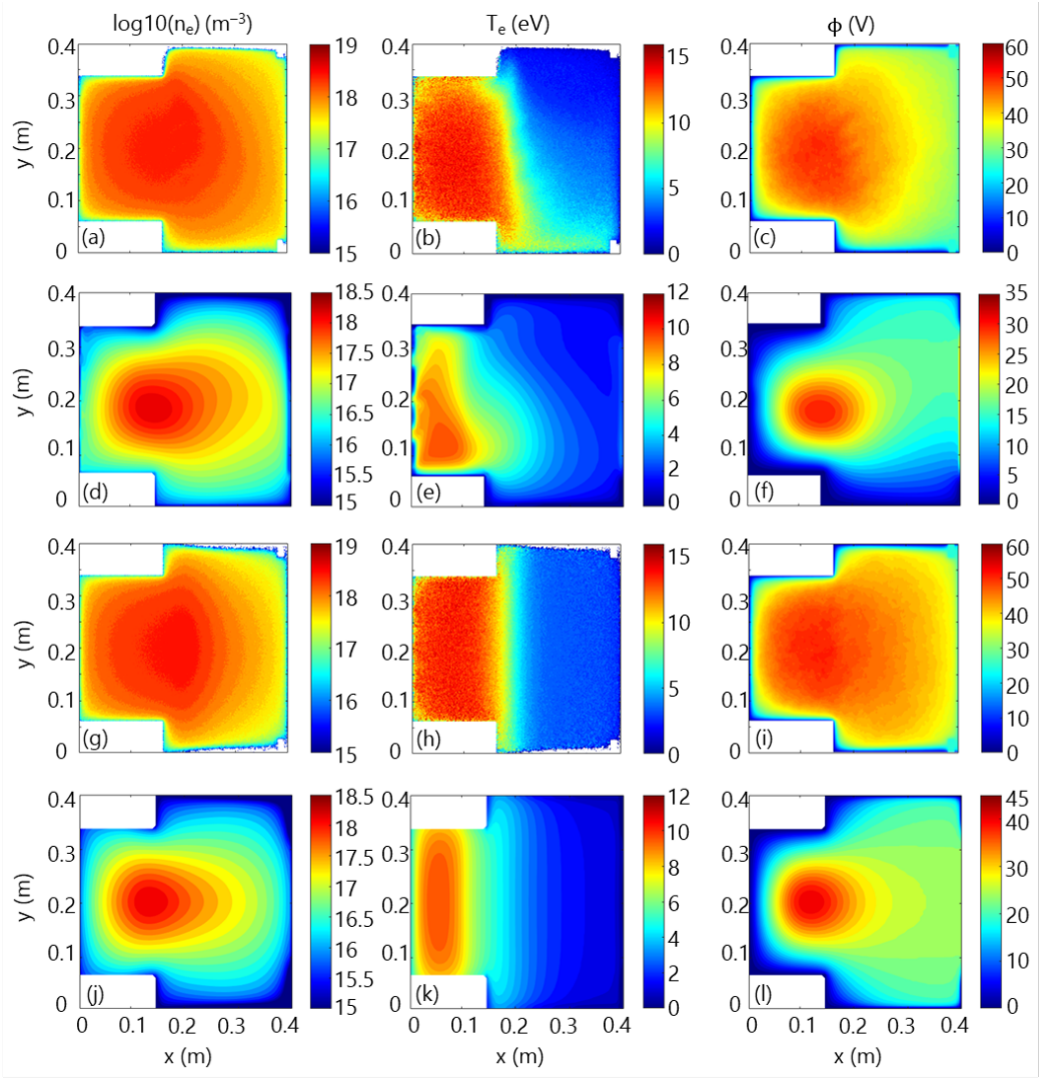

Figure 6.4: Electron density $\log_{10} n_e$, electron temperature T_e, and plasma potential ϕ obtained with GPPIC-FSFS2D on the perpendicular (a,b,c-d,e,f) and parallel (g,h,i-j,k,l) plane with respect to the FF direction. Parameters: FF at PG 2 mT, p=0.4 Pa, driver peak density and temperature tuned to match experimental values. Fluid code results courtesy of R. Zagorski.

When investigating the parallel direction, instead, plasma properties are much more uniform. The electron temperature obtained with the FSFS2D code is more shifted towards the rear region of the driver, since the coupling region is better defined. In the GPPIC code, a thermostat heats the electrons up to the imposed temperature, and acts on the entire driver area. Also in this case, there is a roughly 10 V difference in the plasma potential estimations.

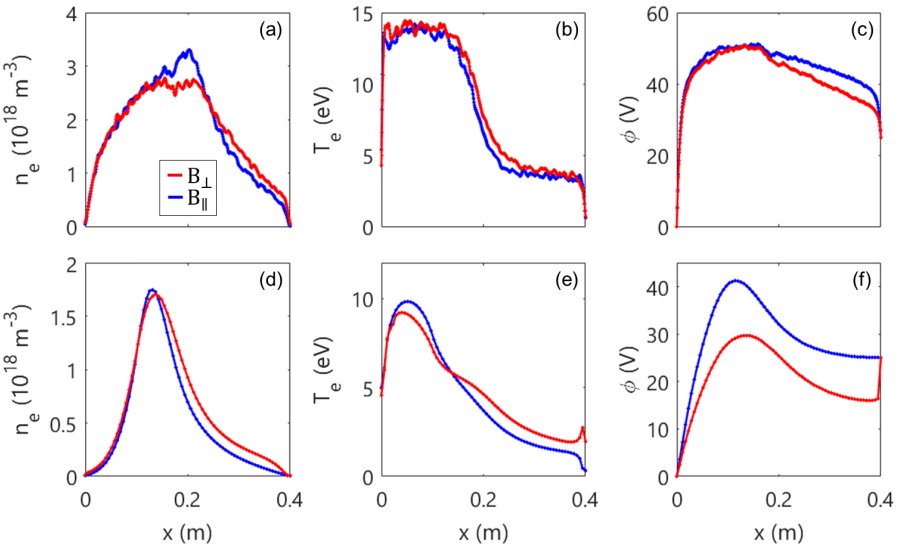

Figure 6.5: (Electron density n_e, electron temperature T_e, and plasma potential ϕ obtained on the perpendicular plane with respect to the FF direction with GPPIC (a,b,c) and FSFS2D (d,e,f). Parameters as defined for Figure 6.4. Fluid code results courtesy of R. Zagorski.

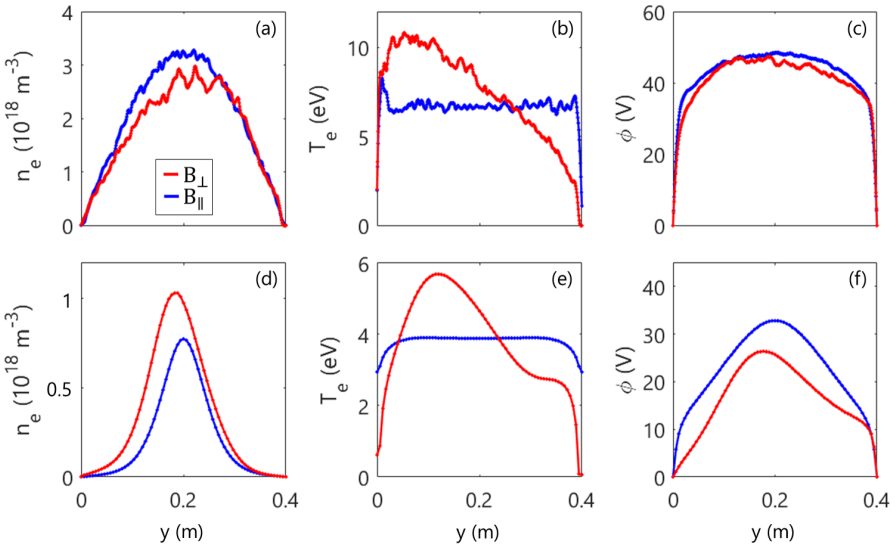

Figure 6.6: Vertical profiles of electron density n_e, electron temperature T_e, and plasma potential ϕ at x=0.2 m obtained on the perpendicular (red) and parallel (blue) planes with respect to the FF direction with GPPIC (a,b,c) and FSFS2D (d,e,f). Parameters as defined for Figure 6.4. Fluid code results courtesy of R. Zagorski.

In order to provide a more accurate comparison between the two simulation planes, Figure 6.5 shows the axial profiles obtained from both simulation codes. From the qualitative point of view, the results are in agreement: in fact, both codes highlight a slight increase of electron density and temperature as well as a decrease of the plasma potential in the expansion region

when going from the $B_{\parallel}$ to the $B_{\perp}$ case, whereas the plasma properties within the driver (up to x=0.16 m) there are no substantial variations, with the exception of the plasma potential obtained with the fluid code. However, as can be seen from Figure 6.5f, the plasma potential in the extraction region is too low with respect to the PG potential, which leads to a non-realistic slope inversion. This might be a consequence of the excessive decrease of the plasma potential value within the driver. The GPPIC code features some anomalies in the electron density inside the driver (Figure 6.5a), possibly deriving from a numerical issue linked to the presence of the magnetic FF.

Figure 6.6 shows vertical profiles of the same quantities obtained at half of the axial direction, namely at x=0.2 m. Also in this case, the results from both codes are in agreement from the qualitative point of view, even though the n_e, T_e, and ϕ peak values obtained with the fluid simulations are slightly smaller with respect to the PIC code. However, the main result is the asymmetric electron temperature profile arising when moving from the $B_{\parallel}$ to the $B_{\perp}$ case. A similar effect is also visible in the plasma potential profile, even though it is much more evident from the fluid results.

6.3 Numerical analysis of FF effect on driver properties

The GPPIC code was used to investigate how the filter field intensity inside the drivers can affect the plasma properties. In this regard, Figure 6.7 shows some axial profiles of electron density, temperature and plasma potential for two different FF values in the driver. Along the filter field direction, the simulated electron temperature inside the driver is uniform, although this is due to the thermostat action in the driver region. At the exit of the driver, the electron temperature decreases in both cases: as expected, the reached temperature is lower for higher filter field intensity within the driver.

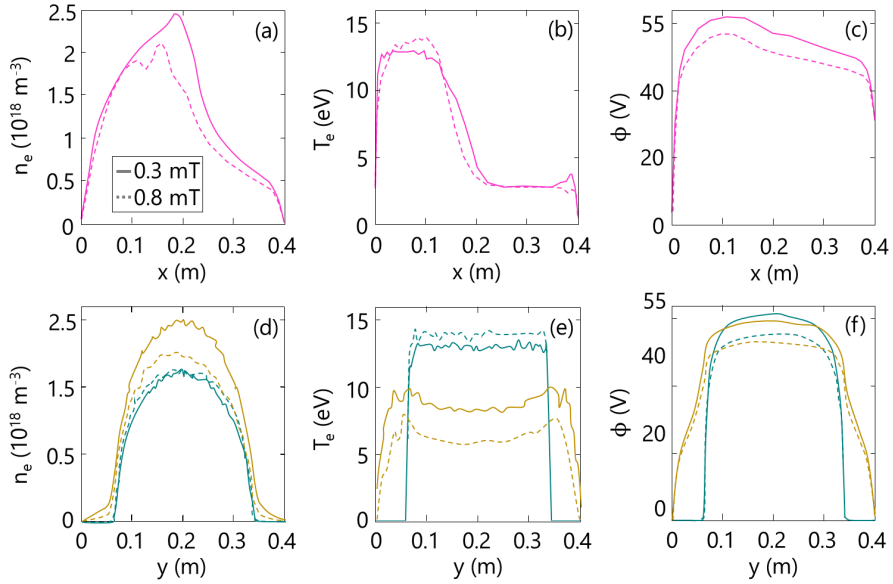

Figure 6.7: Electron density n_e, electron temperature T_e, and plasma potential ϕ along the horizontal axis at y=0.2 m (a,b,c) and vertical direction at x=0.08 m in green and x=0.165 m in dark yellow (d,e,f), for FF intensity inside the driver of 0.3 mT (solid lines) and 0.8 mT (dashed lines).

A similar effect can be seen on the horizontal profiles, where the T_e decrease is steeper for

the higher field case (dashed magenta line in Figure 6.7). The electron density increases right outside the driver when reducing the filter field intensity: this is not in agreement with the experimental findings shown in Figure 6.2, although it can be easily explained by considering the fact that the peak values of n_e and T_e inside the driver are PI controlled, therefore the information about the density increase is not valid, although the broadening of the density peak towards the expansion chamber might be a correct result. For the same reason, the vertical density profile of electron density does not change within the driver due to the PI tuning, but is different in the expansion region. Finally, the plasma potential is found to increase for higher FF intensity in the driver, which can be explained in terms of better plasma confinement. As can be seen from the ϕ vertical profiles, the plasma potential is increased along the entire axis of the source.

In reality, the plasma expansion mechanism will be a combination of the perpendicular and parallel cases. Therefore, in order to better investigate this feature and its dependence on the FF intensity, a movable axial Langmuir probe to be permanently installed in the SPIDER ion source has been designed[71], as described in the following section.

6.4 Design of a movable electrostatic probe for SPIDER

A detailed description of Langmuir probes as plasma diagnostic tool can be found in[72]. When used in electronegative plasmas, the probe current results from the sum of the positive ion, electron and negative ion contributions[73],[74], thus $I_{tot}(V) = I_+(V)+I_e(V)+I_-(V)$. The positive ion current reads:

$$\begin{aligned} I_+(V) &= -qn_+A_{eff}(V)u_B\sqrt{\frac{1+\alpha}{1+\gamma\alpha}} \quad (V \le \phi) \\ I_+(V) &= -\frac{1}{4}qn_+A_g\sqrt{\frac{8qT_+}{\pi m_+}}\exp\left(-\frac{V-\phi}{T_+}\right) \quad (V > \phi) \end{aligned} \tag{6.1}$$

where ϕ is the plasma potential, q is the elementary charge, n_+ is the positive ion density at sheath edge, $u_B = (qT_e/m_+)^{0.5}$ is the Bohm ion speed, $\alpha = n_-/n_e$ is the plasma electronegativity, $\gamma = T_e/T_-$ is the ratio between electron and negative ion temperature, T_+ is the positive ion temperature (in eV), m_+ is the ion effective mass, A_g is the geometrical collecting surface of the probe and A_{eff} is an effective collecting surface which accounts for the sheath expansion, thus it depends on the probe voltage. The electron current contribution can be written as:

$$\begin{aligned} I_e(V) &= \frac{1}{4}qn_eA_g\sqrt{\frac{8qT_e}{\pi m_e}}\exp\left(\frac{V-\phi}{T_e}\right) \quad (V \le \phi) \\ I_e(V) &= \frac{1}{4}qn_eA_g\sqrt{\frac{8qT_e}{\pi m_e}}\cdot\left[2\sqrt{\frac{V-\phi}{\pi T_e}} + \exp\left(\frac{V-\phi}{T_e}\right)\mathrm{erfc}\left(\sqrt{\frac{V-\phi}{T_e}}\right)\right] \quad (V > \phi) \end{aligned} \tag{6.2}$$

where n_e is the electron density at sheath edge, T_e and m_e are the electron temperature in eV and the electron mass respectively.

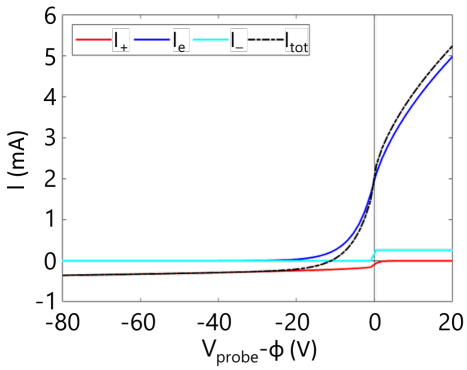

Figure 6.8: CV characteristic example for a cylindrical single Langmuir probe, together with the single current contributions I_+, I_e and I_- shown in red, blue and cyan respectively. The considered probe electrode has 0.25 mm diameter, 5 mm length.

Finally, the negative ion contribution reads $I_-(V) = 0$ for $(V \leq \phi)$, otherwise it is defined as:

$$I_-(V) = qn_-A_g\sqrt{\frac{qT_+}{m_-}} \quad (V > \phi) \tag{6.3}$$

where n_- and m_- are the negative ion density at sheath edge and mass respectively. Figure 6.8 shows an example of all the aforementioned contributions for a Langmuir probe with a cylindrical electrode of diameter 0.25 mm, length 5 mm.

As this probe is supposed to move along the source axis, the heat load to which it will be subjected will depend on the local plasma parameters. More in general, the power density W on a surface exposed to the plasma can be described as:

$$W = j_+(V_w - \phi) + 4\pi j_e T_e + j_- T^+ \tag{6.4}$$

where V_w is the surface potential, j_+, j_e and j_- are the positive ion, electron and negative ion current densities respectively defined as:

$$j_+ = \frac{1}{4}qn_+u_B, \;\; j_e = \frac{1}{4}qn_e\sqrt{\frac{8qT_e}{\pi m_e}}\exp\left(\frac{V_w-\phi}{T_e}\right), \;\; j_- = \frac{1}{4}qn_-\sqrt{\frac{qT_+}{m_-}} \tag{6.5}$$

With the exception of the elementary charge q and the electron mass m_e, all the quantities in Eq.6.4 and 6.5 depend on the spatial coordinate z along the source axis. As already mentioned, Eq.6.4 can be applied to any surface exposed to the plasma; however, for metallic surfaces, the surface voltage $V_w(z)$ is either equal to an externally imposed potential, or to the floating potential V_f. In the case of a non-homogeneous plasma, V_f can be obtained by imposing the floating condition (i.e. zero net collected current) on the entire surface S, thus $I_s = \int_S (j_+(z) - j_e(z) - j_-(z))dS = 0$.

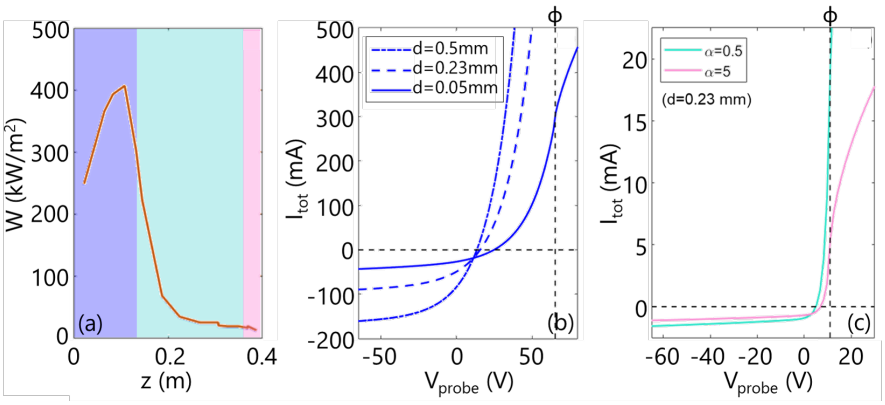

Figure 6.9: Expected power density for a floating object as a function of the position along the source axis (a), simulated CV characteristic for the driver plasma with three different electrode diameters, electrode length L=5 mm, n=3.5 × 10^{18} m^{-3}, T_e=17 eV, ϕ=65 V (b) and for the expansion and extraction region (c) assuming electronegativity α=0.5 and α=5 respectively, electrode diameter 0.23 mm and length 5 mm, n=2 × 10^{17} m^{-3}, T_e=2 eV, ϕ=10 V.

The movable Langmuir probe will have a total stroke of roughly 40 cm, in such a way to measure the plasma properties in both the driver and the expansion region. Figure 6.9a shows the expected plasma power density flux calculated for plasma parameters measured in SPIDER with an injected RF power of 50 kW per driver, calculated by means of Eq.6.4. Figure 6.9b shows expected CV characteristics for a single cylindrical Langmuir probe measuring the driver plasma, with different electrode diameters. Figure 6.9c instead shows simulated CV curves for the expansion region, considering two electronegativity values. It is worth pointing out that operating the probe in different conditions might require to apply different theories for the analysis of the Current-Voltage (CV) characteristics, which in turn can have specific validity ranges depending also on the electrode dimensions[75].

6.4.1 Probe head design

The probe head will be composed of a tungsten (W) electrode of cylindrical shape, insulated by a multibore tube made of alumina (Al_2O_3). The electrode diameter and length are chosen with the aim of maximizing the collected current, without causing too strong plasma perturbations. The ratio between the electrode radius r and the Debye length λ_{De} determines which Langmuir probe theory can be used to analyse the CV characteristics, hence the accuracy of the estimation of the plasma parameters.

On the other hand, the risk of melting the probe head increases for smaller electrodes. In order to define electrode dimensions that can ensure system reliability, some thermal analyses of the electrode behaviour have been performed while considering the plasma properties in the driver, where the highest heat load is expected. When not polarized, the electrode is expected to reach a temperature of 2071 K, 1888 K or 1789 K a diameter d of 0.05 mm, 0.23 mm and 0.5 mm respectively. When biased with respect to plasma potential, the electrode temperature will depend on both the sweeping time Δt, defined as the time needed for completing an entire potential ramp, and on the range of the potential sweep, as shown in Figure 6.10. In order to keep the electrode temperature safely below the tungsten melting point (T=3695 K), one should either perform scans with long sweeping time but reduced potential sweep, or the other way round (see Figure 6.11).

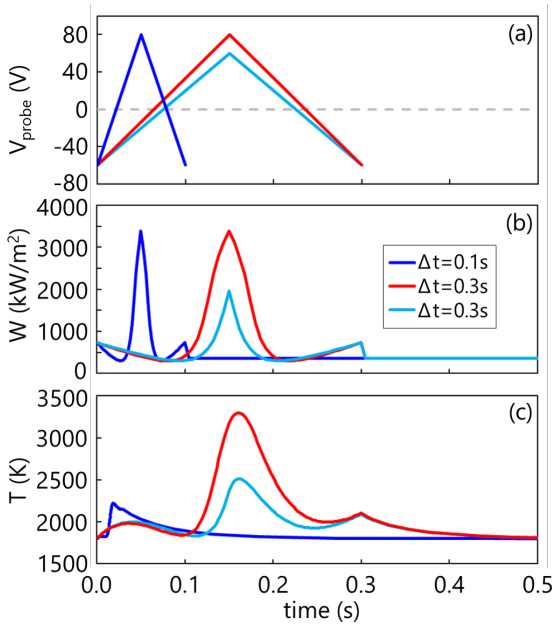

Figure 6.10: Probe voltage V_{probe} (a), power density W (b) and electrode temperature T (c) as a function of time for three different combinations of sweeping time Δt and maximum probe potential.

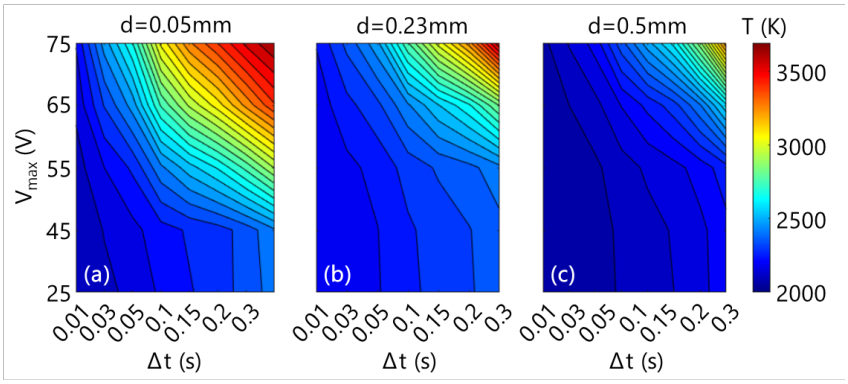

Figure 6.11: Maximum temperature reached by the electrode for (a) d=0.05 mm, (b) d=0.23 mm, (c) d=0.5 mm as a function of the maximum probe potential V_{max} and the potential sweep time Δt.

6.4.2 Probe support design

As already mentioned, the probe support consists of a bare alumina (Al_2O_3) tube or multi-bore tube with or without a molybdenum (Mo) shielding thin tube (design 1 and 2 respectively); the presence of an external metallic surface makes the probe support structure similar to a coaxial cable, possibly shielding the RF noise, thus improving the quality of the collected signal. The multi-bore tube solution is considered with a view to designing future probe heads with multiple electrodes, or even to allow the installation of a thermocouple to monitor the support temperature. Both designs have already been employed in the SPIDER ion source.

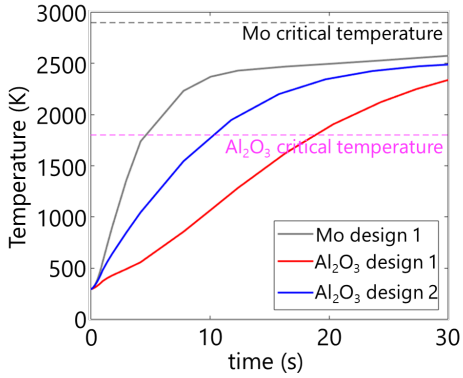

Figure 6.12: Temperature reached by the alumina tube and Mo shielding as a function of time while exposed to a constant power density flux of $450\,\mathrm{kWm^{-2}}$.

The probe support endurance should ensure the capability of performing either single or multiple measurements. According to Figure 6.9a, the power density profile is not uniform along the source axis, showing a peak value of roughly $400\,\mathrm{kWm^{-2}}$; however, in order to guarantee a safety margin, the thermal analyses of both designs were performed while considering a constant power flux profile $P(z) = P_{peak}$ =$450\,\mathrm{kWm^{-2}}$ for the entire support length (40 cm). Figure 6.12 shows the maximum temperature reached by the Al_2O_3 tube as a function of the exposition time, for both designs.

The bare alumina design yields a maximum exposition time of t=10 s, whereas in the shielded design the alumina tube resists to the thermal load for a longer time, reaching its critical temperature at t=18 s; however, the external molybdenum rapidly heats and reaches a temperature close to its melting point: this can be an issue for the other probe components which are in contact with the support, as for instance the manipulation system (see Section 4), since the accumulated heat would be inevitably transferred.

6.4.3 RF compensation

The probe will be operated in a RF environment, therefore it is necessary to limit the RF noise via both passive and active compensation. Dealing with the former, the use of a compensation electrode[62],[76] is needed especially for measuring low electron temperatures, thus mainly in the expansion and extraction regions. As explained in the following section, this Langmuir probe will be at first operated without an RF compensation electrode: indeed, the initial phase of the resumption of SPIDER operations will be mainly devoted to the characterisation of the new solid state amplifiers, therefore a simpler probe design that can be routinely operated is preferable.
Active compensation is performed by means of LC notch filters, which can be installed either:

a) as close as possible to the electrode-cable transition, in a very limited space: to this purpose, SMD-based components should be used given their reduced dimensions, although a preliminary characterisation of their behaviour at high temperatures would be mandatory;

b) further away from the electrode-cable transition, using standard components; in this case, the filters are not necessarily mounted on the probe support and this would significantly simplify the probe head design.

6.4.4 Integration in the SPIDER source

In order to integrate the probe in the SPIDER ion source[28], several aspects such as the endurance to the thermal stresses, space availability and vacuum compatibility need to be addressed. The main constraint was derived from the thermal analyses on the probe support, i.e. the maximum exposure time: the choice of the manipulation system and, consequently, the integration in the ion source have been addressed accordingly. In particular, the manipulation system impacts the probe measurements from different points of view: first of all, it defines the maximum probe stroke, that can be considered to be equal to the travel length of the manipulator. It also determines whether single or multiple measurements can be performed during a single exposition of the probe to the plasma, and also how many exposures the probe can endure during an experimental session. The time window available for a single measurement includes the measurement time itself, as well as the time needed for the manipulator to shift the probe in position and pull it back after the measurement is done. In this sense, the manipulation system should be chosen in such a way to maximize the actual measurement time. A detailed description of the manipulation choice and the integration of the system in SPIDER can be found in[71].

Chapter summary

The effect of having a non-negligible filter field contribution in the RF drivers was discussed in this chapter. In particular, the plasma expansion perpendicular and parallel to the filter field was analysed, showing some significant differences: in fact, the plasma properties in the expansion chamber result asymmetric only in the first case. In the second case, however, the plasma peak within the drivers becomes more elongated due to diffusion along the field lines. Overall, the presence of this filter field contribution breaks the cylindrical symmetry of the RF drivers and, consequently, three-dimensional models are mandatory for correctly describing the power coupling and plasma behaviour. Furthermore, the actual expansion mechanism will most probably result to be in between the two cases, making the experimental characterization necessary: for this reason, a dedicated movable Langmuir probe was designed, as described in the last section of this chapter.

Chapter 7

Non-uniformity in large RF sources

The uniformity of plasma properties in the expansion chamber of large negative ion sources is discussed in this chapter, taking as reference the SPIDER beam source. At first, some experimental evidence of plasma non-uniformity is discussed and qualitatively compared with numerical results. Finally, results from the triple Langmuir probe as a function of the FF direction and intensity are presented.

7.1 Vertical drift motions

By interpreting Cs line emission at 852 nm with a CR model[77], a vertical profile of $n_e T_e^{0.5}$ can be obtained, as shown in Figure 7.1. This profile can be compared with the measured H_β emission, which is due to the atomic hydrogen de-excitation from the $n = 4$ to the $n = 2$ state.

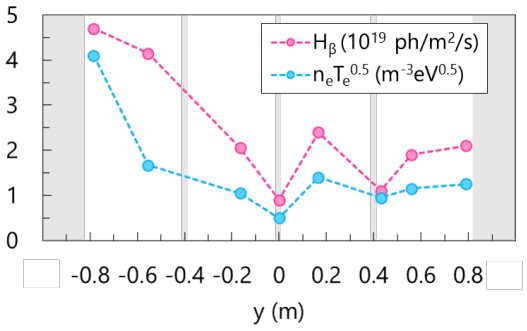

Figure 7.1: 852 nm line emission of neutral Cs (top) and H_β emission (bottom) measured along the vertical direction in the SPIDER ion source. Operating parameters: P_{RF}=50 kW per driver, 2.4 mT FF at the PG, I_{BI} ≈26 A, I_{BP} ≈28 A, Cs injection rate 6 mg/h. Data courtesy of B.P. Duteil[77] and B. Zaniol, adapted from[78].

Both profiles feature higher values towards the bottom of the SPIDER source. The beam current density extracted from the bottom of the ion source was also found to be lower with respect to the other segments (not shown), implying a reduced negative ion availability. On this basis, it can be deduced that both Cs and H_β emissions are mostly due to (e,H) and (e,Cs) interaction, rather than mutual recombination between negative ions and H+, Cs+ ions. A possible insight on this phenomenon is given by numerical simulations of the plasma expansion from two RF drivers showing a Hall electron current flowing from the drivers towards the bottom region of the domain that reaches the extraction region notwithstanding the FF presence.

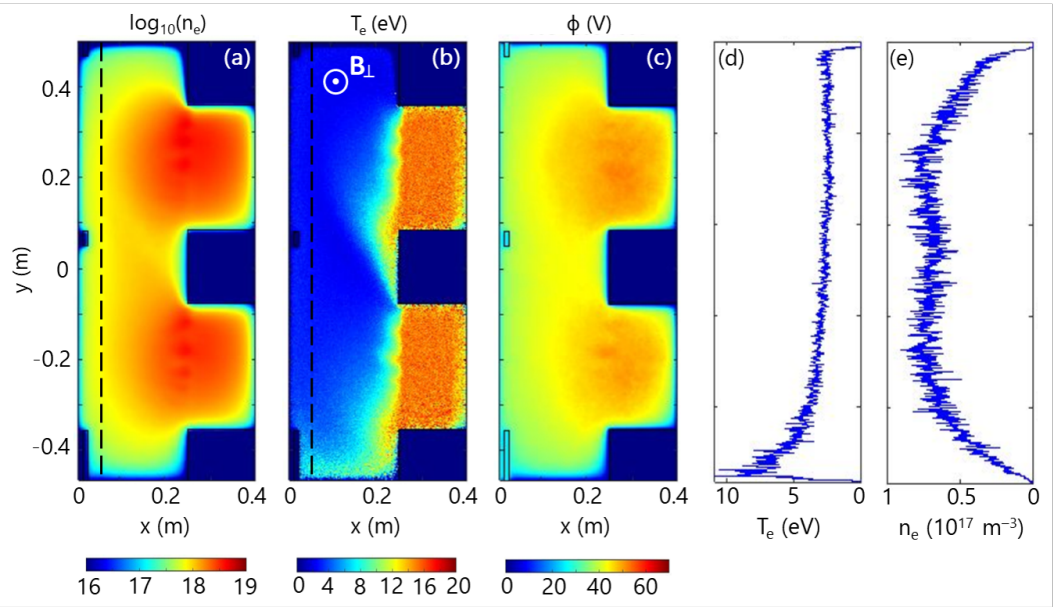

Figure 7.2: Two dimensional maps of logarithm of electron density n_e (a), electron temperature T_e (b), and plasma potential ϕ (c); vertical profiles of electron temperature (d) and density (e) taken in correspondence of the black dashed line (40 mm from PG. Parameters: 4 mT magnetic filter field at the PG electrode, 0.3 Pa source operating pressure, density and temperature inside the drivers PI-tuned to match experimental profiles measured at 50 kW per driver.

Despite being obtained without describing the RF power coupling (a thermostat is used for heating the electrons inside the driver) and using different parameters with respect to the experimental ones, the two-dimensional map of electron temperature T_e provides a qualitative description of the expansion process immediately out of the RF drivers. In fact, energetic electrons flow perpendicularly with respect to the source axis, causing a high electron temperature in the proximity of the rear surface of the expansion chamber (plasma driver plate). It is worth pointing out that the direction of the hot electron flow depends on the magnetic FF configuration; however, due to the presence of permanent magnets on the lateral walls surface and on the drivers' backplates, the plasma behaviour in the reversed FF configuration is not symmetric with respect to the standard case, as will be further discussed in Section 7.2.

The simulated electron density shows how, at a distance of 4 cm from the PG surface, the central part of the vertical profile is still not completely uniform. Looking at the two-dimensional map, this non-uniformity might be traced back to the plasma outflow from two different RF drivers. Unfortunately, the density scaling parameter of this simulation is too high to thoroughly investigate this feature, as can also be seen from the too wide plasma sheath in front of the lower and upper surfaces. In the following section, the plasma parameters measured in SPIDER at the driver exit will be discussed. As will be shown, the obtained results are coherent with the indications from this numerical simulation.

7.2 Triple Langmuir probe measurements in the expansion chamber

The installation of a triple Langmuir probe[79] in the rear of the expansion region (Figure 7.3) allowed to investigate the local properties of the source plasma with different operating conditions, also during beam extraction. In addition, it was possible to follow the evolution of the

plasma properties during the early stages of caesium operation.

7.2.1 Experimental setup

The probe head is composed by four tungsten electrodes of 6 mm length and 0.8 mm diameter, insulated by a four-bore alumina tube of 5 mm diameter. The probe tip lies 3.5 cm and 5 cm away from the back wall and the lateral wall respectively. Figure 7.3 shows the probe assembly before installation.

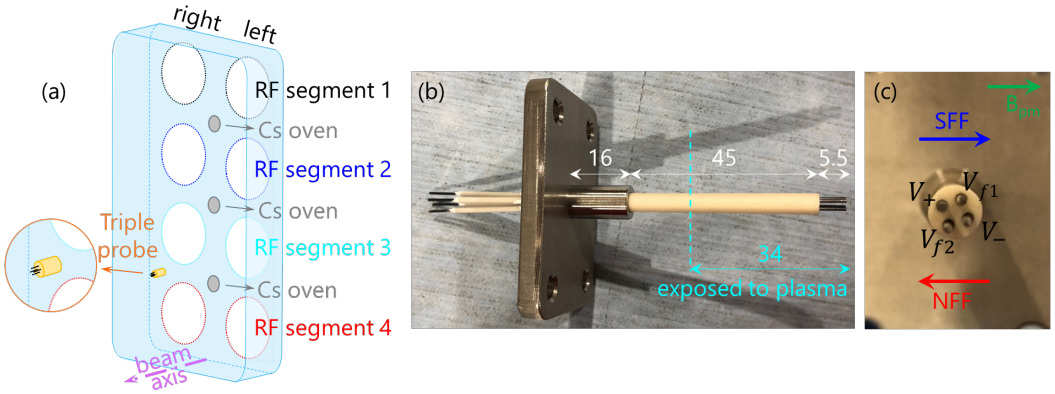

Figure 7.3: Schematic view of the triple probe in SPIDER source (a); side view (b) and front view (c) of the triple probe assembly.

The V_+ and V_- electrodes are biased with respect to each other with a total polarisation voltage V_{pol} between 50 V and 100 V; the V_{f1} electrode is referred to V_+; it is worth pointing out that, in this configuration, the three electrodes V_+, V_- and V_{f1} are floating with the plasma itself, as they are not referred to ground potential. Finally, the fourth electrode V_{f2} has no external polarisation and its voltage is referred to the source potential. The electrical setup simultaneously provides three signals, namely the current I_s flowing between V_+ and V_-, the potential difference between V_+ and V_{f1} and the V_{f2} potential; following the triple probe theory[80], the plasma density n, the electron temperature T_e and the floating potential V_f can be estimated as follows:

$$n(t) = \frac{I_s(t)}{0.5 q c_s A_{coll}} \tag{7.1}$$

where q is the elementary charge, c_s is the ion sound speed, and A_{coll} is the effective collecting surface of the electrodes. The electron temperature reads:

$$T_e(t) = \frac{V_+ - V_{f1}}{\ln\left(\frac{1+\alpha}{\alpha}\right)} \tag{7.2}$$

where $\alpha = I_{sat,+}/I_{sat,-}$, e.g. the ratio between the ion saturation current of V_+ and V_-. Since the distance between the electrodes is smaller than the characteristic length of plasma variations and, furthermore, the electrodes have the same dimensions, α is assumed to be equal to 1. Finally, the floating potential is measured with respect to the source wall potential V_S, hence $V_f = V_{f2} - V_S$.

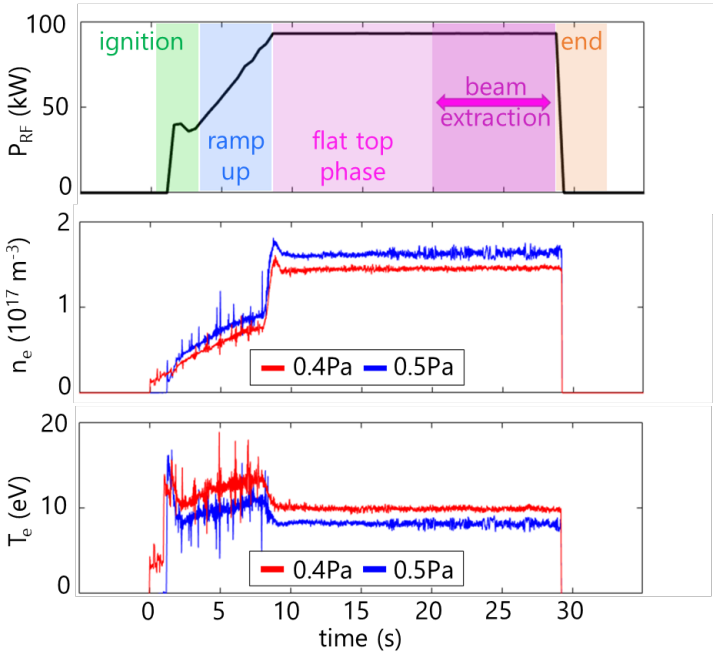

Figure 7.4: RF power (a), plasma density (b) and electron temperature (c) as a function of time for two different shots with different source pressure.

Figure 7.4 shows an example of Continuous Wave (CW) measurements, which allow to follow the time evolution of the plasma parameters for the entire plasma discharge; in this case, pairs of LC choke filters were used to cut-off both the fundamental RF frequency and its second harmonic.

7.2.2 Influence of filter field

The magnetic field intensity at the probe location is given by the combination of the FF, B_{FF}, with the field due to the permanent magnets placed on the outer side of the source lateral walls, B_{pm}. The latter has constant orientation and its intensity at the probe location is approximately 2 mT. In particular, the two contributions are summed for standard configuration of B_{FF}, whereas they have opposite direction with reversed B_{FF} field (see Figure 7.5). It is worth pointing out that this simplified scheme is valid only on the direction parallel to the filter field. However, within this approximation, in the RFF configuration the total magnetic field along the FF direction can be strongly reduced or even reversed.

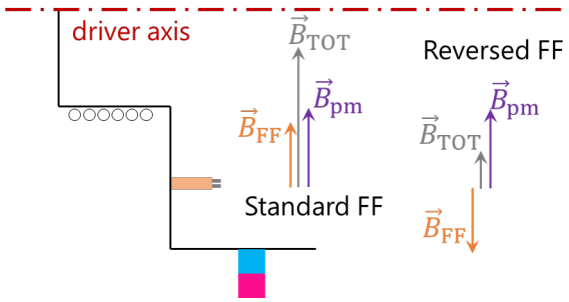

Figure 7.5: Simplified scheme of the total magnetic field at the triple probe location in the standard and reversed FF configurations.

Figure 7.6 shows a comparison of plasma density and electron temperature measured with the two possible FF configurations. With a relatively low FF intensity, the net B_{tot} field at the exit of the drivers is lower in the standard FF configuration, resulting in a more pronounced plasma expansion out of the driver cylinders; as a consequence, the probe measures a higher density and electron temperature.

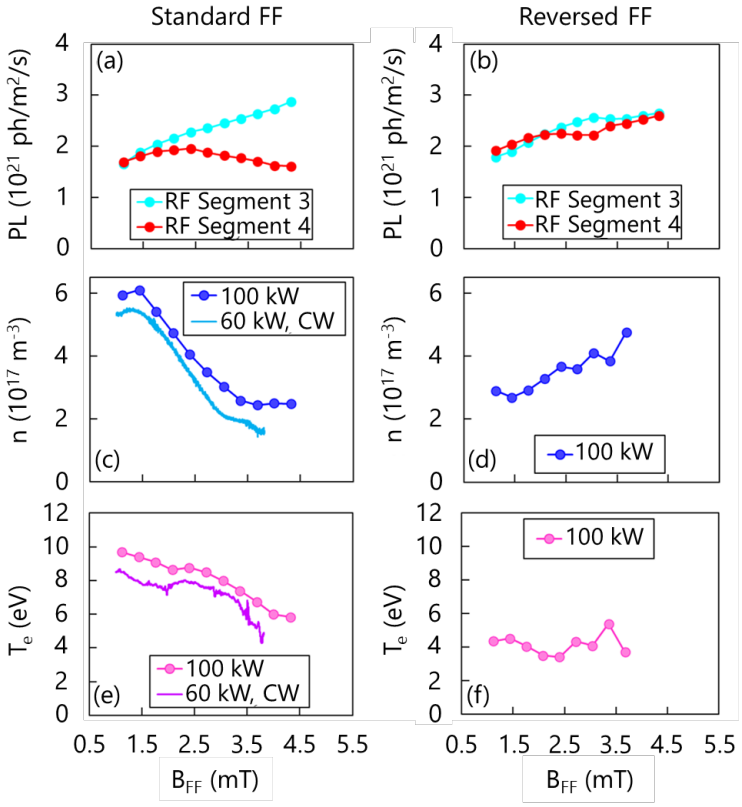

Figure 7.6: Plasma light from the drivers near the probe, plasma density n, and electron temperature T_e as a function of the field intensity for standard (a,c,e) and reversed (b,d,f) field direction. Dotted data were taken by repeating identical pulses while changing the filter field intensity. For the standard FF case, single pulse measurements performed with a B_{FF} intensity ramp are also shown. Operating conditions: p=0.3 Pa, I_{BI}=I_{BP}=80 A. Plasma Light data courtesy of B. Zaniol.

The plasma properties at the probe location will depend on the behaviour of the closest drivers; on this basis, the probe measurements can be compared with the Plasma Light[69] of the drivers in segments 3 and 4 of the right column (see Figure 7.3). Being line-integrated along the driver axis, the PL measurement takes into account the plasma emission of both the driver and the expansion chamber. From Figures 7.6b and 7.6d it results that, in the reversed B_{FF} case, the plasma density n measured by the triple probe follows the same trend as the PL. The electron temperature T_e (Figure 7.6f) shows no dependence on the field intensity, and its value (approximately 4 eV) might imply that, at the beginning of the expansion chamber, the electrons have already cooled down through the filter field lines. In the normal B_{FF} case, the probe measurements are strongly influenced by the behaviour of the driver from RF segment 4. The PL of the latter (Figure 7.6a) shows an unexpected behaviour, as it decreases whilst the B_{FF} field intensity increases, demonstrating a poor confinement, possibly due to the combined effect of B_{FF} itself and the permanent magnets field B_{pm}. This is consistent with the probe measurements: in fact, T_e is much higher (Figure 7.6e), as if the inductive coupling occurs outside the driver cylinder.

As a consequence, also the plasma density n is higher, and it decreases with T_e (Figure 7.6c). A similar behaviour was found in SPIDER with the movable Langmuir probes[34]. Figure 7.6c and 7.6e show a comparison between data measured with different values of injected power. As expected, both the n and T_e signals are shifted towards higher values when increasing the RF power per generator from 60 kW to 100 kW, while their behaviour with respect to the B_{FF} field intensity does not change. According to these results, the normal B_{FF} case provides an anomalous operating condition for the bottom RF segment, requiring further investigation.

Chapter summary

Experimental evidence of strong non-uniformity both in the expansion chamber and in the extraction region of the SPIDER beam source along the vertical direction has been described. This directly affects the beam extraction, with poor negative ion current density obtained at the bottom of the source in correspondence of an unexpected plasma emission probably related to an unbalanced presence of electrons. A tentative explanation has been provided also with the aid of numerical simulations, which highlighted the presence of a hot electron flow at the driver exit that might be responsible for the non-uniformity of the plasma properties also close to the PG electrode. A slight non-uniformity of the vertical profile of the simulated electron density was also highlighted: this might be correlated to the local-non uniformity of the vertical profile of the extracted beam current density, although the simulation was not accurate enough to provide a reliable investigation of this feature. The non-symmetric effect of reversing the FF direction was also mentioned and further supported with experimental measurements by a triple Langmuir probe, which was installed in the rear region of the expansion chamber. According to these results, the plasma properties at the probe location are strongly dependent on the filter field intensity within the standard configuration, whereas in the reversed configuration no strong dependence on the field intensity was highlighted. The presented numerical simulation might be repeated in the future aiming at studying possible counter-measurements to minimise the electron flow reaching the extraction region either acting on the profile of magnetic field, or on electric biases of the metallic surfaces of the ion source, or introducing additional electrodes in the bottom region of the source.

Chapter 8

Influence of bias electrodes on source plasma properties

The influence of bias electrodes within large negative ion sources has been widely investigated in recent years and continues to be an active area of study. The polarisation of the PG electrode was found to affect the properties of the source plasma and, consequently, of beam extraction. This chapter is devoted to the analysis of the bias electrodes influence on the plasma properties in both the expansion chamber and the extraction region.

8.1 State of the art

Past experimental results[81] have shown that a biased PG can function as a Langmuir probe with a very large collection area, attracting either positive or negative charges towards the extraction region. Numerous experimental findings have demonstrated that increasing the positive bias of the PG results in an enhanced extraction of negative ion currents, accompanied by a reduction of the co-extracted electrons. It's worth noting that the extent of the PG bias influence also depends on the strength of the magnetic filter field[82]. Higher field intensities lead to a decrease in electron density and temperature. In such cases, excessive positive bias on the PG might deplete the population of negative ions.

In the MANITU facility[83], the Bias Plate electrode has been introduced, positioned upstream of the PG. The BP is designed to cover the unused portion of the PG area for beam extraction. Initially, the BP was electrically connected to the source walls, preventing it from being polarised with respect to the plasma. The presence of this electrode has proven effective in reducing the electron-to-ion ratio in the extraction region, while allowing to operate the source with a less intense filter field with respect to the case without BP, especially during deuterium operations[84]. Further enhancements in electron suppression were achieved in MANITU by polarizing the BP electrode[85], similarly to what was done for the PG.

As previously mentioned, the SPIDER source design allows the independent biasing of both the PG and BP electrodes with respect to the source walls. During operation in a pure volume production, it was observed that the electron-to-ion ratio is strongly influenced by the polarization of these electrodes[86].

8.2 Bias polarisation influence in the expansion region

Given their very large areas, both bias electrodes can affect the plasma properties in the expansion region, as highlighted by measurements performed with the TLP probe described in Section 7.2.1. Figure 8.1 shows the effect of the PG bias V_{BI} on the plasma properties: higher PG polarisation leads to an increase in plasma density, electron temperature and floating potential. This behaviour appears to be independent on the filter field intensity (although the considered variations are very small), and is consistent also while varying the source pressure. Generally speaking, a 10 V increase of V_{BI} yields a 4 V increase of V_f at the rear of the source, regardless of the other source parameters. The same occurs when considering V_{BP} instead of V_{BI}, although the data are not shown.

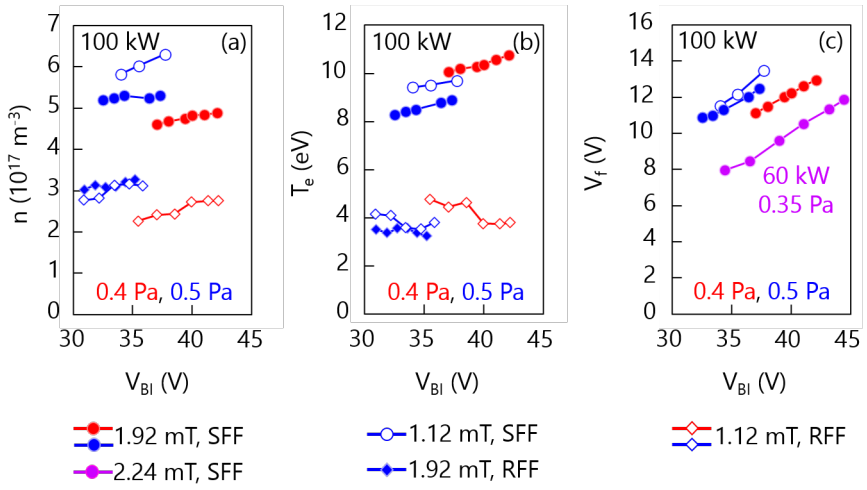

Figure 8.1: Plasma density n (a), electron temperature T_e (b) and floating potential V_f (c) as a function of V_{BI}. The total magnetic field at the probe location can be obtained by combining B_{pm} (2 mT, standard configuration) with the B_{FF} field intensities in the legend. The RF power is 100 kW unless otherwise stated. All measurements were taken during Cs-free operation.

With caesium injection, the plasma potential is expected to be reduced[66] because of the increased negative ion density. Figure 8.2 shows the floating potential V_f measured by the triple probe during the first hours of caesium injection in SPIDER. The V_{BI} bias and the plasma potential ϕ are also shown for comparison. The growth of the accelerated current I_{AG} and the simultaneous decrease of the extracted current I_{EG} (Figures 8.2c and 8.2d) imply that the negative ion density at the extraction region is increasing, altering the net current collected by the PG electrode and, consequently, changing the V_{BI} potential in response to the imposed current control. With reference to the values measured in pure volume operation, the PG bias V_{BI} drops of roughly 4.5 V in the first day of caesium injection (Figure 8.2a), and the floating potential V_f decrease measured by the triple probe at the end of the first day of caesiation is about 3.3 V: this implies that, as soon as caesium is injected, the plasma potential decreases in the entire expansion chamber. At the end of the second day of caesium injection, the measured floating potential V_f increases (Figure 8.2b), possibly as a consequence of the source pressure increase. The electron temperature decreases from 10 eV to 8.5 eV.

Caesiation is a rather complex process, and reaching stable conditions requires a more or less extended transient phase, whose length depends on several factors such as variation of operating parameters or pause of the experimental session. Figure 8.3 shows how the triple probe measurements of plasma density, electron temperature and floating potential change in response to variations of the bias electrodes driving currents I_{BI} and I_{BP}, as well as the transient phases before reaching stable caesiation conditions.

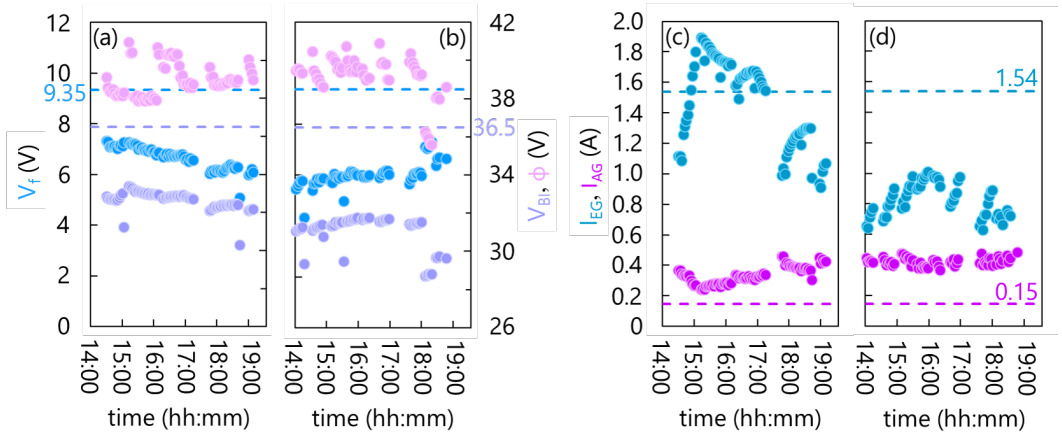

Figure 8.2: Floating potential V_f, plasma potential ϕ, bias voltage V_{BI}, accelerated current I_{AG} and extracted current I_{EG} during 1$^{\mathrm{st}}$ (a,c) and 2$^{\mathrm{nd}}$ day (b,d) of caesium evaporation. The dashed lines represent the reference values measured without Cs for each quantity, with the same operating conditions. The operating parameters (30 kW per driver, 0.35 Pa, I_{BI} 80 A, I_{BP} 80 A, I_{PG} 1.35 kA) were kept constant throughout both days, with the exception of the source pressure, which was increased at the end of the second day (region highlighted in light blue).

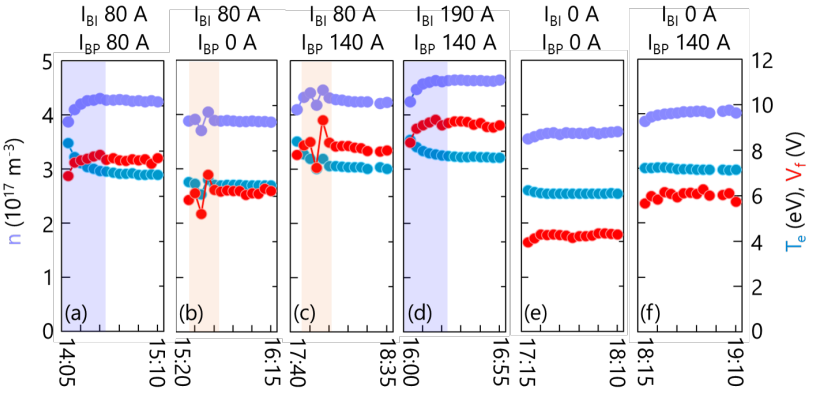

Figure 8.3: Plasma density n, electron temperature T_e and floating potential V_f measured during two experimental sessions (a,b,c and d,e,f) as functions of I_{BI} and I_{BP} currents. The transient phases are highlighted in blue. The measurements highlighted in orange were performed with different bias currents than the ones written on top of the figures. The bias currents values shown here are the ones measured at the power supplies.

The trends of the measured plasma properties and with respect to the bias currents shown in Figure 8.3 are summarised in Figure 8.4. As already discussed for the measurements in pure volume production, all the measured quantities increase with the bias currents, hence for higher V_{BI}, V_{BP} values. The influence of the PG and BP biases has the same extent for both n and T_e, whereas the floating potential V_f is more influenced by I_{BI} (e.g. V_{BI}) variations. The plasma density and electron temperature increase might imply that, for higher V_{BI} values, the potential difference between the driver plasma and the source walls becomes larger, improving the electron confinement within the driver itself. At the same time, the potential drop between the driver and the extraction region becomes smaller, thus less positive ions will be able to reach the electrodes; nonetheless, the triple probe measurements alone are not sufficient to determine how the PG bias is influencing the expansion chamber plasma, mainly because the probe is very

close to the lateral walls and to the drivers' exit and, consequently, it might intercept a strong enough magnetic field for plasma particles to be confined and driven towards the electrodes.

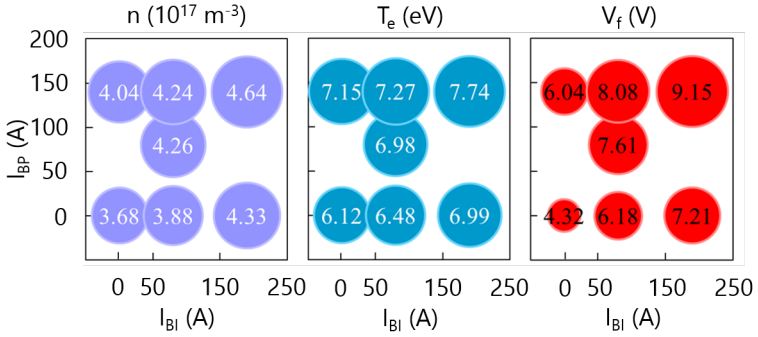

Figure 8.4: Plasma density n, electron temperature T_e, and floating potential V_f measured by the triple probe as a function of the bias currents I_{BI} and I_{BP}. Source pressure 0.35 Pa, RF power 45 kW, B_{FF} 1.68 mT standard configuration. The bias currents values shown here are the ones measured at the power supplies.

8.3 Bias polarisation influence in the extraction region

In order to understand how the PG and BP biases are affecting the source plasma expansion in SPIDER, it is necessary to analyse how the plasma properties vary closer to the extraction region. To this purpose, Figure 8.5 shows the plasma properties measured by the embedded Langmuir probes.

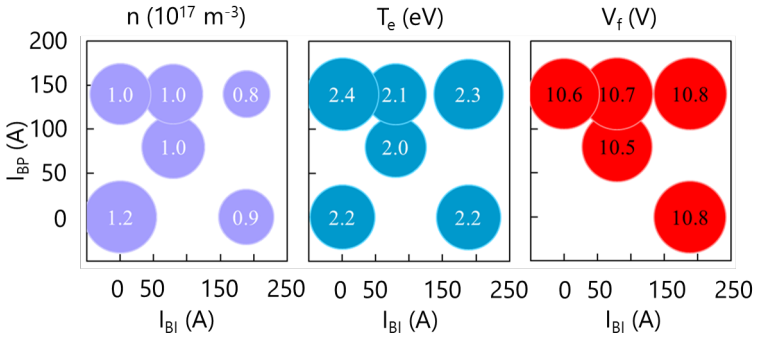

Figure 8.5: Plasma density n, electron temperature T_e, and floating potential V_f measured by the embedded probes on the bias electrodes as a function of the bias currents I_{BI} and I_{BP}. Source pressure 0.35 Pa, RF power 45 kW, B_{FF} 1.68 mT standard configuration. The bias currents values shown here are the ones measured at the power supplies. Data courtesy of C. Poggi.

Both the electron temperature and the floating potential in front of the grids are roughly constant when varying the bias; the plasma density instead decreases for higher biases, which is in accordance with the TLP measurements shown before (Figure 8.4), assuming that the plasma is being pushed away from the extraction region because of the higher potential. Indeed, the bias electrodes are large enough to influence the plasma properties along the entire expansion chamber and, moreover, the plasma diffusion towards the grids is driven by the plasma ions rather than by the plasma electrons, which instead are restrained by the filter field. Similarly to Figures 8.4 and 8.5, Figure 8.6 shows the negative ion current at the GG, the electron current at the EG, and the PG bias V_{BI}, as a function of the bias currents.

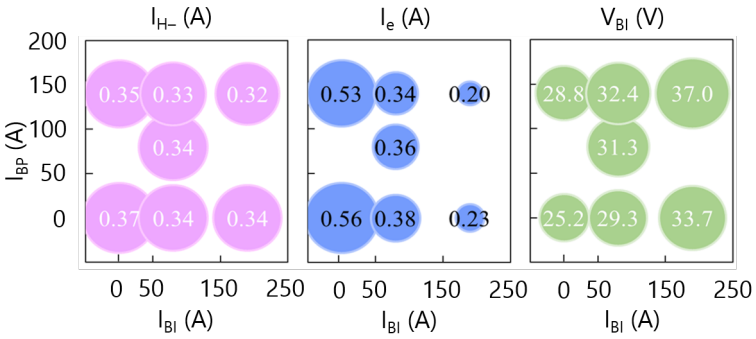

Figure 8.6: Negative ion current I_{H}^{-} and electron current I_e at the GG, and PG bias V_{BI} as a function of the bias currents I_{BI} and I_{BP}. Source pressure 0.35 Pa, RF power 45 kW, B_{FF} 1.68 mT standard configuration. Data courtesy of NBTF experimental team.

The accelerated negative ion current is not affected by variations of the bias currents. The electron current is strongly reduced for high I_{BI} currents, whereas it is almost unvaried when changing the I_{BP} current. The lower electron current might be a result of the reduced positive ion diffusion towards the extraction region; in addition, the presence of surface produced negative ions downstream of the PG and BP electrodes can be increased by the higher bias potentials (not necessarily implying an increased extracted beam current) and, as a consequence, plasma electrons can be depleted.

8.3.1 Effect of BP electrode on plasma properties in the extraction region

In order to better understand what is the role of the Bias Plate electrode on the plasma properties close to the extraction region, a simple analytic one-dimensional model was applied to investigate this phenomenon, as described in the following.

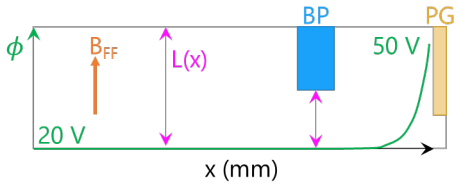

Figure 8.7: One dimensional domain: both the BP and PG electrodes are included, as well as the assumed potential profile highlighted in green. Symmetry with respect to the x axis is assumed.

In a one-dimensional system as the one depicted in Figure 8.7, crossing the BP and reaching the upstream side of the PG aperture, one can obtain a second order differential equation describing the spatial evolution of the electron density n_e by imposing flux conservation[62], hence $\nabla \cdot \Gamma_e = S - L$ with S and L representing the volumetric source and loss terms respectively:

$$D_{\perp}\frac{d^2 n_e}{dx^2} + \mu_{\perp} E \frac{dn_e}{d_x} + \left(\mu_{\perp}\frac{dE}{dx} + L_{\mathrm{BP}}(x)\right) n_e = 0 \tag{8.1}$$

where E is the local electric field which can be obtained from the imposed potential profile ϕ, $\mu_{\perp}$ and $D_{\perp}$ are the electron mobility and diffusion coefficients respectively. The potential profile is an educated guess considering a plasma bulk potential of 20 V, with a rapid increase in the proximity of the PG electrode for including the penetration of the extraction field. In this case,

only a loss term $L_{\mathrm{BP}}(x)$ was considered, which accounts for the losses at the BP and can be estimated as:

$$L_{\mathrm{BP}}(x) = \frac{1}{4L(x)} v_e^{th} \exp\left(\frac{V_W(x) - \phi(x)}{\mathrm{T}_e}\right) \tag{8.2}$$

where $v_e^{th} = (8q\mathrm{T}_e/\pi/m_e)^{0.5}$ is the thermal electron velocity, $\phi(x)$ is the assumed plasma potential profile, $L(x)$ is the distance between the centre of the beamlet group and the upper surface intersecting the magnetic field lines (see Figure 8.9), and $V_W(x)$ is the potential of that surface.

By solving Eq. 8.1 with the FDM, the spatial evolution of the electron density can be obtained. In order to study the effect of the bias plate electrode, the value of $V_W(x)$ at the BP was changed while keeping B_{FF}=1.6 mT, as shown in Figure 8.8.

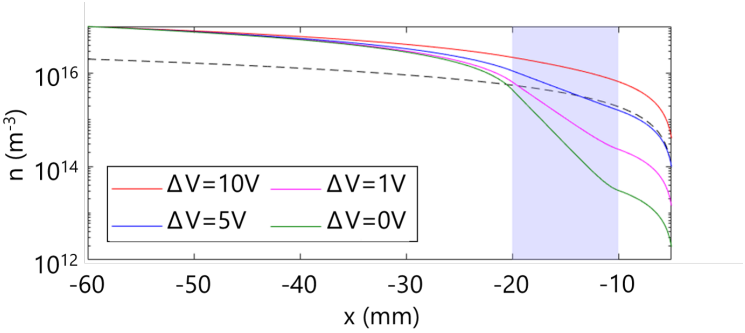

Figure 8.8: Electron density profiles for different values of $\Delta V = \phi - V_{\mathrm{BP}}$. The dashed black line shows the negative ion density, unaffected by the bias electrodes. The BP position is highlighted in light blue.

For decreasing potential difference between plasma and BP potential the electron density reduction in correspondence of the BP electrode is enhanced, with the maximum reduction obtained when the potential difference is reduced to 0 V. In this latter case, the potential drop in the perpendicular direction (e.g. along the field lines) is reduced and, as a consequence, the electrostatic confinement of the electrons in the beamlet centre is less effective. The negative ion density profile is also shown and, as expected, BP bias does not affect the plasma ions as they are weakly magnetised. The BP electrode acts as a scrape-off layer for the plasma electrons, with the scraping being more effective when bringing the BP bias closer to the plasma potential. Nonetheless, this simple one-dimensional model does not take into account several other factors that might influence the result, such as the presence of positive ions that would favour electron transport towards the PG, the losses along the perpendicular direction, and a consistent solution of the Poisson equation. In addition, this model is only valid before the meniscus formation. For all these reasons, the GPPIC code was applied to investigate the same problem, considering a two-dimensional domain as the one depicted in Figure 8.9.

The simulated domain was designed on the basis of the SPIDER source geometry. The domain lies on a plane cutting the source volume horizontally, including both the PG and BP, with the PG featuring three out of five apertures. The EG is simulated as a solid metallic wall biased at V_{ext} with respect to the source walls, and coincides with the right boundary of the domain. According to the Child-Langmuir law[17], the extracted current density scales with $V_{\mathrm{ext}}^{3/2}$, therefore the actual extraction potential has to be multiplied by a factor $\beta^{2/3}$ in such a way to obtain a current density that can be correlated to the real plasma density n. The left boundary represents the source plasma and it is also simulated as a plain metallic wall with fixed potential V_p. Periodic boundary conditions are imposed between the top and bottom surfaces. A limited region of the expansion chamber is included upstream of the grids. Both the magnetic filter field and the deflection magnetic field produced by the CESM[87] are included.

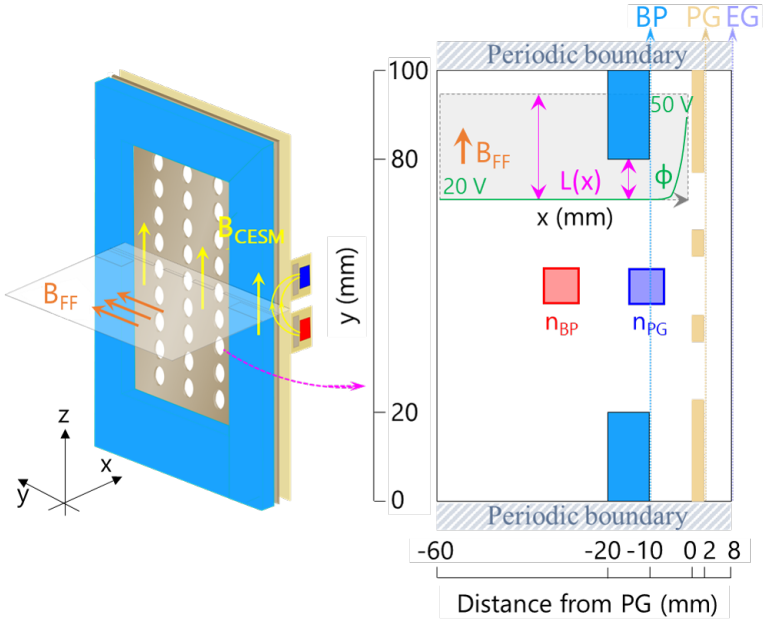

Figure 8.9: Two-dimensional domain used for GPPIC simulations investigating the bias plate influence on plasma properties in the extraction region. The BP and PG are represented in blue and yellow respectively. The B_{FF}, B_{CESM} fields are directed as indicated by the arrows. For the sake of completeness, the one-dimensional domain is also shown in the figure.

Parameter	Description	Value
p_{bg}	background gas pressure	0.34 Pa
n	target plasma density	1×10^{17} m^{-3}
β	density scaling factor	0.5,0.3
T_e	electron temperature	2.5 eV
T_+	positive ion temperature	0.8 eV
T_-	negative ion temperature	1.5 eV
V_{left}	left wall potential	30 V
V_{ext}	EG voltage (right wall)	1.8 kV
V_{BI}	PG potential	[10 V-35 V]
V_{BP}	BP potential	[10 V-40 V]
B_{FF}^{max}	max FF field intensity	[0 mT-4 mT]
B_{CESM}^{max}	max deflection field intensity	3.6 mT

Table 8.1: Main simulation parameters and their values.

The magnetic filter field is directed along the y direction and is constant in time, although its intensity depends on the x coordinate as:

$$B_{\mathrm{FF}}(x) = \frac{B_{\mathrm{FF}}^{max}}{3}\left(1.5 - \tanh\left(\frac{x - 2\,\mathrm{mm}}{2\,\mathrm{mm}}\right)\right) \tag{8.3}$$

The deflection field is also constant in time, but it is oriented along the z direction; as for the filter field, its intensity depends only on the x coordinate as:

$$B_{\mathrm{CESM}}(x) = \frac{B_{\mathrm{CESM}}^{max}}{0.0759}\frac{\exp\left(\frac{x-13\,\mathrm{mm}}{2\,\mathrm{mm}}\right)}{1+\exp\left(\frac{x-13\,\mathrm{mm}}{2\,\mathrm{mm}}\right)} \tag{8.4}$$

The background gas is molecular hydrogen, H_2, with a fraction $f = 0.3$ of dissociated H atoms. The background neutral density (i.e. the gas pressure) is assumed to be uniform over the simulation domain. At the beginning of the simulation run, a uniform plasma composed of 45% electrons e, 5% negative ions H^-, 20% protons H^+, 15% of each molecular ion species H_2^+, H_3^+ is generated. A constant flux $\Gamma_i = 0.25 n_i v_i$, uniform along y and oriented along x, is injected from the left boundary so as to represent the plasma flowing from the expansion region. The i index labels the plasma species, with the sum of the n_i densities keeping the same plasma composition as the initial one. The timestep of the simulation is dt=10 ns, and the dimensions of the mesh cell along both x and y directions is dx=dy=0.16 mm. The main simulation parameters and their values are listed in Table 8.1.

Figure 8.10 shows the two-dimensional maps of electron density n_e, electron temperature T_e and plasma potential ϕ obtained for V_{BI}=V_{BP}=20 V and B_{FF}^{max}=1.6 mT. When crossing the BP region, the electron density is roughly halved, whereas the electron temperature T_e decreases by roughly 0.5 eV. The plasma potential is uniform with an average value of 30 V, until the plasma meniscus forms when approaching the PG. For all three beamlets, the meniscus is largely extended towards the plasma region, possibly because of the large extraction voltage.

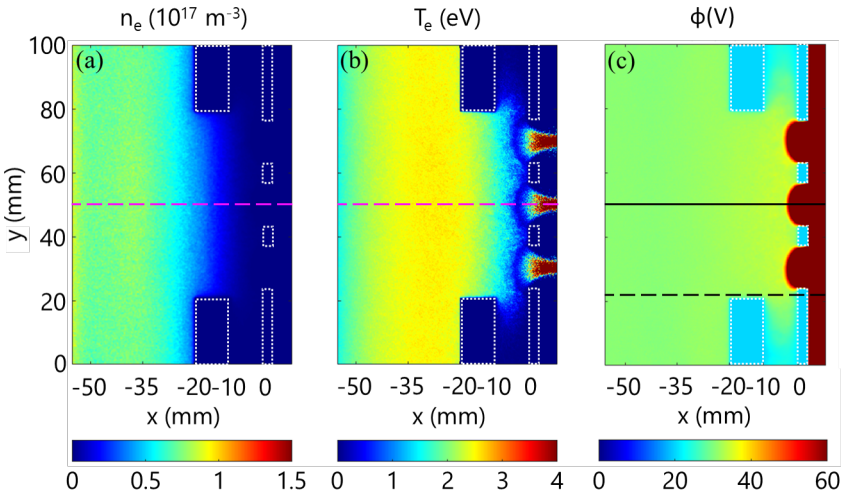

Figure 8.10: Two-dimensional maps of electron density n_e (a) and temperature T_e (b), plasma potential ϕ (c), all values are time-averaged over 100 consecutive iterations. Other parameters are V_{BI}=V_{BP}=20 V, B_{FF}^{max}=1.6 mT.

The horizontal profiles of plasma density, electron temperature and plasma potential are shown in Figure 8.11. The positive ion composition is different from the initial one: in particular, the H_2^+ fraction is decreased, possibly implying that there are some missing destruction channels for the other ion species. Within the extraction region, the negative ion density is almost a factor 10 higher than the electron density; in these conditions, the extracted ion current density though will still be lower than the electron one, as shown later in this work. The plasma meniscus position along the x axis corresponds to the sudden drop of positive ions, which are repelled by the extraction field. Two plasma potential profiles are shown in Figure 8.11, one in correspondence of the beamlet group centre (solid black line) and the other one intersecting the PG surface (dashed black line). In the first case, the PGbias is completely screened by the extraction field; as a consequence, the V_{BI} influence on the plasma parameters will be less than the V_{BP}. In fact, the PIC algorithm is 2D3V, thus the PG apertures are effectively reproduced as horizontal slits rather than round openings; this results in an enhancement of the EG field penetration in the source volume. The magnetic field topology might also be affected when

considering a 2D geometry rather than a 3D one.

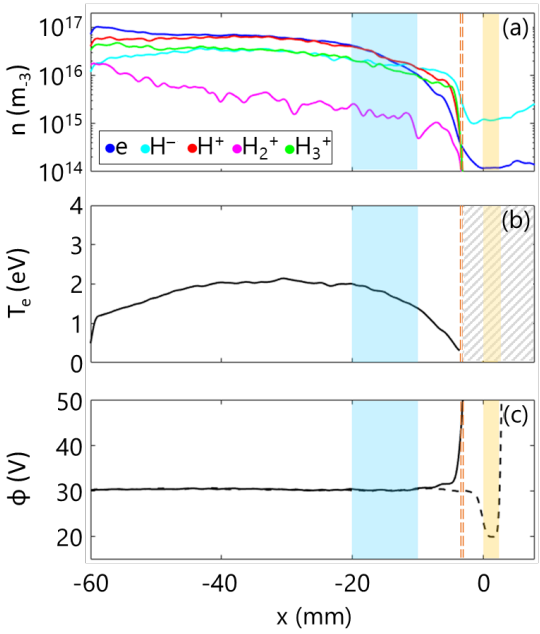

Figure 8.11: Plasma densities n, T_e up to the meniscus, and ϕ profiles along y=50 mm, as highlighted in Figure 8.10 (all values are time-averaged over 100 consecutive iterations). The dashed black line in (f) shows a ϕ profile crossing the PG at y=17 mm, as highlighted in Figure 8.10. The meniscus position in (d,e,f) is shown by the dashed orange line; the bias electrodes positions are highlighted in blue and yellow respectively. In this case, V_{BI}=V_{BP}=20 V and B_{FF}^{max}=1.6 mT.

Figure 8.12 shows horizontal profiles of electron density and temperature, as well as of plasma potential, for different V_{BP} polarization values. The electron scraping on both density and temperature is enhanced with increasing V_{BP}, therefore the ratio between the extracted electron and negative ion currents is expected to decrease. The negative ion density (not shown) is almost unaffected by the variation of the bias plate voltage, confirming that the plasma ions are weakly magnetised. A significant variation of electron density and temperature only appears when $V_{\mathrm{BP}} \geq$30 V, that is when the BP is positively polarised with respect to the plasma. In this condition, a local electric field will set in in such a way that the electrons will diffuse towards the upstream surface of the BP: this explains the electron depletion in front of the electrode. Figure 8.12 shows that the potential profile is also slightly modified in the proximity of the meniscus. In the 1D analytical model, the electron scraping was found to be much more intense (see Figure 8.8). Indeed, the 2D model accounts for the positive ions and, consequently, the electron confinement due to the plasma itself ($\phi > V_{\mathrm{BP}}$). However, despite this discrepancy, it is worth pointing out that the shape of the density profiles is comparable between the two cases: for ($V_{\mathrm{BP}} < \phi$), the n decay is almost unaffected by the presence of the BP. On the contrary, when ($V_{\mathrm{BP}} \geq \phi$), the n slope varies in a similar way both in Figure 8.8 and in Figure 8.12.

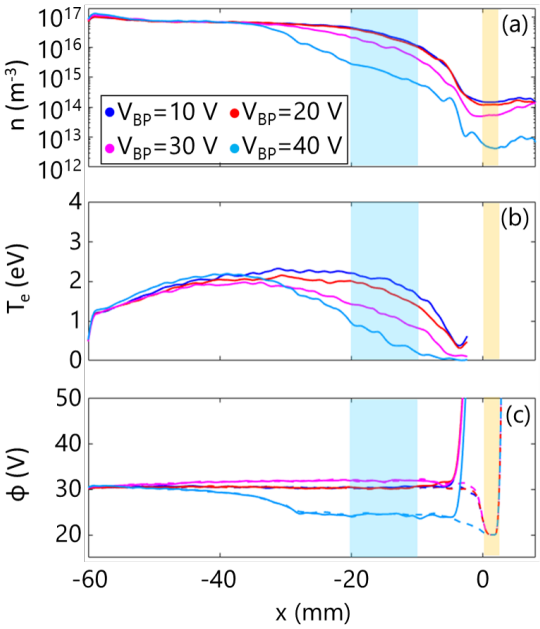

Figure 8.12: Electron density n (a) and temperature T_e (b), and plasma potential ϕ (c) profiles for different values of bias plate potential. All the other parameters are fixed as for Figure 8.10. Dashed lines in (c) represent potential profiles crossing the PG.

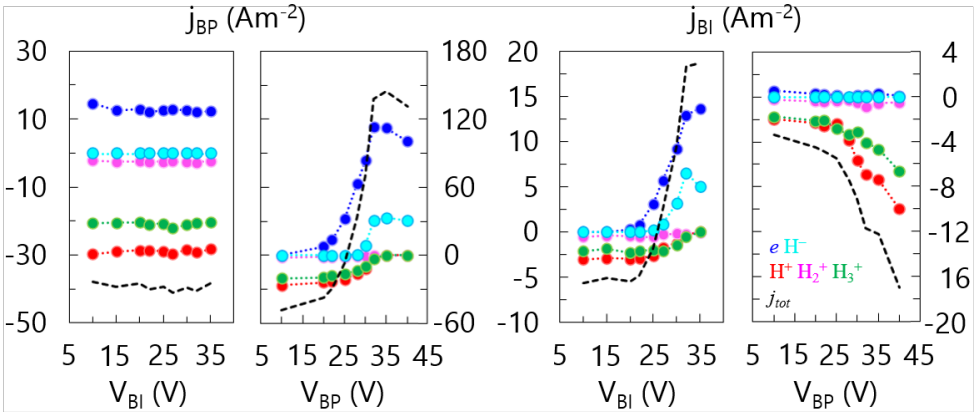

Figure 8.13: PG and BP current densities j_{BI}, j_{BP} as a function of V_{BI} and V_{BP}. Current contributions have positive sign for e, H^-, negative sign for H^+, H_3^+, H_3^+. B_{FF}=1.6 mT.

The behaviour of several plasma parameters with respect to the bias voltages is discussed in the following. The two biases were varied one at a time, upon keeping the other fixed at 20 V. The net current densities collected by the BP and PG electrodes as functions of their biases V_{BI}, V_{BP} are shown in Figure 8.13. As expected, the current-voltage characteristics of both grids are similar to the ones of single Langmuir probes[72]. In particular, whilst the j_{BP} current density shows no dependence on the bias of the other electrode V_{BI}, the plasma grid current density j_{BI} is affected by the BP polarisation. The bias plate shows a much stronger influence on the plasma properties when polarised with respect to the plasma itself. Nonetheless, it is worth recalling that the plasma flux incoming from the expansion region is kept constant: this is not verified in

the real experiment, as the plasma properties in the rear region of the expansion chamber are also influenced by the bias electrodes.

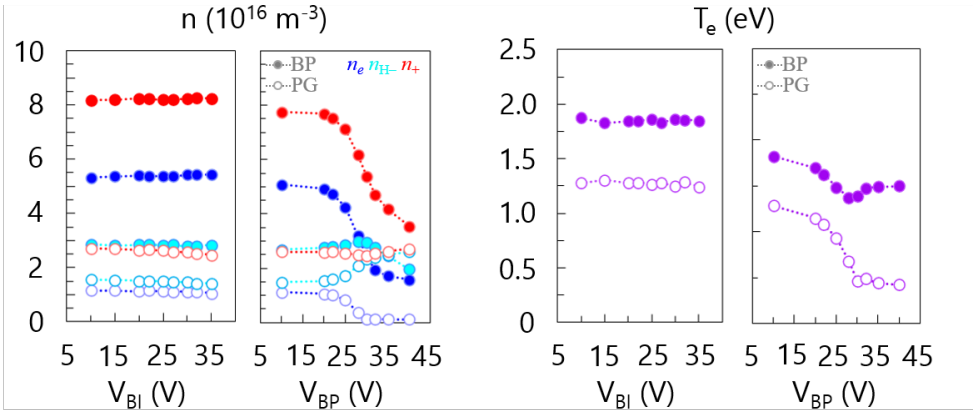

Figure 8.14: e, H^- and positive ion densities (a,b) and T_e (c,d) in front of the BP (filled circles) and in the extraction region (empty circles) as a function of V_{BI} and V_{BP}. B_{FF}=1.6 mT.

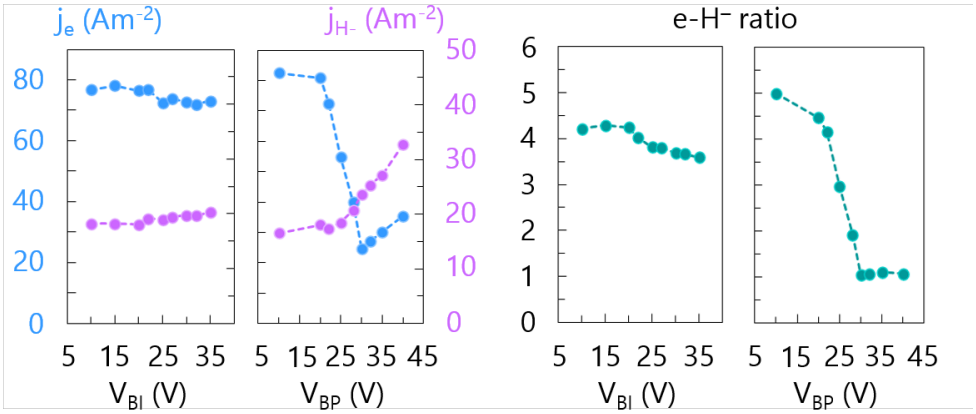

Figure 8.15: Electron and negative ion extracted current densities j_e, j_{H^-} (a,b) and e-H^- ratio (c,d) as a function of V_{BI} and V_{BP}. B_{FF}=1.6 mT.

Figure 8.14 shows the densities of electrons, negative ions and positive ions averaged over reduced areas in front of the BP, n_{BP}, and upstream of the PG apertures, n_{PG}. The considered areas are indicated by the red and blue rectangles in Figure 8.9. The n_{BP} densities show no dependence on V_{BI}, whereas they are strongly affected by the BP voltage. In the latter case, the total plasma density decreases for high V_{BP} values, although the major difference is in the plasma composition: for higher bias values, the negative ion density is comparable to the electron one, as the electrons are scraped off by the bias plate itself. The H^- density at the PG increases for higher V_{BP}, until the H^- become the dominant negatively charged species, though no effect is visible on the correspondent j_{PG} as the PG bias is lower than the plasma potential. Neither n_{BP} nor n_{PG} show a significant dependence on V_{BI}; as previously stated, this might be due to geometrical effects. However, the BP effect is still visible in the plasma composition: as already seen in Figure 8.14, the negative ion density in front of the PG becomes comparable to the electron one. Similarly, the electron temperature T_e decreases by roughly 0.6 eV when crossing the BP, although no dependence on V_{BI} is visible since $V_{BP} < \phi$. Indeed, as soon as the BP is

changed –more precisely for $V_{BP} \geq \phi$– the electron temperature reduction is enhanced. The bias plate results more effective also in reducing the electron-to-ion ratio, as shown in Figure 8.15. The H^- density increase in Figure 8.14 leads to a more intense extracted ion current, j_{H^-}. These results are consistent with the fact that the plasma grid bias V_{BI} is screened by the extraction potential.

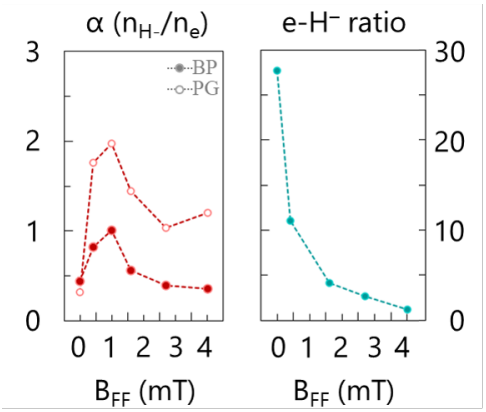

Figure 8.16: Electronegativity α (a) and e-H^- ratio (b) as a function of B_{FF} (V_{BI}=V_{BP}=20 V).

The effect of the filter field intensity on the plasma properties was also investigated, as shown in Figure 8.16. As expected, the electron-to-ion ratio is significantly influenced by the B_{FF} intensity, as the latter defines the strength of the scraping at the BP; the plasma electronegativity $\alpha = n_{H^-}/n_e$[88] in front of the PG electrode increases for higher B_{FF}, as the latter hinders fast electron transport towards the extraction region. Figure 8.16 also suggests that the effectiveness of the BP scraping is not significantly improved for $B_{FF} \geq$1.6 mT; however, as previously stated, having considered a constant plasma flux incoming from the left boundary might have influenced these results.

Chapter summary

By comparing experimental measurements of the triple Langmuir probe and of the electrostatic probes embedded on both PG and BP electrodes taken in the SPIDER source, it appears that higher V_{BI} bias can reduce positive ion flow towards the grids, consequently increasing plasma confinement. According to the experimental results, the PG electrode polarization influence on the plasma properties is stronger than the BP electrode one, although further studies should be carried out increasing the bias voltage and current provided by the BP power supply, in order to better evaluate the effect of having bias voltages close to the plasma potential or above. Nonetheless, according to numerical results, the BP can cause a significant reduction of the electron density and temperature, with higher V_{BP} bias values yielding stronger influence. In discussing the results, we must consider that the complex magnetic field topology given by the electron deflection magnets (i.e. those integrated in the extraction grid) could not be considered in the two-dimensional simulation. Therefore, the role of the bias plate described here could be strongly reduced by the non-ideal magnetic configuration, in which the 1D filter field combines with a magnetic field structure similar to cusp magnets along the vertical direction perpendicular to the simulated plane. With the 2D model, the plasma meniscus formation was reproduced, together with the ion-ion layer in front of the plasma grid. The PG bias, V_{BI}, was also found to affect the plasma properties at the extraction region in the same fashion, even though with minor influence both because of the model geometry, which causes an underestimation of the effective PG surface exposed to the plasma, and the boundary conditions: in fact, it is worth pointing out that the effect of the bias electrodes was investigated with fixed plasma properties in the expansion region (e.g. at the left boundary). However, during the real experiments, plasma density, electron temperature and plasma potential do vary when V_{BI}, V_{BP} and also the B_{FF} intensity are changed[89]. For instance, if the density gradient across the expansion chamber or the axial plasma potential profile are different, the electron diffusion towards the extraction region and the scraping effect of the bias will be inevitably affected. In addition, the presented results can be related to pure volume production of negative ions; indeed, the trends would be significantly different if the surface production of negative ions was also included.

Chapter 9

Influence of bias electrodes on H- beam properties

Having discussed the influence of bias potentials on the source plasma properties (Chapter 8), the effect of both PG and BP biases on the SPIDER beam features will be discussed, focusing on beam uniformity.

9.1 Global beam non-uniformity

During caesium operations in SPIDER[46], several beam diagnostics including the STRIKE calorimeter and visible beam tomography highlighted the presence of a global non-uniformity of the extracted beam density along the entire source height. A correlation between beam and plasma properties downstream of the PG was found, as further investigated in[78].

Figure 9.1 shows the vertical profiles of the accelerated beam current j_{H^-} measured by the STRIKE calorimeter, while varying the bias currents. Only few beamlets are visible since SPIDER was operated with a Plasma Grid Mask; furthermore, these measurements were performed during caesium operation, during which beam extraction took place only from half of the beam area, namely from the beamlet groups placed in front of the right column of RF drivers. The profiles on the left correspond to the outer beamlet group column, whereas the ones on the right to the inner column. A vertical section of the SPIDER ion source is also depicted for the sake of clarity. Each plot shows four beam profiles measured at the same extraction and acceleration potentials, namely V_{ext}=4.6 kV and V_{acc}=44 kV, same RF power per driver P_{RF}=25 kW, and same FF current I_{PG}=1 kA. For both the outer and inner profiles, the I_{BI}=I_{BP}=0 A condition appears to yield a more uniform profile, with the average single beamlet current density being roughly 100 A/m^2. As the bias currents increase, the beam current extracted from the bottom segment decreases until it is almost halved for I_{BI}=190 A, I_{BP}=140 A. A slight decrease can be seen also in the central segments, whereas the extracted current density at the top segment is almost unvaried.

With reference to what was already discussed in Chapter 8, higher bias currents imply higher V_{BI}, V_{BP} polarisation, hence plasma positive ions will less likely reach the extraction region, as the electric field that attracts them towards this area is progressively reduced. In the expansion region of negative ion sources, electron diffusion is strongly limited by the Filter Field, so that positive ion diffusion plays an important role and it receives a further push when an electric field is formed. If the positive ion density in the extraction region is reduced, due to charge conservation the negative ion availability will also decrease, yielding lower extracted

current density. As already mentioned, this effect is non uniform among the segments, as better visible in Figure 9.2. In both cases, the upper segment is almost unaffected by the bias current increase, whereas for the other three the extracted current decreases roughly linearly with the decreasing y position.

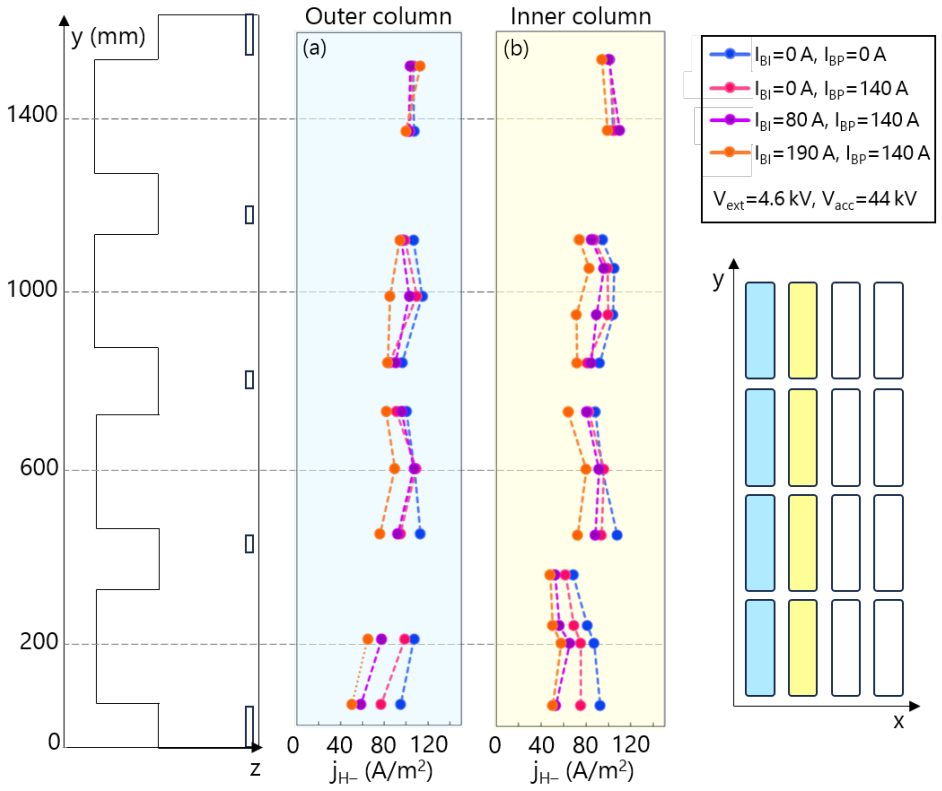

Figure 9.1: Vertical beam profiles accelerated from the outer (a) and inner (b) column of beamlet groups measured by the STRIKE calorimeter. Data courtesy of A. Pimazzoni.

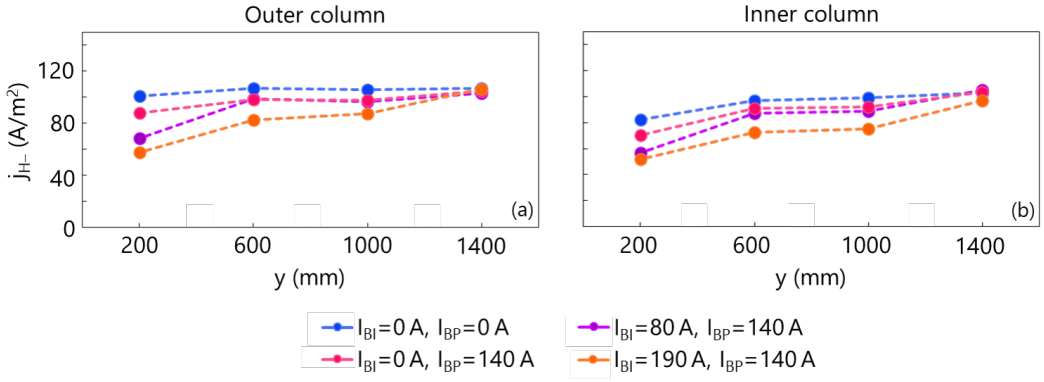

Figure 9.2: Average extracted current per segment accelerated from the outer (a) and inner (b) column of beamlet groups measured by the STRIKE calorimeter. Data courtesy of A. Pimazzoni.

As previously stated, the low bias condition I_{BI}=I_{BP}=0 A appears to yield a uniform extracted beam current density profile. However, having applied a rather low extraction voltage of 4.6 kV, the extracted current was possibly space charge limited in the extraction gap. Indeed, despite not showing current variations while changing the bias currents, the divergence of the

top beamlets was changing (not shown). This implies different beamlet optics in the upper segment, which possibly caused the available negative ions in that region to be only partially extracted, resulting in a vertical non-uniformity. Unfortunately, due to machine limitations it was not possible to operate the ion source with higher acceleration voltage. These results were hence obtained at fixed voltages while allowing full beam transmission through the accelerator (i.e. acceptable beamlet optics), without ensuring the extraction of the maximum negative ion current. To conclude, this topic deserves further experimental investigation.

9.2 Local beam non-uniformity

On top of the global non-uniformity discussed in Section 9.1, in both volume[43] and caesium[46] operations the extracted beam current density profile featured a non-uniformity along the beamlet group scale, with a parabolic profile arising within the beamlet groups.

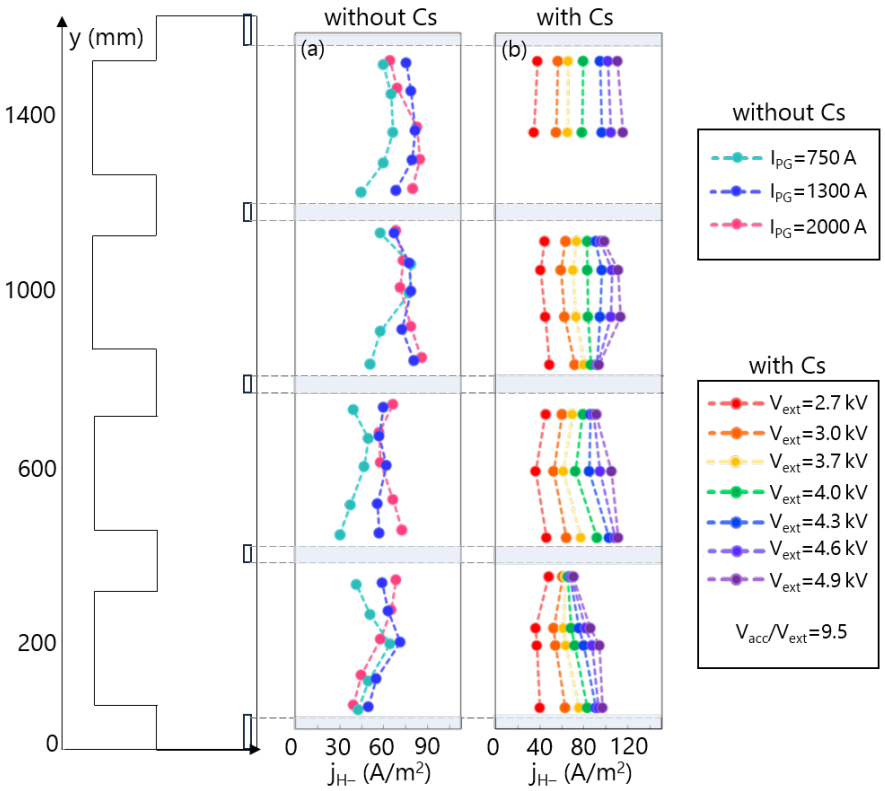

Figure 9.3: Vertical beam profiles accelerated from the inner column of beamlet groups measured by the STRIKE calorimeter without Cs, as a function of the I_{PG} current (a), and with Cs, as a function of the extraction voltage V_{ext} (b). Data courtesy of A. Pimazzoni.

The pattern shown in Figure 9.3 was measured by several beam diagnostics, including the STRIKE calorimeter, beam tomography, and BCM[90]. Also the Balmer and excited neutral caesium lines[77] emissions are consistent with the beam measurements, whereas the embedded electrostatic probes[41] had no suitable space resolution for providing accurate measurements on the beamlet group scale. According to beam profiles measured in pure volume operation, higher values of I_{PG} current (hence stronger FF) enhance the presence of this pattern. As for the profiles measured with caesium evaporation, the same parabolic pattern appears when increasing the V_{ext} voltage, that is when most of the available negative ions are actually extracted from

the source. In particular, at all segments but the top one, the edge beamlet clearly reached a saturation of the negative ion current, even before the maximum extraction voltage of 4.9 kV was reached. Nonetheless, despite the different source parameters between the two cases (with and without Cs) the beam profiles have quite similar shape, as shown in Figure 9.4. As the source operating conditions are so different between the compared cases, the reason for this parabolic non-uniformity is most probably related to the source plasma properties: for instance, a strong magnetic filter field might reduce plasma transport also along the vertical direction. Also the role of the BP electrode shall be better clarified. Nonetheless, it is worth recalling that SPIDER was the only facility operated with a PG masking in both volume and caesium operation. Although the PGM was different for the cases compared in Figure 9.4, still the mask itself might affect the plasma properties at the extraction region, hence the beam profile. For this reason, the influence of the PGM on the extracted beam was investigated by means of the GPPIC code, as described in the following.

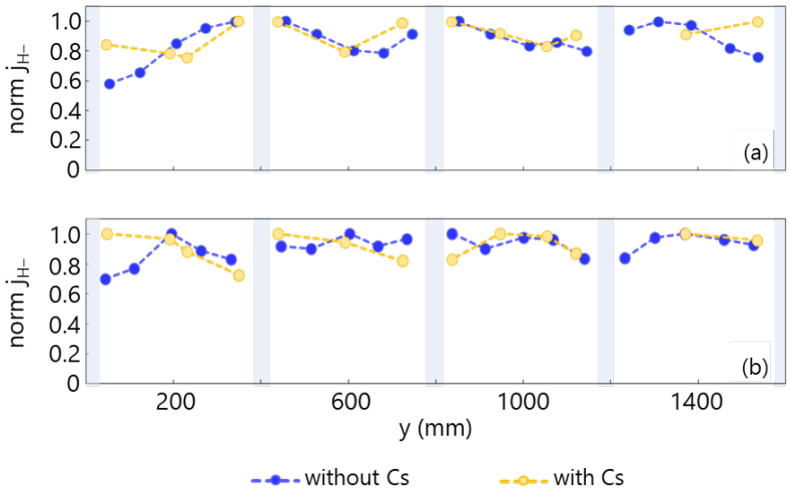

Figure 9.4: Comparison between the profiles measured by the STRIKE calorimeter without (blue) and with (yellow) Cs for the cases in which the local non-uniformity is less (a) and more (b) visible. The current density of each beamlet is normalised with respect to the maximum beamlet current of its beamlet group. Data courtesy of A. Pimazzoni.

9.2.1 Numerical investigation of PG masking effect on beam extraction

The simulation domain is two-dimensional plane of size 120×166.8 mm^2, vertically cutting the source. The mesh is composed of 500×695 squared cells with side dx=dy=0.024 mm. The uniform background gas is composed of H_2 molecules with a $f = 0.3$ fraction of dissociated H atoms. The density scaling factor is $\beta = 1/80$, the simulated density is n_{PIC}=1.25 × 10^{15} m^{-3}, and the simulation timestep is dt=25 ns. As shown in Figure 9.5, periodic boundary conditions are applied at the top and bottom boundaries. The left boundary represents the plasma bulk and is reproduced as a plain metallic wall with potential V_p=25 V or V_p=36 V depending on the simulated case. A plasma flux Γ_{plasma} enters from the left boundary, with assumed composition of 50% e, 20% H^+, 15% H_2^+ and 15% H_3^+. While electrons are injected with thermal velocity, positive ions also have a drifting component of energy E_{drift}=5 eV in such a way to take into account the axial plasma potential drop measured in SPIDER[34].

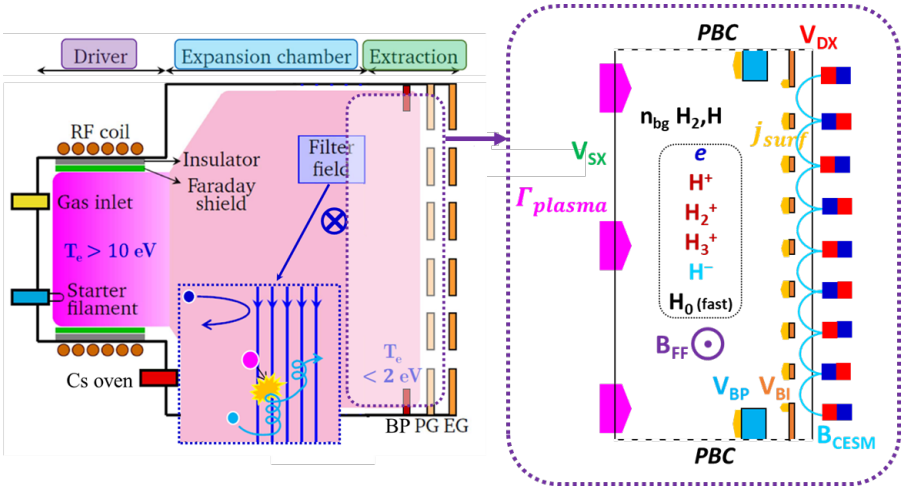

Figure 9.5: On the left: simplified scheme of the SPIDER ion source; on the right: simulation domain used in the GPPIC code.

The extraction potential V_{ext}, scaled according to both the position along the PG-EG and to β, is applied to the right boundary. Both biases V_{BI} and V_{BI} were tuned in such a way to keep the same values for the I_{BP}, I_{BI} currents in all the simulation runs, so that the bias electrodes resulted current-controlled as in the real experimentation. The BP electrode is 10 mm thick as in the actual SPIDER source, whereas the PG electrode is much thinner (2 mm) in order to have more representative shape of the plasma meniscus, since the conical shape of the real PG could not be reproduced.

A negative ion current density j_{surf} is emitted from the BP and PG surfaces, as highlighted in yellow in Figure 9.5. This current density represents the net contribution flowing towards the plasma, and not the actual current produced at the surface. The magnetic FF is perpendicular to the simulation domain, with uniform intensity B_{FF}=1.6 mT and orientation. The multi-cusp field generated by the CESM magnets is also included. As for the previously discussed simulations, most of the typical collision processes of a low temperature H discharge are included. In this case, Coulomb collisions between negative and positive ions were also implemented as they are crucial for beam extraction. The main simulation parameters are summarized in Table 9.1.

Parameter	Description	Value
V_p	Plasma/left boundary potential	25/36 V
V_{ext}	Extraction voltage	10 kV
V_{BI}	PG potential	15/20 V
V_{BP}	BP potential	1520 V
B_{FF}	Filter field intensity	1.6 mT
B_{CESM}	CESM field intensity	max 10 mT
p_{bg}	Background gas pressure	0.3 Pa
β	Density scaling factor	1/80
T_e	Electron temperature	3 eV
T_+	Positive ion temperature	0.8 eV
j_{surf}	Surface emitted H^- current density	400 Am^{-2}

Table 9.1: Main simulation parameters.

In order to assess the effect of the plasma grid masking on beam extraction, two simulations will be compared: the first one with all the 8 apertures left open, the second one with only 3 out of 8 apertures left open. It was necessary to include 8 apertures instead of 16 as in the actual source in such a way to respect the computational constraints, and to guarantee a sufficiently accurate space resolution for eventually detecting the non-uniformity. It was decided to keep the plasma flux entering from the left boundary uniformly distributed along the y direction, so that any in-homogeneity arising in the beam profile can only be attributed to the PG masking; on the other hand, if the beam profile was found uniform, the parabolic pattern seen in the previous section is most likely to be caused by non uniform source plasma properties in the expansion region.

Figure 9.6 shows the two-dimensional maps of electron density n_e, positive ion density n_+, and negative ion density n_{H^-} for the cases without and with PG masking, as well as the negative ion flux topology. The most evident difference is the much higher negative ion availability for the PGM case, which is due to the fact that the mask itself can act as a converter, producing negative ions. For these simulations, the PGM was assumed to have the same negative ion yield as the PG electrode itself, which is reasonable since the PG electrode and mask are in electrical contact and reach the same temperature, thus the caesium coverage is equally efficient. Additionally, the beam extraction area is strongly reduced, hence less negative ions will be able to leave the source volume.

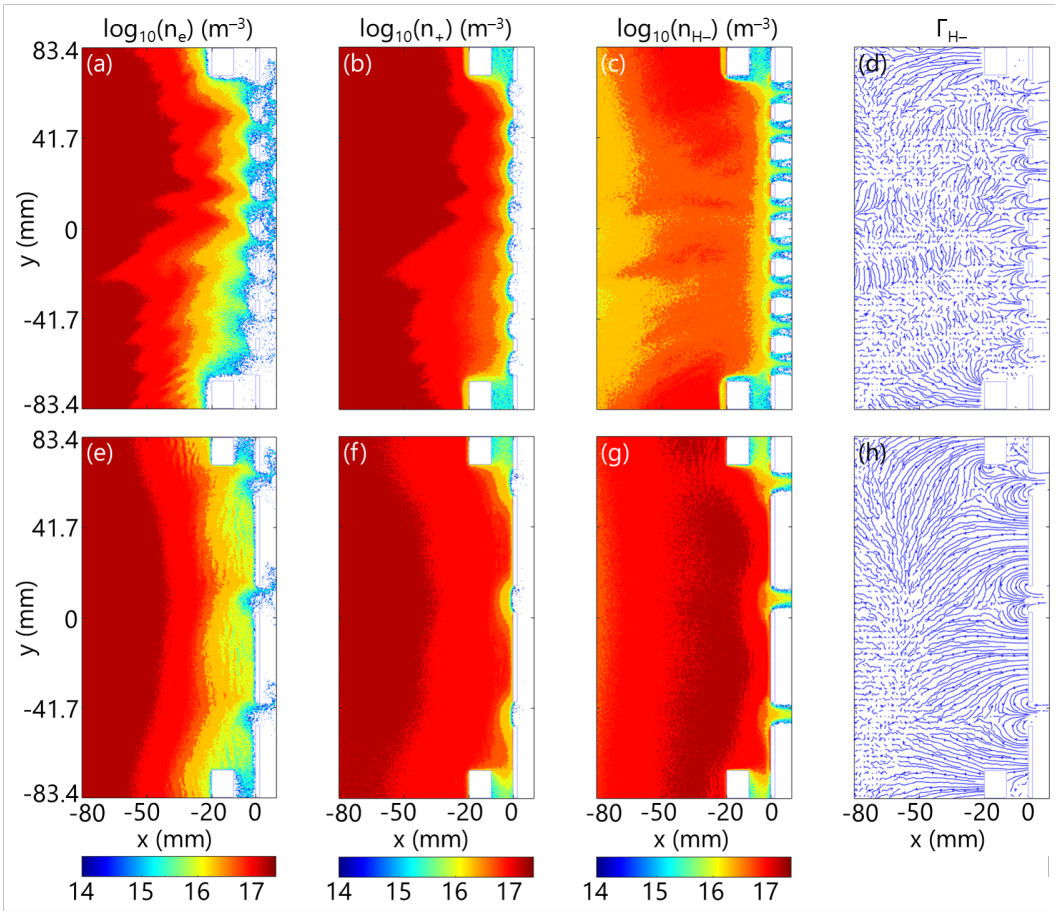

Figure 9.6: From left to right, electron density, positive ion density, negative ion density, and negative ion flux for the simulation without (a,b,c,d) and with (d,e,f,g) PG mask.

The higher negative ion density causes a depletion of the electron density in front of the PG electrode, as can be seen by comparing the n_e maps. The expected vertical drifts are more significant for the case without PGM: this can be explained in terms of plasma potential gradients. In fact, the plasma potential at the left boundary is higher in the case without masking, possibly because the extraction field extends further in the source volume due to the higher number of apertures. With higher plasma potential gradient along the x direction, the electric field is also higher, causing stronger $\vec{E} \times \vec{B}$ drift and, consequently, a more evident top-bottom asymmetry within the beamlet group. With the vertical drifts being reduced in the PGM case, also the co-extracted electron current is more evenly distributed.

As expected, the extracted beamlet current density is also larger for the PGM case, as shown in Figure 9.7. Nonetheless, the vertical profile of the current density extracted from the simulated beamlet group is uniform along the y direction, and no significant variations are visible in the PGM case. As both cases have comparable positive ion density n^+ at the center of the plasma domain, they can be fairly compared. In conclusion, according to these simulations, the PG masking is not causing the parabolic pattern measured in the SPIDER beam. This qualitative result appears valid despite the approximations required for the PIC algorithm, mainly the reduction of the problem to two dimensions and the density scaling factor to reduce the computational cost.

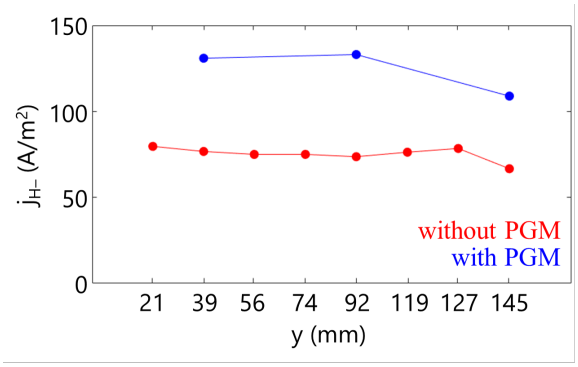

Figure 9.7: Extracted current density for the case with masked apertures (curve with three points, in blue) and without masked apertures (eight points, in red) as a function of the vertical position.

9.2.2 Horizontal uniformity within the beamlet groups

Some experimental evidence of a parabolic pattern also along the horizontal direction was derived from STRIKE measurements. Figure 9.8 shows the ratio of the negative ion current extracted from the two external beamlets of a row, B24 and B25, with respect to the central one belonging to another beamlet group but placed at the same vertical height, B22, as a function of the potential difference between the two bias electrodes, $V_{\mathrm{BI}} - V_{\mathrm{BP}}$. As it is clearly visible, the current extracted from beamlets B25 and B24 is different independently of $V_{\mathrm{BI}} - V_{\mathrm{BP}}$: this is possibly due to the measurement technique, which is based on integrating the single-beamlet gaussian on the diagnostic calorimeter STRIKE. Unfortunately, due to the incorrect compensation of the horizontal beamlet deflection, the B25 beamlet is partially masked by a kerb on the calorimeter, and a fraction of its power might be lost. One should note also that this lost fraction mostly depends on the rigidity of the ion beam, i.e. on its energy, and only at a minor level on its perveance, so that the presented result is anyway correct.

Due to the PGM structure it was not possible to compare three beamlets belonging to the same row; however, the ratio between the two bottom beamlets highlighted in orange was found to be very close to 1, thus one can assume that the current extracted from the two central beamlets is comparable. In addition, according to source measurements[77] and with reference

to the beam area scheme in Figure 9.8, the electron density is expected to increase when moving from the right towards the left column of beamlet groups, hence worse performances in terms of beam extraction shall be expected in that region. As a consequence, this non-uniformity might be slightly underestimated.

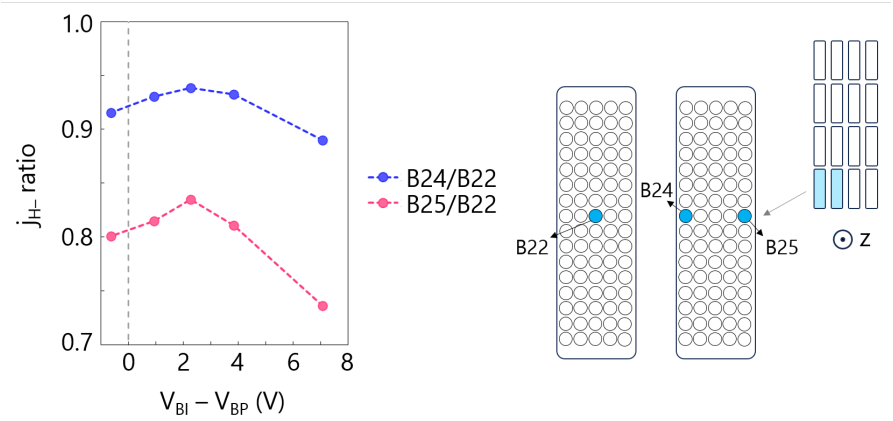

Figure 9.8: On the left: extracted beamlet current ratio measured by STRIKE as a function of the potential difference between PG and BP potential; on the right: beamlet arrangement on the extraction area. Data courtesy of A. Pimazzoni.

Given the ratios shown in Figure 9.8, it appears that the extracted current from the lateral beamlets is always smaller than the central one, yielding a parabolic pattern also along the horizontal direction. Both ratios feature a quite clearly defined maximum for $V_{BI} - V_{BP} \approx 2\,V$, implying that the horizontal uniformity of the beam can be improved by properly tuning the bias electrodes.

Chapter summary

The effect of the polarisation of PG and BP electrodes on the extracted beam features along both the vertical and horizontal direction has been discussed. It was possible to investigate the beam profiles with sufficient spatial resolution thanks to the operation of a Plasma Grid Mask in the accelerator, which was closing most of the beamlet apertures. The onset of a global non-uniformity with increasing bias potentials was confirmed by STRIKE measurements, shown in this work, as well as by beam tomography. A local non-uniformity instead was found to be triggered by increasing the magnetic FF in the ion source, in pure volume operation. The same pattern was seen in caesium operation by increasing the extraction potential V_{ext}; however, the beam profiles measured with and without caesium evaporation appear to be very similar (after being normalized), despite the different operating conditions. A numerical investigation regarding the influence of the PGM as a possible cause for the local non-uniformity is presented. On the basis of the simulation results, it appears that closing the beamlet apertures did not affect the extracted beam features. Finally, some experimental evidence of a parabolic structure of the beam profile also along the horizontal direction is presented.

Chapter 10

Permanent magnets in negative ion sources

The application of multi-cusp magnetic fields in fusion relevant negative ion sources will be discussed in this chapter. Indeed, permanent magnets are exploited in both filament[91] and RF[46],[78],[92] based sources for different applications, including the increase of the ionisation rate, the limitation of plasma losses at the walls, and the reduction of the co-extracted electron fraction[87].

10.1 Multi-cusp magnetic confinement

The *cusp* field topology can be obtained by arranging permanent magnets on uniformly spaced rows, with alternate magnetization orientation, as shown in Figure 10.1. Thanks to this configuration, for a sufficiently strong field plasma particles are more likely to be lost at the walls where the magnetic field lines are perpendicular with respect to the surface, whereas they will mostly bounce back towards the plasma volume when they approach the regions where the field lines are parallel to the surfaces.

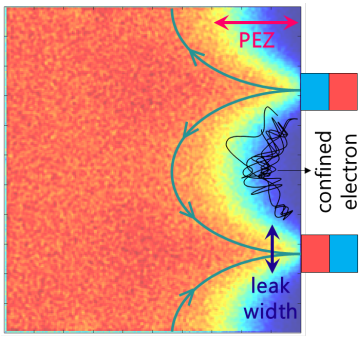

Figure 10.1: Scheme of multi-cusp confinement: the leak width definition, as well as a sample electron trajectory within the cusp field are included.

The overall plasma loss fraction f at the walls is reduced, and can be defined as the ratio between the *leak width*, w, and the distance between the magnets, d_{mag}. The leak width can be

thought of as the width of the plasma loss cone and, according to[74], can be estimated as:

$$w_{\mathrm{H}} \approx 4(\rho_{ce}\rho_{ci})^{0.5} = 4\frac{(m_e m_i)^{0.5}(\mathrm{T}_e \mathrm{T}_i)^{0.25}}{|B|} \tag{10.1}$$

where ρ_{cx}, m_x and T_x are the Larmor radius, mass and temperature of the x-th plasma species, and $|B|$ is the magnetic field intensity at the magnets' surface. Eq.10.1 can be modified by introducing a dependence on the mean free paths λ_x of the x-th plasma species in order to include the effect of collisions[93], yielding:

$$w_{\mathrm{KM}} \approx \frac{2}{\pi}(\rho_{ce}\rho_{ci})^{0.5}\frac{d_{\mathrm{mag}}}{(\lambda_e\lambda_i)^{0.5}} = \frac{w_{\mathrm{H}}}{2\pi}\frac{d_{\mathrm{mag}}}{(\lambda_e\lambda_i)^{0.5}} \tag{10.2}$$

As plasma can freely diffuse only in correspondence of the permanent magnets, a region without plasma called Plasma Exclusion Zone (PEZ) is formed. The characteristic dimension of this region was estimated to be $\approx 1.5 d_{\mathrm{mag}}$[94].

10.2 Cusp confinement in RF negative ion sources

In RF-based negative ion sources, the magnetic Filter Field strongly reduces the electron temperature in the expansion region, yielding values T_e <2 eV with a plasma potential of the order of 20 V. Furthermore, the source plasma can be strongly electronegative due to the surface production of negative ions[95]. These conditions are significantly different from the ones usually assumed for the investigation of the cusp-field confinement efficiency. For this reason, the dependencies of both the PEZ size and the leak width on magnetic field intensity and plasma potential were investigated with the GPPIC code[96], as described in the following.

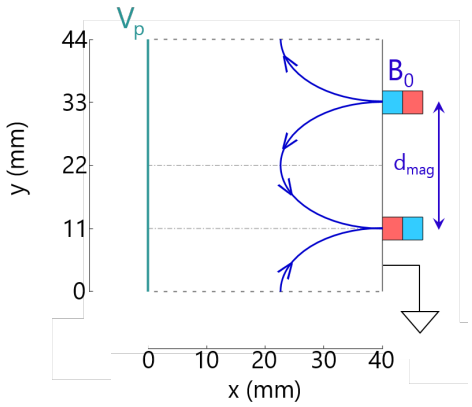

Figure 10.2: Representation of the simulation domain.

To this purpose, an hydrogen plasma discharge in a two dimensional domain (see Figure 10.2) of 40×44 mm^2 divided in squared cells of size $dx = 0.2$ mm is considered, with the left boundary representing the plasma bulk, and the right boundary being a plain, grounded metallic wall. Periodic conditions are imposed on the bottom and top boundaries. The left boundary is positively biased at $V = V_p$ with respect to ground, with a constant plasma flux entering in the domain uniformly distributed along the y direction:

$$\Gamma_i = \frac{\alpha}{4} n_{\mathrm{PIC}} \sqrt{\frac{8q\mathrm{T}_+}{\pi m_i}} \tag{10.3}$$

where q is the elementary charge, i labels the positive ion species (H^+, $H_2{}^+$ or $H_3{}^+$), T_+ is the positive ion temperature, $\alpha = 0.4$ for protons and $\alpha = 0.3$ for the heavier species. This positive ion composition is an educated guess resulting in an effective positive ion mass $m_{\text{eff}} = 1.9 m_{\text{H}}$. The electron and negative ion fluxes are defined as:

$$\begin{aligned} \Gamma_e &= \frac{\alpha}{4} n_{\text{PIC}} \sqrt{\frac{8qT_e}{\pi m_e}} \\ \Gamma_{H^-} &= \frac{1-\alpha}{4} n_{\text{PIC}} \sqrt{\frac{8qT_-}{\pi m_{H^-}}} \end{aligned} \tag{10.4}$$

with $\alpha = 0.9$. The dissociation fraction of the H_2 background gas is $f = 0.3$. Other simulation parameters are listed in Table 10.1.

The magnetic cusp topology is obtained thanks to two permanent magnets with opposite orientation placed at the right boundary, as shown in Figure 10.2. The magnetic field components are analytically described as[62]:

$$\begin{aligned} B_x(x,y) &= -B_0 \exp\left[\frac{\pi(x-x_0)}{d_{\text{mag}}}\right] \cos\left(\frac{\pi y}{d_{\text{mag}}}\right) \\ B_y(x,y) &= \ B_0 \exp\left[\frac{\pi(x-x_0)}{d_{\text{mag}}}\right] \sin\left(\frac{\pi y}{d_{\text{mag}}}\right) \end{aligned} \tag{10.5}$$

with $x_0 = 0.04\,\text{m}$ B_0 the cusp field intensity at the right wall and d_{mag} the distance between the magnets, which is equal to 22 mm.

Parameter	Description	Value	Parameter	Description	Value
β	density scaling factor	0.05	p_{bg}	background gas pressure	0.3 Pa
dx	cell size	0.2 mm	δ	dissociation fraction	0.3
dt	timestep	0.15 ns	T_e	electron temperature	2 eV
V_{right}	right wall potential	0 V	T_+	positive ion temperature	0.8 eV
d_{mag}	step between magnets	22 mm	T_-	negative ion temperature	1.5 eV

Table 10.1: Main simulation parameters for the numerical investigation of cusp confinement.

Two-dimensional maps of electron and positive ion densities, plasma potential, and electron temperature obtained with $B_0 = 120\,\text{mT}$ are depicted in Figure 10.3. Th cusp structure is clearly visible in the density maps. The electron temperature in between the magnets is reduced in the proximity of the right surface since, at this location, plasma electrons are diffusing perpendicularly with respect to the magnetic field lines. The horizontal spatial profiles of the plasma properties are represented in Figure 10.4. It is worth to mention that, in this case, the magnetic field intensity in the proximity of the left wall is of the order of a few mT, thus the injected plasma flux is also magnetized.

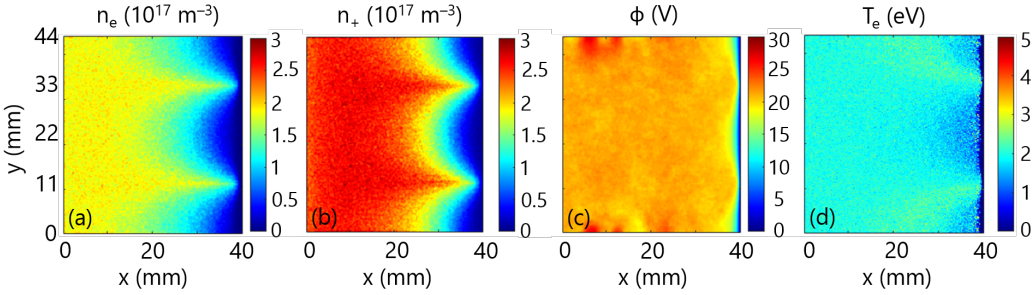

Figure 10.3: Simulated electron density n_e (a), positive ion density n_+ (b), plasma potential ϕ (c) and electron temperature T_e (d) for B_0=120 mT, $V_p = 21\,\text{V}$, and $T_e = 2\,\text{eV}$.

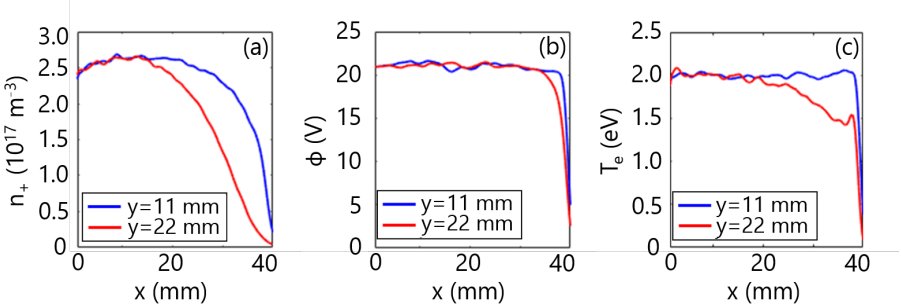

Figure 10.4: Positive ion density (a), plasma potential (b) and electron temperature (c) horizontal profiles taken in between the magnets (y =22 mm, in red) and in correspondence of the bottom magnets (y =11 mm, in blue) for the same case shown in Figure 10.3.

10.2.1 Influence of field intensity on plasma properties

The loss fraction f can be evaluated as the positive ion current flowing out from the right boundary, normalised to the unmagnetized case:

$$f = \frac{n_{+,0}}{n_+}\frac{I_+}{I_{+,0}} = \frac{n_{+,0}}{n_+}\frac{\int_0^{y_{\max}} j_+(y)|_{x=x_{\max}} dy}{\int_0^{y_{\max}} j_{+,0}(y)|_{x=x_{\max}} dy} \tag{10.6}$$

where n_+ is the bulk positive ion density and the subscript 0 labels the unmagnetized plasma parameters. The PEZ is defined as the distance from the right wall at which the positive ion density is equal to one third of its bulk value. Figure 10.5 shows the two-dimensional distribution of the positive ion density obtained while varying B_0. As expected, plasma losses are more localised for stronger fields and, at the same time, the bulk plasma density increases. The electronegativity $\alpha = n_{H^-}/n_e$ in the proximity of the right wall is approximately equal to $\alpha = 0.2$.

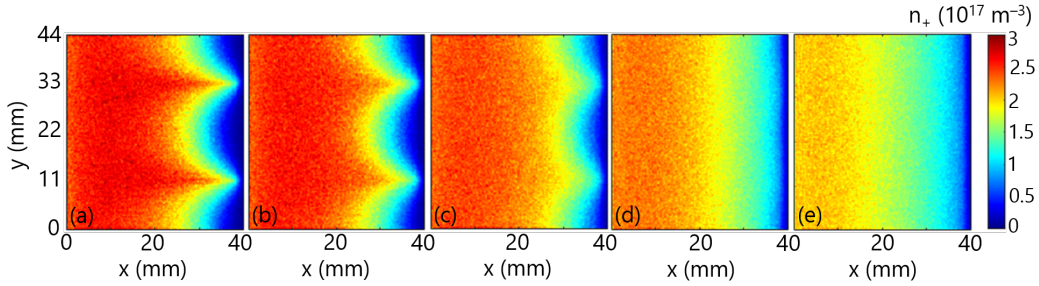

Figure 10.5: Two-dimensional maps of the positive ion density n_+ with different values of magnetic field intensity: (a) B_0 = 120 mT; (b) B_0 = 60 mT; (c) B_0 = 10 mT; (d) B_0 = 5 mT; (d) B_0 = 0 mT. The plasma potential is set at V_p = 21 V.

Both the loss fraction f and the Plasma Exclusion Zone (PEZ) are estimated from the PIC results while varying the magnetic field intensity at the right wall B_0. In particular, three cases with different boundary conditions are considered:

- V_p = 21 V and T_e = 2 eV;
- $V_p \approx V_f$ and T_e = 2 eV, with V_f being the floating potential, thus the flux at the right wall is ambipolar (e.g. the net current at the grounded boundary is equal to zero);
- $V_p \approx V_f$ and T_e = 2 eV, with halved effective mass. The obtained loss fraction f and the normalised PEZ are shown in Figure 10.6, together with the theoretical estimation $f_H = w_H/d_{mag}$. All the simulated curves are normalised to the unmagnetized case.

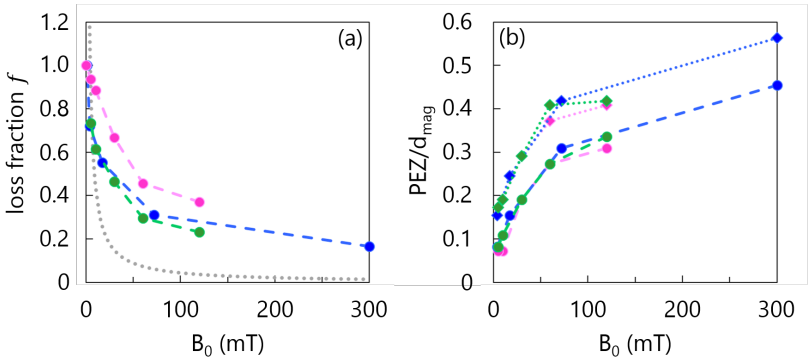

Figure 10.6: Loss fraction f (a) and PEZ (b) as a function of the magnetic field intensity B_0 for the non-ambipolar and ambipolar cases in magenta and green respectively, whereas blue points are obtained in ambipolar conditions without molecular ions. A theoretical estimations of the loss fraction obtained from w_{H} is also shown in (a) by the grey line. The circle and diamond points in (b) are obtained with $n/n_{\mathrm{bulk}} = 0.3$ and $n/n_{\mathrm{bulk}} = 0.5$ respectively. For the non-ambipolar case, $V_p = 21\,\mathrm{V}$.

The simulated loss fraction is roughly proportional to $B_0^{-1/3}$ rather than to B_0^{-1} as for the theoretical case, hence the PIC code yields larger f values for stronger field intensities. This result is still valid if w_{KM} is considered in place of w_{H}, although it is not shown. According to Figure 10.6a, the loss fraction f is slightly larger in the non-ambipolar case (magenta), therefore the $V_p > V_f$ condition worsens the plasma confinement; by comparing the blue and green curves, one can infer that being the $V_p \approx V_f$ condition verified, lowering the effective mass from ≈ 2 (green) to 1 (blue) does not affect the loss fraction evaluation. Figure 10.6b shows that the PEZ never reaches the $1.5 d_{mag}$ prediction: this is still verified if a stricter criterion is chosen for the PEZ definition, e.g. if the density threshold limit is increased up to 50%. Finally, it is worth to point out that both f and PEZ$/d_{mag}$ tend to reach a stationary value for increasing magnetic field intensities.

10.2.2 Influence of the bulk plasma potential

The plasma potential V_p was found to strongly affect the plasma properties in the cusp region, as can be seen from Figure 10.7: reducing V_p has a similar effect as increasing the field intensity, yielding more localised losses and reducing the loss fraction f, as shown in Figure 10.8. This effect was studied in two different cases, namely with B_0=5 mT and T_e=2 eV, aiming at reproducing the plasma properties at the extraction region, and with B_0=60 mT and T_e=2 eV, representing the plasma close to the lateral walls of the expansion chamber.

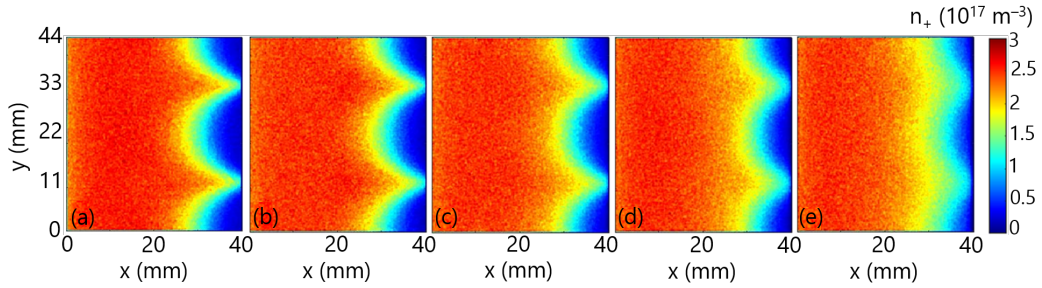

Figure 10.7: Two-dimensional maps of the positive ion density n_+ with different values of the left wall potential: (a) $V_p = -1\,\mathrm{V}$; (b) $V_p = 0\,\mathrm{V}$; (c) $V_p = 1\,\mathrm{V}$; (d) $V_p = 2\,\mathrm{V}$; (e) $V_p = 4\,\mathrm{V}$. All cases with $B_0 = 120\,\mathrm{mT}$ and $T_e = 2\,\mathrm{eV}$. The floating potential is approximately equal to 7.5 V.

In order to verify that the simulation parameters are not significantly affecting the results, one of the cases shown in Figure 10.8 was repeated with reduced cell size and increased $\beta = 0.1$, as depicted by the yellow points. Both the f and the PEZ estimations are in agreement with the results calculated with the simulation parameters from Table 10.1.

For higher values of V_p, plasma electrons are repelled by the sheath potential: negative charge builds up within the cusp structure, allowing positive ions to travel freely towards the surface; as a consequence, the loss fraction increases. For high B_0, the condition $V_p > V_f$ is always verified and the confinement is significantly improved with respect to the low B_0 case, as shown by the blue points in 10.7a. At the same time, the PEZ appears to be approximately equal to $0.25 d_{mag}$ independently of V_p. On the other hand, in the low B_0 case (magenta), the estimated loss fraction strongly decreases for lower V_p values, as shown in Figure 10.8a: in this condition, the potential decay is less steep and the confined electrons are able to reach the right wall despite their low temperature; this effect is more and more visible for decreasing V_p values, as electrons are lost from field lines extending deeper in the plasma bulk. Accordingly, the PEZ dimension increases for lower V_p values, resulting in a more effective confinement since the positive ions can no longer reach the right wall due to the reduction of the electron space charge.

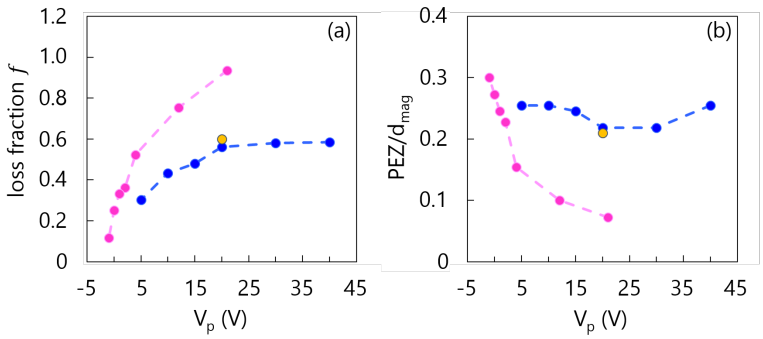

Figure 10.8: Loss fraction f (a) and normalised PEZ (b) as a function of V_p for $B_0 = 5\,\mathrm{mT}$ and $B_0 = 60\,\mathrm{mT}$ in magenta and blue respectively, with $T_e = 2\,\mathrm{eV}$. The yellow points represent a simulation performed with a reduced cell size $dx/3$ and $\beta = 0.1$.

Still regarding the low B_0 case, Figure 10.9a shows the total current $I_{\mathrm{tot}} = I_e + I_{H^-} - I_+$ collected at the right wall. The $I_{\mathrm{tot}} \approx 0\,\mathrm{A}$ condition is reached for $V_p = V_f \approx 7.5\,\mathrm{V}$. When the plasma potential is more positive than the floating potential, the electron current I_e at the right wall is strongly reduced, whereas the positive ion current increases, as shown in Figure 10.9b. As previously mentioned, this causes a worsening of the confinement efficiency.

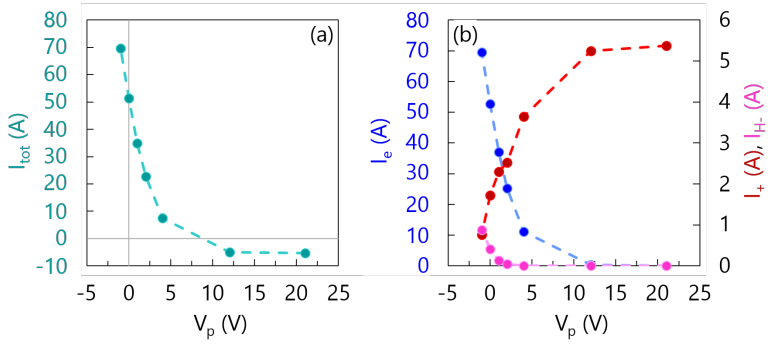

Figure 10.9: Total current I_{tot} (a), electron I_e, positive ion I_+ and negative ion I_{H^-} currents (b) at the right wall as a function of the left wall potential V_p, with $B_0 = 5$ mT and $T_e = 2$ eV.

10.2.3 Cusp confinement within the RF drivers

The GPPIC code was applied o investigate the effect of the RF-induced EM field on the magnetic cusp configuration in hydrogen plasma discharges. In this case, the simulation domain is a rectangle of size 144 × 72mm^2, lying on the $\langle x, y \rangle$ plane. The mesh is given by 576 × 288 squared cells of size dx=0.25 mm, and the timestep is dt=7.5 × 10^{-11} s. The left and right walls are represented as grounded, plain metallic walls, whereas periodic boundary conditions are assumed on the top and bottom walls. The density scaling factor is $\beta = 0.01$. The domain is initially pre-populated with the following composition: e-45%, H^+-20%, H_2^+-15%, H_3^+-15%, and H^--5%. These fractions are not fixed as the plasma evolves self-consistently thanks to the collision processes. Differently from the simulations shown in the previous section, the number of positive ions is kept constant by re-introducing an electron-ion pair each time a plasma ion is lost at the walls. The electron temperature T_e is kept constant at 6 eV by a thermostat. As for the magnetic cusp field, the permanent magnets are located at both the left and right walls, with B_0=45 mT and d_{mag}=36 mm.

As the simulation timestep is much smaller than the RF period, the induced EM fields were introduced first as constant quantities, and as a second step while considering the sinusoidal dependence on time of the field intensity. The "static" approximation though holds for $t \leq T_{RF}$; in this case, the induced E field reads:

$$E_{ind}(x) = E_0 \frac{x - 0.144\,\text{m}}{0.072\,\text{m}} \tag{10.7}$$

and is oriented either along y or z, with E_0=500 V; the latter value was chosen in such a way to keep the same ratio between the potential difference across a cusp ($E \cdot d_{mag}$) and the plasma potential of the real case, namely:

	SPIDER	GPPIC
E_{ind} (V/m)	1500	500
d (mm)	70	36
ϕ (V)	45	9
$E_{ind} \cdot d/\phi$	2.3	2

Table 10.2: Real (first column) and simulated (second column) values of induced electric field, distance between the magnets, plasma potential.

The five cases shown in Figure 10.10 were analysed, namely:

- Case 1: $\vec{E}_{\text{ind}} = E_{\text{ind}}\hat{y}$, no cusp field;
- Case 2: $\vec{E}_{\text{ind}} = E_{\text{ind}}\hat{z}$, no cusp field;
- Case 3: no induced E field, cusp field;
- Case 4: $\vec{E}_{\text{ind}} = E_{\text{ind}}\hat{y}$, cusp field;
- Case 5: $\vec{E}_{\text{ind}} = E_{\text{ind}}\hat{z}$, cusp field;

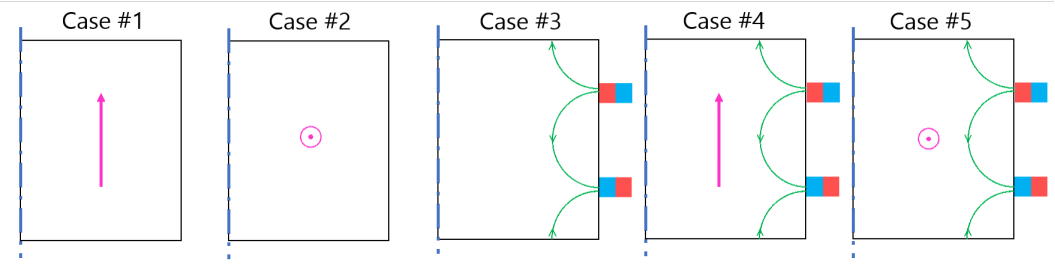

Figure 10.10: Cases with constant induced E field (in magenta); cusp field is shown by the green arrows. The domain is symmetric with respect to the dash-dot blue line, although E changes sign.

Static induced field

Table 10.3 shows the positive ion loss at the walls normalised to the case without any cusp nor RF-induced field, for which $\Gamma_{0,+}$=8.6 × 10^{20} s^{-1}. The values were averaged over the last 500 iterations before reaching $0.2T_{\text{RF}}$.

Case	#1	#2	#3	#4	#5
$\Gamma_+/\Gamma_{0,+}$	0.86	0.60	0.27	0.31	0.58

Table 10.3: Ion flux at the lateral wall normalised to the case without any E or B field.

The presence of an induced electric field along the y direction (Case #2) causes the electrons to be accelerated along the direction parallel to the walls, as shown in Figure 10.11. As the induced E field changes sign along the x axis, the electrons will move either upwards or downwards according to their position along the horizontal axis. As the electrons are accelerated, they energy increases thus T_e and, consequently, ϕ are much higher than in the reference case. A similar reasoning holds also for Case #3, although in this case the electrons are accelerated along the z direction. The loss at the lateral surfaces is reduced possibly because the flow in either the y or z direction prevents the electrons to move along the x axis.

When included, the cusp field alone reduces the ion loss of roughly a factor 3 (Table 10.3); a comparable result is found for Case #5, shown in Figure 10.12, that is when the cusp field is coupled with $\vec{E} \parallel \hat{y}$. Finally, when $\vec{E} \parallel \hat{z}$, the cusp confinement is worsened and the ion loss ratio grows back to the same value obtained for Case #3, that is without magnetic cusp confinement.

The average values at the domain center of plasma density, electron temperature and plasma potential are listed in Table 10.4. By comparing Cases #1 and #4, one can see how the plasma potential is strongly decreased by the presence of the cusp field, whilst leaving all the other parameters almost unvaried.

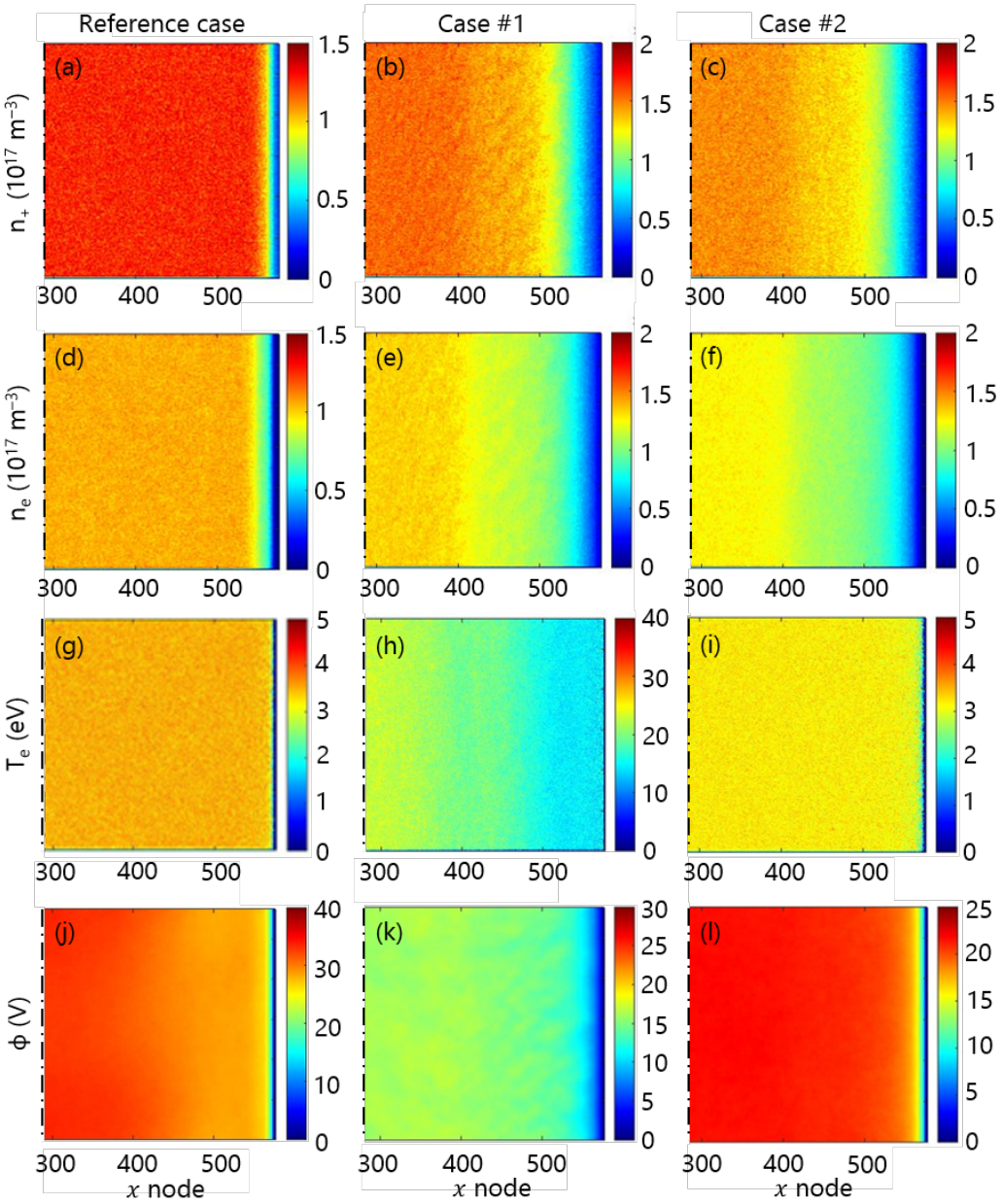

Figure 10.11: Positive ion density n_+, electron density n_e, electron temperature T_e and plasma potential ϕ for the reference case (a,d,g,j), case #1 (b,e,h,k), and case #2 (c,f,i,l). The maps are symmetric with respect to the dash-dot black line.

Case	Ref	#1	#2	#3	#4	#5
n_e (10^{17} m^{-3})	1.05	1.33	1.25	0.97	0.97	1.02
n_+ (10^{17} m^{-3})	1.25	1.54	1.47	1.2	1.2	1.28
T_e (eV)	3.5	22.6	3.2	3.0	4.2	6.8
ϕ (V)	32.6	16.3	21.6	13.9	12.8	53.6

Table 10.4: Average plasma properties at the domain center.

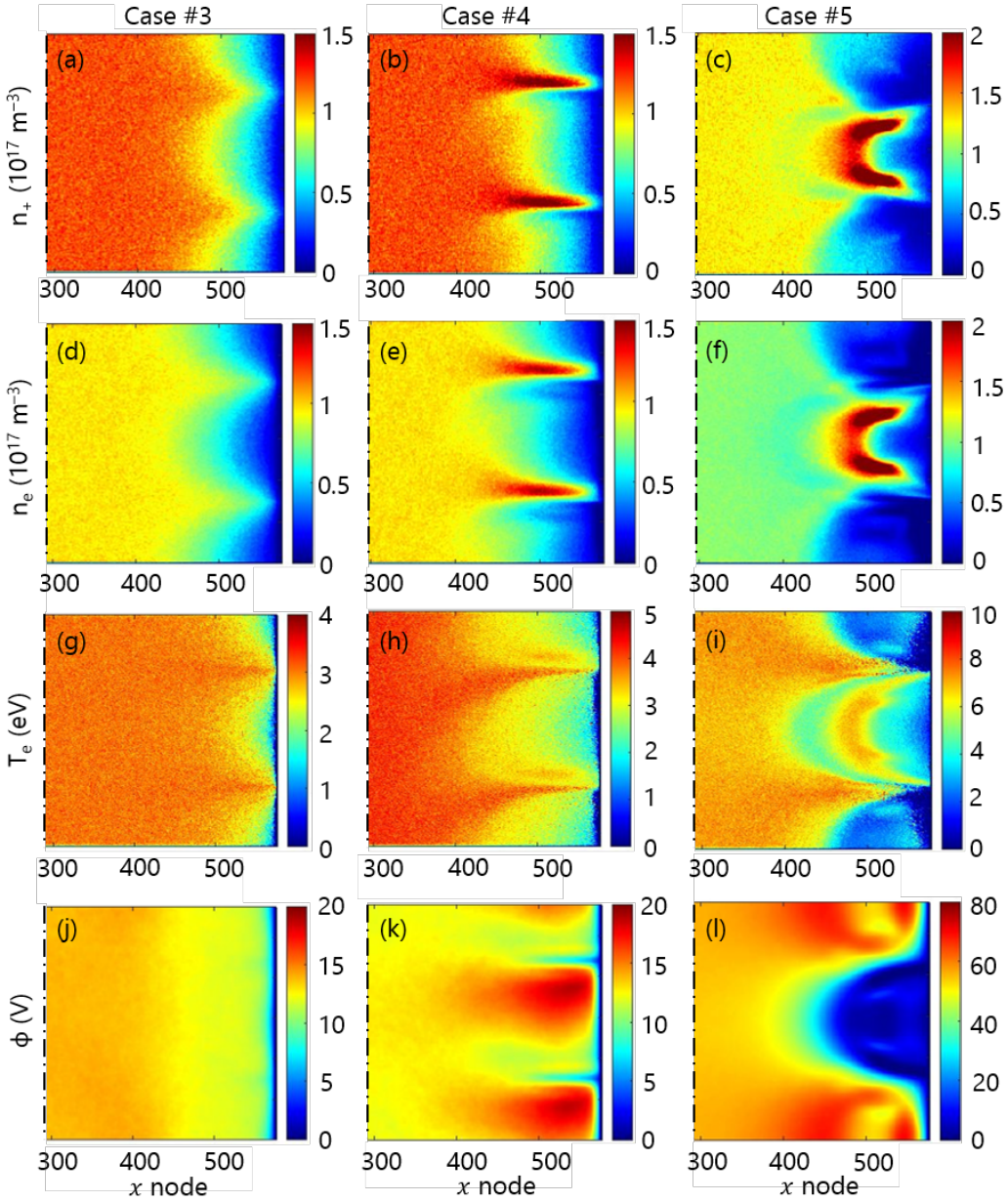

Figure 10.12: Positive ion density n_+, electron density n_e, electron temperature T_e and plasma potential ϕ for case #3 (a,d,g,j), case #4 (b,e,h,k), and case #5 (c,f,i,l). The maps are symmetric with respect to the dash-dot black line.

Time varying induced field

Time-dependent $\vec{E}$ and $\vec{E}$ field induced by the RF coupling were also included in the simulation. On the basis of the results obtained in the case of static field, the electric field $\vec{E}$ was assumed to be oriented along the y direction, thus it can be described as:

$$\begin{aligned} E_{\text{ind}}(x,t) &= E_{\text{max}}(x)\sin(2\pi f_{\text{RF}} t) \\ E_{\text{max}}(x) &= E_0 \frac{x - 0.144\,\text{m}}{0.072\,\text{m}} \end{aligned} \tag{10.8}$$

with f_{RF}=1 MHz and E_0=500 V/m. The magnetic field instead is uniform in space and it is parallel to the z direction, namely:

$$B_{ind}(t) = B_0 \cos(2\pi f_{RF} t) \tag{10.9}$$

where the B_0 value is obtained by applying the Faraday-law as follows:

$$\begin{aligned} \oint_\gamma \vec{E} \cdot \hat{t}\, dl &= -\frac{d}{dt} \int_A \vec{B} \cdot \hat{n}\, dS \\ E_{max}(x) \sin(2\pi f_{RF} t)\left(2h + 4x'\right) &= -\frac{d}{dt}\left[B_0 A(x') \sin(2\pi f_{RF} t + 90°)\right] \end{aligned} \tag{10.10}$$

with reference to Figure 10.13 and $A(x') = 2x'h$.

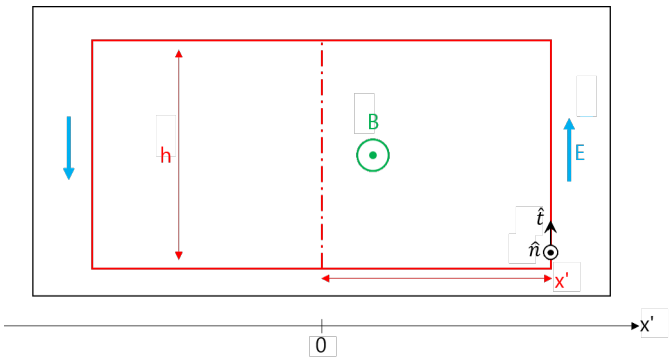

Figure 10.13: Definition of time-dependent induced EM field: contour path and area for the Faraday-Neumann law.

With respect to the x' coordinate, one can obtain B_0 as:

$$\begin{aligned} E_{max}(x') \sin(2\pi f_{RF} t) &= -B_0 \frac{2x'h}{2h + 4x'} \frac{d}{dt} \left[\sin(2\pi f_{RF} t + 90°)\right] \\ &= -2\pi f_{RF} B_0 \frac{2x'h}{2h + 4x'} \sin(2\pi f_{RF} t + 180°) \\ &= -2\pi f_{RF} B_0 \frac{2x'h}{2h + 4x'} \sin(2\pi f_{RF} t) \\ B_0 &= \frac{E_{max}(x)}{2\pi f_{RF}} \frac{2h + 4x'}{2x'h} \end{aligned} \tag{10.11}$$

that in this case yields B_0=1.2 mT. Figures 10.14 and 10.15 show the two-dimensional maps of positive ion density n_+, electron density n_e and plasma potential ϕ at four time instants over the RF period, namely at $t/T_{RF} = 0$, $t/T_{RF} = 0.25$, $t/T_{RF} = 0.5$, and $t/T_{RF} = 0.75$. In the first quarter of the RF period, the induced electric field is pointing upwards along the y direction, and the magnetic field intensity increases up to its maximum value B_0. The electric fields accelerates the magnetized electrons within the cusp, either pushing them towards the wall or confining them if $\vec{E}$ is anti-parallel or parallel to the v_y component of he electrons respectively. The positive ion density is affected by the variation of the electron density, although their motion is slower due to their larger mass.

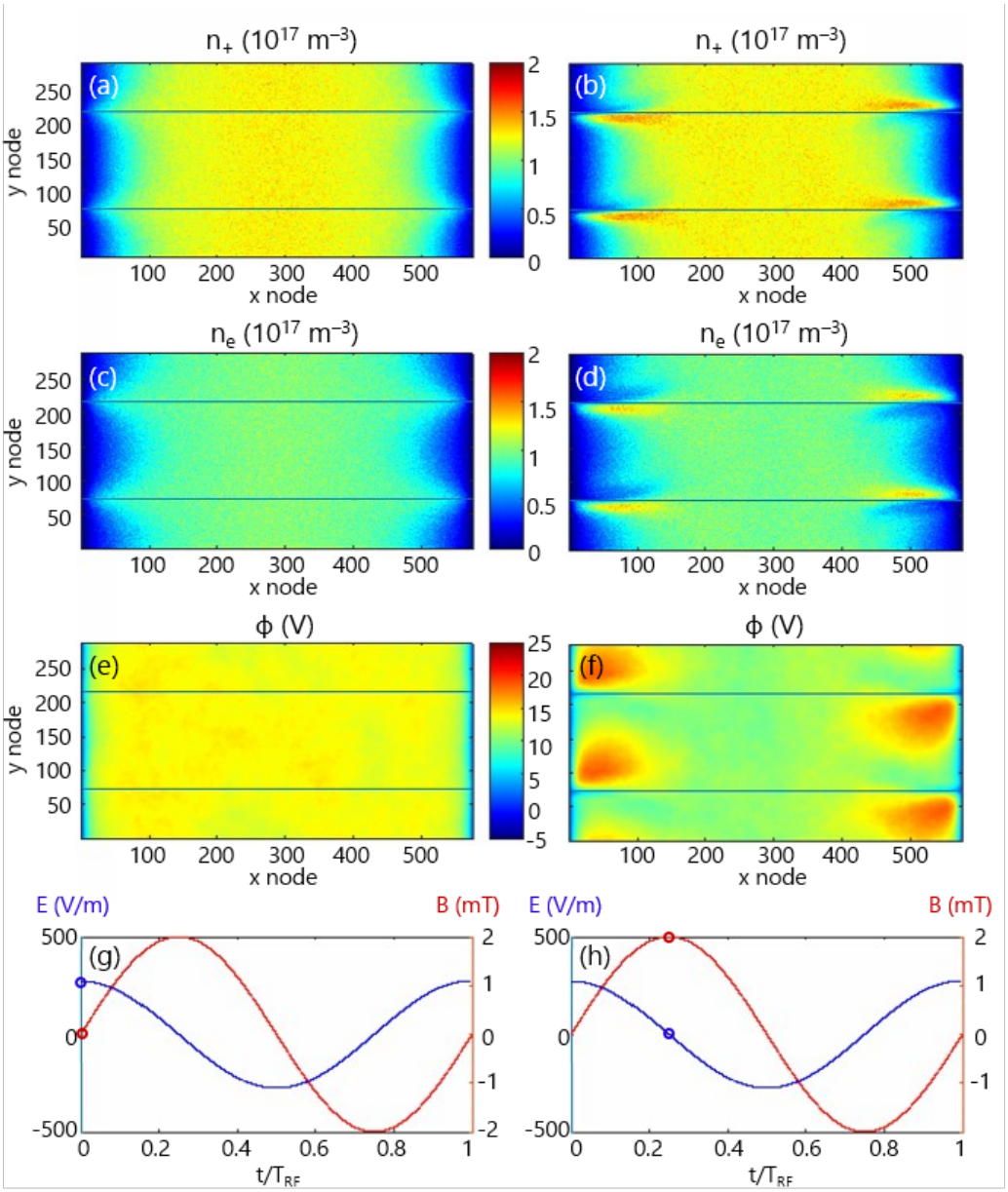

Figure 10.14: Two-dimensional maps of positive ion density, electron density, plasma potential, and E,B field values obtained for t/T_{RF}=0 (a,c,e,g) and t/T_{RF}=0.25 (b,d,f,h).

Within the second quarter of the RF period, the electric field becomes negative, thus it changes direction; the induced magnetic field instead decreases to zero. As the electric field is now in the opposite direction, the aforementioned effect of electron acceleration will take place in the opposite way, causing electrons from the bulk to start forming again a cusp structure in the regions were it was destroyed in the previous quarter of RF period. As can be seen by comparing the right column from 10.14 and the left column in Figure 10.15, the plasma density in the center is slightly increased, possibly because the induced EM field causes an $\vec{E} \times \vec{B}$ drift pointing inwards the domain.

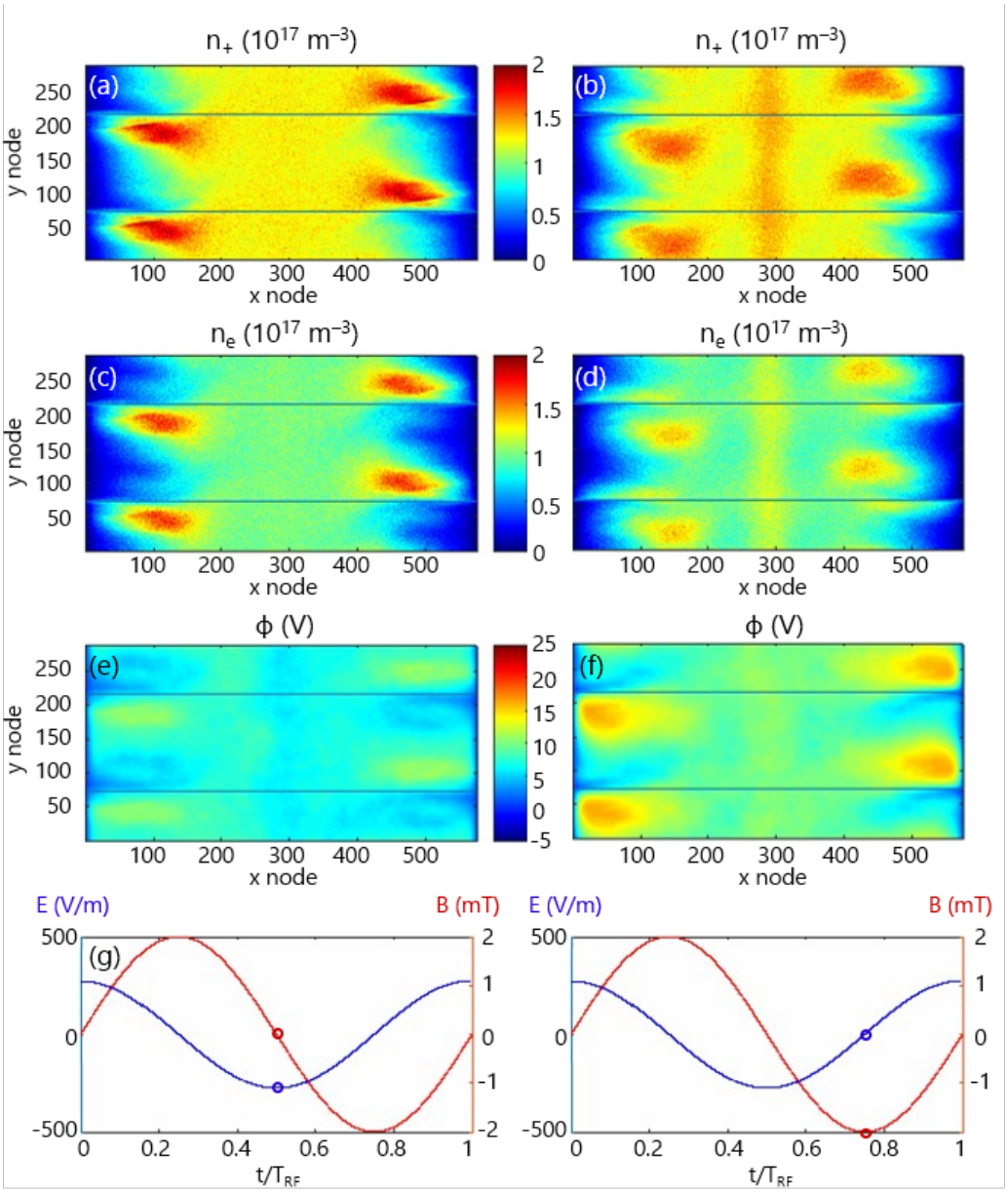

Figure 10.15: Two-dimensional maps of positive ion density, electron density, plasma potential, and E,B field values obtained for t/T_{RF}=0.5 (a,c,e,g) and t/T_{RF}=0.75 (b,d,f,h).

In the third quarter of T_{RF}, the induced magnetic field has opposite direction with respect to the first half of the RF period, and the electric field increases up to 0. The "new" cusp becomes more evident as the positive ion start to follow the electron dynamics.

Figure 10.16 shows the average plasma properties and the ion flux at the walls (for the latter, each point is time-averaged over 100 iterations) over two entire RF periods. A plasma potential oscillation of approximately 15 V at the domain center is obtained, with the electron temperature T_e being roughly constant. The average plasma density is increasing, in accordance with the reduced positive ion flux towards the walls.

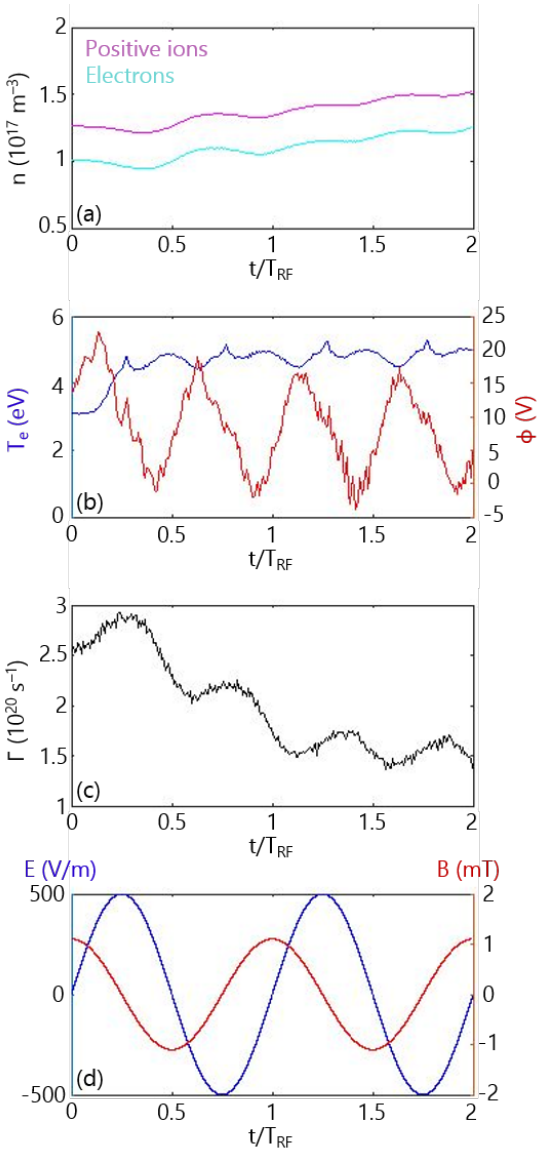

Figure 10.16: Main plasma properties as a function of time: positive ion and electron densities (a), plasma potential and electron temperature (b), positive ion flow at the walls (c), induced E, B (d). Two entire RF periods are considered.

Chapter summary

Before discussing the aforementioned results, it is worth reminding that the latter are valid provided that any electric field contributions along the third dimension (which can derive from $\vec{E} \times \vec{B}$ drifts) are negligible, since the Poisson equation is solved on the (x, y) plane only. This being said, without the induced RF field, the loss fraction was estimated to be significantly larger than the theoretical estimation for high field intensities. The plasma potential was found to affect the result for low field intensities, worsening the confinement for $V_p \geq V_f$: in these conditions, the plasma electrons cannot reach the cusp region, hence the positive ion charge is under-compensated. As for the PEZ, the obtained values never exceed $0.5\, d_{\mathrm{mag}}$. As expected, the PEZ dimension increases for stronger B_0 since the cusp field lines can extend deeper into the plasma; for low field intensities, the PEZ was found to be reduced for increasing V_p values due to the lack of magnetized electrons.

When a static electric field is taken into account, one obtains that the cusp confinement is strongly affected if $\vec{E} \parallel \hat{z}$, whereas it is only slightly modified if $\vec{E} \parallel \hat{y}$. However, as can be seen by comparing the first two columns in Figure 10.12, the plasma losses are more localised in one half of the cusp structure. This might be an issue regarding the installation of permanent magnets on the lateral walls of the SPIDER RF drivers. Furthermore, an oscillating plasma potential might also be an issue.

Chapter 11

Left-right asymmetry in SPIDER and cusp confinement

The horizontal in-homogeneity of the source plasma properties in SPIDER will be discussed in this chapter. Among the possible reasons, the influence of the permanent magnets installed on the source lateral walls will be discussed.

11.1 Experimental measurements of horizontal non-uniformity

The presence of a left-right asymmetry in the source plasma properties was experimentally verified through different measurements, including PL, movable Langmuir probes and PG/BP Electrostatic Probes ones.

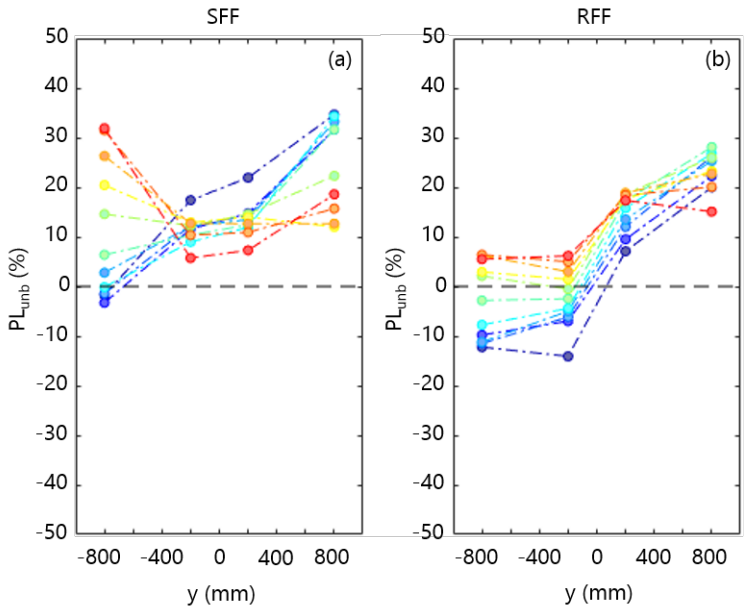

Figure 11.1: Vertical profiles of the emitted plasma light in the SFF (a) and RFF (b) configurations for different I_{PG} current values. Data courtesy of B. Zaniol.

Figure 11.1 shows the left-right unbalance measured by the PL telescopes, defined for each RF segment as:

$$\mathrm{PL_{unb}}(\%) = \frac{\mathrm{PL_{DX}} - \mathrm{PL_{SX}}}{0.5(\mathrm{PL_{DX}} + \mathrm{PL_{SX}})} \tag{11.1}$$

The PL unbalance is more pronounced for the SFF configuration. In this case, both the lower and upper RF segment are strongly affected by the PG current value, although with opposite trends. It is worth to remind that vertical drifts arise for higher filter field values, partially explaining the rather strong discrepancy between the top and bottom segment measurements.

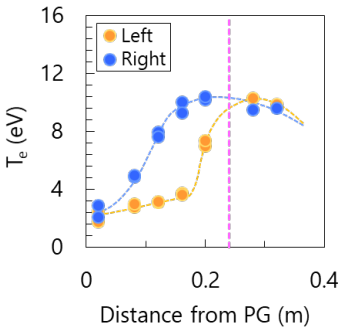

Figure 11.2: Axial profiles of electron temperature T_e measured by two movable Langmuir probes sampling the drivers belonging to the bottom RF segment. Pulse settings are P_{RF}=25 kW/driver, FF intensity 1.5 mT at PG (SFF), p=0.35 Pa, floating PG,BP biases. Data courtesy of E. Sartori.

However, with the PL measurements being line-integrated along the entire source depth, it is not possible to infer where the non-homogeneity is localised. In this regard, figure 11.2 shows the electron temperature estimations obtained with the movable Langmuir probes in the bottom RF segment of the SPIDER source. The right driver features a wider T_e profile, which is extending in the expansion chamber. The measured values inside the drivers are comparable, suggesting that the left/right unbalance detected by the PL measurements might be due to non-uniform conditions in the expansion chamber. The embedded Langmuir probes on the PG and BP electrodes also measured a non-uniformity along the horizontal direction within the extraction region of the SPIDER ion source.

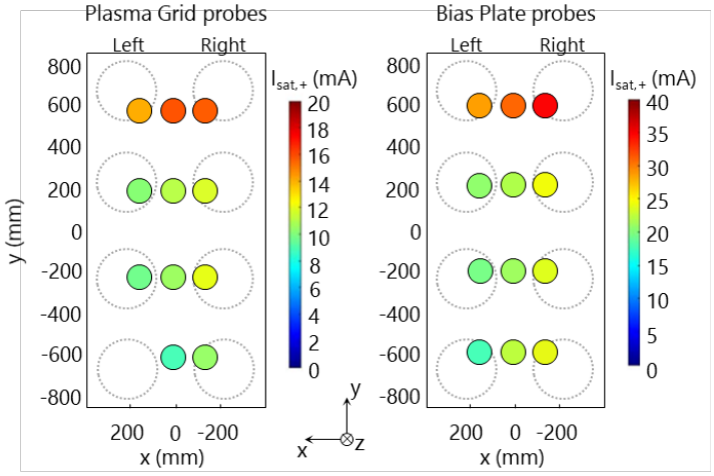

Figure 11.3: Ion saturation current $I_{sat,+}$ measured by the electrostatic probes embedded on the PG and BP electrodes. The beam axis is parallel to the z direction. The position of the drivers on the beam area is highlighted by the grey, dotted circles. Data courtesy of C. Poggi.

This asymmetry might result from different causes, including power unbalance between the RF drivers, and non-uniformity of the filter field. Each pair of segment is supplied by a RF generator, with the two drivers in each segment connected in series: eventual current unbalances between the two RF coils were estimated to be at most 4%, leading to RF power difference within 10%, which still cannot fully account for the strong horizontal plasma non-uniformity. Nonetheless, in view of the future SPIDER operations, several improvements on the RF system will be implemented[35].

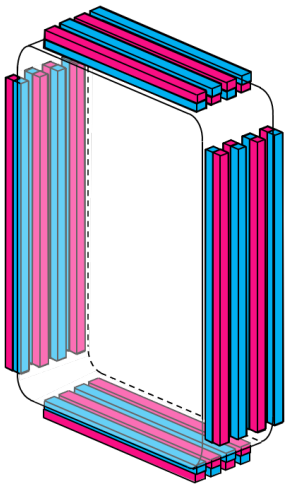

Figure 11.4: Arrangement of the permanent magnets on the lateral walls of the SPIDER ion source as in the original design.

Concerning the filter field uniformity, experimental measurements performed by means of Hall sensors confirmed the presence of a left-right asymmetry in the filter field intensity[30], possibly related to the presence of permanent magnets on the lateral walls of the expansion chamber. Indeed, as already mentioned, the SPIDER ion source is equipped with these permanent magnets in order to reduce the plasma losses on the walls. In accordance with the original mechanical design of the source, the installed permanent magnets generate a magnetic field of roughly 120 mT in correspondence of the inner surfaces of the expansion chamber. As shown in Figure 11.4, the magnets are oriented in such a way that the magnetization of correspondent magnets belonging to opposing surfaces is either pointing inwards of outwards for both magnets.

This cusp field contribution is superimposed to the magnetic FF, which is static and horizontally oriented: as a consequence, the resulting magnetic field is asymmetric, independently of the PG current flow direction. Indeed, the filter field will be either strengthened or reduced in correspondence of the magnets, depending on the cusp field orientation. If the field generated by the permanent magnets is too high, the cusp field can significantly alter the FF in the proximity of the lateral walls, possibly hampering the filter efficacy.

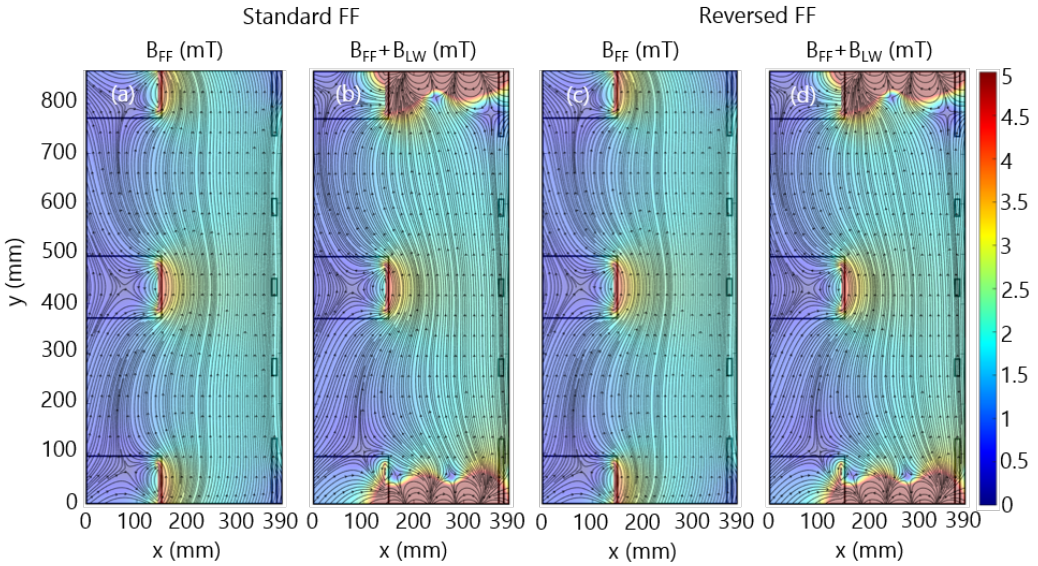

Figure 11.5: SPIDER filter field in the standard configuration without (a) and with (b) the magnetic field generated by the permanent magnets; in the reversed configuration without (c) and with (d) the magnetic field generated by the permanent magnets.

The magnetic field topology on a two-dimensional plane horizontally cutting the SPIDER source volume along the mid-plane of one pair of drivers is depicted in Figure 11.5. The two cases refer to the two available experimental settings of the source, i.e. with the PG current flowing either downwards (SFF) or upwards (RFF) along the PG electrode. As already mentioned, the presence of the magnetic cusps on the lateral walls modifies the filter field topology even at 100 mm from the chamber wall surfaces, also inside the drivers. This possibly affects the left-right uniformity in the expansion chamber, as shown by the numerical analysis discussed in the following.

11.2 Numerical investigation of the left-right asymmetry

The GPPIC code was applied to simulate a two-dimensional plane as the one shown in Figure 11.6. The simulation domain is a 866 × 390 mm^2 rectangle, with a mesh composed of squared cells of size dx =1 mm. The right boundary is a plain metallic wall representing the PG electrode, without resolving the PG apertures. The BP is also included in the domain, as depicted in Figure 11.6. Both the PG and BP biases with respect to the source walls can be set to constant values V_{BI}, V_{BP}. The actual shape of the ion source is obtained by including grounded metallic boxes defining the driver volumes within the left region of the domain.

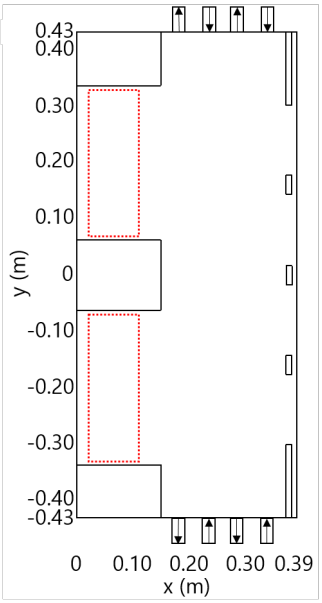

Figure 11.6: Simulation domain for simulating an horizontal plane cutting the SPIDER source volume along the midplane of one RF segment. The regions where the thermostat heats the electrons is highlighted by the dotted red rectangle. The position and orientation of the permanent magnets on the lateral walls is also depicted.

The system evolution is rate-driven. Plasma particles interact with a neutral background of H_2 molecules, with a dissociation fraction δ=0.3. The gas density profile along the horizontal direction features a sigmoidal shape in order to take into account the neutral depletion[64] effect. The maximum gas density value is tuned with a PI feedback control, in such a way to drive the system towards a stationary state while achieving a target electron density value in the upper RF driver, which is defined *a priori* according to experimental measurements. The RF heating is reproduced by means of a Berendsen thermostat acting on a limited region of both drivers. Similarly to the gas density, the coupled RF power, numerically obtained in terms of

deposited electron energy, is tuned with a PI feedback control aiming at reaching an electron temperature value in the top driver derived from experimental measurements. Indeed, both PI loops act taking the electron density and temperature of the upper driver as reference; the electron temperature at which the electron velocities in the lower driver are re-sampled is obtained as $T_{\text{heat,low}} = T_{\text{heat,top}}(N_{e,\text{low}}/N_{e,\text{top}})$, with $T_{\text{heat,top}}$ being the sampling electron temperature of the top driver, and N_e the number of electron particles inside the driver region. Finally, the magnetic filter field topology loaded in the simulation is the same as the one shown in Figure 11.5. The electron density and temperature maps obtained with and without the permanent magnets contribution are shown in Figure 11.7.

It is immediately noticeable that the maximum plasma density is found at the axial position where the filter field rapidly increases at the exit of the drivers, where the electron temperature is above ionization thresholds (Figure 11.7), differently than what was experimentally measured. This is partially caused by the fact that the two-dimensional map of filter field is exploited for the first time in this simulation, whereas in the previous cases (also the ones shown in Chapter 6) an analytical estimation was used. In this simulation, hot electrons move along the curved field lines out of the drivers, so that electrons at relatively high temperature can reach the mid of the expansion region. This is also due to the simplified heating scheme which act on the entire driver area, including the central region, which is directly connected by the field lines to the the expansion region on the sides of the drivers. This result could be mitigated if electron heating was applied only at an outer-to-intermediate radius of the driver region, but further numerical studies shall be carried out on these aspects. The effects just discussed strongly increase the source term out of the driver regions, making it difficult to provide quantitative estimations; however, these results are still useful to discuss the different magnetic field structure precisely at the exit of the drivers towards the lateral walls.

The case without permanent magnets on the lateral walls indicates that the aforementioned strategy to redistribute the coupled RF power on the two drivers is adequate, as it can provide a uniform result in the case of symmetric downstream expansion region. On the other hand, the presence of the permanent magnets field strongly affects the source plasma properties, causing a rather strong asymmetry in the expansion region. The simulation results show that, at the exit of the right driver, the electron temperature has a higher value in the case with the permanent magnets field, similarly to the experimental measurements shown in 11.2. Moving towards the expansion region, one can see how the plasma density in front of the electrodes is also higher in the bottom driver: this result is in agreement with the experimental measurements of the embedded Langmuir probes 11.3, since also in that case the ion saturation current of the right column (i.e. for negative values of the x axis) is slightly larger with respect to the left column. Finally, also the plasma light unbalance (Figure 11.1) shows how the light signal collected within the right column are more intense than the left column ones. This being said, it is worth pointing out that the simulated electron temperature inside the drivers is significantly different, whereas the experimental measurements show very similar estimations. This might be due to the fact that the sampling temperature of the right driver is linearly dependent on the $(N_{e,\text{low}}/N_{e,\text{top}})$ ratio, thus it can grow up to very high values. As a possible solution, one might try to change the heating frequency of the thermostat rather than the sampling temperature.

This non-uniformity inevitably affects the positive ion and atom fluxes on the PG surface, ultimately affecting the surface production of negative ions, as shown in Figure 11.8. In the case with the permanent magnets on the lateral walls, the atom flux towards the PG electrode is more intense for the third beamlet group (counting from top); similarly, the positive ion flux downstream the BP is more localised in the bottom half of the simulation domain, corresponding to the RF drivers on the right column.

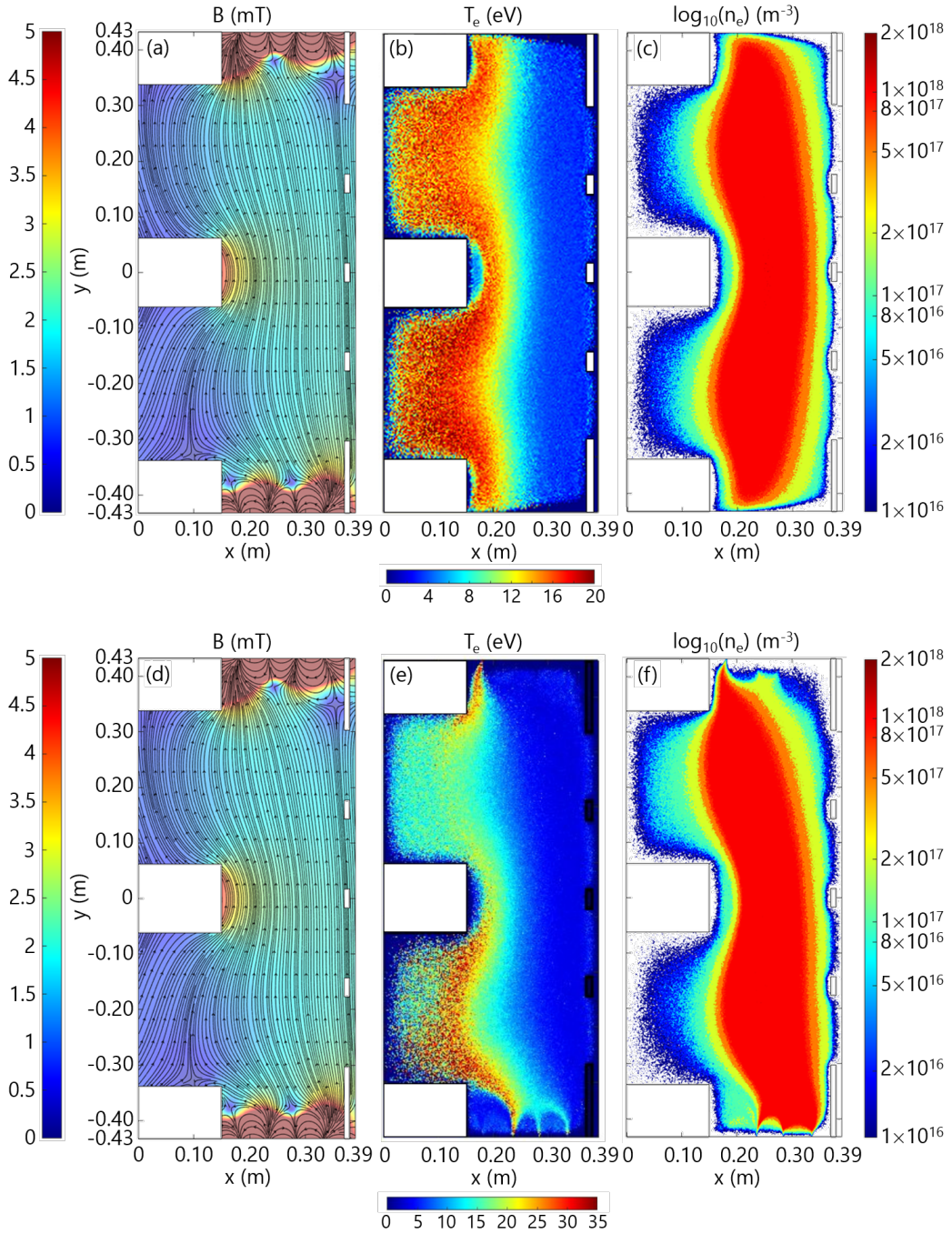

Figure 11.7: Assumed magnetic field intensity and direction, electron temperature, and electron density map obtained on an horizontal section of the SPIDER source without (a,b,c) and with (d,e,f) the magnetic field contribution due to the permanent magnets on the lateral walls.

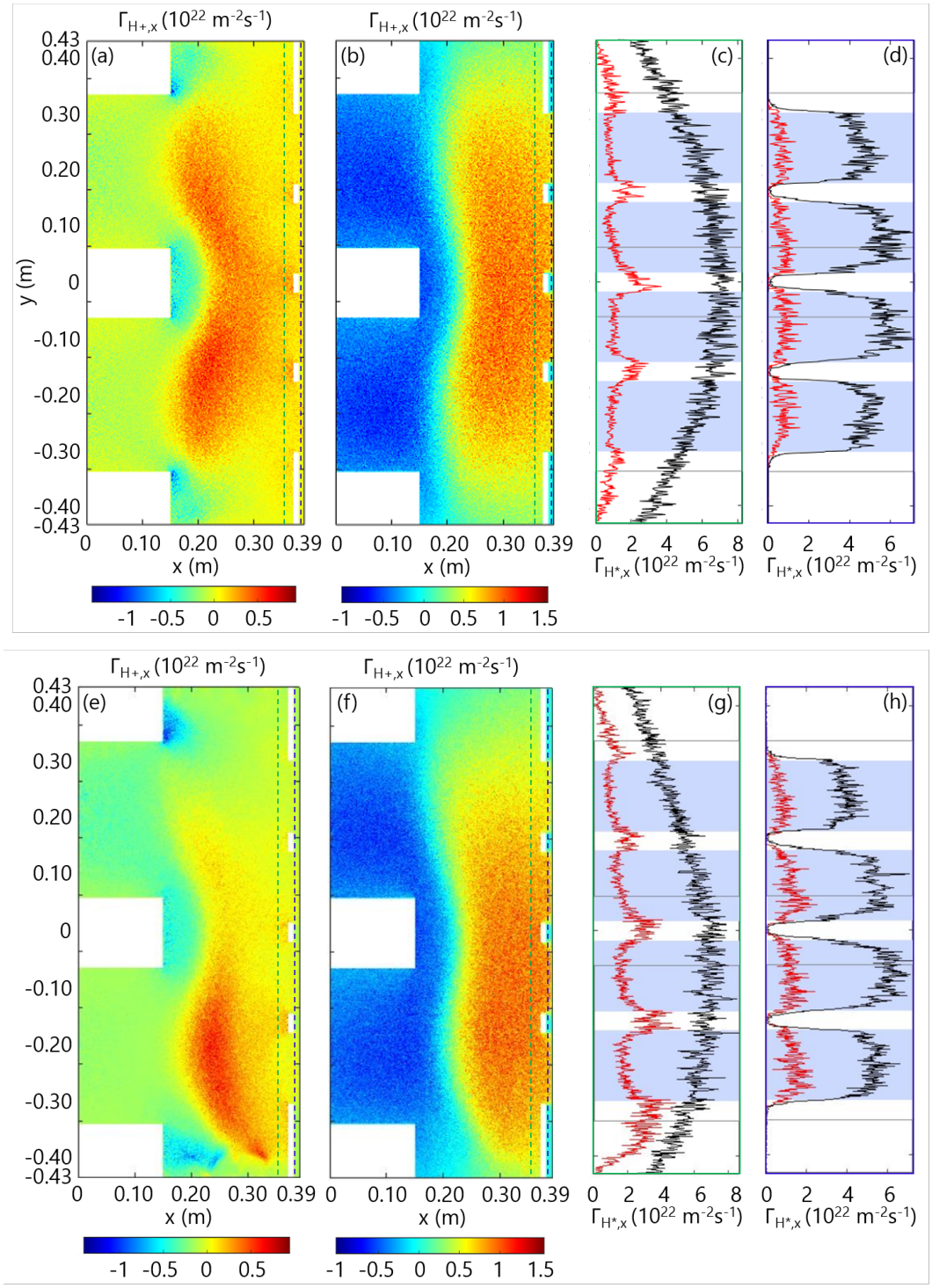

Figure 11.8: From left to right: two-dimensional maps of positive ion and neutral atom flux towards the PG obtained on an horizontal section of the SPIDER source, vertical profiles of positive ion (red) and atom (black) fluxes taken downstream the BP (green rectangle) and in between the BP and PG (blue rectangle) without (a,b,c,d) and with (e,f,g,h) the magnetic field contribution due to the permanent magnets on the lateral walls.

11.3 New permanent magnets configuration for the expansion chamber in SPIDER

Given the numerical and experimental results on the left-right asymmetry, the magnetic cusp field at the lateral walls in the SPIDER source will be modified. Particularly, both the magnetic field strength and the spacing between the magnets will be modified on the lateral walls. Additional permanent magnets will be placed also in correspondence of the corners and on the rear surface of the expansion chamber[97]. Unlike the actual configuration, the permanent magnets will be arranged in a chequered way, with the aim of averaging out any net components of the cusp magnetic field.

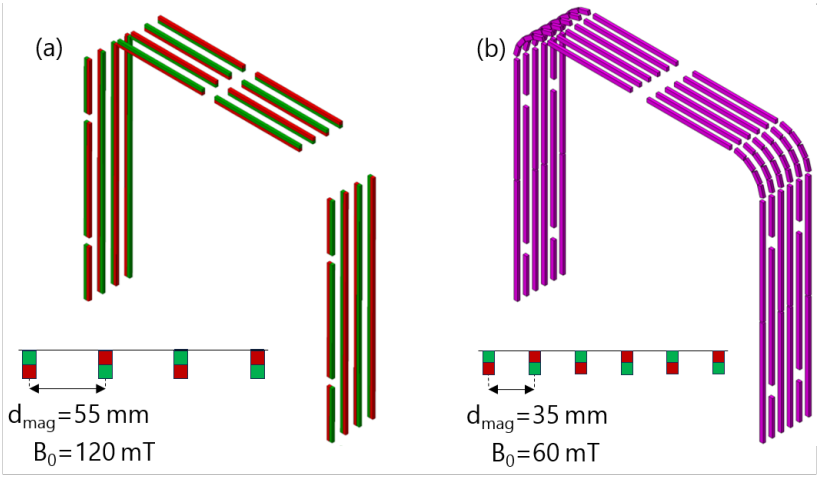

Figure 11.9: Old (left) and new (right) permanent magnets arrangement on the SPIDER lateral walls. Due to its symmetry, the configuration is shown for only half of the ion source.

As shown in Figure 11.9, in the new configuration the distance between the magnets d_{mag} will be reduced from 55 mm to 33 mm. In addition, smaller permanent magnets will be installed, halving the magnetic field intensity B_0 at the walls surface. The plasma loss fraction f is estimated to increase from 14% to 16%; however, the overall source performance is expected to improve since the magnetic field generated by these magnets will decay faster when extending towards the source center, thus its impact on the plasma properties will be reduced. Moreover, the reduction of d_{mag} will cause a smaller PEZ in front of the lateral walls.

11.4 Homogeneity among the RF drivers

In order to further characterize the homogeneity between the drivers, a system of eight Langmuir probes has been designed for SPIDER. These electrostatic sensors will be helpful to verify the uniformity of power coupling in the eight drivers. These probes are designed to be permanently installed, hence they will be able to perform measurements both with and without caesium evaporation, and also during the beam extraction phase. Besides providing additional insights on the underlying cause for plasma asymmetry, these probes can be exploited to gain useful information about the RF coupling in view of the commissioning of the new solid-state amplifiers[98], and they will provide a reference measurement for other diagnostics such as OES and PL.

11.4.1 Sensor design

Probe head

The sensor is a double Langmuir probe with cylindrical tungsten electrodes of 0.5 mm diameter, insulated by an alumina (Al_2O_3) tube with two bores of 1.2 mm diameter. The electrodes are protected by additional thin alumina tubes at their basis for preventing unwanted short-circuiting of the electrodes caused by tungsten (or molybdenum from the ion source walls) sputtering. The exposed electrode length is equal to 5 mm, yielding a r/L ratio of 0.05.

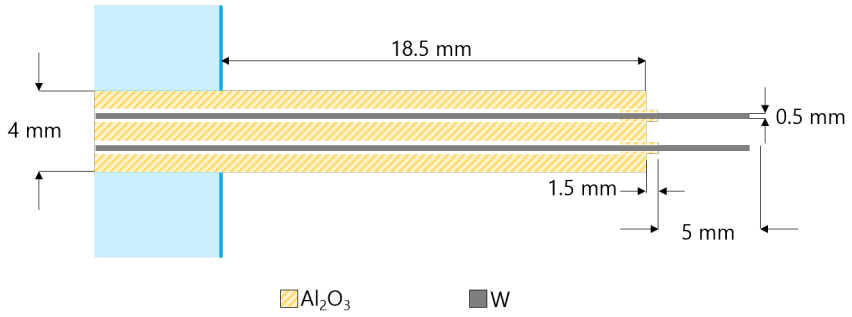

Figure 11.10: Section view of the probe head design envisaged for the new fixed Langmuir probes to be installed in SPIDER. The thick blue line represent the boundary between the RF driver backplate (left) and the plasma chamber (right).

Probe support

The probes will be installed downstream of the drivers' backplates, as shown in Figure 11.11. The electrodes tips will lie at 25 mm from the driver backplate, allowing to acquire strong enough signals while exploiting the cusp field itself for shielding the probe from the high n and T_e of the driver plasma. In fact, the expected ion saturation current at this location with full RF power is of the order of 20 mA and, according to thermal analyses, the maximum temperature reached by the alumina is below its melting point (2072 °C). Other components are also not over-heated, as they reach ≈ 100 °C. This choice for the probe positioning is also compatible with the PEZ dimension, which is estimated to be ≈10 mm.

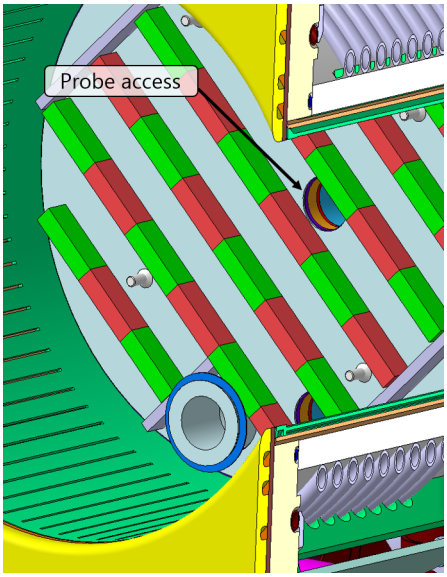

Figure 11.11: Access for the driver fixed probes. The configuration of the permanent magnets on the driver backplate is also visible.

The probe support is custom-shaped stainless steel element featuring a 6 mm deep socket of area 12 mm ×43 mm, as shown in Figure 11.12. This support will also host a Kapton PCB board featuring the electronics for active RF compensation. More precisely, a series of two LC choke filters tuned on the RF frequencies of 1 MHz and its first harmonic at 2 MHz will be used for each of the eight probes. This type of compensation has already been used for other Langmuir probes previously installed in SPIDER[34],[99]. The probe will be kept in its position by means of a PEEK element, which is fixed on the stainless steel element.

Figure 11.12 shows the estimated magnetic field intensity as a function of the distance from the driver backplate. At the probe electrode location, the field is expected to be of the order of 5 mT, thus plasma ions can still be considered to be not magnetized.

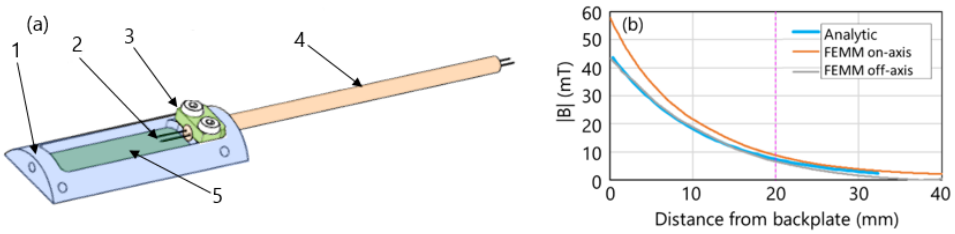

Figure 11.12: (a) Isometric view of the probe assembly, including the stainless steel (AISI 316L) probe support (1), the electrodes (2), the PEEK element for securing the probe position (3), and the alumina insulator (4), the LC filter location is highlighted in dark green (5); (b) Magnetic field intensity as a function of the distance from the driver backplate. The analytic estimation is shown in light blue, whereas the FEMM results on the driver axis and on the probe axis are shown in orange and grey respectively.

As can be seen in Figure 11.13, the probe access is shared with the PL telescope, which are mounted downstream of the KF25 tube hosting the gas injection tube. However, the fixed probes design is fully compatible with the PL system, preserving its lines of sight.

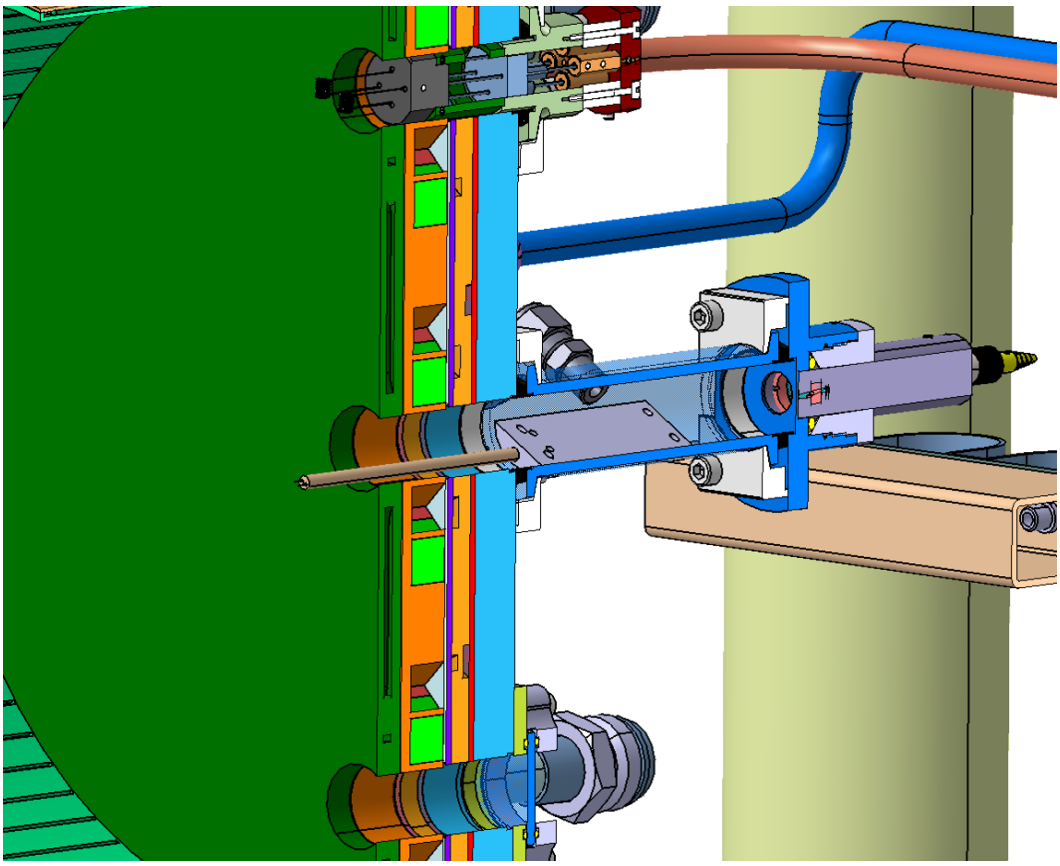

Figure 11.13: 3D CAD cut view of the probe assembly on one of the RF drivers in SPIDER. The Plasma Light telescope downstream of the KF25 tube hosting the gas inlet is also visible.

Chapter summary

Experimental results from several diagnostics (plasma light, temporary movable Langmuir probes, embedded Langmuir probes) regarding the horizontal non-uniformity of the source plasma properties are presented. It was hypothesized that the possible cause for this non-uniformity could be the superposition of magnetic filter field and of the magnetic field generated by the permanent magnets installed on the lateral walls of the expansion chamber. In order to verify this hypothesis, a numerical simulation was performed, with the results being shown in this chapter. In comparative terms, the permanent magnets were found to strongly affect plasma expansion from the drivers, in a compatible way with the experimental results. On this basis, a modification of the lateral walls permanent magnets in the SPIDER beam source was proposed and implemented, as briefly described. In addition, the confinement effect of cusp magnets in presence of unusually high plasma potential with respect to wall potential was quantified: due to electron cooling by the filter field, this condition occurs at most surfaces around the expansion region of SPIDER. The numerical estimation indicated that the confinement mechanism should still be valid, even though at a reduced effectiveness, so that permanent magnets were also integrated in the backplate of the ion source. Finally, the design of a set of fixed Langmuir probes to be installed one for each driver is presented. As discussed, the aim of these diagnostics is to verify if the plasma properties among the drivers are well balanced.

Chapter 12

Plasma properties in filament-arc negative ion sources

Filament-arc negative ion sources have been widely investigated and used for NNBI systems, as opposed to RF sources, on which the R&D activities have more recently started. The largest filament sources, such as the ones hosted at QST and NIFS facilities, are capable of delivering high energy negative ion beams with very low beam divergence. With the aim of understanding what are the source plasma features that allow to obtain such low values of beam divergence, a numerical investigation of a plasma discharge in a filament-based negative ion source will be discussed in this chapter. Commonly, test particle codes are used to approach one of the main issues of non uniformity in filament arc sources along the vertical direction, originated by a $\vec{B} \times \nabla\vec{B}$ drift. which is particularly effective on fast electrons, i.e. on the primary electrons emitted from filaments. This kind of numerical models helped in optimizing the discharge uniformity of filament arc sources[100]. This study, based on the GPPIC code, is focused on the role of neutrals in the discharge and on both equilibrium and dynamics of the ion species.

12.1 Filament and RF negative ion sources: a comparison

Both filament and RF negative ion sources share the presence of a magnetic filter field aimed at reducing the electron temperature in the proximity of the extraction region, and the surface production of negative ions through caesiation of the PG electrode surface. The main difference between the two type of sources is of course the plasma formation mechanism: as already discussed, in RF sources the electron heating is based on the inductive coupling between a RF antenna and the plasma itself, which allows to accelerate some electrons generated by a hot filament and, consequently, start the avalanche process which leads to plasma formation. In filament sources, the ignition process is entirely based on the electron thermionic emission by hot ($T \propto 1000\,K$) filaments. The higher the filament temperature, the more intense the emitted electron current density, as stated by the Richardson's law[101].

Another difference between RF and filament sources is the magnetic confinement topology: regarding the former, a set of permanent magnets on the lateral walls was included in the SPIDER design[28], in addition to the permanent magnets set at the drivers' backplates, which were already installed in both BUG and ELISE facilities. Filament sources instead are provided with a multi-cusp magnetic confinement on all the chamber surfaces: this design is usually called Kamaboko ion source, as the first prototype developed by the Japan Atomic Energy Research Institute and operated on the MANTIS test facility, in France[102]. Furthermore, in RF sources

the magnetic FF is obtained by letting a current flow along the PG electrode and a system of return busbars, whereas in filament sources permanent magnets are employed. Figure 12.1 shows a schematic comparison of RF and filament based negative ion sources.

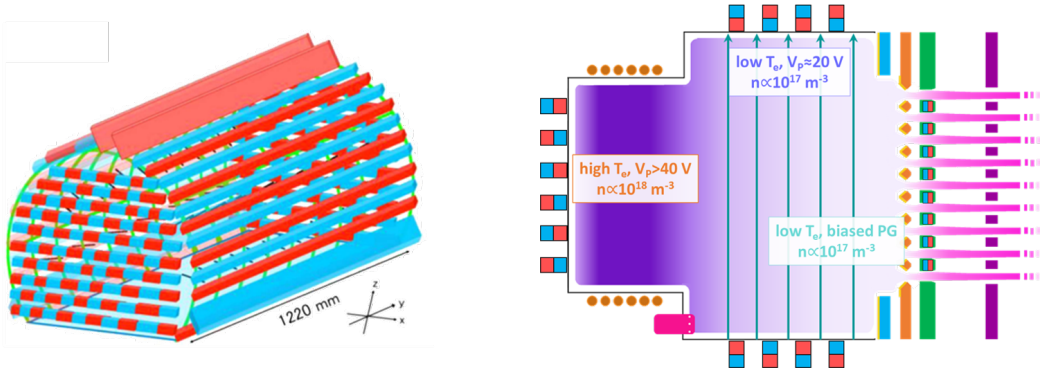

Figure 12.1: On the left: scheme of a filament based negative ion source, with multicusp confinement on all chamber surfaces; on the right: scheme of a RF based negative ion source, highlighting plasma properties in the different regions.

12.2 Why are the source performances so different?

As anticipated, filament sources are capable of delivering high current negative ion beams with very low divergence. In the Megavolt Test Facility (MTF), hosted at QST, a 1 MeV negative ion beam was obtained with a 3 mrad beam divergence[103]. The lowest beam divergence measured in SPIDER is roughly 12 mrad, with a beam energy of roughly 50 keV[46]. As discussed in Section 2.3.3, the beam divergence can be defined for each beamlet as the average exit angle at the accelerator of the negative ions composing the beamlet itself, with respect to its axis. Higher beam divergence then implies a poor focussing of the negative ion trajectories, which might stem either from not optimised extraction and acceleration voltages, or from the properties of the source plasma.

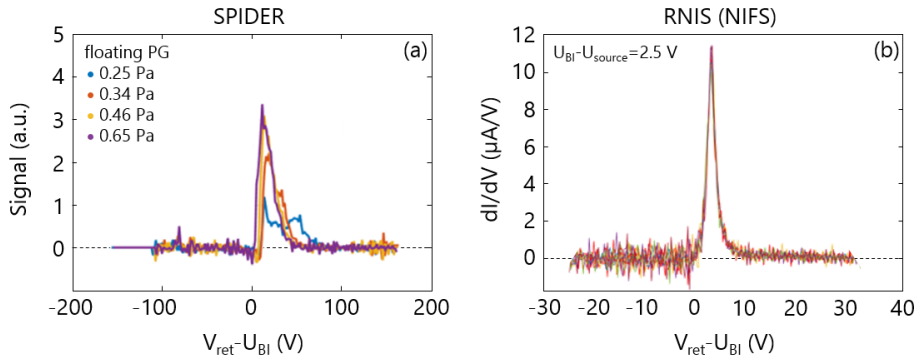

Figure 12.2: Positive ion energy distribution measurements taken in SPIDER (a) and RNIS (b) negative ion sources. Presented on March 11th 2022 during the ITER NBTF Experimental Advisory Committee by E. Sartori.

Numerous numerical studies have been carried out for optimising the accelerating column in terms of applied voltages, V_{acc}/V_{ext} ratio, and grid apertures shape, hence the very large beam divergence measured in SPIDER was not straightforwardly explainable in the aforementioned terms.

The measurements performed in SPIDER with a temporary set of movable Langmuir probes[34] provided some information on the axial profiles of the plasma properties, highlighting the presence of a significant positive potential peak within the driver, on top of an overall rather high plasma potential (see Chapter 5). Additionally, movable RFEA sensors measured positive ion energy distributions of $\propto$10 eV width close to the PG electrode; particularly, the distribution width was correlated with the potential peak difference between the drivers and the expansion chamber, as shown in Figure 5.7. If compared with analogous RFEA measurements performed during a dedicated experimental campaign at the RNIS test-facility (NIFS) on a filament negative ion source, one can immediately notice how the distribution width is much more smaller in this latter case.

In a first approximation, with the positive ions being one of the precursor species for surface production mechanism, this difference in the energy distribution function might be one of the reasons for the higher beam divergence: indeed, when analysing the beam optics through the accelerating column, negative ions at the plasma meniscus are usually assumed not to have a perpendicular velocity component with respect to the beamlet axis. However, the precursor species properties might cause the surface-produced negative ions to be moving also along the perpendicular direction, possibly worsening the extracted beam optics. As already mentioned in Chapter 5, Coulomb collisions between surface produced negative ions and positive ions (H^-,H^+) were found to be fundamental for negative ion extraction[15] as they contribute to reverse the H^- velocity component tangential to the beam axis, which at first is directed towards the source. This process is more effective for small $v_{H^+} - v_{H^-}$ velocity differences, hence wider positive ion energy distributions might be detrimental for the beam extraction process.

Together with positive ions, fast atoms are the other precursor species for surface produced H^-. For this reason, also the background gas dissociation degree is an important parameter for improving the extracted beam optics. In particular, electron and ion temperature, as well as the plasma potential with respect to the source walls are generally much lower in filament sources than in RF sources, possibly leading to different source plasma properties.

12.3 Numerical investigation of the kamaboko source

For the aforementioned reasons, the GPPIC code was applied to investigate filament based hydrogen plasma discharges, taking as reference the negative ion source hosted at QST-MTF. As a first step, it was decided to investigate the two-dimensional plane horizontally cutting the ion source, as shown in Figure 12.3. All the walls hosting the permanent magnets are reproduced as plain, grounded metallic walls, and represent the chamber inner surfaces. The bottom wall represents the PG electrode and is polarised at V_{BI}=2 V with respect to the other surfaces. The magnetic field was obtained as described in Section 4.1.1, considering a set of 14 permanent magnets placed on the round wall with regular spacing. Two additional stronger magnets placed close to the extraction region ensure the presence of a filter field with roughly 6 mT intensity in correspondence of the PG center.

An improved description of the background gas dynamics was implemented as described in Section 4.2. More precisely, H_2 molecules were injected in the simulation domain from a 10 mm wide aperture in the upper section of the round walls. The number of molecules to be injected at each iteration is obtained as $N_{MP,\mathrm{H_2}} = \Phi_{\mathrm{H_2}} \cdot dt$, with the flow defined as $\Phi_{\mathrm{H_2}} = \Gamma_{\mathrm{H_2}} \cdot A_{\mathrm{inj}}$. The flux Γ is defined as:

$$\begin{aligned} \Gamma_{\mathrm{H_2}} &= 0.25 n_{eq} v \\ &= 0.25 \frac{p_{eq}}{k_B T_{\mathrm{room}}} \left(\frac{8 k_B T_{\mathrm{room}}}{\pi m_{\mathrm{H_2}}} \right)^{0.5} \end{aligned} \tag{12.1}$$

with p_{eq} and T_{room} being the target gas pressure and room temperature respectively. For the simulations shown in this chapter, no collisions between H_2 molecules were included.

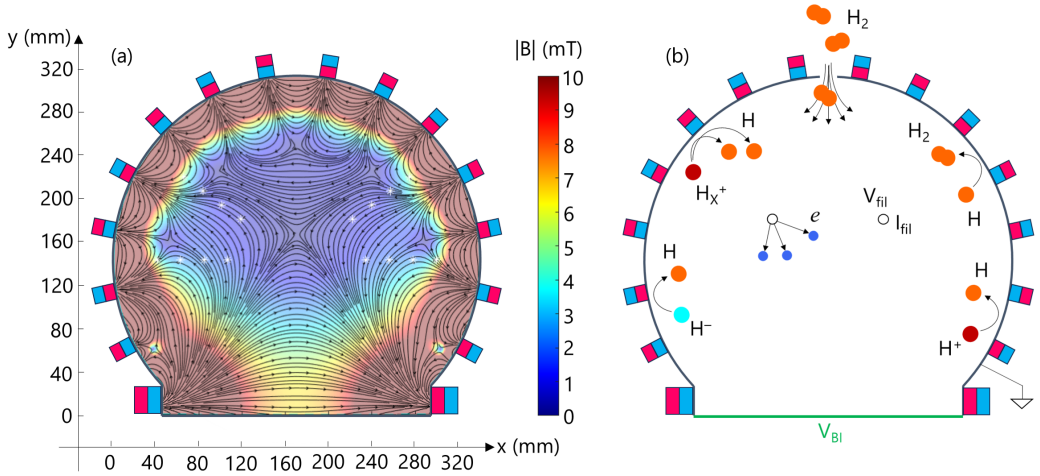

Figure 12.3: (a) Magnetic field assumed for the kamaboko source; (b) simulation domain and schematic representation of the main features.

In the real kamaboko source, filaments are entering from the lateral walls, and they are radially oriented; nonetheless, reproducing the same geometry would have caused most of the electrons to be emitted with a non-negligible velocity component along the non simulated direction. For this reason, it was decided to include the filaments as two small circles of 2.5 mm placed at roughly 200 mm height with respect to the PG, with their position being symmetric with respect to the vertical direction. Since the cell size along the z direction is 1 m, the filament bias V_{fil} and current I_{fil} are defined in such a way to deliver the same arc power per unit length as in the real case.

Parameter	Description	Value
β	Density scaling factor	10^{-4}
dt_{vac}	Simulation timestep for gas solution	5 ns
dt_{vac}	Simulation timestep for plasma solution	1 ns
$dx{=}dy$	Unit cell size	0.8 mm
V_{BI}	PG potential	2 V
p_{bg}	Background gas pressure	0.3 or 0.6 Pa
V_{fil}	Filament polarisation voltage	−80 V
I_{fil}	Filament current	280 A
P_{arc}	Arc power	45 kW/m

Table 12.1: Main simulation parameters.

The domain is initially filled with H_2 molecules until a stationary state is reached. At this point, electron emission from the hot filaments begins, starting the plasma discharge. The system then evolves towards a new stationary state: it is important to point out that, for these simulations, the only fixed parameters are the initial chamber gas pressure and the arc power. The obtained plasma solution is the result of the included collision processes, both interaction with the background gas and Coulomb collisions, and of the PWI as described in 4.3. The main simulation parameters are listed in Table 12.1. Two different cases are simulated, namely one with gas filling pressure 0.3 Pa, and the other one with pressure 0.6 Pa. The other parameters were left unchanged.

12.3.1 Low background gas pressure

Figure 12.4 shows the time evolution of the number of macroparticles N_{MP}, their rates, and temperature averaged over the entire domain. Three different phases are shown, namely the only gas one, highlighted in yellow, the plasma one, highlighted in light blue, and the one with Coulomb collision between positive ions, highlighted in pink.

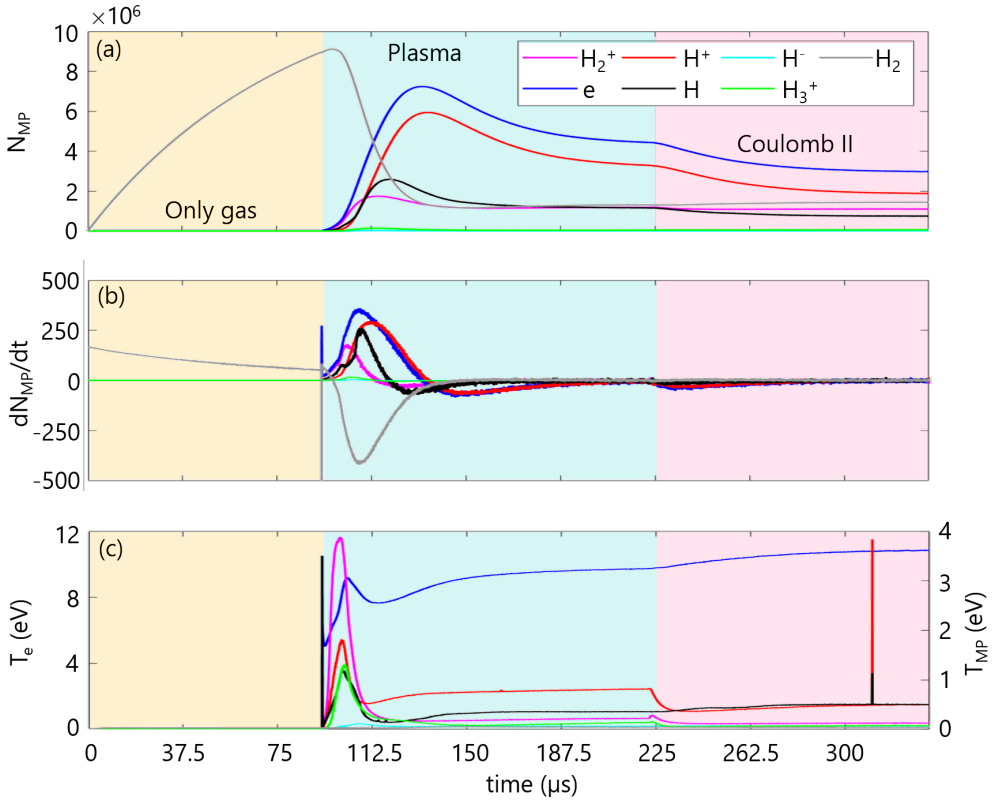

Figure 12.4: Number of macroparticles N_{MP} (a), macroparticle rates dN_{MP}/dt (b), and temperature (c) as a function of the simulated time.

As soon as plasma is ignited, the number of electrons and H_2^+ ions grows exponentially and, at the same time, the number of molecules decreases due to background gas ionization. The number of positive ions and atoms starts growing after some time, that is when dissociation starts. When Coulomb collisions between positive ions are added, their average temperature is significantly decreased.

Figure 12.5 shows the two dimensional maps of H_2 density and pressure at the end of the only gas phase, then the H_2 and H densities for the other two plasma phases. As can be seen from the average pressure value, the target pressure of 0.3 Pa was not fully reached yet, although this is only because more time was needed. The shadow below the two filaments is due to the fact that the H_2 molecules cannot collide among themselves, and the filaments are being obstacles for the gas flux incoming from the top. When the plasma discharge is started, neutral depletion takes place in the central region of the simulation domain, where the H_2 density drops of about one order of magnitude. At the same time, the H density increases up to roughly 1×10^{19} m^{-3}, comparable with the molecular density. Finally, when Coulomb collisions are included, the atom density decreases in favour of the molecular density: this might be related to the fact that, being the positive ion temperature reduced, background gas dissociation by means of positive ion impact becomes a less probable process.

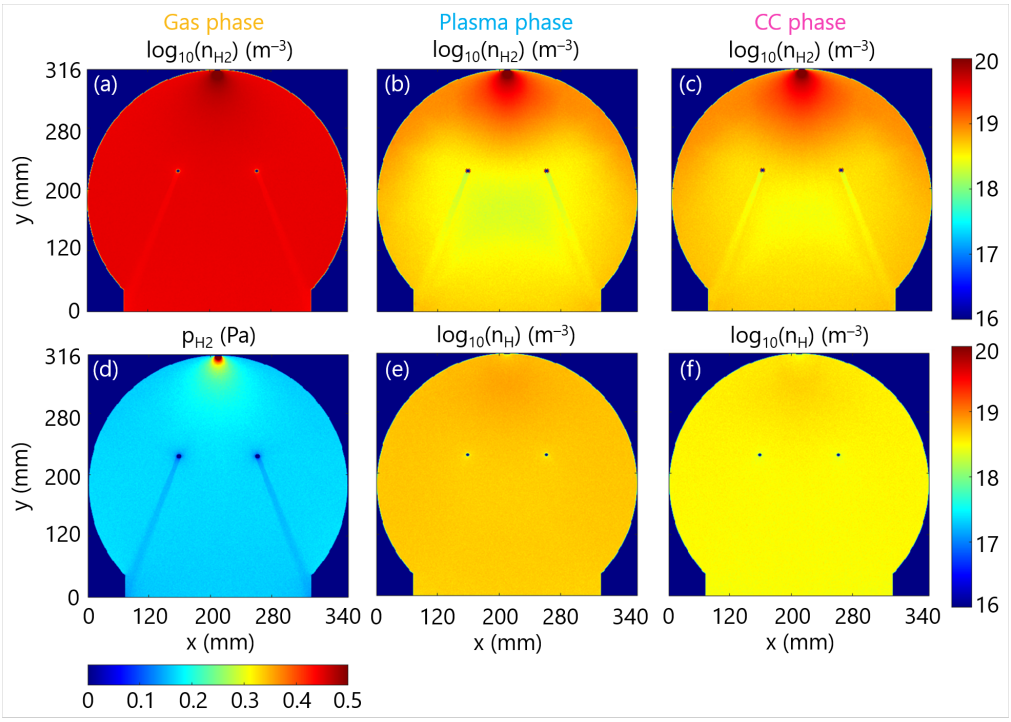

Figure 12.5: Molecular gas density for gas only (a), plasma (b), and CC (c) phases; H_2 pressure for the gas only phase (d); neutral atom density for the plasma (e) and CC (f) phases.

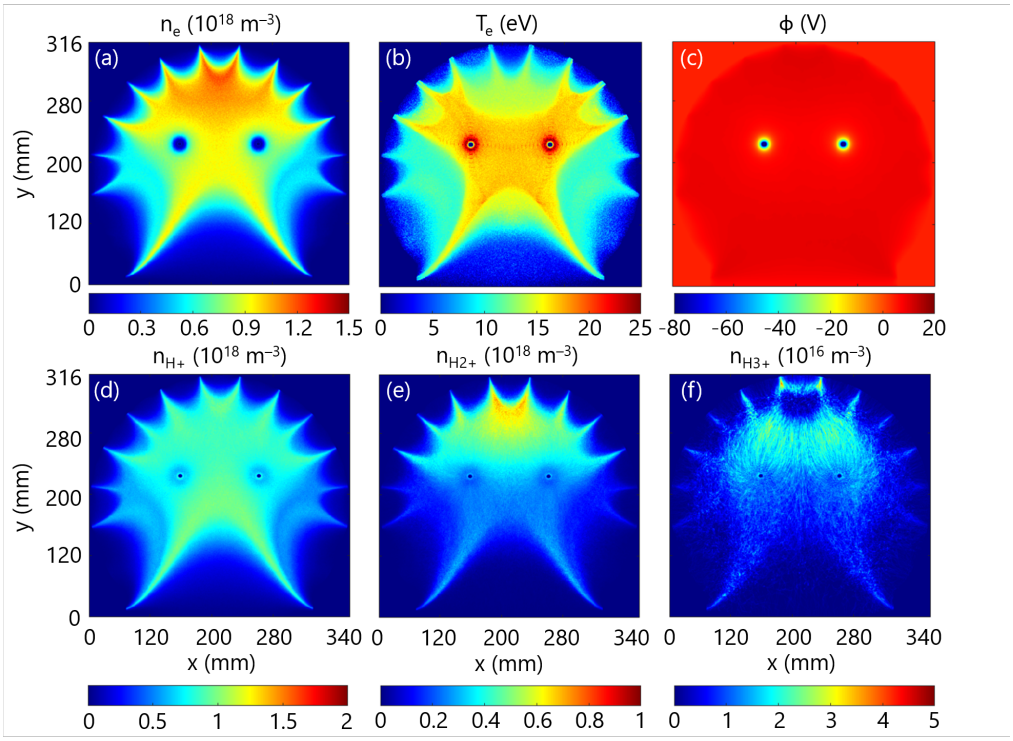

Figure 12.6: Electron density n_e (a), electron temperature T_e (b), plasma potential ϕ (c), H^+, H_2^+, and H_3^+ ion densities (d,e,f). All maps are obtained from a stationary state at 0.3 Pa background gas pressure, after having included the Coulomb collisions between positive ions.

The maximum plasma density obtained in the low background pressure regime is roughly $2 \times 10^{18}\,\mathrm{m}^{-3}$, as can be seen from the n_e map in Figure 12.6. Half of the positive ion density is given by H^+ ions, which are evenly distributed along the entire plasma volume, whereas the heavier species are more abundant in the rear part of the simulation domain, specifically on top of the filaments. This might be caused by the fact that this region is continuously filled with injected H_2 molecules, therefore H_2^+ and H_3^+ ions are more easily generated by electron impact ionization. On the bottom half of the source, instead, dissociation might be the dominant process.

12.3.2 High background gas pressure

The high pressure case was obtained starting from the stationary solution at 0.3 Pa background pressure, with the number of injected molecules per timestep being doubled. Figure 12.7 shows the time evolution of the macroparticle number N_{MP}, the growth rates, and the macroparticle temperature T_{MP} averaged on the entire domain.

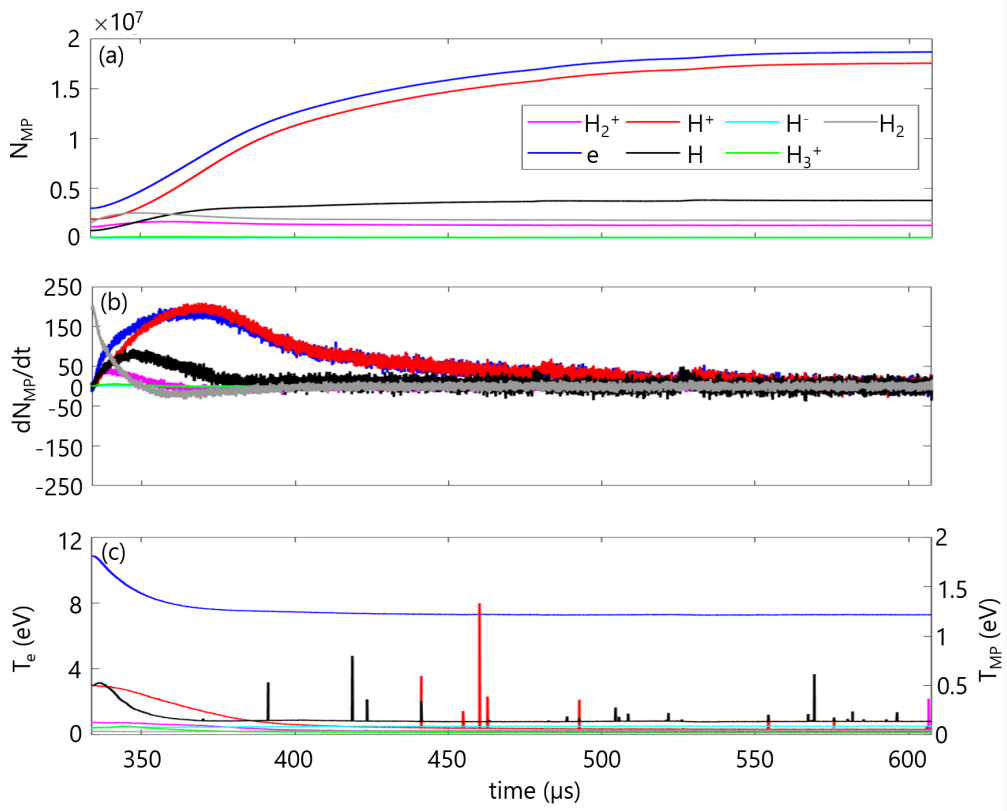

Figure 12.7: Number of macroparticles N_{MP} (a), macroparticle rates dN_{MP}/dt (b), and temperature (c) as a function of the simulated time.

As already seen for p_{bg}=0.3 Pa case, at first the growth rate of electrons and H_2^+ ions grows significantly due to the ionization of background gas molecules. After that, dissociation and atom ionisation become dominant, yielding to the formation of a large fraction of H^+ ions, which in this case account for the almost totality of positive ion density, as can be seen from Figure 12.8. Also in this case, the heavier species are localized in the upper region of the chamber, close to the injection boundary. In accordance with the plasma parameters shown in Figure 12.8, the neutral depletion is much more evident in this case, as can be seen from Figure 12.9. In particular the atom density at the center of the chamber becomes dominant over the molecular density.

As shown by the n_e map in Figure 12.8, by doubling the injected H_2 flow the plasma density is tripled with respect to the low pressure case. At the same time, the plasma potential is increased of a few V, whereas the electron temperature decreases with respect to the low pressure case. Other plasma species show the same behaviour, as can be seen in Figure 12.7.

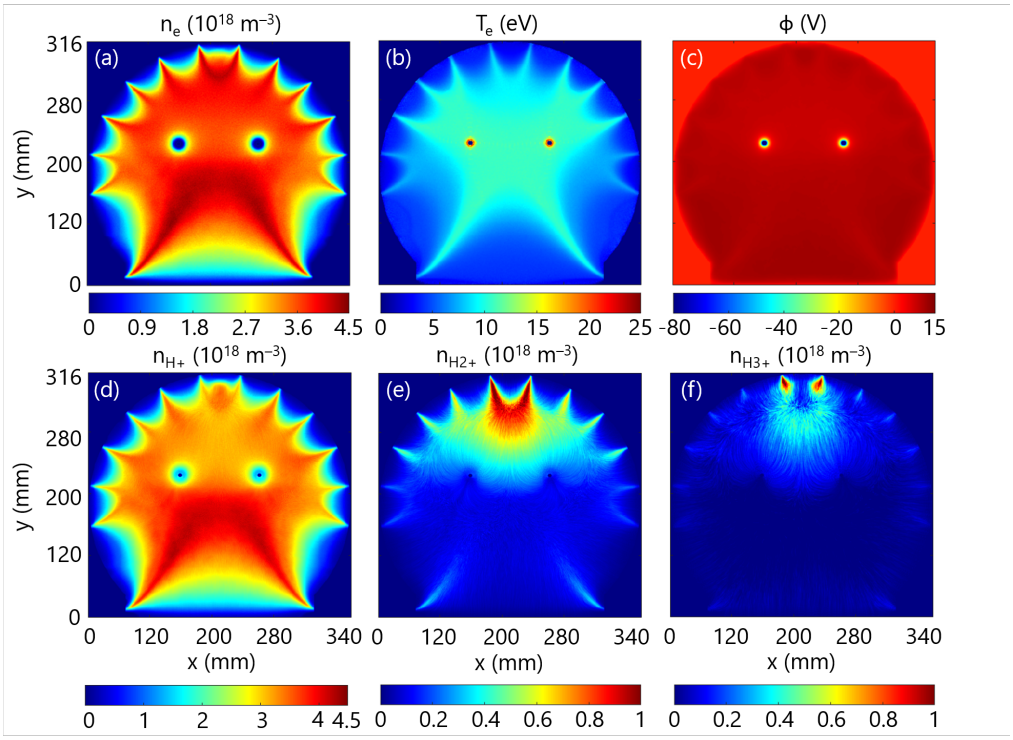

Figure 12.8: On the top row, from left to right: electron density n_e, electron temperature T_e, and plasma potential ϕ; on the bottom row, from left to right: H^+, H_2^+, and H_3^+ ion densities. All maps are obtained from a stationary state at 0.6 Pa background gas pressure.

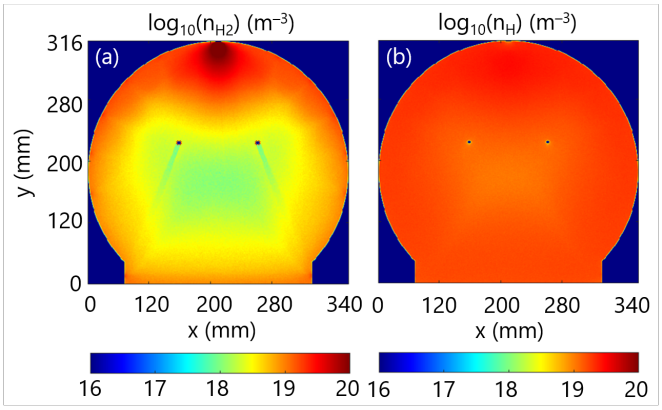

Figure 12.9: Molecular (left) and atomic (right) hydrogen densities obtained for a stationary solution in the high pressure case.

12.3.3 Comparison between low and high pressure cases

Figure 12.10 shows the vertical axial profiles of electron density, temperature, and plasma potential, for both the low and high background gas pressure values. The most evident difference is the plasma density in the proximity of the PG electrode.

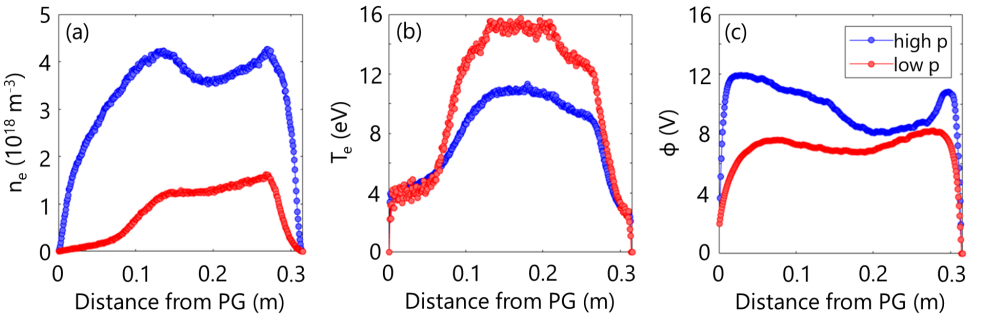

Figure 12.10: Electron density n_e (a), electron temperature T_e (b), and plasma potential ϕ (c) for the low (red) and high (blue) background gas pressure cases.

In the low pressure case, the density value at the PG is very low, of the order of 10^{16} m^{-3}, whereas in the high pressure case it becomes much larger. This might be explained by the reduction of the electron temperature in correspondence of the peak density: in fact, less energetic electrons are more likely to diffuse across the perpendicular magnetic field. However, the electron temperature in the proximity of the PG electrode is the same for both cases, which is around 4 eV. This rather high value might imply that some collisional processes are still missing; for instance, electrons might lose some energy due to either vibrational or rotational excitation of the background molecules, which is not currently included in this model. The plasma potential close to the PG electrode, which is biased at 2 V, is doubled in the high pressure case.

Dissociation degree and ion effective mass

Given all the density maps obtained from the simulation, the total background gas dissociation degree δ and the positive ion effective mass m_{eff} can be obtained as:

$$\delta = \frac{n_{\text{H}}}{n_{\text{H}} + n_{\text{H}_2}} \tag{12.2}$$

$$m_{\text{eff}} = \frac{n_{\text{H}^+} + 2n_{\text{H}_2^+} + 3n_{\text{H}_3^+}}{n_{\text{H}^+} + n_{\text{H}_2^+} + n_{\text{H}_3^+}} \tag{12.3}$$

Figure 12.11 shows the two-dimensional maps of the aforementioned quantities for both the low and high pressure cases. The average values are:

	low p	high p
δ	0.52	0.75
m_{eff}	1.23	1.07

Table 12.2: Averaged values of dissociation degree δ and ion effective mass m_{eff} for the low and high pressure regimes.

In both low and high pressure regimes, the background gas dissociation degree is larger than 50%, causing the ion effective mass to be very close to the proton mass, especially in the high pressure case.

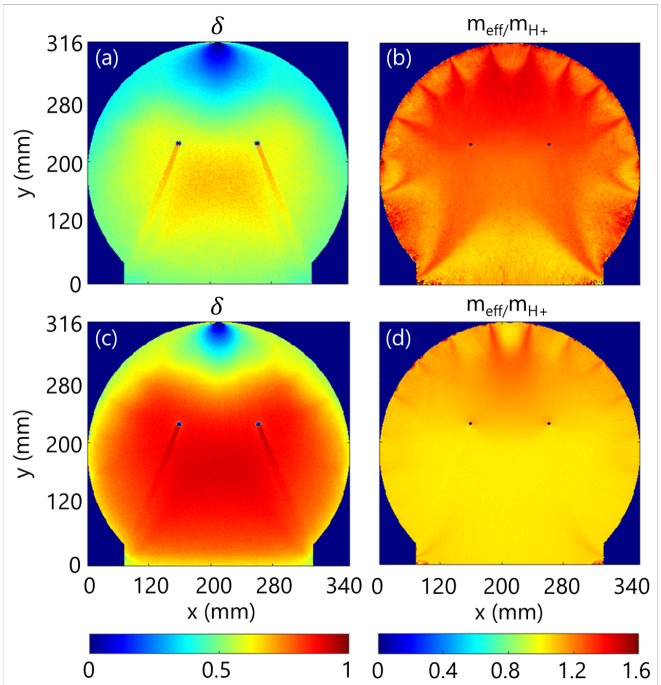

Figure 12.11: Background gas dissociation degree δ and positive ion effective mass m_{eff} for the low (a,b) and high (c,d) background gas pressure cases.

With reference to the spatial distribution of both quantities, the dissociation degree is higher where the neutral depletion takes place. It is worth noticing that, in the proximity of the chamber surfaces, δ is lower due to wall recombination. In both pressure regimes, the ion effective mass is lower in the bottom half of the plasma chamber, underneath the two filaments, with the effect being more visible in the high pressure case.

Chapter summary

A first numerical characterization of the plasma discharge in a kamaboko-like negative ion source was presented. As discussed at the beginning of this chapter, the motivation of this study lies in the fact that, with the same accelerator design, filament-based sources have better performances in terms of beam divergence. This difference is related to source plasma behaviour, more precisely to the properties of the precursor species, fast atoms and positive ions. The first important result is the simulation capability of reaching a reasonable stationary state given only three input parameters, the background gas pressure, the arc current, and the filament bias. In addition, two cases are compared, featuring low and high background gas pressure respectively. The plasma behaviour with increasing gas pressure is as expected, with the plasma density and potential increasing, whereas the electron temperature decreases. By analysing the gas dissociation degree and the ion effective mass, it appears that the dissociation processes are dominant over the molecular ionization, causing the ion effective mass to be very close to the proton mass and yielding a total dissociation fraction higher than 50%.

Conclusions and future work

Conclusions

The purpose of this PhD project was to understand the physics of fusion relevant negative ion sources, aiming at the identification of the most relevant processes to be investigated for future optimization. This is motivated by the present research and development of the ITER neutral beam injector, for which a RF driven ion source will be exploited. Despite its unprecedented use in negative ion beams for fusion, this choice was necessary to avoid maintenance in a neutron-activated environment, as ITER will be in the future. Improving the present performances of such design is a very challenging objective, and becomes even more complex when both tight technical constraints and demanding requirements such as the ones for the ITER source need to be addressed.

Pursuing the goal of my research project encouraged me to devote a great and fruitful effort in developing a wider perspective on the topic. At first, it was necessary to understand well the operation of the machine. The operation of the ITER NBI will require to accelerate large negative ion currents to high energies. To this purpose, the ion beam will be extracted from the ion source in a multi-beamlet configuration. Given the high energies, all beamlets are required to be well focused so as to avoid overheating of the accelerator electrodes. In order to efficiently accelerate negative ions, the fraction of co-accelerated electrons needs to be reduced. This is realised in most of the ion source by means of a magnetic filter field, and specifically in the extraction region by dedicated suppression magnets. Other stray electrons are produced by beam-gas interaction; they also must be reduced to avoid unwanted thermal loads: for this reason, the background gas pressure inside the ion source needs to be limited. Another main challenge is negative ion generation in the source: indeed, the volumetric production rate is not sufficient to provide the needed negative ion availability in the extraction region; furthermore, they are easily destroyed by plasma electrons with high enough temperature. To overcome these issues, caesium is evaporated inside the source in such a way to exploit the surface production mechanism, which allows the formation of a plasma rich in negative ions within the extraction region. To preserve these ions, the electron temperature needs to be reduced using the already mentioned magnetic filter field. The overall complexity of such concept is reflected and exacerbated when transferred into engineering specifications and technological constraints of the design, resulting in limits on heat loads, insulation requirements for ensuring high-voltage holding, vacuum tightness and compatibility, requirements for compatibility of electrical circuits with high RF power. All these aspects need to be addressed while taking into account the limited space availability as well as mechanical tolerances for alignment and construction. As a consequence of the design complexity, the behaviour of this source is strongly dependent on the operating parameters which, in turn, are significantly correlated among each other. This results in considerable challenges for data interpretation, as well as for modelling activities.

My research work required the synergic use of different tools and this provided several inputs, which had to be correlated in order to acquire a deeper understanding of plasma behaviour. By participating in the operations and often managing the experiment, I also had the chance to acquire a more general knowledge of the most relevant cold plasma diagnostics, learning their

individual assets and liabilities, as well as understanding how they can be used together for attaining a deeper knowledge about the source plasma. On the other hand, I needed to cope with limited diagnostic capabilities: although SPIDER is equipped with a larger diagnostics set than any other ion source in the field of fusion (and of particle accelerators for other purposes), the size and complexity of the SPIDER source are such that even more measurements are required for understanding and improving its performances. Indeed, negative ion sources for fusion, particularly RF based machines, are characterized by strong spatial variations of plasma properties and this can be challenging for diagnostic purposes: for instance, line-averaged measurements such as optical ones cannot provide spatially resolved estimations and, for this reason, they need to be complemented with other diagnostic tools capable of providing local estimations of the plasma properties.

Numerical modelling also proved to be strategic: indeed, comparing the numerical and experimental results was undoubtedly useful for improving the simulation code by identifying what was missing for achieving a successful benchmark against experimental data and, in turn, this allowed me to gain insights on the most relevant physical processes at the basis of the experimental evidences. This knowledge was also fundamental for understanding what types of measurements and diagnostics should be developed and installed, both for addressing open points highlighted during the source operation, and for providing quantitative estimations of the already identified issues.

Installing the triple Langmuir probe on SPIDER, as well as participating in the design of new electrostatic sensors, provided me some knowledge about part of the steps required for operating a diagnostic in the SPIDER source. In particular, in addition to the aforementioned hands-on experience on mechanical interfaces and thermal loads, on electrical insulation and on vacuum compatibility, I also had the opportunity to compare my experience in SPIDER with a smaller development source such as Batman Upgrade (BUG), during a one-month joint experimental campaign. After the restrictions due to the Covid-19 pandemic, I was really longing for having direct experience of an international collaboration and for exchanging ideas and opinions with an expert team such as the BUG one. Participating in the operation of a much simpler but yet more mature facility made me even more aware of the challenge (and ambition) of the R&D activities devoted to the full-scale ITER neutral beam injectors and their beam sources.

The main results of my work will be briefly summarised in the following, since all of them were already discussed at the end of each chapter. After this, the outcomes of this work and some ideas for future developments will be described.

Summary of the main results

The need for interpreting the SPIDER experimental findings I needed to upgrade the GPPIC code in many respects, including magnetic field topology, neutral kinetics, plasma-wall interaction, thermionic emission, surface production, and Coulomb collisions. These features were fundamental for studying:

- the horizontal uniformity of the source plasma properties, which was proven to be caused by too strong permanent magnets at the lateral surfaces;
- how plasma properties affect magnetic cusp confinement, providing a useful comparison between analytical and numerical estimations of leak width and Plasma Exclusion Zone (PEZ);
- plasma discharge in filament-based negative ion sources, providing some first insights on the plasma properties to be compared with the findings from RF sources.

The numerical models were also useful for interpreting some experimental findings regarding

the energy distribution of the positive ions reaching the extraction region in RF sources, and measured data from the triple Langmuir probe. Regarding the former topic, the presence of a wide ion energy distribution in RF sources was confirmed also in numerical simulations, which provided qualitatively similar trends. As for the triple probe findings, the noticeable difference between standard and reversed FF configurations was explained also with the aim of numerical results from the investigation of plasma expansion from two drivers along the plane perpendicular to the magnetic FF itself. In addition, I studied the influence of the bias electrodes on both source plasma and beam properties on the basis of experimental evidences.

Outcomes of this work

Through this work, I was able to participate in the R&D activities on the SPIDER ion source, and on negative ion sources for fusion in general, while actively contributing to the development of specific expertise within the research team.

From a more practical point of view, part of my numerical studies were useful for designing some modifications of the SPIDER beam source that are being implemented, such as the replacement of the permanent magnets on the lateral walls. In a similar way, the electrostatic sensors designed during my work will be actually installed and operated in SPIDER, with the aim of providing spatially resolved measurements of the source plasma properties.

Concerning simulation activities, a first numerical characterisation of the plasma discharges in filament-arc based negative ion sources by PIC method was carried out. The approach I followed for this study is quite new, and can potentially deliver very useful information in the future.

According to my experience, applying the PIC method to specific problems always requires a strong effort in developing dedicated code. In this sense, my work did not provide a general purpose numerical tool: in other words, good competences in both code development and plasma physics must be acquired for its use. Nonetheless, the GPPIC code can be further improved by including a more accurate implementation of the surface production mechanism, by taking into account the actual atom and positive ion fluxes reaching the converter surfaces. In addition, the integration of a dedicated RF module, for estimating the spatial distribution of the RF power deposition within the drivers, would strongly improve the simulation results, allowing a more direct comparison with the experimental findings.

Future developments

The SPIDER source will soon resume operations: a first phase will be devoted to investigating specific scientific topics, including the comparison of the original RF drivers and the design modifications, to which I gave a relevant contribution. To this purpose, both diagnostic systems I designed during this work will be capable of providing very valuable measurements of the plasma behaviour, helping at assessing the improvements.

Based on the results of the first SPIDER operations as well as of my investigations, it is clear that understanding the neutrals dynamics inside the ion source is a very urgent issue: indeed, the background gas properties affect the electron density and temperature in the ion source. For instance, the dissociation degree and the temperature of the dissociated atoms are directly linked to the negative ion production: this should be investigated also in filament-arc based ion sources, as it might be one of the key features for explaining the very different properties of the extracted beam with respect to RF-based ion sources.

As discussed at the beginning of this section, the source operating pressure is limited to 0.3 Pa. However, as also experimentally verified, RF sources would surely benefit from operating

with larger background gas pressure: a larger background gas density would lead to a denser plasma. However, since increasing the source pressure is not acceptable for the accelerator, alternative solutions for increasing the source plasma density should be employed: for instance, this can be achieved by improving the magnetic confinement in the ion source. In the SPIDER source, a new configuration of permanent magnets will be installed, covering all the surfaces of the expansion chamber (only the lateral walls were covered in the original design).

Finally, having a non-negligible transverse magnetic field also within the RF drivers was found to considerably affect the plasma properties within the drivers and, consequently, the RF coupling. Investigating this phenomenon requires new three-dimensional models, as the cylindrical symmetry approximation no longer applies to this case. The experimental characterization of such an issue will also be possible in the next future thanks to the construction of a new test facility at the NBTF, dedicated to detailed studies on the operation of the RF source.

Bibliography

[1] A. Grubler et al. “Energy Transitions”. In: *Encyclopedia of Earth (Environmental Information Coalition, National Council for Science and the Environment)* (2008).

[2] International Energy Agency (IEA). URL: http://www.iea.org.

[3] International Atomic Energy Agency (IAEA). URL: https://www.iaea.org/publications/15268/energy-electricity-and-nuclear-power-estimates-for-the-period-up-to-2050.

[4] BP Energy Outlook 2023. URL: http://www.bp.com.

[5] E. Rachlew A. Horvath. “Nuclear power in the 21st century: challenged and possibilities”. In: *Ambio* 45 (2016), pp. 38–49. DOI: https://doi.org/10.1007/s13280-015-0732-y.

[6] ITER organization. URL: http://www.iter.org.

[7] M. Kikuchi et al. “Fusion Physics”. In: International Atomic Energy Agency (IAEA), 2012.

[8] F. Taccogna et al. “Modeling of negative ion source. I. Gas kinetics and dynamics in the expansion chamber”. In: *Phys. Plasmas* 14 (2007). DOI: https://doi.org/10.1063/1.2752514.

[9] M. Wada M. Bacal. “Negative hydrogen ion production mechanisms”. In: *Appl. Phys. Rev.* 2 (2015). DOI: https://doi.org/10.1063/1.4921298.

[10] G.D. Alton. “Semi-empirical relationships for work function changes”. In: *Surface Science* 175 (1986), pp. 226–240. DOI: https://doi.org/10.1016/0039-6028(86)90094-4.

[11] M. Seidl et al. “Negative surface ionization of hydrogen atoms and molecules”. In: *J. Appl. Phys.* 79 (1996). DOI: https://doi.org/10.1063/1.361285.

[12] R. McAdams et al. “Transport of negative ions across a double sheath with a virtual cathode”. In: *Plasma Sources Sci. Technol.* 20 (2011). DOI: https://doi.org/10.1088/0963-0252/20/3/035023.

[13] U. Fantz D. Wuenderlich R. Gutser. “PIC code for the plasma sheath in large caesiated RF sources for negative hydrogen ions”. In: *Plasma Sources Sci. Technol.* 18 (2009). DOI: https://doi.org/10.1088/0963-0252/20/3/035023.

[14] J.R. Coupland et al. “A Study of the Ion Beam Intensity and Divergence Obtained from a Single Aperture Three Electrode Extraction System”. In: *Rev. Sci. Instrum.* 44 (1973). DOI: https://doi.org/10.1063/1.1686366.

[15] A. Pimazzoni et al. “Influence of positive ions on the beamlet optics for negative-ion neutral beam injectors”. In: *Nucl. Fusion* 63 (2023). DOI: https://doi.org/10.1088/1741-4326/acd12d.

[16] K. Miyamoto et al. “Effect of basic physical parameters to control plasma meniscus and beam halo formation in negative ion sources”. In: *J. Appl. Phys.* 114 (2013). DOI: https://doi.org/10.1063/1.4820571.

[17] J.J. Barroso K.G. Kostov. “Space-charge-limited current in cylindrical diodes with finite-length emitter”. In: *Phys. Plasmas* 9 (2002). DOI: https://doi.org/10.1063/1.1446876.

[18] S.R. Lawrie et al. “Detailed beam and plasma measurements on the vessel for extraction and source plasma analyses (VESPA) Penning H- ion source”. In: *Rev. Sci. Instrum.* 87.02B122 (2016). DOI: https://doi.org/10.1063/1.4934580.

[19] M. Barbisan et al. “First results from beam emission spectroscopy in SPIDER negative ion source”. In: *Plasma Physics and Controlled Fusion* 63.125009 (2021). DOI: https://doi.org/10.1088/1361-6587/ac2eb2.

[20] Y. Haba et al. “Characterisation of negative ion beam focusing based on phase space structure”. In: *New J. Phys.* 22 (2020). DOI: https://doi.org/10.1088/1367-2630/ab6d41.

[21] G. Chitarin et al. “Improvements of the magnetic field design for SPIDER and MITICA negative ion beam sources”. In: *AIP Conf. Proc.* 1655 (2015). DOI: https://doi.org/10.1063/1.4916450.

[22] L. Schiesko et al. “A study on backstreaming positive ions on a high power negative ion source for fusion”. In: *Nucl. Fusion* 51 (2011). DOI: https://doi.org/10.1088/0029-5515/51/11/113021.

[23] R.S. Hemsworth et al. “Overview of the design of the ITER heating neutral beam injectors”. In: *New J. Phys* 19 (2017). DOI: https://doi.org/10.1088/1367-2630/19/2/025005.

[24] D. Wuenderlich et al. “NNBI for ITER: status of long pulses in deuterium at the test facilities BATMAN Upgrade and ELISE”. In: *Nucl. Fusion* 61 (2021). DOI: https://doi.org/10.1088/1741-4326/ac1758.

[25] Y. Takeiri et al. “High-power and long-pulse injection with negative-ion-based neutral beam injectors in the Large Helical Device”. In: *Nucl. Fusion* 46 (2006). DOI: https://doi.org/10.1088/0029-5515/46/6/S01.

[26] M. Kuriyama et al. “Development of Negative-Ion Based NBI System for JT-60”. In: *J. Nucl. Sci. Technol.* 35 (1998). DOI: https://doi.org/10.1080/18811248.1998.9733940.

[27] V. Toigo et al. “Progress in the ITER neutral beam test facility”. In: *Nucl. Fusion* 59 (2019). DOI: https://doi.org/10.1088/1741-4326/ab2271.

[28] D. Marcuzzi et al. “Detail design of the beam source for the SPIDER experiment”. In: *Fus. Eng. Des.* 85 (2010). DOI: https://doi.org/10.1016/j.fusengdes.2010.05.039.

[29] A. Rizzolo et al. “Characterization of the SPIDER Cs oven prototype in the CAesium Test Stand for the ITER HNB negative ion sources”. In: *Fus. Eng. Des.* 146 (2019). DOI: https://doi.org/10.1016/j.fusengdes.2019.01.053.

[30] N. Marconato et al. “Numerical and experimental assessment of new magnetic field configuration”. In: *IEEE Trans. Plasma Sci.* 50.11 (2022). DOI: https://doi.org/10.1109/TPS.2022.3167859.

[31] A. Zamengo et al. “Power supply system for large negative ion sources: Early Operation experience on the SPIDER experiment”. In: *Fus. Eng. Des.* 173 (2021). DOI: https://doi.org/10.1016/j.fusengdes.2021.112790.

[32] R. Pasqualotto et al. “Progress on development of SPIDER diagnostics”. In: *AIP Conf. Proc.* 1869 (2017). DOI: https://doi.org/10.1063/1.4995740.

[33] R. Pasqualotto et al. “Improvement of SPIDER diagnostic systems”. In: *Fus. Eng. Des.* 194 (2023). DOI: https://doi.org/10.1016/j.fusengdes.2023.113889.

[34] E. Sartori et al. “Development of a set of movable electrostatic probes to characterize the plasma in the ITER neutral beam negative-ion source prototype”. In: *Fus. Eng. Des.* 169 (2021). DOI: https://doi.org/10.1016/j.fusengdes.2021.112424.

[35] A. Maistrello et al. “Overview on electrical issues faced during the SPIDER experimental campaigns”. In: *Fus. Eng. Des.* 190.113510 (2023). DOI: https://doi.org/10.1016/j.fusengdes.2023.113510.

[36] M. Pavei et al. “SPIDER plasma grid masking for reducing gas conductance and pressure in the vacuum vessel”. In: *Fus. Eng. Des.* 161 (2020). DOI: https://doi.org/10.1016/j.fusengdes.2020.112036.

[37] L. Garrigues J.P. Boeuf B. Chaudhury. “Physics of magnetic filter for negative ion sources. I. Collisional transport across the filter in an ideal, 1D filter”. In: *Phys. Plasmas* 19 (2012). DOI: https://doi.org/10.1063/1.4768676.

[38] U. Fantz et al. “Plasma expansion across a transverse magnetic field in a negative hydrogen ion source for fusion”. In: *Pasma Sources Sci. Technol.* 23 (2014). DOI: https://doi.org/10.1088/0963-0252/23/4/044002.
[39] G. Fubiani et al. “Modelling of plasma transport and negative ion extraction in a magnetized radio-frequency driven source”. In: *New J. Phys.* 19.015002 (2017). DOI: https://doi.org/10.1088/1367-2630/19/1/015002.
[40] P. Minelli F. Taccogna. “PIC modelling of negative ion sources for fusion”. In: *New J. Phys.* 19.015012 (2017). DOI: https://doi.org/10.1088/1367-2630/aa5305.
[41] C. Poggi et al. “Langmuir Probes as a Tool to Investigate Plasma Uniformity in a Large Negative Ion Source”. In: *IEEE Trans. Plas. Sci.* 50 (2022). DOI: https://doi.org/10.1109/TPS.2022.3181805.
[42] G. Serianni et al. “SPIDER, the Negative Ion Source Prototype for ITER: Overview of Operations and Cesium Injection”. In: *IEEE Trans. Plas. Sci.* 50 (2023). DOI: https://doi.org/10.1109/TPS.2022.3226239.
[43] A. Pimazzoni et al. “Co-extracted electrons and beam inhomogeneity in the large negative ion source SPIDER”. In: *Fus. Eng. Des.* 168 (2021). DOI: https://doi.org/10.1016/j.fusengdes.2021.112440.
[44] M. Ugoletti et al. “SPIDER Beam Homogeneity Characterization Through Visible Cameras”. In: *IEEE Trans. Plas. Sci.* 50 (2022). DOI: https://doi.org/10.1109/TPS.2022.3218129.
[45] I. Mario et al. “Reconstruction of the large multi-aperture beam via IR calorimetry technique and beam emission spectroscopy at the ELISE test facility”. In: *Nucl. Fus.* 60.066025 (2020). DOI: https://doi.org/10.1088/1741-4326/ab8573.
[46] E. Sartori et al. “First operations with caesium of the negative ion source SPIDER”. In: *Nucl. Fus.* 62 (2022). DOI: https://doi.org/10.1088/1741-4326/ac715e.
[47] C. Poggi et al. “First tests and commissioning of the emittance scanner for SPIDER”. In: *Fus. Eng. Des.* 168 (2021). DOI: https://doi.org/10.1016/j.fusengdes.2021.112659.
[48] R. Agnello et al. “Study of Negative Ion Beamlets Produced in SPIDER by Beam Emission Spectroscopy”. In: *IEEE Trans. Plas. Sci.* 50 (2022). DOI: https://doi.org/10.1109/TPS.2022.3180169.
[49] P. Veltri et al. “Towards low divergence beams for the ITER neutral beam injection system”. In: (2022).
[50] K. Tsumori et al. “Construction of a Filament-RF driven hybrid negative ion source at NIFS”. In: *8th International symposium on Negative Ion Beams and Sources (NIBS)*. 2022.
[51] CUDA. URL: https://developer.nvidia.com/cuda-zone.
[52] C. K. Birdsall and A. B. Langdon. “Plasma Physics via Computer Simulation”. In: Adam Hilger, 1991.
[53] P. Monasse. “Extraction of the Level Lines of a Bilinear Image”. In: *Image Processing On Line* 9 (2019). DOI: https://doi.org/10.5201/ipol.2019.269.
[54] M. Stynes C. Grossmann H. Roos. “Numerical treatment of partial differential equations”. In: Springer New York, 2007.
[55] M.H. Schultz Y. Saad. “GMRES: A Generalized Minimal Residual Algorithm for solving nonsymmetric linear systems”. In: *SIAM Journal of Scientific and Statistical Computing* 7.3 (1986). DOI: https://doi.org/10.1137/0907058.
[56] H.A. van der Voorst. “Bi-CGSTAB: A Fast and Smoothly Converging Variant of Bi-CG for the Solution of Nonsymmetric Linear Systems”. In: *SIAM Journal of Scientific and Statistical Computing* 13.2 (1992). DOI: https://doi.org/10.1137/0913035.
[57] J. P. Boris. “Relativistic plasma simulation-optimization of a hybrid code”. In: *Proceedings of the Fourth Conference on Numerical Simulation of Plasmas* 2.3 (1970), pp. 3–67.
[58] W.H. Weinberg. “Direct Reactivity of Gas Phase Atomic Hydrogen with Adsorbed Species”. In: *J. Am. Chem. Soc.* 29 (1996). DOI: https://doi.org/10.1021/ar9500980.

[59] V. Vahedi and M. Surendra. “A Monte Carlo collision model for the particle-in-cell method: applications to argon and oxygen discharges”. In: *Comput. Phys. Commun.* 87 (1995), pp. 179–198. DOI: https://doi.org/10.1016/0010-4655(94)00171-W.
[60] K. Nanbu. “Theory of cumulative small-angles collisions in plasmas”. In: *Phys. Rev. E* 55.4 (1997). DOI: https://doi.org/10.1103/PhysRevE.55.4642.
[61] U. Samm R.K. Janev D. Reiter. “Collision processes in Low-Temperature Hydrogen Plasmas”. In: EIRENE database, 2003. URL: https://www.eirene.de/index.html.
[62] M. A. Lieberman and A. J. Lichtenberg. “Principles of Plasma Discharges and Materials Processing”. In: John Wiley and Sons, 2005.
[63] N. Marconato et al. “An optimized and flexible configuration for the magnetic filter in the SPIDER experiment”. In: *Fus. Eng. Des.* 166.112281 (2021). DOI: https://doi.org/10.1016/j.fusengdes.2021.112281.
[64] P. McNeely et al. “Neutral depletion in an H- source operated at high RF power and low input gas flow”. In: *Plasma Sources Sci. Technol* 20.045005 (2011). DOI: https://doi.org/10.1088/0963-0252/20/4/045005.
[65] K. Jousten. “Handbook of Vacuum Tehcnology”. In: Wiley, 2016.
[66] P. McNeely et al. “A Langmuir probe system for high-power RF-driven negative ion sources on high potential”. In: *Plasma Sources Sci. Technol.* 18.014011 (2009). DOI: https://doi.org/10.1088/0963-0252/18/1/014011.
[67] D. Zielke et al. “RF power transfer efficiency and plasma parameters of low pressure high power ICPs”. In: *J. Phys. D: Appl. Phys.* 54.15 (2021). DOI: https://doi.org/10.1088/1361-6463/abd8ee.
[68] E. Sartori et al. “Plasma properties in giant negative ion sources for fusion”. In: ICIS Conference, 2023.
[69] B. Zaniol et al. “First measurements of optical emission spectroscopy on SPIDER negative ion source”. In: *Rev. Sci. Instrum.* 91.013103 (2020). DOI: https://doi.org/10.1063/1.5128900.
[70] U. Fantz et al S. Briefi. “Spectroscopic investigations of the ion source at BATMAN upgrade”. In: *AIP Conf. Proc.* 2052.040005 (2018). DOI: https://doi.org/10.1063/1.5083739.
[71] V. Candeloro et al. “Design of an optimised movable electrostatic diagnostic for the investigation of plasma properties in a large negative ion source”. In: *Fus. Eng. Des.* 190.113652 (2023). DOI: https://doi.org/10.1016/j.fusengdes.2023.113652.
[72] F.F. Chen. “Langmuir probe analysis for high density plasmas”. In: *Phys. Plasmas* 8.3029 (2001). DOI: https://doi.org/10.1063/1.1368874.
[73] E. Sartori et al. “Analysis of current–voltage characteristics for Langmuir probes immersed in an ion beam”. In: *Rev. Sci. Instrum.* 91.023504 (2020). DOI: https://doi.org/10.1063/1.5128669.
[74] T. Romesser N. Hershkowitz K.N. Leung. “Plasma Leakage Through a Low-beta Line Cusp”. In: *Phys. Rev. Lett.* 35.277 (1975). DOI: https://doi.org/10.1103/PhysRevLett.35.277.
[75] R.C. Woods I.D. Sudit. “A study of the accuracy of various Langmuir probe theories”. In: *J. Appl. Phys.* 76.4488 (1994). DOI: https://doi.org/10.1063/1.357280.
[76] I.D. Sudit and F.F. Chen. “RF compensated probes for high-density discharges”. In: *Plasma Sources Sci. Technol.* 3.162 (1994). DOI: https://doi.org/10.1088/0963-0252/3/2/006.
[77] B. Pouradier-Duteil et al. “Development of a Collisional Radiative Model for Hydrogen-Cesium Plasmas and Its Application to SPIDER”. In: *IEEE Trans. Plasma Sci.* 50.11 (2022). DOI: https://doi.org/10.1109/TPS.2022.3190561.
[78] G. Serianni et al. “Spatially resolved diagnostics for optimization of large ion beam sources”. In: *Rev. Sci. Instrum.* 93.081101 (2022). DOI: https://doi.org/10.1063/5.0084797.

[79] T. Sekiguchi S. Chen. “Instantaneous Direct-Display System of Plasma Parameters by means of Triple Probe”. In: *J. Appl. Phys.* 36.2363 (1965). DOI: https://doi.org/10.1063/1.1714492.
[80] I.H. Hutchinson. “Principles of plasma diagnostics”. In: Cambridge University Press, 2002. DOI: https://doi.org/10.1017/CBO9780511613630.
[81] M. Bacal et al. “Roles of a Plasma Grid in Negative Hydrogen Ion Source”. In: *AIP Conf. Proc.* 1655.020001 (2015). DOI: https://doi.org/10.1063/1.4916410.
[82] M. Hanada et al. “A 14cm x 36cm volume negative ion source producing multi-ampere H- ion beams”. In: *Rev. Sci. Instrum.* 61.499 (1990). DOI: https://doi.org/10.1063/1.1141233.
[83] E. Speth et al. “Overview of the RF source development programme at IPP Garching”. In: *Nucl. Fus.* 46.S220 (2006). DOI: https://doi.org/10.1088/0029-5515/46/6/S03.
[84] P. Franzen et al. “The IPP RF source: a high power, low pressure negative ion source for the neutral bema injection system of ITER”. In: *AIP Conf. Proc.* 993 (2008). DOI: https://doi.org/10.1063/1.2909175.
[85] W. Kraus et al. “Long pulse H- beam extraction with a RF driven ion source with low fraction of co-extracted electrons”. In: *AIP Conf. Proc.* 1097 (2009). DOI: https://doi.org/10.1063/1.3112522.
[86] G. Serianni et al. “First operation in SPIDER and the path to complete MITICA”. In: *Rev. Sci. Instrum.* 91.023510 (2020). DOI: https://doi.org/10.1063/1.5133076.
[87] P. Agostinetti et al. “Physics and engineering design of the accelerator and electron dump for SPIDER”. In: *Nucl. Fus.* 51.063004 (2011). DOI: https://doi.org/10.1088/0029-5515/51/6/063004.
[88] R.N. Franklin et al. “Electronegative plasmas - why are they so different?” In: *Plasma Sources Sci. Technol.* 11 (2002). DOI: https://doi.org/10.1088/0963-0252/11/3A/304.
[89] U. Fantz et al. “Negative Hydrogen Ion Sources for Fusion: From Plasma Generation to Beam Properties”. In: *Frontiers Physics* (2021). DOI: https://doi.org/10.3389/fphy.2021.709651.
[90] A. Shepherd et al. “Initial Results From the SPIDER Beamlet Current Diagnostic”. In: *IEEE Trans. Plasma Sci.* 50.11 (2022). DOI: https://doi.org/10.1109/TPS.2022.3176757.
[91] A. Kojima et al. “Progress in long-pulse production of powerful negative ion beams for JT-60SA and ITER”. In: *Nucl. Fus.* 55.063006 (2015). DOI: https://doi.org/10.1088/0029-5515/55/6/063006.
[92] U. Fantz et al. “Ion source developments at IPP: On the road towards achieving the ITER-NBI targets and preparing concepts for DEMO”. In: *J. Phys.: Conf. Ser.* 2244.012049 (2022). DOI: https://doi.org/10.1088/1742-6596/2244/1/012049.
[93] G. Matthieussent C. Koch. “Collisional diffusion of a plasma in multipolar and picket fence devices”. In: *Phys. Fluids* 26 (1983). DOI: https://doi.org/10.1063/1.864139.
[94] Y. Jiang et al. “Magnetic cusp confinement in low-beta plasmas revisited”. In: *Phys. Plasmas* 27.113506 (2020). DOI: https://doi.org/10.1063/5.0014058.
[95] M. Wada M. Bacal M. Sasao. “Negative ion sources”. In: *J. Appl. Phys.* 129.221101 (2021). DOI: https://doi.org/10.1063/5.0049289.
[96] V. Candeloro et al. “Influence of plasma parameters on the effectiveness of multi-cusp magnetic field confinement in negative ion sources”. In: *J. Instrum.* 18.C06028 (2023). DOI: https://doi.org/110.1088/1748-0221/18/06/C06028.
[97] N. Marconato et al. “Integration of new sets of magnets for improved plasma confinement in the SPIDER experiment”. In: *Fus. Eng. Des.* 193.113805 (2023). DOI: https://doi.org/10.1016/j.fusengdes.2023.113805.
[98] R. Casagrande et al. “Integration studies of RF solid-state generators in the electrical system of NBTF experiments and ITER HNB”. In: *Fus. Eng. Des.* 189.113478 (2023). DOI: https://doi.org/10.1016/j.fusengdes.2023.113478.

[99] V. Candeloro et al. “Development of a Triple Langmuir Probe for Plasma Characterization in SPIDER”. In: *IEEE Trans. Plasma Sci.* 50.11 (2022). DOI: https://doi.org/10.1109/TPS.2022.3173885.
[100] A. Hatayama et al. “Present status of numerical modeling of hydrogen negative ion source plasmas and its comparison with experiments: Japanese activities and their collaboration with experimental groups”. In: *New Journal of Physics* 20.065001 (2018). DOI: https://doi.org/10.1088/1367-2630/aac0c6.
[101] O.W. Richardson. “Thermionic Emission from Hot Bodies”. In: Watchmaker Publishing, 2003.
[102] J. Pamela et al. “European negative ion based neutral beam developments”. In: *Fus. Eng. Des.* 26 (1995). DOI: https://doi.org/10.1016/0920-3796(94)00207-N.
[103] M. Kashiwagi et al. “Study of beamlets extracted from a multiaperture and five stage acceleration system”. In: *Rev. Sci. Instrum.* 93.053301 (2022). DOI: https://doi.org/10.1063/5.0080804.
[104] D.R. Schultz P.S. Krstic. “Consistent definitions for, and relationships among, cross sections for elastic scattering of hydrogen ions, atoms, and molecules”. In: *Phys. Rev. A* 60.2118 (1999). DOI: https://doi.org/10.1103/PhysRevA.60.2118.
[105] FEMM. URL: https://www.femm.info/wiki/HomePage.